Nonlinear dynamics of one-dimensional Josephson junction arrays

by

Shinya Watanabe

Master of Engineering, University of Tokyo (1991)
Master of Science, University of Illinois, Urbana-Champaign (1990)

Submitted to the Department of Mathematics
in partial fulfillment of the requirements for the degree of

Doctor of Philosophy

at the

MASSACHUSETTS INSTITUTE OF TECHNOLOGY

June 1995

Signature of Author ....
Department of Mathematics
May 5, 1995

Certified by.. ....
Steven H. Strogatz
Associate Professor
Thesis Supervisor

Accepted by ....
Richard Stanley, Chairman
Applied Mathematics Committee

Accepted by ....
David Vogan, Chairman
Departmental Graduate Committee

Nonlinear dynamics of one-dimensional Josephson junction arrays

by

Shinya Watanabe

Submitted to the Department of Mathematics
on May 5, 1995, in partial fulfillment of the
requirements for the degree of
Doctor of Philosophy

Abstract

This thesis presents a study of electronic circuits containing superconducting devices called Josephson junctions. Such circuits may be viewed mathematically as collections of coupled nonlinear oscillators. Two types of circuits are analyzed in detail: one-dimensional arrays of N junctions, connected either in series or in parallel.

For the series arrays, a longstanding mystery surrounds the stability properties of a certain disordered periodic solution known as the splay state. Contrary to what one would expect from bifurcation theory, this solution appears to be almost always neutrally stable in $O(N)$ directions in phase space. This peculiarity is studied here, first for the important limiting case $\beta = 0$, where β is the McCumber parameter. A fully nonlinear global result has been obtained: an explicit coordinate transformation has been found that generates $O(N)$ constants of motion, reduces the dimension of the system by $O(N)$, and uncovers a remarkable picture of the phase space foliated by invariant low-dimensional subspaces.

As β is perturbed away from 0, the global structure becomes weakly broken. Solutions now drift slowly from one subspace to another, as revealed by accurate computations of the Floquet multipliers about the splay state for various values of β. In the large-β limit, the stability of the splay state is determined by an asymptotic analysis. The asymptotic results show excellent agreement with the numerical computations.

The situation is more complicated for the parallel arrays, whose model equation is the damped driven discrete sine-Gordon equation. The phase space is non-degenerate, and multiple attractors are observed to coexist. These attractors are manifested experimentally as steps and hysteresis loops in the current-voltage characteristics of the circuit. My work is aimed at explaining the experiments of my collaborators. By a local analysis around two types of periodic solutions, predictions have been obtained which show good agreement with the data.

Thesis Supervisor: Steven H. Strogatz
Title: Associate Professor

Contents

Introduction

Many systems in nature may be regarded as collections of coupled nonlinear oscillators [Str&Ste93]. The dynamics of such systems is important in connection with such diverse disciplines as astronomy, mathematics, mechanics, physics, and engineering [Guc&Hol83, Arn89, Lic&Lie92, Str94]. More recently, problems in biology [Win80] and in chemistry [Kur84] have also been treated from this point of view. Mathematically, an oscillator system is described as a (possibly large) number of coupled ordinary differential equations.

This thesis is concerned with a specific class of dissipative systems composed of N *identical* limit cycle oscillators. To study such dissipative systems analytically, it is natural to start from the uncoupled limit, and then to introduce a weak coupling among the oscillators. In the limit of zero coupling, all the oscillators simply converge to a common limit cycle, but with arbitrary phase differences among them.

When coupling among oscillators is included but is "weak" (compared to the attraction strength of the limit cycle), the limit cycle hardly deforms, and amplitude variations are negligible [Kur84]. In this case, the state of an oscillator can be well-approximated by a single variable, its phase on the orbit. However, the coupling has a major effect in the direction tangential to the orbit, leading to a slow drift of the relative phases. Now the phase relationships are no longer arbitrary, and the coupling interactions among oscillators can result in mutual entrainment. In particular, for identical oscillators, this entrainment of phases often leads to complete phase-locking, in which the phase differences converge to certain fixed values. If all the phase differences vanish, the system is said to be completely synchronized or phase coherent. If not, the final phases are "disordered" to some extent. In any case, the oscillators rotate at the same frequency, and the solution is periodic.

Periodic attractors are of great importance in many applications, and we are most interested in these solutions in this thesis. Also, the stability of periodic solutions is well understood in terms of Floquet theory, even though the characteristic exponents are often hard to evaluate. Thus, there is the possibility of treating such stability problems analytically in practical problems. Our approach in this thesis is to apply the tools of nonlinear oscillations and dynamical systems theory to practical problems, rather than to develop new techniques which may be applicable in more complicated situations.

Collections of limit cycle oscillators naturally arise in engineering. In microelectronics, for instance, advances in material science have made it possible to fabricate massive numbers of oscillators on a single chip. Semiconductor lasers are one such example. Because each element is tiny, such systems have several advantages, such as well-controlled material properties, energy efficiency, and a long life span. On the other hand, there is a disadvantage that only minute amounts of power can be generated, unless many elements are operated collectively. Therefore, it is desirable to form a large array of the elements, and to operate the whole array in a coherent in-phase oscillation.

Since it is impractical (if not impossible) to manipulate the state of individual lasers, the array must be synchronized either by a spontaneous mechanism or by a simple external condition. The appropriate tricks are usually found by trial and error, and this is not an easy task. Often, disordered solutions rather than coherent ones are observed, much to the disappointment of the experimenters. Even when coherent oscillations are achieved, one lacks a systematic knowledge of what parameters affect the performance in which way. For example, it is reported [Mor&Koj93] that coherent oscillation has been achieved in a two-dimensional 8×8 array of a certain type of semiconductor lasers. However, these authors also reported that a transition from an out-of-phase mode to a coherent mode occurs as the injection currents are increased, but this observation was explained only in a heuristic way.

Josephson junctions and arrays

A superconducting device called a Josephson junction is another microscopic structure with great technological potential. A single junction is already used as the standard voltage reference, while pairs of junctions (SQUIDs) are widely used for high-sensitivity measurements of magnetic fields. However, more elaborate uses of many coupled junctions are expected [ASC94] because of their extraordinarily high oscillation frequencies and ease of fabrication, from one junction to thousands of junctions on a chip as desired [Ben&Bur91].

Physically, a Josephson junction is an insulating (or normal-state) layer of $\sim$10Å thickness between two superconducting domains. The layer breaks the macroscopic wavefunctions of the superconductors [Orl&Del91], and couples the two sides only weakly through a quantum tunneling effect. The state variable of a junction is the phase difference ϕ between the two wavefunctions.

A widely used RCSJ (resistively and capacitively shunted junction) model assumes that a junction is equivalent to a circuit with three branches in parallel: a capacitive, a resistive, and a superconducting one. By writing Kirchhoff's current law, the model equation in a dimensionless form becomes [Orl&Del91]:

$$\beta\ddot{\phi} + \dot{\phi} + \sin\phi = I/I_c \tag{1}$$

where I is the current through the junction, and I_c (the critical current) and β (the dimensionless Stewart-McCumber parameter) are material constants.

The variable ϕ is an angle variable. In fact, Eq.(1) is analogous to the equation of motion for a mechanical pendulum, with a linear damping and a drive I/I_c. Then, ϕ is analogous to the pendulum angle measured from the downward vertical. For any $\beta > 0$, it is known that for sufficiently large I, Eq.(1) has a unique limit cycle solution $\phi(t+T) = \phi(t) + 2\pi$ (where T is the period). (Note that we consider rotating solutions rather than librating ones.) Thus, a Josephson junction can be viewed as a limit cycle oscillator.

The time unit in Eq.(1) is normalized by the so-called plasma frequency of a junction, which is typically in the range of GHz to THz. It is this ultra-high frequency that makes Josephson junctions technologically attractive. Josephson junctions have many of the same advantages and disadvantages as the semiconductor lasers. The material properties can be controlled over a wide range and can be made nearly uniform; the McCumber paramcter, in particular, can be varied from 10^{-6} to 10^{7} with a deviation less than 10% (see Chap. 3). However, single junctions produce only very small signals, say currents of around 1mA or voltages of around 1mV.

One way to generate more power is to find a mechanism that brings many coupled junctions into coherent oscillation. For this purpose, both one-dimensional (1D) [Jai&al84] and two-dimensional (2D) [Ben&Bur91] arrays have been tested intensively. ("Stacked arrays" consisting of layers of 1D and 2D arrays have also been attracting attention recently [Ust&al93]. Much less research has been done on three-dimensional arrays, and the existing studies are mostly numerical, e.g. [Sug&al93].) The 1D arrays can be further classified as either series or parallel. Figure 1 shows several typical array configurations.

One-dimensional series arrays with $\beta = 0$

The 1D series array (Fig. 1(a)) is the simplest of all. Efforts to synchronize such arrays are reviewed in detail in [Jai&al84]. Hadley and Beasley [Had&Bea87] were the first to analyze series arrays from the point of view of dynamical systems theory. Following their pioneering work, a number of physicists and mathematicians have participated in the subsequent study of series arrays. In the past few years, a peculiar behavior of

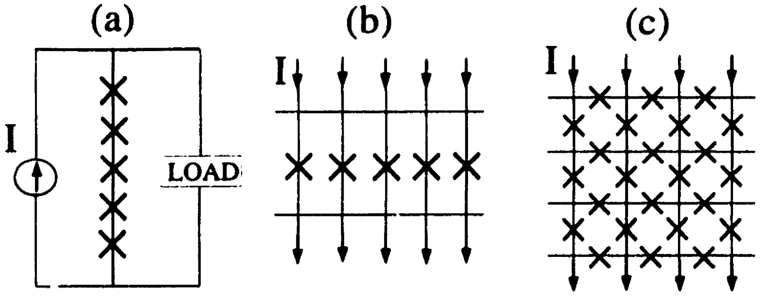

Fig. 1 Typical Josephson array configurations. The crosses denote junctions. (a) 1D series arrays, (b) 1D parallel arrays, (c) 2D arrays

series array was discovered. Chapters 1 and 2 of this thesis are devoted to a further study of this peculiarity.

Equations of motion for series arrays are derived in Chap. 1 (Sec. 2). N junctions are connected in series, but an external load shunted in parallel to the array turns out to be necessary to provide coupling among the junctions. The equations have a coherent in-phase periodic solution. The local stability of this solution was studied in [Had&Bea87, Had&al88] by numerically evaluating the Floquet multipliers. The stability depends on the parameters I/I_c and β, and the type and the values of the load parameters. In the "overdamped" limit $\beta = 0$, the solution was found to be stable when the load looks inductive and unstable when it looks capacitive.

This overdamped limit seemed analytically tractable since the limit cycle solution of an uncoupled junction Eq.(1) can be explicitly obtained in this case. Thus, analytical papers which followed [Had&Bea87, Had&al88] have mostly assumed this limit. Also, the difference in dynamics with $\beta = 0$ and with a small but finite β is expected to arise only in the initial transient during which the junctions settle down to the limit cycle. Thus, as far as the long-term dynamics are concerned, the results obtained for the overdamped limit were also expected to be applicable to systems in the vicinity of the limit.

The main question asked was, when the in-phase solution is destabilized with a capacitive load, which solution does the system converge to? Numerically, a disordered periodic solution, in which phases of junctions are staggered equally in time, was observed in this case. This solution was given different names by various authors (such as the anti-phase state), but following [Tsa&al91] we call it the splay state since the phases are splayed over one period.

Then, the linear stability of the splay state was studied. One naturally expected switching between stability and instability, but the results were surprising. Numerical computation [Tsa&Sch92, Nic&Wie92] found that at least $N-2$ Floquet multipliers are all *unity*, meaning that there are that many linearly *neutrally* stable directions to infinitesimal perturbations. This observation remained true for most types of load, regardless of the values of the parameters. This conclusion was unexpected. According to bifurcation theory, one generically expects to find neutral stability only at the critical values of parameters. Also, since the splay state certainly appears attracting, one wondered whether the splay state was not linearly stable but nonlinearly stable.

Meanwhile, analytical progress on the stability of the splay state was carried out mostly for the case of a purely resistive load. This load is expected to be close to the critical situation when the in-phase solution switches its stability, but the governing equations become considerably simpler with more symmetries to rely on. The linear stability analysis was then carried out after the equations are averaged over a fast time scale [Swi&al92] or in the $N=\infty$ limit [Str&Mir92]. It appeared, deepening the mystery further, that all N Floquet multipliers were unity in these approximations. Numerical integration of the unaveraged governing equations [Tsa&al91] not only agreed with this local analysis, but showed an even more remarkable observation that all trajectories lie on nested invariant 2-tori in the phase space.

All the above peculiar observations suggested that series arrays must have a special property. Chapter 1 of this thesis is devoted to explaining these observations and to uncovering the nature of this special property in the $\beta=0$ limit. In particular, an unusual global structure in the N-dimensional phase space is identified as responsible. To state briefly, the structure can be understood from the "toy-model" system:

$$\dot{\theta}_j = \frac{1}{N}\sum_{k=1}^{N}\cos(\theta_k-\theta_j-\delta) \quad , \quad j=1,\ldots,N \tag{2}$$

which is not merely a toy, but actually the weak-coupling limit of the governing equations obtained by averaging over a fast time scale [Wie&Swi95]. The angles θ_j are the slowly modulated part of the phases ϕ_j, and the parameter δ may be expressed in terms of the load and the current I/I_c.

This averaged system is fully nonlinear in appearance, but is completely solved in Chap. 1 (Sec. 4). By use of a coordinate transformation shown in Sec. 3, the system is first reduced to merely three equations. This transformation generates $N-3$ constants of motion, and uncovers a remarkable global picture of the phase space foliated by invariant three-dimensional subspaces. The dynamics only occurs within a subspace in which the initial condition is chosen to be.

Moreover, a Lyapunov function can be found for the reduced dynamics, and it shows that the direction of the flow is either toward a coherent in-phase oscillation or toward a disordered solution, depending on the sign of $\sin \delta$. The disordered solution can be the splay state, but Eq.(2) shows that there is a whole $(N-2)$-dimensional invariant manifold of disordered periodic solutions in which the splay state is the most symmetric one. The observed neutral stability corresponds to perturbations along this invariant manifold.

The averaged equations are only approximate, but it can be proven that the most important result, the foliated structure of the phase space, still persists in the original equations for the series array. The array hence belongs to the "almost completely integrable" class of dynamical systems which, I believe, does not have many examples.

The analysis is valid for all $N \geq 3$. In particular, the $N = \infty$ limit of the system reduces to a continuity equation in a periodic domain with a simple velocity field. Here we also have a rare example of an infinite-dimensional system that is explicitly reducible to a small system of ordinary differential equations (Chap. 1, Sec. 5). The reduction process from the PDE to the ODE's is somewhat similar to the inverse scattering method for completely integrable Hamiltonian systems (Chap. 1, App. B).

One-dimensional series arrays with $\beta > 0$

Chapter 2 of this thesis continues the study of the 1D series array. The analysis so far has been limited to the overdamped limit $\beta = 0$. One would usually expect that such delicate features as foliations and integrability would be destroyed when the system is perturbed away from the limit of zero β. However, numerical evidence to the contrary was offered by Nichols and Wiesenfeld [Nic&Wie92]. They reported that $N-2$ Floquet multipliers of the splay periodic solution are still unity even when $\beta > 0$ for most types of the load. Thus, an early conjecture was that the phase-space structure might persist for $\beta > 0$, and one might hope to *prove* that the splay state is neutrally stable.

However, as we show numerically in Chap. 2 (Sec. 2), the splay solution is *not* neutrally stable when $\beta > 0$. Indeed, an asymptotically stable splay state can be found. This does not mean that our calculation is in contradiction to Nichols and Wiesenfeld's. In Sec. 3, we present systematic computations of the Floquet multiplier dependence as β is varied, and $N-2$ multipliers are found to be *extremely* close to, but not exactly equal to, unity for the parameters used in [Nic&Wie92]. (One trivial multiplier is always equal to unity.) Or rather, it is more correct to say that the multipliers deviate substantially from unity only when β is relatively small. This explains all the previous observations without a paradox, and thus the mystery surrounding the neutral stability of the splay state seems to be mostly solved.

This computation of Floquet multipliers, however, has led to a new analytical result as its byproduct. We have noticed that the multipliers behave in a simple fashion when $\beta \gg 1$. To explain this observation, we have carried out a perturbation analysis and derived the averaged equations to account for the slow modulation of the phases, under the assumption that a combination parameter $\epsilon = 1/(I\sqrt{\beta})$ is small (Sec. 4). Somewhat surprisingly, the averaged equations are identical in form to Eq.(2). Only the dependence of the parameter δ on the load is different. Estimates of the Floquet multipliers by this analysis show excellent agreement with the numerics.

To summarize the results for 1D series arrays, the analysis in Chaps. 1 and 2 predicts the stability of the coherent in-phase periodic solution in two opposite limits of the parameter β. In the $\beta = 0$ limit it is common knowledge [Jai&al84, Had&Bea87, Wie&Swi95] that the in-phase state is stable for inductive loads and unstable for capacitive loads. In the weak coupling limit, our analysis of Chap. 1 proves this statement. In the opposite limit of $\beta \gg 1$ (or more precisely $\epsilon \ll 1$), the opposite statement is now seen to be true: the in-phase state is unstable when inductance is included in the load and stable for a purely capacitive load. Since ϵ involves a combination of both β and I/I_c, there is an interesting singular behavior near $\beta = 0$ when $I \gg I_c$ (Chap. 2, Sec. 5). This result provides a warning and a practical statement that needs to be considered when one selects the load in applications.

Decoupling in two-dimensional arrays

Before we turn to the parallel arrays in Fig. 1(b), it seems more straightforward to discuss the 2D arrays of Fig. 1(c). The 2D arrays are probably the most interesting of all three configurations in Fig. 1, and at the same time the most difficult to analyze. There have been many numerical as well as experimental papers, in addition to more theoretical ones in the overdamped limit, written on these arrays. The great interest in 2D arrays comes (at least in part) from their ability to *spontaneously* phase-lock. Note that 1D series arrays require an external load to couple the junctions, whereas 2D arrays do not require such an external device; by just uniformly injecting and extracting the current, the arrays can become phase-locked. Although the dynamics has not been directly visualized yet, an indirect indication of coherent oscillation in the 2D arrays has been obtained experimentally [Ben&Bur91].

The 2D arrays can be also viewed as a clean laboratory model for the study of the high-T_c superconductors. The structure of the high-T_c materials is still not understood, but it is known that the grain structure of the materials forms natural Josephson weak contacts at the grain boundaries, and the whole crystal can be viewed as a network of distributed Josephson junctions, e.g. [Sch&al94]. A transition from the normal state to the superconducting state might be modelled by studying a simple 2D array.

Couplings in the 2D arrays are provided via two mechanisms. One is through the inductances between cells, as occurs in any electronic circuits of a similar shape. Another mechanism is from the "flux-quantization" condition, and this is unique to superconductors. This condition requires the directed sum of the ϕ's around each cell to balance the total magnetic flux penetrating through the cell, and thus provides couplings among nearby junctions. Influence of the induced fields is known to affect certain static properties significantly (e.g. current distribution) in the 2D arrays [Phi&al93]. However, it is perhaps better to start analysis of the phase-locking mechanism by considering one coupling mechanism at a time.

A preliminary study of the dynamics of the 2D arrays, excluding the effects of inductances, has been carried out [Wat&al95] though not included in this thesis. In simulations, the arrays are observed to phase-lock even if the coupling is due only to flux-quantization. This occurred only when an external field is applied and when a sufficiently large bias current is injected. Interestingly, the convergence process toward the phase-locked state involves different time scales that become more widely separated as the junctions become underdamped. Providing a random initial condition of ϕ's and $\dot{\phi}$'s, the velocities $\dot{\phi}$'s become almost uniform in the fast time scale; the vertical junctions start to rotate in a similar frequency while the horizontal junctions come to rest. Then, vertical junctions phase-lock in each row on the intermediate time scale. Finally, the vertical junctions in the column direction phase-lock on the slow time scale.

The separation of the intermediate and the slow time scales depends on the applied magnetic field, and becomes very different when the field is weak. It is clear that the coupling mechanism within a row is different from that within a column. In fact, the two directions almost decouple, and one can think of the 2D array as being made up of N nearly independent rows only weakly coupled in the vertical direction. It appears that the weak coupling is in some sense similar to the coupling mechanism in the series arrays although this similarity has not yet been explored deeply. Each row, then, may be viewed as a one-dimensional parallel array of the sort depicted in Fig. 1(b).

Such a picture becomes increasingly valid when the injected current is reduced and the array does not have enough energy to rotate all the vertical junctions. Then, in simulations, only several "switched" rows are observed to actively oscillate as if they were independent one-dimensional parallel arrays. The other "non-switched" rows become nearly quiescent, with small voltage drops across them. (These "row-switched states" have been also experimentally observed [vdZ&al88].) In these states the switched rows become phase-locked [Phi&al94] even when they are separated by quiescent rows. This indicates that the rows still feel one another, and are coupled weakly. For these observations, we see that the study of the dynamics of one row is very important and useful for understanding of the two-dimensional problems.

One-dimensional parallel arrays

The 1D parallel arrays, shown in Fig. 1(b), are interesting from this connection to the 2D arrays, but they have, in their own right, another more straightforward connection to a problem that has been studied for decades. The 1D arrays can be viewed as discrete versions of one-dimensional long continuous Josephson junctions ("long" so that the spatial dependence of the phase ϕ must be taken into account). The long junctions are governed by the damped driven sine-Gordon equation. The connection to the completely integrable unperturbed sine-Gordon problem has been studied since the 1970's [McL&Sco78], e.g. the effect of dissipation on the propagation of solitons. Long junctions are also studied from a technological point of view as a possible high-frequency oscillator.

Similarly, 1D arrays of (small area) junctions are governed by the damped driven sine-Gordon equation in the discrete domain. There are many similarities to the continuous case, but there are also phenomena unique to the discrete nature of the system. For technological applications, there is also recently growing interest in the discrete arrays because they have advantages over their continuous counterparts in that the output impedance and frequencies can be higher (see Chap. 3).

The 1D parallel arrays can be phase-locked coherently and achieve an in-phase oscillation only when there is no external magnetic field. When an external field is applied, the flux-quantization requires that the phases of neighboring junctions be spread apart. In this case, a train of kinks (or vortices) propagate through the arrays, providing even stronger coupling of the phases.

When kinks propagate, the boundary conditions become important. Arrays with open ends are simpler to fabricate, and are suitable for an important application as flux-flow oscillators [Lik86]. However, reflected waves from the boundaries complicate the dynamics, and make it hard to study the phase-locking of junctions.

An annular geometry, which leads to periodic boundary conditions, avoids such complications, and is more suitable for analytical treatment. Moreover, because of flux-quantization, this geometry "traps" an integer number of kinks within itself [Dav&al83, Ust&al92], thus it becomes possible to study the dynamics of a single isolated kink.

Chapter 3 of this thesis is devoted to a systematic study of a 1D parallel array of N junctions in a circular geometry. It soon becomes clear that the governing equations do not possess simple properties like the integrability found in the original sine-Gordon equation or the 1D series arrays; instead the phase space is non-degenerate and complex, as we observe apparently chaotic attractors in our simulations. Multiple attractors coexist and hysteresis loops are observed in the current-voltage characteristics as the bias current is swept up and down.

Therefore, my work in this chapter is aimed mainly at explaining the experiments of my collaborators. Experimentally measurable quantities are the current-voltage (I–V) characteristics of the whole array. As the control parameter I/I_c is changed, the frequency of oscillation (averaged over all junctions and in time) changes. The frequency is proportional to the voltage via Josephson's voltage relation, thus the effect appears in the I–V as a shift in the voltage. When the system remains on the same attractor in the phase space, the characteristic draws a continuous curve as I/I_c is varied. When the system suddenly jumps from one attractor to another, it is manifested in the I–V as a discontinuous change in the voltage.

When an array with underdamped junctions is measured, a novel structure appears in the I–V; some parts of the characteristic become almost "vertical," or with a nearly constant voltage, even when I is changed. These so-called "steps" reflect the system's preference to lock in to that voltage, or frequency. Such experimental structures are due to resonances and phase-locking in the system. Prediction of the voltage locations of these steps necessarily requires study of the dynamics of the system.

This problem was approached by first studying the continuous counterpart of the arrays. The continuous sine-Gordon equations are much better studied than the discrete ones, and a review of the previous results shows two useful clues for further investigation (Chap. 3, Sec. 2). First, such equations in a periodic domain support two branches of traveling wave solutions, and second, the waveforms are very different in the two branches. For low voltages, the system supports characteristic kink-like waves with a strongly non-uniform shape. For high voltages, the waveform becomes nearly uniform, as if the kinks were "stretched".

The I–V curve predicted from the continuum approximation does not explain several features observed in the experiments and simulations of the discrete arrays. Still, it is found that the traveling waves persist in the discrete arrays, and there are still two branches in the I–V curve. Steps are observed in both branches, but the mechanisms responsible for their creation are found to be different for the two branches (Sec. 4).

In the low-voltage region, a propagating kink induces radiation that phase-locks to the kink. This phase-locking is responsible for the creation of the steps (Sec. 5). In the high-voltage region, on the other hand, the traveling wave solutions are spatially and temporally uniform. These "whirling periodic solutions" undergo parametric instabilities at certain drive strengths. The instabilities cause the system to bifurcate from the traveling wave solutions, and more complicated attractors emerge from the onset (Sec. 6). By a local analysis around each type of traveling wave solution, the locations of the steps are predicted. They are in good agreement with the experimental data obtained for a ring of $N = 8$ junctions.

Format of the thesis

Each of the three chapters is prepared as a publishable unit, and includes its own introduction, background, and references.

Chapter 1 is written with Steve Strogatz, and is reproduced from *Physica*, **74D**, pp.197–253 (1994). Preliminary results on the averaged equations Eq.(2) were reported earlier in *Physical Review Letters*, **70**, 2391 (1993).

Chapter 2 is written with Jim Swift, and has been recently submitted to *Journal of Nonlinear Science.*

Chapter 3 is coauthored by Steve Strogatz, Herre van der Zant, and Terry Orlando, and is still in a draft stage. Preliminary reports have already been published; the results of Section 5 were announced in *Physical Review Letters*, **74**, 174 (1995), and the results of part of Section 6 appeared in *ibid.*, **74**, 379 (1995).

As the first author of each chapter, I have carried out a "substantial" part of the research described here. There were numerous ideas and steps contributed by the coauthors, in addition to contributions from people acknowledged in each chapter, but it seems inappropriate to identify these contributions one by one. However, I would like to emphasize that the experiments in Chap. 3 were carried out solely by Herre van der Zant and Terry Orlando.

References

[Str&Ste93] S.H. Strogatz and I. Stewart, *Sci. Am.*, **269**, 102 (1993).

[Guc&Hol83] J. Guckenheimer and P. Holmes, *Nonlinear oscillations, dynamical systems, and bifurcations of vector fields* (Springer, New York, 1983).

[Arn89] V.I. Arnol'd, *Mathematical methods of classical mechanics*, (2nd ed., Springer, New York, 1989).

[Lic&Lie92] A.J. Lichtenberg and M.A. Lieberman, *Regular and chaotic dynamics* (2nd ed., Springer, New York, 1992).

[Str94] S.H. Strogatz, *Nonlinear dynamics and chaos* (Addison-Wesley, Reading, MA, 1994).

[Win80] A.T. Winfree, *The geometry of biological time* (Biomath., vol.8, Springer, New York, 1980).

[Kur84] Y. Kuramoto, *Chemical oscillations, waves, and turbulence* (Springer, New York, 1984).

[Mor&Koj93] R.A. Morgan and K. Kojima, *Opt. Lett.*, **18**, 352 (1993).

[ASC94] Appl. Supercond. Conf. (Boston, MA, 1994), to appear in *IEEE Trans. Appl. Supercond.* (Sept. 1995).

[Ben&Bur91] S.P. Benz and C.J. Burroughs, "Two-dimensional arrays of Josephson junctions as voltage-tunable oscillators", *Supercond. Sci. Tech.* **4**, 561–567 (1991).

[Orl&Del91] T.P. Orlando and K.A.Delin, *Foundations of Applied Superconductivity* (Addison-Wesley, Reading, MA, 1991).

[Jai&al84] A.K. Jain, K.K. Likharev, J.E. Lukens and J.E. Sauvageau, *Phys. Rep.*, **109**, 310 (1984).

[Sug&al93] R. Sugano, T. Onogi, and Y. Murayama, *Phys. Rev. B*, **48**, 13784 (1993).

[Ust&al93] A.V. Ustinov, H. Kohlstedt, M. Cirillo, N.F. Pedersen, G. Hallmanns, and C. Heiden, *Phys. Rev. B*, **48**, 10614R (1993).

[Had&Bea87] P. Hadley and M.R. Beasley, *Appl. Phys. Lett.*, **50**, 621 (1987).

[Had&al88] P. Hadley, M.R. Beasley, and K. Wiesenfeld, *Phys. Rev. B*, **38**, 8712 (1988).

[Tsa&Sch92] K.Y. Tsang and I.B. Schwartz, *Phys. Rev. Lett.*, **68**, 2265 (1992).

[Nic&Wie92] S. Nichols and K. Wiesenfeld, *Phys. Rev. A*, **45**, 8430 (1992).

[Swi&al92] J.W. Swift, S.H. Strogatz, and K. Wiesenfeld, *Physica* **D 55**, 239-250 (1992).

[Tsa&al91] K.Y. Tsang, R.E. Mirollo, S.H.Strogatz, and K. Wiesenfeld, *Physica*, **D 48**, 102 (1991).

[Str&Mir92] S.H. Strogatz and R.E. Mirollo, *J. Stat. Phys.*, **63**, 613 (1991).

[Wie&Swi95] K. Wiesenfeld and J.W. Swift, to appear in *Phys. Rev. E*, (1995).

[Sch&al94] K. Schlenga, G. Hechtfischer, W. Walkenhorst, P. Müller, F.X. Régi, H. Savary, J. Schneck, M. Veith, W. Brodkorb, and E. Steinbeiß, *Proc. Appl. Supercond. Conf.* (Boston, MA, 1994).

[Phi&al93] J.R. Phillips, H.S.J. van der Zant, J. White, and T.P. Orlando, *Phys. Rev. B*, **47**, 5219 (1993).

[Wat&al95] S. Watanabe, M. Barahona, E. Trías, H.S.J. van der Zant, S.H. Strogatz, and T.P. Orlando, to be published.

[vdZ&al88] H.S.J. van der Zant, C.J. Muller, L.J. Geerligs, C. Harmans, and J.E. Mooij, *Phys. Rev. B*, **38**, 5154 (1988).

[Phi&al94] J.R. Phillips, H.S.J. van der Zant, and T.P. Orlando, *Phys. Rev. B*, **50**, 9380 (1994).

[McL&Sco78] D. McLaughlin and A.C. Scott, in *Solitons in Action*, (eds. K. Lonngren and A.C. Scott, Academic Pr., New York, 1978).

[Lik86] K.K. Likharev, *Dynamics of Josephson junctions and Circuits*, Gordon and Breach, New York (1986).

[Dav&al83] A. Davidson and N.F. Pedersen, *Appl. Phys. Lett.*, **44**, 465 (1984); A. Davidson, B. Dueholm, B. Kryger, and N.F. Pedersen, *Phys. Rev. Lett.*, **55**, 2059 (1985).

[Ust&al92] A.V. Ustinov, T. Doderer, R.P. Huebener, N.F. Pedersen, B. Mayer, and V.A. Oboznov, Phys. Rev. Lett. **69**, 1815 (1992).

Chapter 1

Constants of motion for superconducting Josephson arrays

Shinya Watanabe and Steven H. Strogatz

reproduced from *Physica*, **74D**, pp.197–253, 1994 with permission

ELSEVIER

Physica D 74 (1994) 197–253

PHYSICA D

Constants of motion for superconducting Josephson arrays

Shinya Watanabe, Steven H. Strogatz

Department of Mathematics, Massachusetts Institute of Technology, Cambridge, MA 02139, USA

Received 10 December 1993; revised 14 February 1994; accepted 14 February 1994
Communicated by H. Flaschka

Abstract

We show that series arrays of N identical overdamped Josephson junctions have extremely degenerate dynamics. In particular, we prove that such arrays have $N-3$ constants of motion for all $N \geq 3$. The analysis is based on a coordinate transformation that reduces the governing equations to an $(N-3)$-parameter family of low-dimensional systems. In the weak-coupling limit, the reduced equations can be analyzed completely. Either all solutions approach the synchronous state or they converge to a continuous family of incoherent oscillations, depending on a certain parameter value. At the transitional value of this parameter, the system becomes completely integrable. Then the phase space is foliated by invariant two-dimensional tori, for any $N \geq 3$. The infinite-N limit of the system is an integro-partial differential equation with rigorously low-dimensional dynamics. It supports solitons in the integrable case, and chaotic waves in the non-integrable case.

1. Introduction

Ever since the pioneering work of Fermi, Pasta and Ulam [1], computers have been used to shed light on the dynamics of many-body systems. Such numerical experiments have often led to serendipitous discoveries, sometimes with important ramifications. For instance, the observation of recurrence phenomena by Fermi et al. ultimately led to the discovery of solitons, the Toda lattice, and the theory of completely integrable systems.

In the past few years, some unexpected results have emerged from numerical experiments on series arrays of superconducting Josephson junctions. One of the goals of this paper is to bring these results to the attention of the dynamical systems community, especially those people interested in integrable systems, coupled oscillators, or condensed-matter physics. A second goal is to present a theory that explains much of what has been observed. Finally, we hope to encourage others to study these problems; the numerics suggest that our theory is incomplete, and that there is further structure waiting to be explained.

The relevant observations concern the following set of equations, obtained as the circuit equations for a broad class of Josephson arrays:

SSDI 0167-2789(94)00033-M

$$\dot{\phi}_j + \sin\phi_j + \dot{Q} = I_b, \quad j = 1, \ldots, N, \tag{1.1}$$

$$L\ddot{Q} + R\dot{Q} + C^{-1}Q = \frac{1}{N}\sum_{k=1}^{N}\dot{\phi}_k, \tag{1.2}$$

where the overdot denotes differentiation with respect to dimensionless time, and R, L, C and I_b are dimensionless circuit parameters.

As long as I_b is not too small, this system has certain periodic solutions known as splay states. Numerical experiments [2,3] show that the splay states have $N-2$ Floquet multipliers equal to $+1$, indicating an enormous degree of neutral stability. This peculiar result holds for a wide range of parameters and circuit configurations. Previous attempts to explain the neutral stability have used averaging theory [4] or continuum limits [5,6], followed by linear stability analysis. While instructive, these approaches are both approximate and local. Rigorous, global results have been lacking.

In this paper we explain the origin of the neutral stability by proving that the system has $N-3$ independent constants of motion. The constants are constructed explicitly, and their geometric meaning is discussed. The key to the analysis is a coordinate transformation that reduces the system to an $(N-3)$-parameter family of low-dimensional systems. Loosely speaking, this transformation plays a role akin to the inverse scattering transform for completely integrable Hamiltonian systems. The analogy is imperfect, however, because the Josephson arrays are typically neither Hamiltonian nor completely integrable — for many array configurations, the associated low-dimensional "reduced systems" can have limit cycles or chaotic solutions.

This paper is organized as follows. Section 2 presents background information on Josephson arrays and summarizes the relevant previous results. In particular, Section 2.4 lists three important numerical observations that have inspired the theoretical work.

The analysis begins in Section 3. We introduce a class of dynamical systems that includes Josephson arrays as a special case. Our transformation method shows that all systems of this class are explicitly reducible to systems with $N-3$ fewer variables. An immediate consequence is a bound on the dynamical complexity of Josephson arrays. For instance, the system (1.1, 1.2) is $(N+2)$-dimensional, yet its dynamics are now seen to be effectively five-dimensional.

Unfortunately, even after the reduction, the system is still difficult to analyze. To make further progress, Section 4 focuses on the averaged equations obtained in the limit of weakly coupled arrays. Now the reduced system can be analyzed completely. A Lyapunov function is obtained and used to prove that the system has a global attracting set. As a certain parameter is varied, the attracting set changes from a synchronous oscillation to a continuous family of incoherent oscillations. At the transitional value of the parameter, the system becomes *completely integrable*. Then almost all solutions are quasiperiodic on 2-tori, and are governed by a Hamiltonian system with one degree of freedom. For this special case, the Hamiltonian provides an extra constant of motion, bringing the total to $N-2$ conserved quantities. This structure underlies the invariant 2-tori detected in the early numerical experiments of Tsang et al. [7]. Of course, one has to be careful about extrapolating from the averaged system to the original, unaveraged Josephson array equations. Some features are destroyed by averaging; for instance, the array equations can have chaotic solutions, but the averaged system cannot. At the end of Section 4, we indicate which features of the averaged system hold in general.

Section 5 deals with reducible systems in the infinite-N limit. Here we have an unusual (but pleasant) example of an infinite-dimensional system whose dynamics are guaranteed *a priori* to be effectively low-dimensional. The results and analysis in Sections 5.1 and 5.2 may be skipped on a first reading; they are similar to the finite-N case. The new results come in Sections 5.3 and 5.4. We investigate a completely integrable limit of the system, and show that it exhibits solitons. We present several numerical examples of soliton interactions as well as a non-integrable case where the waves are chaotic.

Section 6 highlights the limitations of the present study and discusses directions for future research. Appendix A shows the details of a calculation needed in Section 5.1. Appendix B presents a more algebraic and symmetric set of constants of motion for the completely integrable, finite-N case, and shows how they are related to the constants found earlier.

A preliminary report of our work on the integrable case has appeared elsewhere [8].

2. Background: Josephson junctions and arrays

Josephson junctions are superconducting devices that can generate voltage oscillations of high frequency, typically 10^{10}–10^{11} cycles per second. They offer exciting technological possibilities as parametric amplifiers, voltage standards, detectors, mixers, and fast switching devices for digital circuits. For an introduction to Josephson junctions and their applications, see [9–11].

2.1. Dynamics of a single junction

The dynamics of a Josephson junction is described in dimensionless form by

$$\beta\ddot{\phi} + \dot{\phi} + \sin\phi = I_b, \tag{2.1}$$

where $\phi(t)$ is the quantum mechanical phase difference across the junction, I_b is the dimensionless bias current and β is the McCumber parameter, a dimensionless measure of the capacitance of the junction [12,13]. We will assume throughout that I_b is time-independent, corresponding to a dc-current bias.

Note that (2.1) is precisely analogous to the equation governing a damped pendulum driven by a constant torque. This mechanical analog is often useful for visualizing the dynamics of Josephson junctions [9].

Depending on the size, geometry, and type of coupling used in the Josephson junction, the value of β can range from $\beta \approx 10^{-6}$ to much larger values, say $\beta \approx 10^{6}$. From now on, we will assume that all junctions have

$$\beta = 0, \tag{2.2}$$

the so-called *overdamped* limit. This limit is commonly studied in the Josephson literature [9–11], but since it is singular, it may cause some mathematical concern. Our justifications are: (1) For a single junction (or pendulum), the effects of the singular limit are confined to an initial transient. After a rapid relaxation onto a slow manifold, the dynamics for small β and zero β are similar. The same is probably true for arrays, although no results in this direction have been proven. (2) In any case, it is unclear how to make analytical progress for arrays of junctions with $\beta > 0$. The only available result is an existence proof for a particular kind of periodic solution [14].

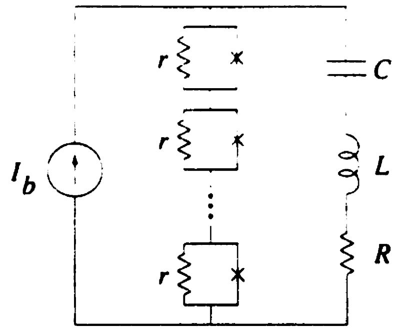

Fig. 1. A series array of Josephson junctions. The array is shunted by an *RLC* load to provide global coupling among the junctions.

2.2. Series arrays

Arrays of Josephson junctions are technologically interesting for their device applications [11,15, 16] and for their possible connection to high-temperature superconductors [17]. From a dynamical systems perspective, they offer intriguing examples of large systems of coupled nonlinear oscillators.

Arrays come in many different configurations: one-dimensional arrays connected in series or parallel, or two-dimensional arrays with various connectivities. We will restrict attention to the simplest case, in which N identical junctions are connected in series and driven by a constant bias current. Following [18,19], we also assume that a load is connected in parallel with the array; otherwise the junctions are not coupled.

Fig. 1 shows an array in which the load is a capacitor, inductor, and resistor in series. Notice that the individual junctions are drawn with an effective resistance r, but *without* an effective capacitance, consistent with our assumption that $\beta = 0$.

In dimensional form, the governing equations are

$$\frac{\hbar}{2er}\frac{d\phi_j}{dt} + I_c \sin\phi_j + \frac{dQ}{dt} = I_b, \quad j = 1,\dots,N, \tag{2.3}$$

$$L\frac{d^2Q}{dt^2} + R\frac{dQ}{dt} + \frac{Q}{C} = \frac{\hbar}{2e}\sum_{k=1}^{N}\frac{d\phi_k}{dt}, \tag{2.4}$$

from Kirchhoff's current law and voltage law, respectively. Here $\hbar$ is Planck's constant divided by 2π, e is the charge on the electron, r is the junction resistance, $\phi_j(t)$ is the phase difference across junction j, I_c is the junction's critical current, $Q(t)$ is the charge on the load capacitor, I_b is the dc-bias current, and L, R, and C are the inductance, resistance, and capacitance of the load, respectively.

Note the permutation symmetry of the equations, as well as the presence of *global coupling* (or all-to-all coupling) in (2.4). One might have thought that the series array would have nearest-neighbor coupling, but in fact each junction is coupled equally to all the others, as (2.4) shows. (Actually, there are interactions that contribute spatially localized coupling, but they are negligibly small in the lump circuit limit.)

To non-dimensionalize the system, let

$$\omega_c = 2erI_c/\hbar, \quad t^* = \omega_c t, \quad Q^* = \omega_c Q/I_c, \quad I_b^* = I_b/I_c,$$

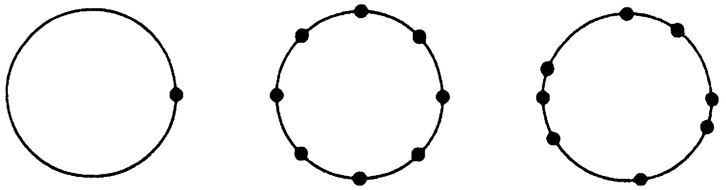
(a) in-phase state (b) splay state (c) incoherent state

Fig. 2. A rough sketch of periodic solutions of Josephson junction series arrays. Each dot on the unit circle represents the phase of a junction. (a) In-phase state: All junctions oscillate in synchrony. (b) Splay state: Phases of the junctions are scattered evenly. (c) Generic incoherent state: Phases are scattered nonuniformly.

$$L^* = \frac{\omega_c L}{rN}, \quad R^* = \frac{R}{rN}, \quad C^* = N\omega_c r C.$$

After substituting these expressions into the governing equations and dropping the asterisks, we obtain

$$\dot{\phi}_j + \sin\phi_j + \dot{Q} = I_b, \quad j = 1,\dots,N, \tag{2.5}$$

$$L\ddot{Q} + R\dot{Q} + C^{-1}Q = \frac{1}{N}\sum_{k=1}^{N}\dot{\phi}_k, \tag{2.6}$$

where the overdot denotes differentiation with respect to dimensionless time.

Of course, there are more general loads than that shown in Fig. 1, but we will concentrate on this case since it has been studied most often in the literature. The methods to be developed in Section 3 are applicable to a broader class of loads (essentially any load describable by an integro-differential relation between current and voltage), but we will not pursue such generalities here.

2.3. Periodic solutions of series arrays

The system (2.5) and (2.6) involves several parameters, and its behavior can be complex. However, for both technological and mathematical reasons, the periodic solutions are the most important. They fall into three categories: in-phase, splay, and incoherent solutions.

2.3.1. In-phase state

As long as I_b is not too small, there is a periodic running solution of the form

$$\phi_1(t) = \phi_2(t) = \cdots = \phi_N(t) \quad \text{for all } t,$$

with a consistent $Q(t)$. If we associate each phase ϕ_j with a particle moving on the unit circle, then this *in-phase state* appears as all N particles moving together around the circle (Fig. 2a). The motion is typically non-uniform, as the analog of a whirling pendulum would suggest.

The in-phase solution is of special interest for device applications [15,16,20], because a coherently oscillating array generates much greater power than a single junction. The mathematical existence of the in-phase state is usually obvious from inspection of the governing equations. On the other hand, its stability is much more difficult to determine. A great deal of research has been devoted to this important question [15,16,18,19].

2.3.2. *Splay state*

A *splay state* is a periodic solution for which the individual waveforms are identical but staggered equally in time:

$$\phi_{p_1}(t) = \phi_{p_2}\left(t + \frac{1}{N}T\right) = \cdots = \phi_{p_N}\left(t + \frac{N-1}{N}T\right) \quad \text{for all } t,$$

where T is the oscillation period, and $(p_1, \ldots, p_N)$ is a permutation of $(1, \ldots, N)$. The name is motivated by the appearance of the state when plotted on a phasor diagram - the phases are "splayed" apart on the unit circle. In a sense, such a solution is maximally out of phase. In the highly special case of averaged systems, where the interactions between oscillators depend only on the *differences* of the phases [4,21], splay states are simply those in which the oscillators are evenly spaced on the circle (Fig. 2b). For further discussion of averaged systems, see Section 2.4.

It is non-trivial to prove the existence of splay states for Josephson arrays [14] or other systems of oscillators [22], although their existence is clear for averaged systems. In practice, splay states are sometimes attracting and are then found easily by numerical integration. (Further discussion of the stability of splay states is also postponed to Section 2.4.)

If a splay state exists, then in fact there are $(N-1)!$ of them, since the indices can be permuted arbitrarily without affecting the governing equations (2.5) and (2.6). This enormous multiplicity has led to the proposal that splay states could be used as possible memory states of a dynamic "multiswitch [23].

2.3.3. *Continuous family of incoherent periodic solutions*

A third and somewhat mysterious class of periodic solutions has been observed numerically in Josephson arrays [2,5]. These *incoherent* states are similar to splay states in that the phases are scattered on the unit circle. The difference is that the phases are not equally staggered in time.

It is an open problem to prove that such periodic solutions exist for Josephson arrays. For the trivial case of averaged systems, such solutions clearly exist; any phase configuration with its centroid at the origin will do. Note however that the higher moments need not vanish (Fig. 2c); this is what distinguishes the incoherent states from the splay state.

In averaged systems the condition of zero centroid imposes two constraints on the incoherent states; therefore they form a codimension-2 submanifold of phase space. The splay state is the most symmetric of all the incoherent states, and lies at the center of this manifold, in some sense. For more general systems, numerical evidence suggests that the incoherent states again form a low-codimension submanifold, but a proof has not been found. A possible strategy for a proof is outlined at the end of Section 4.5.

2.4. *Previous results*

2.4.1. *Stability of the in-phase state*

Early analyses of Josephson junction series arrays were based mainly on regular perturbation theory and numerical simulations [15,16]. More recent approaches have combined Floquet theory and numerics. In pioneering work, Hadley and Beasley [18] found numerically that for overdamped arrays, the in-phase state is stable if the load is inductive and unstable if it is capacitive. Hadley et al.[19] explained these results with Floquet theory, and also considered arrays with more general loads. The local stability of the in-phase state was found to depend in a complex way on the circuit parameters. Much remains to be understood here, but we shall be concerned with a different set of questions in what follows.

2.4.2. *Ubiquitous neutral stability of the splay state*

Tsang et al.[7] tried to get an analytical handle on Josephson arrays by studying the simplest possible case: an array with a pure resistive load. Then $Q(t)$ can be eliminated from (2.5) and (2.6), yielding a set of N first-order equations for the phases. They showed that the system had a generalized time-reversal symmetry, which implied that the in-phase state could not be attracting. So where would trajectories go in the long run? Their numerical simulations revealed something totally unexpected: as long as I_b is not too small, all trajectories seemed to be confined to invariant 2-tori, no matter what N they considered! The tori were nested, with the splay state at the center. The invariance of the tori implied that the splay state was neutrally stable in all N directions. Tsang et al.[7] guessed that these highly non-generic results might be due to the reversibility symmetry, but that later turned out to be only part of the story.

The situation was clarified by several studies. First, Golomb et al.[5] analyzed a model system of phase oscillators, and found that the degeneracy disappeared when higher harmonics were included in the governing equations. This suggested that the pure sinusoidal form of the Josephson current relation was responsible for the original degeneracy. They also considered a model with first harmonics only:

$$\dot{\phi}_j = 1 + a\sin\phi_j + \frac{\varepsilon}{N}\sum_{k=1}^{N}\sin(\phi_k + \alpha), \quad j = 1,\ldots,N, \tag{2.7}$$

where a, ε, and α are constants. (The notation differs from their original paper.) When $\alpha = 0$, this system reduces to that studied by Tsang et al.[7]. Using linear stability analysis in the infinite-N limit, Golomb *et al.*[5] found that when $\alpha = 0$, the splay state was indeed neutrally stable in all directions. If $\alpha \neq 0$, then all but two directions were neutrally stable, regardless of the value of α.

In a complementary study, Swift et al.[4] considered the limit of weak coupling, rather than large N. They analyzed (2.7) for $\alpha = 0$ and for $|\varepsilon| \ll 1$, using the method of averaging [29,35]. This method exploits the presence of two widely separated time scales: the fast oscillations of the individual junctions occur on an $O(1)$ time scale, whereas the relative phase drift between junctions occurs on a much longer $O(1/\varepsilon)$ time scale. Swift et al. averaged over the fast oscillations to obtain a simpler *averaged system* that governs the long-term drift. The splay state of the averaged system was found to be neutrally stable in N directions, as expected. Moreover, nested 2-tori were proven to exist for the averaged system linearized about the splay state. This approach also provided accurate analytical approximations for the two frequencies on the tori.

The next round of studies revealed that splay states are neutrally stable for an unexpectedly wide class of Josephson arrays. Tsang and Schwartz [2] considered an array with a series LC-load. This system is not reversible, but they found that the splay state was still neutrally stable in an enormous number of directions: now $N - 2$ Floquet multipliers were equal to $+1$. Nichols and Wiesenfeld [3] then computed the Floquet multipliers of the splay state for several kinds of loads; at least $N - 2$ multipliers were always equal to $+1$. This remained true even for junctions with $\beta > 0$ (except, curiously, when the load was purely capacitive – the splay state was linearly stable in that case). Strogatz and Mirollo [6] showed that the ubiquitous neutral stability could be understood analytically in the infinite-N limit. Their approach also predicted the non-neutral

Floquet multipliers to within 0.1% of their numerically computed values.

We summarize the local stability results as follows:

Observation 1. The periodic splay state of (2.5) and (2.6) is neutrally stable in at least $N - 2$ directions, for a wide range of parameters and choice of loads.

For the exceptional case of the pure resistive load, the degeneracy was observed not only locally but also globally:

Observation 2. For the resistively loaded array (2.7) with $\alpha = 0$, the splay state is neutrally stable in all N directions, for a wide range of parameters. Moreover, all trajectories seem to be confined to invariant 2-tori.

Actually, the statement about the 2-tori is now thought to be false, strictly speaking. Golomb et al.[5] and Swift [24] have shown numerically that chaotic trajectories can occur for certain choices of parameters and initial conditions. This occurs even for $N = 3$. Nonetheless, it is still intriguing that "typical" trajectories appear to lie almost exactly on 2-tori, for a fairly wide range of parameters.

2.4.3. *Hints of global structure*

The local analyses cited above do not get at the root of the degeneracy. A more global analysis is needed. Nichols and Wiesenfeld [3] expressed optimism about the possibility of progress in this direction:

> ...Under ordinary circumstances, analytic headway for nonlinear systems is notoriously difficult, without some special properties on which to capitalize. Since the neutral stability of orbits is decidedly nongeneric behavior, there must be some deep explanation for it. Moreover, since it is common to many different circuit configurations, the origin of the underlying structure must be quite general, ... This structure, in turn, may make the Josephson-junction arrays tractable, analogous to a Hamiltonian system being integrable.

We show in the following sections that this comment was prophetic.

Previously, there were indications that the key role was played by the incoherent periodic solutions (not only the splay state). In their numerical study of (2.7), Golomb et al.[5] observed that for a certain parameter range, almost all trajectories were attracted to a manifold of incoherent periodic states. Tsang and Schwartz [2] also numerically found a similar attracting manifold of periodic states in the LC-loaded Josephson arrays. Furthermore, their observations of the phase portrait of $N = 4$ oscillators led them to an important conjecture: each incoherent state has a two-dimensional surface as its basin of attraction.

These numerical results are summarized as:

Observation 3. There appears to be a manifold of incoherent periodic states. It seems to be related to the degeneracy found in the local analysis of the splay state.

In Section 4.5 we give a unified explanation of all three observations, taking care to indicate which parts of our explanation are rigorous, and which parts are plausible but still unproven.

3. Reducible systems

In this section we introduce a nonlinear transformation that explicitly reduces a fairly large class of N-dimensional oscillator systems ($N \geq 3$) to three-dimensional ones. The method is explained in Section 3.1, starting from the most general form of the equations to which the transformation applies (as far as we know). The governing equations for Josephson arrays are reducible by this transformation, as we show in Section 3.2.

3.1. *Reduction*

3.1.1. *General reducible systems*

Consider N identical phase oscillators governed by a system of ordinary differential equations of the form

$$\dot{\theta}_j = f + g\cos\theta_j + h\sin\theta_j, \qquad j = 1, \cdots, N, \tag{3.1}$$

where θ_j is the phase of the jth oscillator, and f, g, h are functions of $\theta_1, \theta_2, \cdots, \theta_N$, and 2π-periodic in each argument. (This is the simplest case. More generally, the right hand sides of (3.1) could depend explicitly on time as well as on any auxiliary dynamical variables, e.g., the charge on a load capacitor in the case of the Josephson arrays described in Section 3.2.) The key restriction is that f, g, h must not depend on the subscript j.

Intuitively, the functions f, g, h describe common *fields* determined by the states of all the oscillators. The situation is similar to that encountered in mean-field models, although the three functions are not necessarily averaged quantities of the state variables. In particular, the system need not have permutation symmetry.

3.1.2. *Change of variables*

The phase space for (3.1) is N-dimensional. *A priori*, a trajectory could explore the entire space. However, we are going to show that each trajectory is actually confined to a three-dimensional subspace. To see this, consider the following change of variables:

$$\tan[\tfrac{1}{2}(\theta_j(t) - \Theta(t))] = \sqrt{\frac{1+\gamma(t)}{1-\gamma(t)}}\tan[\tfrac{1}{2}(\psi_j - \Psi(t))], \quad j = 1, \cdots, N, \tag{3.2}$$

where ψ_j are *constants*, and $0 \leq \gamma < 1$. We claim that an *arbitrary* solution $\{\theta_j(t)\}$ of the system (3.1) has the form (3.2), and that it can be generated from a set of parameters $\{\psi_j\}$ that is *frozen* in time. The evolution of $\Theta(t)$, $\gamma(t)$, and $\Psi(t)$ is unknown for now. We will shortly derive the governing equations for these variables.

First, a few words about where (3.2) comes from. It was originally motivated by an analogy with the method of "variation of parameters." We had been studying a special case of (3.1) in the infinite-N limit, and we found that the transformation (3.2) arose naturally when studying the travelling waves for that system (see Section 5.3). In this simpler problem, the quantities $\Theta(t)$ and $\Psi(t)$ were simply proportional to t, and $\gamma(t)$ was constant. Later we realized that by allowing those quantities to have arbitrary time-dependence, we could apply the same transformation to the finite-N system. Another, perhaps more natural, way to motivate (3.2) has been pointed out by J. Swift (personal communication). Consider the finite-N system for the special case where f, g, h

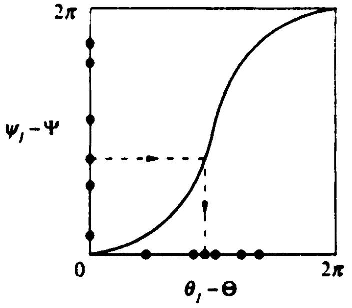

Fig. 3. Graph of the time-dependent transformation (3.2). The transformation converts solutions $\theta_j(t)$ into *constants* ψ_j. The mapping depends on a distortion parameter $\gamma(t)$, as well as two reference phases $\Theta(t)$ and $\Psi(t)$.

are constants. Then the solution for $\theta_j(t)$ can be found explicitly; it has the form of (3.2), but again with $\Theta(t)$ and $\Psi(t)$ simply proportional to t and $\gamma(t)$ constant. By variation of parameters, one is led to (3.2).

We are going to use (3.2) to change variables in (3.1), but before going into the algebra, let us consider what the transformation (3.2) means geometrically. It is a change of coordinates that relabels the phases from θ_j to ψ_j (see Fig. 3). First we go into a non-uniformly rotating coordinate system, characterized by the angle $\Theta(t)$. Then we reparametrize the circle by a time-dependent, nonlinear transformation characterized by a distortion parameter $\gamma(t)$. Finally, if we rotate again, but now according to $\Psi(t)$, we claim that *all* the oscillators appear motionless – we have converted an arbitrary solution $\{\theta_j(t)\}$ into a frozen state $\{\psi_j\}$.

The meaning of $\Theta(t)$ and $\Psi(t)$ is clear, but what does $\gamma(t)$ measure? The transformation curve of Fig. 3 is linear when $\gamma = 0$. As γ increases, the curve becomes bent and the distribution of ψ_j is increasingly distorted from that of θ_j. The curve is monotonic for all γ, so we can think of the inverse mapping in a similar manner. Now we interpret ψ_j as the preimages, and θ_j as their images. This is often the more useful point of view.

3.1.3. Reduced equations

Readers with a background in celestial mechanics may recognize the tranformation $\tan(v/2) = \sqrt{(1+\gamma)/(1-\gamma)}\tan(E/2)$. It appears in the analysis of the gravitational two-body problem. Here, v, E, and γ correspond to the true anomaly, the eccentric anomaly, and the eccentricity, respectively. The relation (3.2) is a time-dependent version of this transformation, with a phase shift applied to all N oscillators.

Now we rewrite (3.1) in terms of the new variables. The following formulas from classical mechanics are well known [25], and allow us to convert between our two "anomalies":

$$\sin(\theta_j - \Theta) = \frac{\sqrt{1-\gamma^2}\sin(\psi_j - \Psi)}{1-\gamma\cos(\psi_j-\Psi)}, \quad \cos(\theta_j - \Theta) = \frac{\cos(\psi_j-\Psi)-\gamma}{1-\gamma\cos(\psi_j-\Psi)}. \tag{3.3}$$

(To derive these formulas, one solves (3.2) for $\theta_j - \Theta$ and then applies trigonometric identities.) These formulas yield

$$\cos\theta_j = \frac{[\cos(\psi_j-\Psi)-\gamma]\cos\Theta - \sqrt{1-\gamma^2}\sin\Theta\sin(\psi_j-\Psi)}{1-\gamma\cos(\psi_j-\Psi)},$$

$$\sin\theta_j = \frac{[\cos(\psi_j - \Psi) - \gamma]\sin\Theta + \sqrt{1-\gamma^2}\cos\Theta\sin(\psi_j - \Psi)}{1 - \gamma\cos(\psi_j - \Psi)}, \tag{3.4}$$

and these expressions are then substituted into the right hand side of (3.1).

To rewrite the left hand side of (3.1), we solve (3.2) for θ_j and differentiate with respect to time. Let $\Gamma(t) = \sqrt{(1+\gamma)/(1-\gamma)}$. Then

$$\begin{aligned}
\frac{d}{dt}(\theta_j - \Theta) &= 2\frac{d}{dt}\{\arctan(\Gamma\tan[\tfrac{1}{2}(\psi_j - \Psi)])\} \\
&= \frac{2}{1 + \Gamma^2\tan^2[\frac{1}{2}(\psi_j - \Psi)]}\left(\dot\Gamma\tan[\tfrac{1}{2}(\psi_j - \Psi)] + \frac{\Gamma}{\cos^2[\frac{1}{2}(\psi_j - \Psi)]}(-\tfrac{1}{2}\dot\Psi)\right) \\
&= \frac{\Gamma}{\cos^2[\frac{1}{2}(\psi_j - \Psi)] + \Gamma^2\sin^2[\frac{1}{2}(\psi_j - \Psi)]}\left(\frac{\dot\Gamma}{\Gamma}\sin(\psi_j - \Psi) - \dot\Psi\right).
\end{aligned}$$

Since

$$\begin{aligned}
\cos^2[\tfrac{1}{2}(\psi_j - \Psi)] + \Gamma^2\sin^2[\tfrac{1}{2}(\psi_j - \Psi)] &= \tfrac{1}{2}(\Gamma^2 + 1) - (\Gamma^2 - 1)\cos(\psi_j - \Psi) \\
&= \frac{1 - \gamma\cos(\psi_j - \Psi)}{1 - \gamma}
\end{aligned}$$

and

$$\frac{\dot\Gamma}{\Gamma} = \frac{1}{2\Gamma^2}\frac{d\Gamma^2}{dt} = \frac{1}{2\Gamma^2}\frac{d}{dt}\left(\frac{1+\gamma}{1-\gamma}\right) = \frac{\dot\gamma}{\Gamma^2(1-\gamma)^2} = \frac{\dot\gamma}{1-\gamma^2},$$

we obtain

$$\begin{aligned}
\dot\theta_j &= \dot\Theta + \frac{\Gamma(1-\gamma)}{1 - \gamma\cos(\psi_j - \Psi)}\left(\frac{\dot\gamma}{1-\gamma^2}\sin(\psi_j - \Psi) - \dot\Psi\right) \\
&= \dot\Theta + \frac{\dot\gamma\sin(\psi_j - \Psi) - (1-\gamma^2)\dot\Psi}{\sqrt{1-\gamma^2}[1 - \gamma\cos(\psi_j - \Psi)]}.
\end{aligned} \tag{3.5}$$

Next, substitute (3.4) and (3.5) into (3.1). After multiplying both sides by $(1 - \gamma\cos(\psi_j - \Psi))$, we obtain:

$$\begin{aligned}
\dot\Theta(1 - \gamma\cos(\psi_j - \Psi)) + \frac{\dot\gamma\sin(\psi_j - \Psi) - (1-\gamma^2)\dot\Psi}{\sqrt{1-\gamma^2}} &= f(1 - \gamma\cos(\psi_j - \Psi)) \\
&\quad + g\{[(\cos(\psi_j - \Psi) - \gamma]\cos\Theta - \sqrt{1-\gamma^2}\sin\Theta\sin(\psi_j - \Psi)\} \\
&\quad + h\{[\cos(\psi_j - \Psi) - \gamma]\sin\Theta - \sqrt{1-\gamma^2}\cos\Theta\sin(\psi_j - \Psi)\}, \quad j = 1, \cdots, N.
\end{aligned}$$

The terms above can be organized as a linear combination of 1, $\cos(\psi_j - \Psi)$, and $\sin(\psi_j - \Psi)$. The fact that no higher harmonics are generated is remarkable. This is the crucial property that underlies the success of the reduction procedure.

Now writing out the linear combination with the appropriate coefficients in brackets, we obtain:

$$\begin{aligned}0 = &\, (\dot{\Theta} - \sqrt{1-\gamma^2}\dot{\Psi} - f + g\gamma\cos\Theta + h\gamma\sin\Theta) \\ &+ \cos(\psi_j - \Psi)(-\gamma\dot{\Theta} + \gamma f - g\cos\Theta - h\sin\Theta) \\ &+ \sin(\psi_j - \Psi)\left(\frac{\dot{\gamma}}{\sqrt{1-\gamma^2}} + g\sqrt{1-\gamma^2}\sin\Theta - h\sqrt{1-\gamma^2}\cos\Theta\right), \quad j = 1,\cdots,N.\end{aligned}$$

Observe that the coefficients do not depend on j since we have assumed that f, g, and h do not depend on j. Thus the equations will be satisfied identically *for all* j *and for all* t if the three coefficients vanish independently. This can be achieved if the unknown functions γ, Θ, Ψ evolve according to

$$\begin{aligned}&\dot{\gamma} = -(1-\gamma^2)(g\sin\Theta - h\cos\Theta), \quad \gamma\dot{\Psi} = -\sqrt{1-\gamma^2}(g\cos\Theta + h\sin\Theta), \\ &\gamma\dot{\Theta} = \gamma f - g\cos\Theta - h\sin\Theta. \qquad (3.6)\end{aligned}$$

This is a closed system for (γ, Ψ, Θ) since $\theta_1, \cdots, \theta_N$ in the functions f, g, h can be expressed in terms of these new dependent variables via (3.2). The frozen phases $\{\psi_j\}$ of the N oscillators appear in the system merely as parameters. As long as these three ordinary differential equations are satisfied, $\{\theta_j(t)\}$ is guaranteed to satisfy the N equations (3.1).

3.1.4. *Converting initial conditions*

Given the reduced system (3.6), two questions immediately arise: how do we obtain initial conditions for the "reduced variables" (γ, Ψ, Θ) to start integrating (3.6), and how do we determine the "system constants" $\{\psi_j\}$? Given an arbitrary initial condition $\{\theta_j(0)\}$ in the old coordinates, we need to convert these N values to the new set of $N+3$ values $\{\psi_j\}, \gamma(0), \Psi(0), \Theta(0)$ so that (3.2) is satisfied at $t = 0$. The equations (3.2) provide N constraints, but we have $N+3$ unknowns. Hence there are many ways to achieve this conversion.

One natural choice is to evolve from the "identity conversion":

$$\gamma(0) = \Theta(0) = \Psi(0) = 0, \quad \psi_j = \theta_j(0), \qquad j = 1,\ldots,N, \qquad (3.7)$$

by which (3.2) is trivially satisfied at $t = 0$. In Section 4.2 we shall see that another way of converting initial conditions provides much more insight into the phase space structure. For the moment, however, we are content to observe that there is at least one way to reduce the N-dimensional problem to a three-dimensional one. Since (3.7) shows that an arbitrary initial condition can be converted, we conclude that (3.2) expresses the *general* solution of the system (3.1).

3.1.5. *Removing a coordinate singularity*

Another question regarding (3.6) is that the equations, in general, cease to be valid at $\gamma = 0$. Unless $g, h \to 0$ as $\gamma \to 0$, $\dot{\Theta}$ and $\dot{\Psi}$ become singular. At the same time, $\dot{\gamma} < 0$ seems possible at $\gamma = 0$ so that γ might not stay positive, contrary to its definition. Such troubles are only artifacts of a coordinate singularity, and can be avoided in the following manner.

The system (3.6) involves one amplitude variable γ and two phase variables Θ and Ψ. To avoid the singularity at $\gamma = 0$, we introduce a Cartesian-type coordinate system

$$x = \gamma\cos\Theta, \quad y = \gamma\sin\Theta, \quad \Phi = \Theta - \Psi, \quad (x^2 + y^2 < 1). \qquad (3.8)$$

Then

$$\begin{aligned}\dot{x} &= \dot{\gamma}\cos\Theta - \gamma\dot{\Theta}\sin\Theta \\ &= -(1-\gamma^2)(g\sin\Theta - h\cos\Theta)\cos\Theta - \sin\Theta(\gamma f - g\cos\Theta - h\sin\Theta) \\ &= -\gamma f\sin\Theta + \gamma^2 g\sin\Theta\cos\Theta + h(1-\gamma^2\cos^2\Theta) \\ &= -yf + xyg + (1-x^2)h. \end{aligned} \tag{3.9}$$

Similarly,

$$\dot{y} = xf - (1-y^2)g - xyh. \tag{3.10}$$

The angle Φ is defined in such a way to subtract out singularities of the two phase equations. Thus,

$$\begin{aligned}\gamma^2\dot{\Phi} &= \gamma^2\dot{\Theta} - \gamma^2\dot{\Psi} \\ &= \gamma(\gamma f - g\cos\Theta - h\sin\Theta) + \gamma\sqrt{1-\gamma^2}(g\cos\Theta + h\sin\Theta) \\ &= \gamma^2 f - (1-\sqrt{1-\gamma^2})(\gamma g\cos\Theta + \gamma h\sin\Theta) \\ &= \gamma^2 f - (1-\sqrt{1-\gamma^2})(xg + yh). \end{aligned}$$

Hence,

$$\dot{\Phi} = f - \frac{1-\sqrt{1-\gamma^2}}{\gamma^2}(xg + yh). \tag{3.11}$$

At $\gamma = 0$, Eqs. (3.9)–(3.11) reduce to a well-behaved set of equations:

$$\dot{x} = h, \quad \dot{y} = -g, \quad \dot{\Phi} = f. \tag{3.12}$$

The initial conditions and the system constants are obtained in this coordinate system by rewriting (3.7):

$$x(0) = y(0) = \Phi(0) = 0, \qquad \psi_j = \theta_j(0), \quad j = 1,\dots,N. \tag{3.13}$$

When a trajectory passes through the origin $\gamma = 0$ in (3.6), Θ and Ψ jump discontinuously by $\pm\pi$. In this new coordinate system, however, their difference Φ still changes continuously. Since γ is now computed by $\gamma = \sqrt{x^2+y^2}$, it remains non-negative. When $\gamma = 0$, Θ and Ψ are not determined. This is reasonable, and poses no problems because we can still compute θ_j via (3.2). For $\gamma = 0$, we find

$$\theta_j = \Theta + (\psi_j - \Psi) = \psi_j + \Phi.$$

So, we do not need to know Θ and Ψ but only their difference Φ. The coordinate singularity at $\gamma = 0$ is resolved in this way.

3.2. Josephson junction arrays as reducible systems

3.2.1. Reduction

The reduction method of the previous section is immediately applicable to the Josephson junction array equations (2.5) and (2.6). To see this, we note that the N equations (2.5) have the form of (3.1) where $\theta_j = \phi_j$, $f = I_B - \dot{Q}$, $g = 0$, and $h = -1$. The function f depends on another dynamical variable $\dot{Q}$, but there is no difference in the reduction procedure. Since we derived the reduced equations (3.9)-(3.11) from (3.1) without applying any operations on f, g, and h, the reduction is still valid even when these functions depend on auxiliary dynamical variables or on time explicitly. The N phase equations can be satisfied by integrating only three equations, but now they are coupled with the evolution equations for the non-reducible auxiliary variables. Specifically, the equations (2.5) and (2.6) become

$$\begin{aligned} \dot x &= -y(I_B - \dot Q) - (1 - x^2) && \text{from (3.9)},\\ \dot y &= x(I_B - \dot Q) + xy && \text{from (3.10)},\\ \dot \Phi &= (I_B - \dot Q) + \frac{1 - \sqrt{1 - \gamma^2}}{\gamma^2} y && \text{from (3.11)}, \end{aligned} \tag{3.14}$$

with

$$L\ddot Q + R\dot Q + C^{-1}Q = \frac{1}{N}\sum_{k=1}^{N}(I_B - \dot Q - \sin\phi_k). \tag{3.15}$$

ϕ_k is expressed by x, y, Φ through the transformation.

It is clear that (3.14) and (3.15) is equivalent to a fifth-order system of ordinary differential equations with variables $(x, y, \Phi, Q, \dot Q)$ when $L \neq 0$. When $L = 0$, (3.15) can be solved for $\dot Q$ to obtain a fourth-order system with variables (x, y, Φ, Q). In any case, we have reduced the N equations (2.5) to three equations (3.14).

3.2.2. Relation to neutral stability

Any trajectory of these Josephson junction arrays is, therefore, confined to a subspace of $N - 3$ fewer dimensions than the whole phase space. Three dimensions of the subspace are accounted for by the transformation (3.2); by allowing γ, Ψ, Θ to vary for fixed $\{\psi_j\}$, the image $\{\theta_j\}$ sweeps out a three-dimensional manifold. Choosing a different set of $\{\psi_j\}$ would produce another manifold. The product of such a manifold with the auxiliary directions (Q and $\dot Q$ if necessary) is the subspace from which a trajectory cannot escape.

These facts are reminiscent of Observation 1 in Section 2.4, which deals with the widespread occurrence of $N - 2$ neutral directions. If one computes the Floquet multipliers of a periodic orbit, one of them is always $+1$, corresponding to perturbations along the orbit. The other $N - 3$ unit multipliers must correspond to the number of dimensions we have reduced. The precise connection will not become clear until Section 4.5, when we demonstrate the foliation of phase space by invariant subspaces. This foliation is the source of the ubiquitous neutral stability.

3.2.3. Chaotic dynamics in resistively loaded arrays

What behavior do we expect from the reduced systems? Although this question has not yet been investigated in general, there is preliminary evidence of complicated behavior.

Consider a purely resistively loaded array. The governing equations are then given by (2.7) with $\alpha = 0$:

$$\dot\phi_j = 1 + a\sin\phi_j + \frac{\varepsilon}{N}\sum_{k=1}^{N}\sin\phi_k, \quad j = 1, \cdots, N. \tag{3.16}$$

Assume that $|a + \varepsilon| < 1$, so that there are no fixed points [5,7]. Then trajectories typically appear to lie on 2-tori as in Observation 2 of Section 2.4. However, Golomb et al.[5,26] found numerical

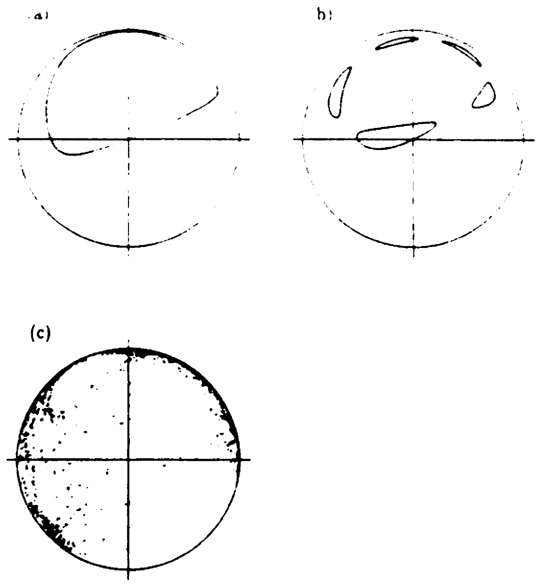

Fig. 4. Poincaré sections of the reduced system (3.17) at $\Phi = 0 \pmod{2\pi}$ for $N = 3$ junctions. Each section shows one trajectory starting at $x = y = \Phi = 0$ at $t = 0$. The initial conditions are $\phi_1(0) = 3\pi/5$, $\phi_2(0) = 0$, $\phi_3(0) = -7\pi/10$. The identity conversion (3.13) requires the preimages to be $\psi_j = \phi_j(0)$. These values are fixed in time.
(a) $a = 1$, $\varepsilon = -0.7$. The section shows an invariant closed curve, suggesting that the trajectory lies on a 2-torus in the original phase space. (b) $a = 1$, $\varepsilon = -1.95$. Period-5 islands. (c) $a = 1.5$, $\varepsilon = -0.7$. Chaos.

evidence for aperiodic trajectories for systems as small as $N = 6$, depending on the parameters a and ε. Swift [24] further demonstrated numerically that chaos occurs even for $N = 3$. He transformed the three angles ϕ_j linearly into the mean phase $\bar{\phi}$ and two phase differences. Since $\bar{\phi}$ is monotonically increasing when $|a + \varepsilon| < 1$, the Poincaré return map at $\bar{\phi} = 0 \pmod{2\pi}$ is well defined. Depending on the parameters, chaotic-looking Poincaré sections were obtained.

We employ the same idea, but using the nonlinear reduction. The equations (3.16) reduce to the three equations corresponding to the special case of (3.14) and (3.15):

$$\dot{x} = -y\left(1 + \frac{\varepsilon}{N}\sum_{k=1}^{N}\sin\phi_k\right) + a(1 - x^2), \quad \dot{y} = x\left(1 + \frac{\varepsilon}{N}\sum_{k=1}^{N}\sin\phi_k\right) - axy,$$

$$\dot{\Phi} = 1 + \frac{\varepsilon}{N}\sum_{k=1}^{N}\sin\phi_k - ay\frac{1 - \sqrt{1 - \gamma^2}}{\gamma^2}, \tag{3.17}$$

where $\phi_k = \phi_k(x, y, \Phi; \{\psi_j\})$ is given by the transformation (3.2), and $\gamma = \sqrt{x^2 + y^2}$. Here Φ plays a similar role to the mean phase of the ϕ's.

Now (3.17) is numerically integrated, and every time $\Phi = 0 \pmod{2\pi}$, a point (x, y) is plotted. (The initial condition is converted by (3.13).) Fig. 4 shows three Poincaré sections obtained for $N = 3$ using a randomly chosen set of $\phi_1(0)$, $\phi_2(0)$, and $\phi_3(0)$.

Fig. 4a shows the section when $a = 1, \varepsilon = -0.7$. We find a set of points on a closed curve; the trajectory is (very nearly) on a 2-torus, and is quasiperiodic. The closed curve passes through the origin because the conversion (3.13) requires the trajectory to start from $x = y = \Phi = 0$ at $t = 0$.

Fig. 4b shows the case $a = 1, \varepsilon = -1.95$. The section produced by *one* trajectory looks like islands surrounding a period-5 orbit.

Fig. 4c is the case $a = 1.5, \varepsilon = -0.7$. This section is clearly chaotic.

These results suggest that the system has invariant tori that break as parameters are varied, a behavior familiar from weakly non-integrable systems [27–29], such as the Hénon-Heiles system [30]. However, the flow here is not Hamiltonian nor even volume-preserving, although it is reversible. The Poincaré map appears to be area-preserving, but only if Φ is strobed at multiples of 2π. Perhaps the KAM theory for reversible flows [31] can be used to shed light on the numerical observations above.

4. Global structure

To make further analytical progress, we consider the limit of weakly coupled arrays. Averaging theory leads to a simpler set of equations that can be analyzed completely.

The equations considered in this section are a generalization of those studied by Swift et al. [4]. They averaged the resistive load equations (3.16), assuming that $|a| < 1$ and $|\varepsilon| \ll 1 - |a|$. The averaged equations were found to take the form

$$\dot{\theta}_j = \omega + \frac{1}{N}\sum_{k=1}^{N}\cos(\theta_k - \theta_j), \quad j = 1,\ldots,N,$$

where ω is a constant, and time has been rescaled. The variable θ_j is a nonlinearly transformed version of the phase ϕ_j in (3.16).

Swift [32] later derived the more general averaged equations governing (2.5) and (2.6) with an arbitrary *RLC* load. Weak coupling was put in by hand, by inserting a small parameter in front of $\dot{Q}$ in (2.5). The resulting equations [32] are

$$\dot{\theta}_j = \omega + \frac{1}{N}\sum_{k=1}^{N}\cos(\theta_k - \theta_j - \delta), \quad j = 1,\ldots,N \tag{4.1}$$

where δ is a parameter that depends on the values of R, L, C, and I_b.

The averaged equations (4.1) are of interest beyond their connection to Josephson arrays. For instance, when averaging theory is applied to the system (2.7) of Golomb et al. in the limit of weak coupling, one again obtains (4.1). In this case δ is given by $\sin\delta = (\operatorname{sign}\varepsilon)\sin\alpha$. Eq. (4.1) also appears as the averaged system for globally coupled van der Pol oscillators with linear coupling [33], and for a globally coupled version of the complex Ginzburg-Landau equation [34]. Finally, from a mathematical point of view, (4.1) is perhaps the simplest nontrivial N-body system coupled by nonlinear interactions.

In Section 4.1, we derive and analyze the reduced equations for (4.1). Section 4.2 presents a way of converting initial conditions that is much more illuminating than the identity conversion (3.7). This new conversion is used in Section 4.3 to provide global information about the dynamics of (4.1). Section 4.4 presents numerical illustrations of the results.

We will see that the phase space of (4.1) possesses highly degenerate global structures. Some of them persist in the Josephson array equations (2.5) and (2.6) *before* averaging. Section 4.5

discusses which structures survive, and explains the three observations previously made in Section 2.4.

4.1. Reduction of averaged systems

In a frame rotating at angular velocity ω, (4.1) is equivalent to

$$\dot{\theta}_j = \frac{1}{N}\sum_{k=1}^{N}\cos(\theta_k - \theta_j - \delta), \quad j = 1,\dots,N. \tag{4.2}$$

Thus the constant ω does not affect the essential dynamics. Eq. (4.2) is in the form of (3.1), where

$$f = 0, \quad g = \frac{1}{N}\sum_{k=1}^{N}\cos(\theta_k - \delta), \quad h = \frac{1}{N}\sum_{k=1}^{N}\sin(\theta_k - \delta). \tag{4.3}$$

The reduced equations in the polar expression (3.6) become

$$\dot{\gamma} = \frac{1-\gamma^2}{N}\sum_{k=1}^{N}\sin(\theta_k - \Theta - \delta), \quad \gamma\dot{\Psi} = -\frac{\sqrt{1-\gamma^2}}{N}\sum_{k=1}^{N}\cos(\theta_k - \Theta - \delta),$$

$$\gamma\dot{\Theta} = -\frac{1}{N}\sum_{k=1}^{N}\cos(\theta_k - \Theta - \delta).$$

We intentionally use these polar coordinates instead of their Cartesian counterpart. Although a coordinate singularity arises, it causes no trouble, as will be seen in Section 4.2.

Using the formula (3.3), this set of equations becomes

$$\begin{aligned}
\dot{\gamma} &= \cos\delta\frac{(1-\gamma^2)^{3/2}}{N}\sum_{k=1}^{N}\frac{\sin(\psi_k - \Psi)}{1-\gamma\cos(\psi_k - \Psi)} + \sin\delta\frac{1-\gamma^2}{N}\sum_{k=1}^{N}\frac{\gamma - \cos(\psi_k - \Psi)}{1-\gamma\cos(\psi_k - \Psi)},\\
\gamma\dot{\Psi} &= \cos\delta\frac{(1-\gamma^2)^{1/2}}{N}\sum_{k=1}^{N}\frac{\gamma - \cos(\psi_k - \Psi)}{1-\gamma\cos(\psi_k - \Psi)} - \sin\delta\frac{1-\gamma^2}{N}\sum_{k=1}^{N}\frac{\sin(\psi_k - \Psi)}{1-\gamma\cos(\psi_k - \Psi)},\\
\gamma\dot{\Theta} &= \cos\delta\frac{1}{N}\sum_{k=1}^{N}\frac{\gamma - \cos(\psi_k - \Psi)}{1-\gamma\cos(\psi_k - \Psi)} - \sin\delta\frac{(1-\gamma^2)^{1/2}}{N}\sum_{k=1}^{N}\frac{\sin(\psi_k - \Psi)}{1-\gamma\cos(\psi_k - \Psi)}.
\end{aligned} \tag{4.4}$$

The system looks intimidating, but it is actually very simple. First, notice that Θ has disappeared from the right hand sides. Hence the dynamics is determined only by (Ψ, γ) while Θ is driven passively by them. Since the dynamics is effectively *two*-dimensional, we know immediately that the system is never chaotic.

Second, note that there are only two types of sums on the right hand sides of (4.4). The form of these sums suggests that they might be partial derivatives of a common function. Indeed, a useful function can be constructed as follows. If we define

$$\mathcal{H}(\Psi, \gamma) = \frac{1}{N}\sum_{k=1}^{N}\log\left(\frac{1-\gamma\cos(\psi_k - \Psi)}{\sqrt{1-\gamma^2}}\right), \tag{4.5}$$

then we produce the two sums mentioned just above:

$$\frac{\partial \mathcal{H}}{\partial \Psi} = -\frac{1}{N}\sum_{k=1}^{N}\frac{\gamma \sin(\psi_k - \Psi)}{1-\gamma\cos(\psi_k - \Psi)} \tag{4.6}$$

and

$$\begin{aligned}\frac{\partial \mathcal{H}}{\partial \gamma} &= \frac{\partial}{\partial \gamma}\left(-\tfrac{1}{2}\log(1-\gamma^2) + \frac{1}{N}\sum_{k=1}^{N}\log[1-\gamma\cos(\psi_k - \Psi)]\right)\\ &= \frac{\gamma}{1-\gamma^2} - \frac{1}{N}\sum_{k=1}^{N}\frac{\cos(\psi_k - \Psi)}{1-\gamma\cos(\psi_k - \Psi)}\\ &= \frac{1}{N(1-\gamma^2)}\sum_{k=1}^{N}\frac{\gamma - \cos(\psi_k - \Psi)}{1-\gamma\cos(\psi_k - \Psi)}.\end{aligned} \tag{4.7}$$

Thus we can express the (γ, Ψ)-dynamics of (4.4) as:

$$\begin{aligned}\frac{\dot\gamma}{1-\gamma^2} &= -\frac{\sqrt{1-\gamma^2}}{\gamma}\frac{\partial \mathcal{H}}{\partial \Psi}\cos\delta + (1-\gamma^2)\frac{\partial \mathcal{H}}{\partial \gamma}\sin\delta,\\ \frac{\dot\Psi}{1-\gamma^2} &= +\frac{\sqrt{1-\gamma^2}}{\gamma}\frac{\partial \mathcal{H}}{\partial \gamma}\cos\delta + \frac{1}{\gamma^2}\frac{\partial \mathcal{H}}{\partial \Psi}\sin\delta.\end{aligned} \tag{4.8}$$

4.1.1. *Hamiltonian when* $\sin\delta = 0$

When $\sin\delta = 0$, the system becomes completely integrable. Consider, for example, the case $\delta = 0$. (The case $\delta = \pi$ is similar.) Then (4.8) shows that $\mathcal{H}$ is conserved:

$$\dot{\mathcal{H}} = \dot\gamma\frac{\partial \mathcal{H}}{\partial \gamma} + \dot\Psi\frac{\partial \mathcal{H}}{\partial \Psi} = (1-\gamma^2)\left[\left(-\frac{\sqrt{1-\gamma^2}}{\gamma}\frac{\partial \mathcal{H}}{\partial \Psi}\right)\frac{\partial \mathcal{H}}{\partial \gamma} + \left(\frac{\sqrt{1-\gamma^2}}{\gamma}\frac{\partial \mathcal{H}}{\partial \gamma}\right)\frac{\partial \mathcal{H}}{\partial \Psi}\right] = 0.$$

For this case, we could express (4.8) as a *one degree-of-freedom* Hamiltonian system. To see this, let $\alpha = 1/\sqrt{1-\gamma^2}$. Then (4.8) becomes

$$\dot\alpha = -\frac{\partial \mathcal{H}}{\partial \Psi}, \quad \dot\Psi = +\frac{\partial \mathcal{H}}{\partial \alpha}$$

which is in Hamiltonian form. The appropriate phase space for this system is a cylinder, since $\mathcal{H}$ is periodic in Ψ. The trajectories lie on contours of $\mathcal{H}$, and are typically closed orbits (or fixed points in exceptional cases). Hence $\Psi(t), \alpha(t)$, and therefore $\gamma(t)$ are typically periodic in t.

What can we say about the remaining Θ-direction? In (4.4), Θ does not appear on the right hand sides. In particular, $\dot\Theta$ is dependent only on (Ψ, γ). Suppose after one period T of the (Ψ, γ) motion, Θ shifts by some amount, say $\Theta(t+T) = \Theta(t) + 2\pi W$, where W denotes the winding number. Then, since Ψ and γ have returned to their starting values, the same shift of Θ occurs on all following cycles. Therefore, when $\sin\delta = 0$, the solutions of (4.4) are typically quasiperiodic, with trajectories confined to invariant 2-tori. Thus (4.1) is completely integrable when $\sin\delta = 0$.

4.1.2. *Lyapunov function for general* δ

When $\sin\delta \neq 0$, we may still compute $\dot{\mathcal{H}}$ from (4.8). As before, terms involving $\cos\delta$ vanish, and now we obtain:

$$\dot{\mathcal{H}} = P\sin\delta\,, \tag{4.9}$$

where

$$P(\Psi,\gamma,\{\psi_j\}) = (1-\gamma^2)\left[(1-\gamma^2)\left(\frac{\partial\mathcal{H}}{\partial\gamma}\right)^2 + \frac{1}{\gamma^2}\left(\frac{\partial\mathcal{H}}{\partial\Psi}\right)^2\right]$$

is a positive definite function since $0<\gamma<1$. (Again, there is slight ambiguity at $\gamma = 0$.) Thus, $\mathcal{H}$ acts as a Lyapunov function in this general case, and the sign of $\sin\delta$ determines the direction of change in $\mathcal{H}$.

To interpret the function P more intuitively, substitute (4.6) and (4.7) back into the right hand side of (4.9):

$$P = \left(\frac{1}{N}\sum_{k=1}^{N}\frac{\gamma-\cos(\psi_k-\Psi)}{1-\gamma\cos(\psi_k-\Psi)}\right)^2 + \left(\frac{1}{N}\sum_{k=1}^{N}\frac{\sqrt{1-\gamma^2}\sin(\psi_k-\Psi)}{1-\gamma\cos(\psi_k-\Psi)}\right)^2 .$$

Using the formula (3.3) also in reverse,

$$P = \left(\frac{1}{N}\sum_{k=1}^{N}\cos(\theta_k-\Theta)\right)^2 + \left(\frac{1}{N}\sum_{k=1}^{N}\sin(\theta_k-\Theta)\right)^2 .$$

Define

$$R(t)\exp[i\phi(t)] = \frac{1}{N}\sum_{k=1}^{N}\exp(i\theta_k)\,, \quad R\geq 0,\ \phi\in\mathbb{R}, \tag{4.10}$$

which denotes the "order parameter", or the centroid vector of the N oscillators located on a unit circle according to their phase angles. Then

$$P = [R\cos(\phi-\Theta)]^2 + [R\sin(\phi-\Theta)]^2 = R^2 .$$

Hence $\dot{\mathcal{H}} = R^2\sin\delta$. So $\mathcal{H}$ is stationary only when $R = 0$, i.e., when the N oscillators are distributed such that their centroid vanishes. From (4.10), these special states satisfy

$$\frac{1}{N}\sum_{k=1}^{N}\cos\theta_k = \frac{1}{N}\sum_{k=1}^{N}\sin\theta_k = 0. \tag{4.11}$$

States satisfying (4.11) play an important role in the rest of the article. From now on, we refer to them as "incoherent" states of the averaged systems.

4.1.3. Remaining issues

Two issues still need to be addressed:

(1) The analysis could potentially fail when $\gamma = 0$. As discussed in Section 3.1, the reduced equations (4.4) can become singular at this value.

(2) We would like to visualize the Lyapunov function $\mathcal{H}$. For instance, what do its level curves look like? And what is the meaning of increasing or decreasing $\mathcal{H}$?

These matters are resolved in the next two sections by locating the incoherent states at the center of a picture that clarifies everything.

4.2. Constraints and constants of motion

4.2.1. Choice of constraints

In this section we reconsider how to convert the original initial conditions $\{\theta_j(0)\}$ into the initial conditions of the reduced variables $\{\gamma(0), \boldsymbol{\Theta}(0), \Psi(0)\}$ and the system constants $\{\psi_j\}$. As explained in Section 3.1, there are many ways to achieve this conversion. Since we determine $N + 3$ values from N constraints, three additional constraints may be imposed to eliminate the multiplicity of the conversion. In Section 3.1 we showed one way of achieving this, namely the identity transformation (3.7). In this approach, *all three constraints are imposed on the reduced variables*, that is, we required that $\gamma(0) = \Psi(0) = \boldsymbol{\Theta}(0) = 0$.

Although it shows that the reduction is valid, this approach is not suitable if one wants to take a global view of the system. Here is the drawback: using (3.7), each initial condition $\{\theta_j(0)\}$ yields different system constants $\{\psi_j\}$ so that the flow (3.6) itself is changed whenever the initial condition is replaced. All solutions originate from the same point $\gamma = \boldsymbol{\Theta} = \Psi = 0$, and evolve under different flows (3.6). Both of these features are confusing and ungeometric: normally we want different solutions to start from *different* points in phase space, and to evolve under the *same* flow.

A better choice of the constraints is to impose all three of them on the system constants rather than on the reduced variables. In this way, we are able to vary initial conditions of the reduced variables while keeping the system constants the same. By changing initial conditions $\gamma(0)$, $\Psi(0)$, and $\boldsymbol{\Theta}(0)$ over their full ranges, a three-dimensional family of trajectories is bundled together and distinguished from all others by the marker $\{\psi_j\}$. The parameters $\{\psi_j\}$ specify a three-dimensional invariant subspace in the original phase space, and therefore can be interpreted as a set of constants of motion. Since there are three constraints on them, the number of *independent* constants of motion is $N - 3$. The whole phase space of $\{\theta_j\}$ is, in this way, decomposed into an $(N - 3)$-parameter family of invariant subspaces.

4.2.2. Parametrization by incoherent states

What are the appropriate constraints to impose on the $\{\psi_j\}$? One of them turns out to be somewhat arbitrary, as we'll see below, while the remaining two constraints are quite natural – they are suggested by the form of the averaged equations (4.4) at $\gamma = 0$.

For $\gamma = 0$, the polar coordinate expression of the reduced equations becomes singular (as expected from Section 3.1). However, this singularity poses no problem (even without resorting to Cartesian expressions) by choosing appropriate constraints on $\{\psi_j\}$. When $\gamma = 0$, the first equation of (4.4) becomes

$$\dot{\gamma} = \frac{1}{N}\sum_{k=1}^{N}[\cos\delta\sin(\psi_k - \Psi) - \sin\delta\cos(\psi_k - \Psi)] = \frac{1}{N}\sum_{k=1}^{N}\sin(\psi_k - \Psi - \delta).$$

We impose two constraints:

$$\frac{1}{N}\sum_{k=1}^{N}\cos\psi_k = \frac{1}{N}\sum_{k=1}^{N}\sin\psi_k = 0. \tag{4.12}$$

Then

$$\dot{\gamma} = \frac{\cos(\Psi + \delta)}{N} \sum_{k=1}^{N} \sin \psi_k - \frac{\sin(\Psi + \delta)}{N} \sum_{k=1}^{N} \cos \psi_k = 0$$

so that $\gamma = 0$ becomes *stationary*. When $\gamma = 0$, the transformation (3.2) reduces to

$$\theta_j(t) = \psi_j + [\Theta(t) - \Psi(t)].$$

Hence, regardless of $(\Theta - \Psi)$, we find

$$\frac{1}{N} \sum_{k=1}^{N} \cos \theta_k = \frac{1}{N} \sum_{k=1}^{N} \sin \theta_k = 0 \quad \text{for all } t, \tag{4.13}$$

and, from (4.2),

$$\dot{\theta}_j = 0 \quad \text{for all } j \text{ and } t.$$

The condition (4.13) is the same as (4.11), i.e., the phases are "incoherent". These states are fixed points of the system (4.2), or rigidly rotating periodic solutions of (4.1) in the original frame. The condition $\gamma = 0$ is now synonomous with the subspace of incoherent states, thanks to (4.12). This subspace is *invariant* under the flow.

The second and third equations of (4.4) are also satisfied consistently by imposing (4.12). Their right hand sides clearly vanish when $\gamma = 0$, as does the coefficient γ of the left hand sides. Now, $\dot{\Psi}$ and $\dot{\Theta}$ do not have to diverge. In fact, Ψ and Θ can be arbitrary as long as $\dot{\Psi} = \dot{\Theta}$ (required from $\gamma \to 0$ limit of (4.4)). This is consistent with the fact that the mapping curve (3.2) is linear when $\gamma = 0$, therefore, we do not need the values of Ψ and Θ themselves.

By imposing the natural constraints (4.12), we have made the polar coordinate expression (4.4) valid everywhere. The constraints are imposed on the system constants, and therefore have a more natural geometric interpretation.

4.2.3. *Convertibility of initial conditions*

When the new constraints (4.12) are imposed, a new problem arises: given an arbitrary initial condition $\{\theta_j(0)\}$ of the original system, we need to be able to convert it into reduced variables $\gamma(0)$, $\Theta(0)$, $\Psi(0)$ and system constants $\{\psi_j\}$, subject to the constraint that the $\{\psi_j\}$ be incoherent. Is such a conversion possible for an arbitrary initial condition $\{\theta_j(0)\}$? If not, then (3.2) would represent only a particular solution, rather than the general solution of the system. The following lemma shows that such a conversion is indeed possible for almost all initial conditions.

Lemma. For almost all values of $\theta_1, \cdots, \theta_N$, there exist reduced variables γ, Θ, Ψ, and constants $\psi_1, \cdots, \psi_N$ such that (3.2) and (4.12) are both satisfied. The only exceptions are "majority clusters" in which $N/2$ or more of the θ_j are equal (mod 2π).

Remark. The following proof will show why majority clusters are special.

Proof. Since (3.2) is invariant under

$$\theta_j \to \psi_j, \quad \Theta \to \Psi, \quad \gamma \to (-\gamma), \tag{4.14}$$

the formulas (3.3) and (3.4) are, too. Therefore the two equations in (3.3) become

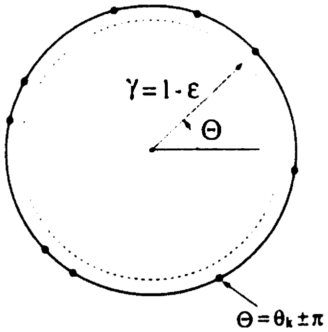

Fig. 5. Index theory is applied to the region inside the dashed circle of radius $1-\epsilon$, $\epsilon \to 0+$. The radial and angular coordinates are γ and $\boldsymbol{\Theta}$, respectively. For each phase θ_k, $\boldsymbol{\Theta} = \theta_k \pm \pi$ on the unit circle becomes a singular point of the vector field $(V_\gamma, V_{\boldsymbol{\Theta}})$.

$$\sin(\psi_j - \Psi) = \frac{\sqrt{1-\gamma^2}\sin(\theta_j - \boldsymbol{\Theta})}{1+\gamma\cos(\theta_j - \boldsymbol{\Theta})}, \quad \cos(\psi_j - \Psi) = \frac{\gamma + \cos(\theta_j - \boldsymbol{\Theta})}{1+\gamma\cos(\theta_j - \boldsymbol{\Theta})}. \tag{4.15}$$

Thus, (4.12) is equivalent to:

$$V_{\boldsymbol{\Theta}} \doteq \frac{1}{N}\sum_{k=1}^{N} \frac{\gamma\sin(\theta_k - \boldsymbol{\Theta})}{1+\gamma\cos(\theta_k - \boldsymbol{\Theta})} = 0, \quad V_\gamma \doteq \frac{1}{N}\sum_{k=1}^{N} \frac{\gamma + \cos(\theta_k - \boldsymbol{\Theta})}{1+\gamma\cos(\theta_k - \boldsymbol{\Theta})} = 0. \tag{4.16}$$

Here, the θ_k are given and fixed, and we seek a solution $(\boldsymbol{\Theta}, \gamma)$ in the allowed region $0 \le \boldsymbol{\Theta} < 2\pi$, $0 \le \gamma < 1$. The strategy is to interpret a solution $(\boldsymbol{\Theta}, \gamma)$ as a fixed point of a continuous vector field defined by $(V_{\boldsymbol{\Theta}}, V_\gamma)$, and then to use index theory to prove that the vector field has a fixed point.

If we interpret $\boldsymbol{\Theta}$ and γ as the angle and radius in polar coordinates (Fig. 5), then the allowed region corresponds to the unit disk, and $V_{\boldsymbol{\Theta}}$ and V_γ represent the angular and radial components of a vector field, respectively. The vector field is continuous in the open disk $0 \le \gamma < 1$. On the circle $\gamma = 1$, (4.16) shows that $V_{\boldsymbol{\Theta}}$ diverges at $\boldsymbol{\Theta} = \theta_k \pm \pi$ for $k = 1, \dots, N$. Thus, when computing the index, we choose a slightly smaller circle $\gamma = 1 - \epsilon$, and then take $\epsilon \to 0+$.

How does V_γ change on this circle? The denominator of the kth term of V_γ, i.e., $(1 + \gamma\cos(\theta_k - \boldsymbol{\Theta}))$, vanishes at $\gamma = 1$ and $\theta_k - \boldsymbol{\Theta} = \pm\pi$. However, the numerator $(\gamma + \cos(\theta_k - \boldsymbol{\Theta}))$ also vanishes. To resolve the kth term around this singularity, let $\gamma = 1 - \epsilon$ and $\mu = \boldsymbol{\Theta} - \theta_k \pm \pi$ where $0 < \epsilon, |\mu| \ll 1$. Then

$$\frac{1}{N}\frac{\gamma + \cos(\theta_k - \boldsymbol{\Theta})}{1 + \gamma\cos(\theta_k - \boldsymbol{\Theta})} = \frac{1}{N}\frac{1 - \epsilon - \cos\mu}{1 - (1-\epsilon)\cos\mu} = \frac{1}{N}\frac{-\epsilon + \mu^2/2 + O(\mu^4)}{\epsilon + \mu^2/2 + O(\epsilon\mu^2, \mu^4)}.$$

Fix ϵ and change μ. As we pass near the singularity, the term tends to $-1/N$ (when $\mu = 0$). Sufficiently far from the singularity, the value of the term is $+1/N$.

Now we derive a condition that ensures that the vector field has non-zero index on the circle $\gamma = 1 - \epsilon$, $\epsilon \to 0+$. (By a standard theorem [35], this will immediately imply the existence of a fixed point inside, as desired.) Specifically, we would like V_γ to be positive everywhere on the circle, so that the the vector field always points outward. Consider the contributions of the various terms to the index. If $\theta_1, \cdots, \theta_N$ are all distinct, then even though the kth term in the sum for V_γ becomes $-1/N$, the other $(N-1)$ terms are all $+1/N$, hence V_γ remains positive. When two θ's are identical, two terms in V_γ become $-1/N$ at the corresponding singularity so that V_γ becomes non-positive unless there are at least three other θ's with different phases from the two. More generally, one can see that V_γ stays positive all over the circle if and only if the largest group of identical θ's (the largest "cluster") contains less than half of the oscillators.

From now on, suppose that the size of the largest cluster is less than $N/2$, so that V_γ is positive everywhere on the circle. Then, since V_Θ is well-behaved everywhere on $\gamma = 1 - \epsilon$, the vector field always points outward. Hence the index along the circle is $+1$. We conclude that the vector field must have at least one fixed point inside the disk. The coordinates of this fixed point are the desired solution (Θ, γ) of (4.16).

Once we obtain Θ and γ at the solution, these values are substituted in (3.2) to obtain N equations for Ψ and $\{\psi_j\}$. Another, somewhat arbitrary, constraint on $\{\psi_j\}$ can be imposed at this moment to determine Ψ uniquely. One candidate is

$$\sum_{k=1}^{N} \psi_k = 0. \tag{4.17}$$

This constraint picks one incoherent set of $\{\psi_j\}$ from others that differ only by a rigid rotation. Solving (3.2) for ψ_j and substituting it into (4.17), we obtain

$$\sum_{k=1}^{N} \left[\Psi + 2\arctan\left(\sqrt{\frac{1-\gamma}{1+\gamma}} \tan[\tfrac{1}{2}(\theta_k - \Theta)] \right) \right] = 0 \tag{4.18}$$

which determines Ψ. Finally, $\{\psi_j\}$ is obtained from (3.2). Thus the conversion is complete. This concludes the proof of the lemma. □

Remarks

(1) The fixed point guaranteed by the lemma seems to be *unique*. Numerical evidence for this conjecture is presented in the subsection after the next. We have been unable to find a proof of the uniqueness.

(2) The lemma fails for states that contain majority ($\geq N/2$) clusters. It turns out that these states are incompatible with the incoherence condition (4.12). To understand why the failure occurs, regard the transformation (3.2) as a reparametrization of the unit circle, mapping ψ_j to θ_j. The circle is stretched in some places and shrunken in others, but the ordering and topology of the oscillators are preserved. For almost all configurations $\{\theta_j\}$, this reparametrization can successfully produce a preimage $\{\psi_j\}$ with its centroid at the origin. However, when there is a cluster containing at least $N/2$ oscillators, the centroid cannot possibly vanish; even if all the remaining oscillators are pushed diametrically opposite the cluster, they still cannot counterbalance it. Hence, there is no hope of expressing such a state in terms of an incoherent preimage.

(3) Although our method of parametrizing the $\{\theta_j\}$ by incoherent $\{\psi_j\}$ was suggested by the particular form of the averaged system (4.4), the method has nothing to do with the evolution equations themselves. The same conversion works for other reducible equations of the form (3.1).

4.2.4. Potential function

The expressions V_Θ and V_γ defined in (4.16) seem to be partial derivatives of some function, just as the sums in (4.4) were partial derivatives of a function $\mathcal{H}$. This analogy is, of course, due to the invariance of (3.2) with respect to the exchanges (4.14). It is easy to see that if we define a function

$$\mathcal{U}(\boldsymbol{\Theta},\gamma) = \frac{1}{N}\sum_{k=1}^{N} \log\left(\frac{1+\gamma\cos(\theta_k-\boldsymbol{\Theta})}{\sqrt{1-\gamma^2}}\right) \tag{4.19}$$

corresponding to $\mathcal{H}$ in (4.5), then we obtain formulas corresponding to (4.6) and (4.7), namely

$$\frac{\partial\mathcal{U}}{\partial\boldsymbol{\Theta}} = \frac{1}{N}\sum_{k=1}^{N}\frac{\gamma\sin(\theta_k-\boldsymbol{\Theta})}{1+\gamma\cos(\theta_k-\boldsymbol{\Theta})} = V_{\boldsymbol{\Theta}},$$

$$\frac{\partial\mathcal{U}}{\partial\gamma} = \frac{1}{N(1-\gamma^2)}\sum_{k=1}^{N}\frac{\gamma+\cos(\theta_k-\boldsymbol{\Theta})}{1+\gamma\cos(\theta_k-\boldsymbol{\Theta})} = \frac{V_\gamma}{1-\gamma^2}, \tag{4.20}$$

where $0 \le \gamma < 1$, as before. Fixed points of (4.16) correspond precisely to stationary points of $\mathcal{U}$. The vector $(V_{\boldsymbol{\Theta}}/\gamma, V_\gamma/(1-\gamma^2))$ points in the direction of steepest ascent on the potential function $\mathcal{U}$.

The functions $\mathcal{H}$ and $\mathcal{U}$ are strikingly similar. In fact, they differ only by a sign. To see this, use the first equation of (3.3) to express $\mathcal{H}$ in (4.5) as

$$\mathcal{H} = \frac{1}{N}\sum_{k=1}^{N}\log\left(\frac{\sin(\psi_k-\Psi)}{\sin(\theta_k-\boldsymbol{\Theta})}\right). \tag{4.21}$$

Using the symmetric counterpart (4.15), $\mathcal{U}$ in (4.19) becomes

$$\mathcal{U} = \frac{1}{N}\sum_{k=1}^{N}\log\left(\frac{\sin(\theta_k-\boldsymbol{\Theta})}{\sin(\psi_k-\Psi)}\right). \tag{4.22}$$

Therefore,

$$\mathcal{U}(\boldsymbol{\Theta},\gamma;\{\theta_j\}) = -\mathcal{H}(\Psi,\gamma;\{\psi_j\}). \tag{4.23}$$

Another interesting relation between the two functions is that $\mathcal{U}$ can be regarded as $\mathcal{H}$ via the transformation

$$\mathcal{U}\to\mathcal{H},\quad \gamma\to\gamma,\quad \theta_j\to\psi_j,\quad \boldsymbol{\Theta}\to\Psi\pm\pi. \tag{4.24}$$

Thus if the given data sets, $\{\theta_j\}$ for $\mathcal{U}$ and $\{\psi_j\}$ for $\mathcal{H}$, are the same, then $\mathcal{U}$ at $(\boldsymbol{\Theta},\gamma)$ gives the same value as $\mathcal{H}$ at $(\Psi\pm\pi,\gamma)$. This is useful when we draw contour curves of both functions and study their surfaces.

4.2.5. Numerical conversion of initial conditions

We have not found an explicit analytical expression for the solution $(\gamma,\boldsymbol{\Theta})$ of (4.16). Computing it numerically, however, is not difficult. The following procedure has worked for all the cases we have tested, and we conjecture that it is valid in general.

For all initial conditions $\{\theta_j\}$ without a majority cluster, the potential $\mathcal{U}$ is found numerically to have a *unique* minimum within $0 \le \gamma < 1$. The minimum can be reached from a suitable starting point by following, for example, the steepest descent path.

To facilitate intuition, we plot typical contour curves of $\mathcal{U}$ in Fig. 6, for $N = 8$. The values of $\theta_1,\ldots,\theta_8$ are indicated by dots on the unit circle; the numbers attached to them indicate the multiplicity of phases at that point. In Fig. 6 there is one cluster of size two, and six isolated

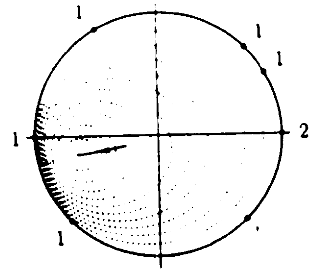

Fig. 6

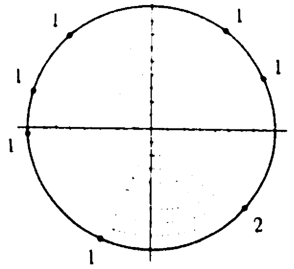

Fig. 7

Fig. 6. A typical contour of $\mathcal{U}$, plotted on the plane with polar coordinates γ and Θ, and assuming there is no majority cluster. The dots on the unit circle represent the phases θ_j, given as parameters. The numbers attached to the dots denote multiplicities. There are $N = 8$ oscillators. The values of θ_j are: π, $2\pi/3$, $\pi/4$, $\pi/6$, 0 (double), $-\pi/4$, and $-3\pi/4$. The level curves are closed and off-centered. The minimum can be easily computed; the solid line is the steepest descent path obtained numerically.

Fig. 7. A typical contour of $\mathcal{H}$, plotted on the plane with polar coordinates γ and Ψ. The incoherent conversion of initial conditions is used. The dots represent the preimages ψ_j computed for the θ_j given in Fig. 6. The centroid of ψ_j is at the origin. The function $\mathcal{H}$ is convex, with its minimum at the origin.

oscillators. The contours of $\mathcal{U}$ (dashed closed curves) decrease monotonically from a maximum near $\gamma = 1$, where $\mathcal{U}$ is large and positive, to a minimum at the innermost contour. This is the stationary point we would like to compute.

The minimum is typically located opposite the centroid of the oscillators with respect to the origin. Hence, $\gamma = R$ and $\Theta = \phi \pm \pi$ is a good initial guess of the location. Integrating along the steepest descent direction from this guess, the path (shown in Fig. 6 as a solid curve) converges to the minimum. The coordinates (γ, Θ) of the minimum yield the initial conditions for the system (4.4) (or other reduced equations), and the minimum value of $\mathcal{U}$ gives the initial value of $-\mathcal{H}$. Recall that this quantity will be conserved in the averaged system with $\sin\delta = 0$.

4.3. The Lyapunov function

This section resolves the second issue posed at the end of Section 4.1: we clarify the geometric meaning of the Lyapunov function $\mathcal{H}$ of the reduced system. By imposing the incoherence condition (4.12) on the system constants $\{\psi_j\}$, we will see that $\mathcal{H}$ measures the phase coherence of the N oscillators.

4.3.1. $\mathcal{H}$ with the incoherence constraints

Recall from (4.7) that

$$\frac{\partial \mathcal{H}}{\partial \gamma} = \frac{F(\Psi,\gamma)}{1-\gamma^2}, \quad \text{where } F(\Psi,\gamma) = \frac{1}{N}\sum_{k=1}^{N} \frac{\gamma - \cos(\psi_k - \Psi)}{1 - \gamma\cos(\psi_k - \Psi)}.$$

Now imposing the constraint (4.12), we obtain

$$F(\Psi, \gamma = 0) = -\frac{1}{N}\sum_{k=1}^{N} \cos(\psi_k - \Psi) = 0.$$

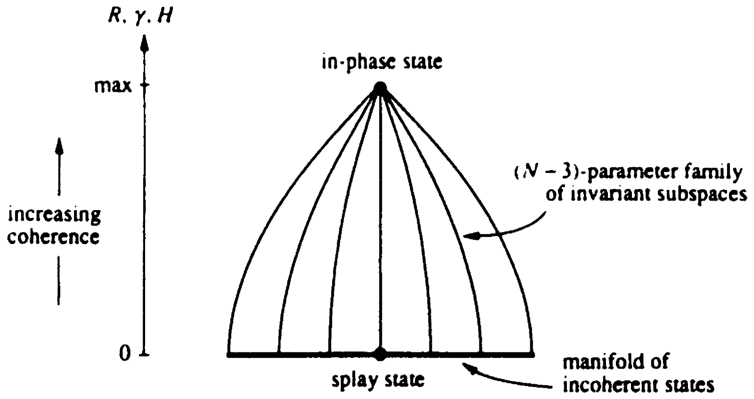

Fig. 8. Foliation of the N-dimensional phase space (schematically) for the averaged systems. Two extreme sets are the in-phase state (maximizing the order parameter R, the distortion parameter γ, and the Hamiltonian $\mathcal{H}$) and the manifold of incoherent states (where R, γ, and $\mathcal{H}$ all vanish). The incoherent states are connected to the in-phase state via an $(N-3)$-parameter family of invariant subspaces, shown as leaves of the foliation.

Thus F and $\mathcal{H}$ vanish on the incoherent manifold.

Moreover, F is strictly increasing in the γ-direction for all Ψ since

$$\begin{aligned}\frac{\partial F}{\partial \gamma} &= \frac{1}{N}\sum_{k=1}^{N} \frac{[1-\gamma\cos(\psi_k-\Psi)]-[\gamma-\cos(\psi_k-\Psi)][-\cos(\psi_k-\Psi)]}{[1-\gamma\cos(\psi_k-\Psi)]^2} \\ &= \frac{1}{N}\sum_{k=1}^{N} \frac{1-\cos^2(\psi_k-\Psi)}{[1-\gamma\cos(\psi_k-\Psi)]^2} > 0\end{aligned}$$

for incoherent $\{\psi_j\}$.

Now adopting radius γ and angle Ψ as the polar variables, the graph of $\mathcal{H}$ becomes a convex well. In this new coordinate system, the contours of $\mathcal{H}$ become concentric curves centered at the *origin*, the minimum of $\mathcal{H}$. Fig. 7 shows typical level curves of $\mathcal{H}$ for $N = 8$. The preimages $\psi_1, \ldots, \psi_8$ satisfying the incoherence constraints are shown as dots, just as the θ's were in Fig. 6.

The function $\mathcal{H}$ has the following properties. From (4.5), $\mathcal{H} = 0$ at $\gamma = 0$. Since F is an increasing positive definite function of γ, $\partial\mathcal{H}/\partial\gamma \to +\infty$ monotonically as $\gamma \to 1$. Moreover, $\mathcal{H}$ itself monotonically increases with respect to γ; in fact, $\mathcal{H} \to \infty$ as $\gamma \to 1$ for any Ψ.

The levels of $\mathcal{H}$ reflect the coherence of the oscillators. For instance, as $\gamma \to 1$, and therefore as $\mathcal{H} \to \infty$, the oscillators are close to the in-phase state. At the other extreme, $\gamma = 0$ and $\mathcal{H} = 0$ implies $\theta_j = \psi_j + (\Theta - \Psi)$, as shown in Section 3.1. In this case $\{\theta_j\}$ becomes the incoherent state $\{\psi_j\}$ itself, only rotated rigidly by the angle $(\Theta - \Psi)$. Hence, the Lyapunov function $\mathcal{H}$ is yet another measure of the phase coherence of the oscillators, as are γ and R.

This interpretation of $\mathcal{H}$ has powerful global implications for the averaged system (4.1). From (4.9), $\dot{\mathcal{H}} = R^2 \sin\delta$. When $\sin\delta > 0$, $\mathcal{H}$ increases in time, and the oscillators approach the in-phase state for almost all initial conditions. When $\sin\delta < 0$, $\mathcal{H}$ decreases, meaning that they spread apart until their centroid vanishes. Thus, the in-phase state is globally attracting when $\sin\delta > 0$, whereas the incoherent manifold is attracting when $\sin\delta < 0$. At the critical value $\sin\delta = 0$, every trajectory runs along a contour of $\mathcal{H}$. As shown above, such contours are closed loops. Each

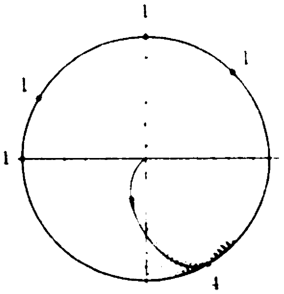

Fig. 9. A typical contour of $\mathcal{H}(\Psi,\gamma)$ when there is a majority cluster of size $N/2$. The dots represent the parameters ψ_j, whose values are: π, $5\pi/6$, $\pi/2$, $\pi/4$, and $-\pi/3$ (multiplicity 4). On the unit circle, $\mathcal{H}$ is infinite everywhere, except at the cluster of four oscillators where it assumes a finite value. The contours are tangent to the circle at the singular point. The solid curve is a computed trajectory of the integrable averaged system ($\delta = 0$). It is not periodic but converges to the singular point. When the cluster size exceeds $N/2$, a similar picture is obtained.

trajectory undergoes periodic motion in the (Ψ,γ) space. In the full phase space, the motion is quasiperiodic on 2-tori, for reasons given in Section 4.1.

Fig. 8 shows a schematic drawing of the N-dimensional phase space. On one side, there is an $(N-3)$-dimensional manifold of incoherent states, the most disordered states of the system. On the opposite side, there is the in-phase state, the most ordered one. There is only one such state although there are many ways to approach it. In fact, each point on the incoherent manifold is connected to the in-phase state through a three-dimensional invariant subspace. Such subspaces are stacked side by side as an $(N-3)$-parameter family, shown in Fig. 8 as a family of curves. The $N-3$ parameters are the $\{\psi_j\}$, subject to the two incoherence constraints (4.12) and the third, arbitrary constraint (4.17). On each invariant subspace, the flow is either toward the in-phase state (if $\sin\delta > 0$), toward the incoherent manifold ($\sin\delta < 0$), or neither ($\sin\delta = 0$). In this last case, the motion is quasiperiodic.

4.3.2. Majority clusters

The analysis in the last section does not apply if there is a majority cluster, i.e., if $N/2$ or more θ's are initially equal. Nevertheless, this (highly exceptional) case can be handled by resorting to the identity conversion (3.7). Recall that the preimage $\{\psi_j\}$ is then taken to be identical to $\{\theta_j(0)\}$, and in return, we restrict attention to the trajectory that starts at $\gamma(0) = \Psi(0) = \Theta(0) = 0$.

When we use the identity conversion, the contours of $\mathcal{H}$ are off-centered like those of $\mathcal{U}$, as described in the preceding section. Indeed, since $\{\psi_j\}$ is now identical to $\{\theta_j\}$, the contour maps for $\mathcal{H}$ and $\mathcal{U}$ are the same after a rotation by 180 degrees, thanks to (4.24).

Fig. 9 shows typical contours of $\mathcal{H}$ for the case where there is a majority cluster. Here, four of the eight oscillators have equal ψ's. The resulting contour map is qualitatively different from Fig. 6 – the critical point occurs on the circle, and all the contours emanate from it. (The contours for larger clusters of size $> N/2$ look similar.)

The change in contours can be explained by a local analysis of $\mathcal{H}$ near $\gamma = 1$. If we rewrite $\mathcal{H}$ in (4.5) as

$$\mathcal{H} = \frac{1}{N}\sum_{k=1}^{N}\log\left[1-\gamma\cos(\psi_k-\Psi)\right] - \tfrac{1}{2}\log(1-\gamma^2),$$

we see that the asymptotic behavior as $\gamma \to 1$ is determined by the competition of the terms on the right hand side. The second term becomes singular like

$$-\tfrac{1}{2}\log(1-\gamma^2) \sim -\tfrac{1}{2}\log(1-\gamma) \to +\infty \quad \text{as } \gamma \to 1\,.$$

The first term becomes singular at $\gamma = 1$ only when $\Psi = \psi_k$ for some k. Then, the kth term in the sum gives a contribution of

$$\frac{1}{N}\log\left[1-\gamma\cos(\psi_k-\Psi)\right] \sim \frac{1}{N}\log(1-\gamma) \to -\infty \quad \text{as } \gamma \to 1\,.$$

Since the singularities of both terms are $\sim \log(1-\gamma)$, we only need to compare the coefficients. We see that as $\gamma \to 1$,

$$\mathcal{H} \longrightarrow \begin{cases} -\infty & \text{if more than } N/2 \text{ of the } \psi_k \text{ equal } \Psi, \\ \text{finite} & \text{if exactly } N/2 \text{ of the } \psi_k \text{ equal } \Psi, \\ +\infty & \text{otherwise.} \end{cases}$$

Therefore, when there is no majority cluster, $\mathcal{H}$ is $+\infty$ everywhere on the circle $\gamma = 1$. When there is a majority cluster, $\mathcal{H}$ still equals $+\infty$ at all points of the circle *except* at the cluster; there it is either finite or $-\infty$. In this case all contour curves originate from one side of the singular point and return to the other side as in Fig. 9.

To illustrate some of the new effects caused by a majority cluster, consider the trajectories of the averaged system, in the case $\sin\delta = 0$. Recall that when we use the identity conversion, only the trajectory starting from $\gamma(0) = \Psi(0) = 0$ is meaningful. This solution is shown in Fig. 9 as a solid curve. It follows a contour of $\mathcal{H}$ and converges to the singular point on $\gamma = 1$. In contrast to Fig. 6, the trajectory does not execute periodic motion in γ and Ψ, but rather terminates at a cluster state.

4.4. *Visualizing flows*

In this section we present numerical phase portraits of the averaged system (4.1) for $N = 3$ and $N = 4$. We assume $\sin\delta = 0$ unless otherwise stated. Although the essential dynamics can be understood already by the (γ, Ψ)-diagram of the reduced system, it is much more instructive to view the dynamics in the original θ-coordinates. We thereby obtain a picture of the phase space that improves upon the schematic Fig. 8. For instance, the incoherent manifold and the $(N-3)$-parameter family of invariant subspaces can be visualized directly.

Without loss of generality, the permutation symmetry of (4.1) enables the oscillators to be ordered as follows:

$$\theta_N \le \theta_{N-1} \le \ldots \le \theta_2 \le \theta_1 \le \theta_N + 2\pi\,.$$

Eq. (4.1) also implies that if $\theta_i = \theta_j$ at any time, they remain equal forever. Thus $\theta_i = \theta_j$ defines an invariant hyperplane for each (i,j) pair, and the whole phase space is partitioned into invariant cells. The ordering given above defines a "canonical invariant region [21,36]. Trajectories that start in this region are stuck in there forever; in more physical terms, the oscillators can never pass each other as they run around the unit circle.

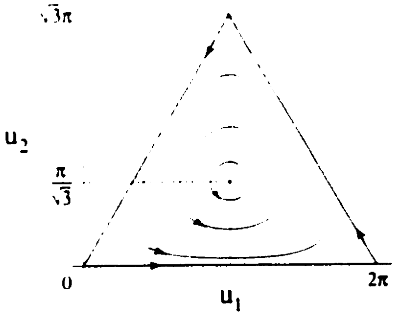

Fig. 10

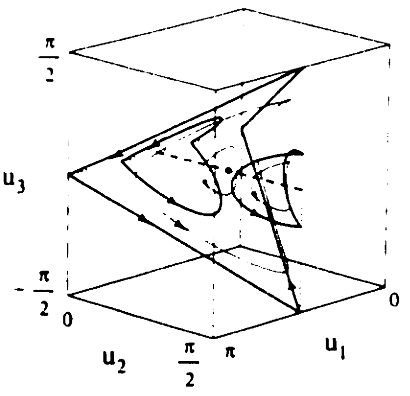

Fig. 11

Fig. 10. Flow of the integrable ($\delta = 0$) averaged system for $N = 3$ in the original coordinates θ_j. The linear transformation $\theta = \sum_{j=1}^{3} \theta_j$, $u_1 = \theta_1 - (\theta_2 + \theta_3)/2$, $u_2 = \sqrt{3}(\theta_2 - \theta_3)/2$ is used to bring out the picture's inherent symmetry. The mean phase θ is decoupled, and is not shown. Only one triangular region, corresponding to the ordering $\theta_3 \le \theta_2 \le \theta_1 \le \theta_3 + 2\pi$ is shown since flows in the other regions are equivalent by symmetry. The phase portrait shows a continuous family of periodic orbits circulating around the splay state (dot in the center). If the mean phase direction were restored, the motion would appear as quasiperiodic motion on 2-tori.

Fig. 11. Flow of the integrable ($\delta = 0$) averaged system for $N = 4$ in the original coordinates θ_j. The linear transformation $\theta = \sum_{j=1}^{4} \theta_j$, $u_1 = (\theta_1 + \theta_2 - \theta_3 - \theta_4)/4$, $u_{2,3} = (\pm\theta_1 \mp \theta_2 + \theta_3 - \theta_4)/4$ is used. The mean phase θ is decoupled, and is not shown. The tetrahedron is the canonical invariant region, corresponding to the ordering $\theta_4 \le \theta_3 \le \theta_2 \le \theta_1 \le \theta_4 + 2\pi$. Notation: dotted edges of the tetrahedron = two pairs of equal θ's; solid edges = three equal θ's; vertices = in-phase solutions; dashed bar inside = filament of incoherent states; dot at center = splay state. Three thin solid loops inside the region are computed trajectories. Four thick curves forming two closed loops are trajectories on the faces of the tetrahedron representing clustered configurations of oscillators.

4.4.1. *Integrable flow for $N = 3$*

Since the right hand side of (4.1) depends only on the phase differences, the mean phase can be removed from the dynamics. For $N = 3$, for example, we may use the linear transformation [2,21]:

$$\bar{\theta} = \tfrac{1}{3}\sum_{k=1}^{3} \theta_k, \quad u_1 = \theta_1 - \tfrac{1}{2}(\theta_2 + \theta_3), \quad u_2 = \tfrac{1}{2}\sqrt{3}(\theta_2 - \theta_3).$$

Since $\bar{\theta}$ is passively driven by the (u_1, u_2) dynamics, it suffices to draw the effective dynamics on the (u_1, u_2)-plane. In Fig. 10, the canonical invariant region $\theta_3 \le \theta_2 \le \theta_1 \le \theta_3 + 2\pi$ appears as a triangle. The sides $u_2 = 0$, $u_1 - u_2/\sqrt{3} = 0$, and $u_1 + u_2/\sqrt{3} = 2\pi$ correspond to $\theta_3 = \theta_2$, $\theta_2 = \theta_1$, and $\theta_1 = \theta_3 + 2\pi$, respectively. The vertices all correspond to the in-phase state $\theta_1 = \theta_2 = \theta_3$ (mod 2π). There are three ways to approach the in-phase state while maintaining the order of the three oscillators. Since the $\bar{\theta}$-direction is projected out, the periodic solutions look like fixed points.

The dot in the center of the triangle is the splay state

$$\theta_1(t) = \theta_2(t) + \tfrac{2}{3}\pi = \theta_3(t) + \tfrac{4}{3}\pi \quad \text{for all } t.$$

It satisfies the incoherence conditions (4.11), and being periodic, it also appears as a fixed point in the figure.

Through the transformation (3.2) and the three constraints (4.12) and (4.17), we must obtain

$$\psi_1 = \tfrac{2}{3}\pi, \quad \psi_2 = 0, \quad \psi_3 = -\tfrac{2}{3}\pi$$

from almost all initial conditions. This is the preimage of the oscillators. Generic trajectories form concentric loops around the splay state. Each trajectory is indeed on a 2-torus when the θ-direction is reinstated.

On the edges of the triangle, two of the oscillators are in phase. Because the size of this cluster exceeds $N/2$, the initial conditions cannot be converted to the splay phase preimage. The edges of the triangle are separatrices (separating neighboring canonical invariant regions corresponding to different choices of the ordering), and the behavior differs qualitatively from the generic case. From Fig. 10 we see that trajectories on the edges are attracted toward the vertices. Starting from one isolated oscillator and a cluster of two others, they eventually merge to form a cluster of three, i.e. they approach the in-phase state. On the separatrices, the motion is not quasiperiodic, but rather appears to have a dissipative character.

4.4.2. *Integrable flow for $N = 4$*

Since θ can be projected out, we may display the phase portrait for $N = 4$ in three dimensions. This turns out very helpful. The dimension of the incoherent manifold becomes $N - 3 = 1$, which is not trivial as it was for $N = 3$.

As pointed out by Tsang and Schwartz [2], a nice transformation in this case is

$$\theta = \tfrac{1}{4}\sum_{k=1}^{4}\theta_k, \quad u_1 = \tfrac{1}{4}(\theta_1 + \theta_2 - \theta_3 - \theta_4), \quad u_{2,3} = \tfrac{1}{4}(\pm\theta_1 \mp \theta_2 + \theta_3 - \theta_4).$$

Fig. 11 shows the projection of the canonical invariant region

$$\theta_4 \le \theta_3 \le \theta_2 \le \theta_1 \le \theta_4 + 2\pi$$

onto the (u_1, u_2, u_3)-space. The four side walls of the tetrahedron $u_2 + u_3 = 0$, $u_1 - u_2 = 0$, $u_2 - u_3 = 0$, and $u_1 + u_2 = \pi$ correspond to $\theta_4 = \theta_3$, $\theta_3 = \theta_2$, $\theta_2 = \theta_1$, and $\theta_1 = \theta_4 + 2\pi$, respectively. There are six edges. Four of them, shown in the figure as solid lines, correspond to three identically phased θ's (the 3+1 states). Two other edges, shown as dotted lines, are two pairs of equal θ's (the 2+2 states). As can be easily checked from (4.1), the points on the 2+2 edges are fixed (meaning the solutions are periodic when θ is reinstated). The four vertices, also shown as fixed points, all correspond to the in-phase solution as before. There are four ways to approach the in-phase state while staying in the canonical invariant region.

There is a dashed bar inside the tetrahedron, connecting the 2+2 edges. It is the one-dimensional *manifold of incoherent states*. Each point on this bar appears fixed since the incoherent states are periodic solutions of (4.1). The dot in the middle of the incoherent manifold is the splay-phase solution, i.e., four oscillators with equally spaced phases.

Generic trajectories are shown as thin solid curves inside the region. They are periodic in the figure, meaning quasiperiodic when θ is included. Trajectories close to the splay state oscillate around the incoherent bar in an almost circular fashion. Trajectories far from the bar are strongly distorted. One large loop shown in the figure visits all four corners closely. The trajectory is slow near corners, and runs rapidly in between. This motion describes the situation when four oscillators are almost in-phase, but one of them suddenly departs from the other three, rotates once, and reapproaches the group. Such "phase slips" appear for any N when a trajectory is close to the in-phase solution. Phase slips also occur for most trajectories when $\sin\delta > 0$ (in-phase is attracting)

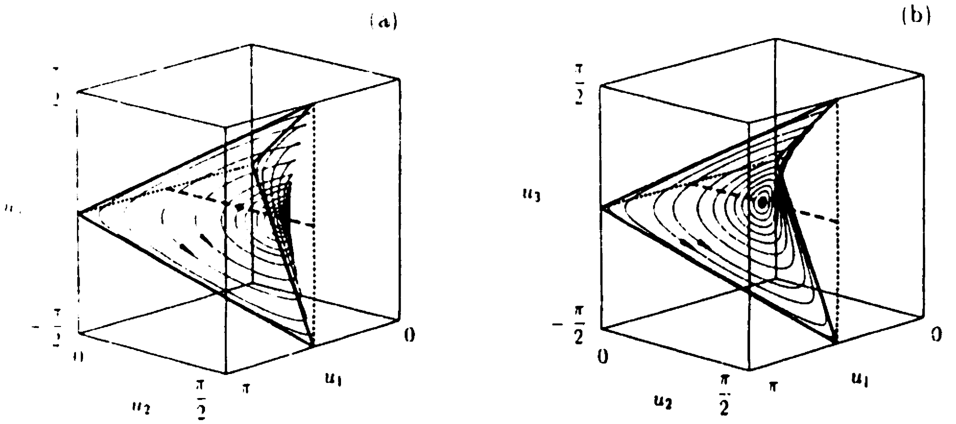

Fig. 12. Trajectories of the integrable flow for $N = 4$, corresponding to a particular preimage $\{\psi_j\}$. The reduced equations (4.4) with $\delta = 0$ are integrated from $\Psi(0) = \Theta(0) = 0$ and various values of $\gamma(0)$. For each $\gamma(0)$, the trajectory is a closed orbit. As $\gamma(0)$ varies, the orbits sweep out a warped surface. The surface intersects the incoherent filament transversely. Changing $\{\psi_j\}$ moves this intersection along the filament.
(a) $\psi_{1,4} = \pm 9\pi/10$, $\psi_{2,3} = \pm\pi/10$. (b) $\psi_{1,4} = \pm 3\pi/4$, $\psi_{2,3} = \pm\pi/4$. This choice of $\{\psi_j\}$ yields the most symmetric possible surface. It emanates from the splay state (solid dot at center).

if we wait for a long time. In this case, the time between slips becomes unbounded as a trajectory approaches the in-phase state.

The four thick curves (forming two closed loops) in Fig. 11 are trajectories on the boundary walls of the tetrahedron, meaning a pair of θ's are identically phased. This is when the size of the largest cluster is exactly $N/2$. The flow is toward the $2+2$ edges, and must end up there. Non-paired oscillators come together to form a cluster that competes with the paired ones.

On the $3+1$ edges (four solid lines) the flow is directed toward the vertices, i.e., the in-phase state. Thus the flow on the separatrix is similar to that of Fig. 4.5; once again, quasiperiodic motion does not occur if there is a sufficiently large cluster.

4.4.3. *Invariant subspaces*

For $N = 4$, we can visualize the $(N-3)$-parameter family of three-dimensional subspaces. If $\bar{\theta}$ is projected out, then Θ is eliminated from the phase portrait. (Note that $\theta_i - \theta_j$ does not involve Θ.) Thus we should see a one-parameter family of two-dimensional surfaces foliating the interior of the tetrahedron. The sole parameter is the location of the surface along the incoherent manifold.

One such surface is computed and shown in Fig. 12a. We chose a set of $\{\psi_j\}$ satisfying the three constraints. The reduced equations (4.4) were then integrated numerically from $\Theta(0) = \Psi(0) = 0$ (without loss of generality), for various values of $\gamma(0)$. Next the transformation (3.2) was applied to the results to recover $\{\theta_j(t)\}$. Finally these phases were themselves converted to the phase differences (u_1, u_2, u_3) shown in Fig. 12a.

When $\gamma(0) = 0$, the trajectory is confined to the incoherent manifold. As $\gamma(0)$ is increased, the orbits sweep out a warped surface, as expected. Each trajectory is periodic. (These closed orbits correspond to invariant 2-tori in the full phase space, after we reinstate $\bar{\theta}$.)

A different choice of $\{\psi_j\}$ would produce another surface. In particular, $\psi_{1,4} = \pm 3\pi/4, \psi_{2,3} = \pm\pi/4$ (evenly spaced oscillators as the preimage) produces a symmetric surface emanating from the splay-phase dot (Fig. 12b). The two principal curvatures of this surface at the splay state have

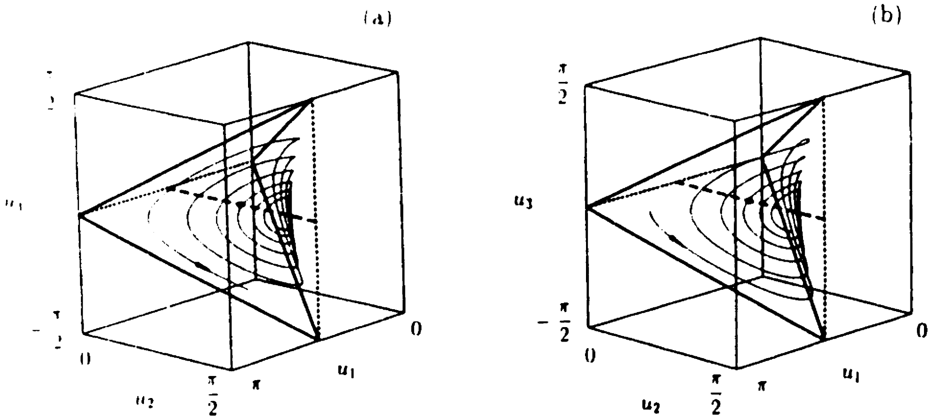

Fig. 13. Trajectories of the averaged system with $\delta \neq 0$. In contrast to Fig. 12, the trajectories are spirals, not closed orbits. However, they still lie on the same warped surface as in Fig. 12, since this surface is determined solely by $\{\psi_j\}$, and the same ψ's as used as in Fig. 12a.
(a) Outward spiral: $\delta = +\pi/100$, $\gamma(0) = 0.5$, $\Psi(0) = \Theta(0) = 0$. (b) Inward spiral: $\delta = -\pi/100$, $\gamma(0) = 0.99$, $\Psi(0) = \Theta(0) = 0$.

the same magnitude.

These membrane-like surfaces are neatly stacked side by side, skewered by the incoherent filament. On each surface the dynamics are governed by a one degree of freedom Hamiltonian system. Note that the "frame" of the membrane surfaces, i.e., the limiting trajectory as $\gamma \to 1$, is formed by the four edges of the 3+1 states, joined at the in-phase vertices.

We now have a global picture of phase space that improves on the earlier schematic Fig. 8. The warped surfaces of Figs. 12a and b correspond to the curves that connect the in-phase state to the incoherent manifold in Fig. 8. The in-phase dot in Fig. 8 should be represented, more precisely, by the whole frame of the 3+1 edges of Fig. 12.

There is also a correspondence between Figs. 10 and 12: if we flatten any of the warped surfaces of Fig. 12, we obtain a picture similar to Fig. 10. In both cases, a continuous family of closed curves is bounded by a polygon; only the number of vertices is increased. Trajectories near the polygonal frame slow down near the vertices and run rapidly in between. They generally have N phase-slips before completing a period of the (Ψ, γ)-dynamics.

We conclude with two examples where $\sin\delta \neq 0$; then $\mathcal{H}$ is no longer conserved. Fig. 13a plots a representative trajectory for the case $\delta = +\pi/100$. For this case, $\mathcal{H}$ is a monotonically increasing function of time, and the trajectory spirals out to the in-phase state. The trajectory is, however, confined to the same warped surface as in Fig. 12a since this surface is determined by $\{\psi_j\}$, and the same $\{\psi_j\}$ have been used in both figures. Fig. 13b shows the case $\delta = -\pi/100$. Now the trajectory spirals down to the incoherent filament, and approaches a final state predetermined by the $\{\psi_j\}$.

4.5. *Origin of degeneracy*

4.5.1. *Degeneracy of averaged systems*

There are three levels of degeneracy exhibited by the averaged system (4.2). We discuss them in order of increasing specialization.

First, the whole phase space has a cellular structure, made up of identically-shaped invariant regions. The flows inside all the cells are equivalent. These properties follow from the permutation symmetry of the system.

Second, each N-dimensional cell is itself partitioned into three-dimensional invariant subspaces. This partitioning occurs for all "reducible" systems of the form (3.1); the averaged system (4.1) belongs to this subclass. This level of degeneracy is due to the absence of explicit higher harmonics in (3.1). The transformation (3.2) works in this case, and converts the N-dimensional system to the reduced three-dimensional system for (γ, Ψ, Θ). Nevertheless, the reduced dynamics can be rich: there can be fixed points, periodic solutions, chaos, coexistence of dissipative and conservative behaviors, etc.

Third, the averaged system (4.1) is more special than other reducible systems because it possesses a rotational invariance – it depends only on the phase differences of the oscillators, not on the phases themselves. When we apply the transformation (3.2) to the averaged system, the variable Θ is canceled upon taking phase differences, and so the right hand sides of (4.1) depend only on γ and Ψ. Thus the averaged system has effectively two-dimensional dynamics, and chaos is therefore impossible.

It is interesting that the effective system turned out to have a Lyapunov function whose properties were independent of $\{\psi_j\}$. This enabled the averaged system to be thoroughly analyzed. Along the way, we found it useful to constrain the $\{\psi_j\}$ to be incoherent. These constraints associated $\gamma = 0$, or equivalently $\mathcal{H} = 0$, with the manifold of incoherent states. Notice that this association was not mandatory; we might have chosen $\gamma = 0$ to label some other states by imposing different constraints. However, the "core" of dynamics of the averaged system happened to be the incoherent manifold, so our choice seemed natural. In particular, given that the incoherent states are stationary under the flow (4.1), it seemed sensible to tailor the coordinate system (Ψ, γ) around them. This explains why we didn't need to resort to Cartesian expressions when analyzing the averaged systems.

4.5.2. *Surviving structure in non-averaged systems*

Many of the results obtained for averaged systems carry over to more general reducible systems, including Josephson arrays. The main difference is that general systems are not rotationally invariant; Θ no longer disappears from the right hand sides of the reduced equations. Thus the reduced system is now three-dimensional, not two-dimensional.

Furthermore, the incoherent states are no longer stationary, and the coordinate system cannot be tailored to the flow. In particular, the states with $\gamma = 0$ are no longer fixed. To avoid a coordinate singularity, we must resort to a Cartesian-type coordinate system, as described in Section 3.1.

However, the conversion of initial conditions is unaffected. The best approach is still to impose the three constraints (4.12) and (4.17) on a set of constants $\{\psi_j\}$. One set of $\{\psi_j\}$ corresponds to a particular three-dimensional subspace. Thus the trajectories of all reducible systems are confined to the same subspaces as before – only the evolution inside the subspaces is different, and depends on the governing equations.

4.5.3. *Explaining previous observations*

Our results shed some light on the observations listed in Section 2.4.

Observation 1 (existence of at least $N - 2$ neutrally stable directions around the splay state) is now proven. The results of Section 3.2 hinted that this observation was somehow related to reducibility, but it was not clear how different subspaces were related to one another. We now see that the neutral stability follows from the foliation of phase space by an $(N-3)$-parameter family of invariant subspaces: $N-3$ neutral directions correspond to perturbations from one subspace to another, and one additional direction corresponds to trivial perturbations along the splay-phase orbit itself.

Then why doesn't the in-phase periodic solution exhibit a similar degeneracy? Because (as shown in Section 4.4) the in-phase solution lies at the "hinge" of the foliation where all the subspaces meet, it is meaningless to speak of perturbations across subspaces at this point, and so the in-phase state can be attracting, at least in some cases.

Although Observation 1 was originally suggested by numerical experiments on the splay state, it is now clear that the same statement holds for *all* incoherent periodic states (if they exist). Moreover, even for arbitrary, non-periodic trajectories, we may conclude that there are at least $N-3$ Lyapunov exponents equal to zero.

The status of Observation 2 (foliation by invariant 2-tori for resistively loaded arrays) is more problematic. We have proven that Observation 2 is correct in the weak-coupling limit – the averaged equations then have $\delta = 0$ and the Hamiltonian $\mathcal{H}$ provides an additional constant of motion, yielding complete integrability and the desired foliation by 2-tori. But for the case of stronger coupling, Observation 2 is probably false, strictly speaking, because the tori seem to break as the coupling increases. Nevertheless, a family of invariant 2-tori might persist near the splay state; perhaps this issue can be settled using KAM theory for reversible systems [31].

Observation 3 (the existence of a manifold of incoherent periodic states) is the most problematic of all. Such a manifold certainly exists in the weak-coupling limit. It is attracting, repelling, or neutral depending on δ, and it organizes the dynamics of the averaged system. But its existence in general is an open problem. In the next subsection we present some tentative ideas on this topic.

4.5.4. *Persistence of incoherent manifold*

Numerical results suggest that a manifold of incoherent periodic states persists if the coupling is not weak, and that such manifold exists for certain Josephson arrays as well. Using the reduction method, we may outline a strategy for an existence proof, at least for the resistively loaded array and for a certain parameter range, as follows.

The reduced equations are (3.17). Numerics suggest (but this is not proven) that for an appropriate range of parameters, the disc $x^2 + y^2 < 1$ at $\Phi = 0$ is mapped into itself at $\Phi = 2\pi$. Since the flow in between is continuous, Brouwer's fixed point theorem implies that the map of the disc to itself has a fixed point, corresponding to a solution of the flow that is 2π-periodic in Φ. From (3.2) it is clear that all θ_j advance by 2π when Φ advances by that amount, and x and y return to their original values. Hence the fixed point of the map corresponds to a time-periodic solution of the array equations.

This argument holds regardless of $\{\psi_j\}$, as long as the map is well-defined. Thus each subspace contains an incoherent periodic solution. (Strictly speaking, the centroid does not vanish for these solutions. However, the word "incoherent" should not be confusing.) Changing $\{\psi_j\}$ continuously, we generate a manifold of incoherent periodic states.

It will be interesting to see if this heuristic argument can be made rigorous.

5. Continuum limit

This section deals with the infinite-N limit of the reducible system (3.1). For series arrays of Josephson junctions, N is typically on the order of 10^3. Thus, the continuum limit is a reasonable approximation. However, our main interest is theoretical: the continuum limit gives rise to an integro-partial differential equation with low-dimensional effective dynamics as well as interesting soliton-like solutions.

For finite N, the dependent variables are the phases $\theta_1, \ldots, \theta_N$, visualized as particles moving on the unit circle. In continuum limit we are less interested in this Lagrangian view. Instead, we concern ourselves with the *density* $\rho(\theta, t)$ of oscillators at a given angle θ at time t. It satisfies the normalization constraint

$$\oint_{-\pi}^{\pi} \rho(\theta, t)\, d\theta = 1 \quad \text{for all } t. \tag{5.1}$$

Each oscillator is now viewed as a constituent particle of a "fluid". The density function, therefore, obeys the conservation law

$$\frac{\partial \rho}{\partial t} + \frac{\partial}{\partial \theta}(\rho v) = 0, \tag{5.2}$$

where $v(\theta, t)$ is the velocity field. The appropriate v must be the generalization of the velocity of an individual oscillator in the finite-N case, given by (3.1). Thus, taking $N \to \infty$, v is given by

$$v(\theta, t) = f + g\cos\theta + h\sin\theta, \tag{5.3}$$

where f, g, h are functions of time t. Eq. (5.2) with (5.3) is the governing equation for the oscillator density ρ. (The finite-N equations can be recovered by taking the density function ρ to be a sum of δ-functions and by considering the characteristics of (5.2).) We are now asked to solve this kinematic wave problem posed on a periodic domain.

Usually, waves in a periodic domain are analyzed by decomposition into Fourier modes and then considering interactions among the modes. However, since we have already analyzed the finite-N version, we only need to extend our reduction method to the infinite-N equation. In Section 5.1, we show that the partial differential equation (5.2) can be reduced to just three ordinary differential equations. Section 5.2 analyzes the averaged equations for this system, obtained in the weak-coupling limit. Then the effective dynamics become two-dimensional, and a Lyapunov function and global stability results can be obtained.

Eqs. (5.2, 5.3) can be viewed as one of the rare examples of an infinite-dimensional evolution equation whose dynamical complexity is rigorously bounded. It can produce at most three-dimensional chaos, as well as quasiperiodicity on 2-tori, depending on the functions f, g, and h. For one special case (Section 5.3) the system becomes completely integrable, and solitons are observed as in other integrable systems. Finally, Section 5.4 shows some illustrative numerical examples of solitary waves, chaos, and wave interactions.

5.1. General reducible systems

5.1.1. Reduction

The reduction of the continuity equation (5.2) with (5.3) is based on the same idea as the reduction of the finite-N equations (3.1). However, the details differ slightly, and are described here for completeness.

The main idea is to reduce (5.2) via a time-dependent change of coordinates from θ to ψ, using (3.2):

$$\tan[\tfrac{1}{2}(\theta - \Theta(t))] = \sqrt{\frac{1+\gamma(t)}{1-\gamma(t)}}\tan[\tfrac{1}{2}(\psi - \Psi(t))]. \tag{5.4}$$

The claim is that the time-dependent density $\rho(\theta, t)$ will transform into a *stationary* density $\sigma(\psi)$ if (γ, Ψ, Θ) satisfy appropriate ordinary differential equations, to be determined. The two densities are related by:

$$\rho(\theta, t)d\theta = \sigma(\psi)d\psi \qquad \text{for all } t, \tag{5.5}$$

to conserve oscillators in any infinitesimal interval.

We organize the necessary formulas. First, (3.3, 3.4) can be used just by reading θ_j as θ and ψ_j as ψ. The symmetric counterpart of (3.3) is (4.15), which can be used in the same manner. Now, solve (5.4) with respect to ψ to obtain

$$\psi = \Psi(t) + 2\arctan(\Gamma(t)^{-1}\tan[\tfrac{1}{2}(\theta - \Theta(t))]), \tag{5.6}$$

where $\Gamma = \sqrt{(1+\gamma)/(1-\gamma)}$ as in Section 3.1. Following the strategy used to derive (3.5), we obtain

$$\frac{\partial\psi}{\partial t} = \dot{\Psi} - \frac{\dot{\gamma}}{1-\gamma^2}\sin(\psi - \Psi) - \frac{1-\gamma\cos(\psi-\Psi)}{\sqrt{1-\gamma^2}}\dot{\Theta}. \tag{5.7}$$

(This relation can be also obtained from (3.5) by considering the symmetry (4.14).) From (5.6) one finds

$$\frac{\partial\psi}{\partial\theta} = \frac{1-\gamma\cos(\psi-\Psi)}{\sqrt{1-\gamma^2}}. \tag{5.8}$$

Using these formulas, (5.2),(5.3) can be expressed in terms of the new coordinate ψ. In Appendix A we show that the continuity equation can be satisfied identically, regardless of $\sigma(\psi)$, by imposing the three equations:

$$\begin{aligned}\dot{\gamma} &= -(1-\gamma^2)(g\sin\Theta - h\cos\Theta),\\ \gamma\dot{\Psi} &= -\sqrt{1-\gamma^2}(g\cos\Theta + h\sin\Theta),\\ \gamma\dot{\Theta} &= \gamma f - g\cos\Theta - h\sin\Theta,\end{aligned} \tag{5.9}$$

which are identical to the reduced equations (3.6) for the finite-N system.

Thus the infinite-dimensional system (5.2, 5.3) is reduced to a system of three ordinary differential equations for (γ, Ψ, Θ). The reduced system involves a time-independent function $\sigma(\psi)$ *as a parameter.*

5.1.2. *Converting initial conditions*

Given an initial density $\rho(\theta,0) = \rho_0(\theta)$, one can determine initial conditions for the reduced variables $\gamma(0)$, $\Psi(0)$, and $\Theta(0)$, as well as the stationary (preimage) distribution $\sigma(\psi)$. As in the finite-N case, we could use the identity conversion

$$\gamma(0) = \Psi(0) = \Theta(0) = 0 \quad (\text{so}, \theta = \psi), \qquad \sigma(\psi) = \rho_0(\theta). \tag{5.10}$$

A better approach is to parametrize by the incoherent states of the averaged system (shown in Section 5.2). We impose three constraints on $\sigma(\psi)$, analogous to (4.12) and (4.17):

$$\oint \sigma(\psi)\cos\psi d\psi = \oint \sigma(\psi)\sin\psi d\psi = \int_{\Psi-\pi}^{\Psi+\pi} \sigma(\psi)\psi d\psi = 0. \tag{5.11}$$

The range of integration $[\Psi-\pi, \Psi+\pi]$ (in the last relation) is chosen so that $\Psi(0)$ can later be computed easily. The normalization (5.1) yields an additional constraint

$$\oint \sigma(\psi) d\psi = 1. \tag{5.12}$$

To use the parametrization by incoherent states, we need to prove that we can find an incoherent preimage $\sigma(\psi)$ as well as initial conditions $\gamma(0), \Psi(0), \Theta(0)$, given an arbitrary initial condition $\rho_0(\theta)$. The index argument in Section 4.2 goes through with little modification, with the usual caveat that $\rho_0(\theta)$ must not have a "majority cluster", i.e., a δ-spike that contains at least half of the oscillators. Once we find (Θ,γ) for $\rho_0(\theta)$, then Ψ and $\sigma(\psi)$ can be determined from (5.11) and (5.5).

Specifically, (γ,Θ) is obtained as the root of the first two equations of (5.11), rewritten as:

$$\oint \frac{\gamma\sin(\theta-\Theta)}{1+\gamma\cos(\theta-\Theta)}\rho_0(\theta)d\theta = \oint \frac{\gamma+\cos(\theta-\Theta)}{1+\gamma\cos(\theta-\Theta)}\rho_0(\theta)d\theta = 0, \tag{5.13}$$

which comes from a potential function

$$\mathcal{U}(\Theta,\gamma) = \oint \log\left(\frac{1+\gamma\cos(\theta-\Theta)}{\sqrt{1-\gamma^2}}\right)\rho_0(\theta)d\theta. \tag{5.14}$$

Then Ψ is given by the third equation of (5.11), written as

$$\int_{\Theta-\pi}^{\Theta+\pi}\left[\Psi + 2\arctan\left(\sqrt{\frac{1-\gamma}{1+\gamma}}\tan[\tfrac{1}{2}(\theta-\Theta)]\right)\right]\rho_0(\theta)d\theta = 0, \tag{5.15}$$

since $\theta \in [\Theta-\pi, \Theta+\pi]$ corresponds to $\psi \in [\Psi-\pi, \Psi+\pi]$. Lastly, the incoherent density preimage $\sigma(\psi)$ is

$$\sigma(\psi) = \rho_0(\theta)\frac{\partial\theta}{\partial\psi} = \rho_0(\theta)\frac{1+\gamma\cos(\theta-\Theta)}{\sqrt{1-\gamma^2}}. \tag{5.16}$$

For any $\sigma(\psi)$ satisfying (5.11) and (5.12), we may associate a three-dimensional set of trajectories by changing γ, Ψ, and Θ over their full ranges. Since infinitely many such $\sigma(\psi)$ can be found, the phase space of (5.2) with (5.3) is foliated by an infinite-parameter family of three-dimensional subspaces. (Recall there used to be $N-3$ parameters for the finite-N systems.) The density $\sigma(\psi)$ characterizes the subspaces.

5.2. Averaged system

It is expected that (5.9) is too hard to analyze in general, so we focus on the averaged system obtained in the weak-coupling limit.

5.2.1. Reduction

Taking the limit $N \to \infty$ of the finite-N averaged system (4.2), we obtain (5.2) and (5.3) with

$$f = 0, \quad g = \oint \rho(\theta,t)\cos(\theta-\delta)d\theta, \quad h = \oint \rho(\theta,t)\sin(\theta-\delta)d\theta. \tag{5.17}$$

Substitution of these expressions into (5.9) gives the reduced equations

$$\begin{aligned} \frac{\dot\gamma}{1-\gamma^2} &= \oint \rho(\theta,t)\sin(\theta-\boldsymbol{\Theta}-\delta)d\theta, \\ \frac{\gamma\dot\Psi}{\sqrt{1-\gamma^2}} &= -\oint \rho(\theta,t)\cos(\theta-\boldsymbol{\Theta}-\delta)d\theta, \\ \gamma\dot{\boldsymbol{\Theta}} &= \frac{\gamma\dot\Psi}{\sqrt{1-\gamma^2}}. \end{aligned}$$

Using (3.4) and (5.5), these equations become

$$\begin{aligned} \frac{\dot\gamma}{1-\gamma^2} &= S(t)\cos\delta + T(t)\sin\delta, \\ \frac{\gamma\dot\Psi}{\sqrt{1-\gamma^2}} &= \gamma\dot{\boldsymbol{\Theta}} = T(t)\cos\delta - S(t)\sin\delta, \end{aligned} \tag{5.18}$$

where

$$\begin{aligned} S(t) &= \oint \frac{\sqrt{1-\gamma^2}\sin(\psi-\Psi)}{1-\gamma\cos(\psi-\Psi)}\sigma(\psi)d\psi \\ T(t) &= \oint \frac{\gamma-\cos(\psi-\Psi)}{1-\gamma\cos(\psi-\Psi)}\sigma(\psi)d\psi. \end{aligned}$$

This is the infinite-N version of the averaged system. Note that $\boldsymbol{\Theta}$ does not appear on the right hand sides, so the essential dynamics is only two-dimensional.

5.2.2. Lyapunov function

It is straightforward to see that when $\sin\delta = 0$,

$$\mathcal{H}(\Psi,\gamma) = \oint \log\left(\frac{1-\gamma\cos(\psi-\Psi)}{\sqrt{1-\gamma^2}}\right)\sigma(\psi)d\psi \tag{5.19}$$

is a conserved quantity for (5.18). For other values of δ, this function is a Lyapunov function since

$$\dot{\mathcal{H}} = R^2\sin\delta, \tag{5.20}$$

where

$$R(t)\exp[i\phi(t)] = \oint \exp(i\theta)\rho(\theta,t)d\theta, \quad R \geq 0;\ \phi \in \mathbb{R} \tag{5.21}$$

denotes the order parameter of the oscillator density.

5.2.3. *Phase coherence*

By imposing the incoherence constraints (5.11), the set where $\gamma = 0$ becomes synonomous with the incoherent states. Moreover, the Lyapunov function $\mathcal{H}$ vanishes at $\gamma = 0$, and its convexity can be easily shown. As in Section 4.3, $\mathcal{H}$ measures the phase coherence of the oscillators.

The dynamics on the invariant subspaces is governed by $\mathcal{H}$. If $\sin\delta = 0$, $\mathcal{H}$ is conserved, from (5.20). Then $\Psi(t)$ and $\gamma(t)$ are periodic, and the system is completely integrable. If $\sin\delta < 0$, $\mathcal{H}$ decreases monotonically and each trajectory spirals down to the incoherent state $\sigma(\psi)$ that labels the invariant subspace. The manifold of incoherent states is a global attracting set. Finally, if $\sin\delta > 0$, then $\mathcal{H}$ increases and all trajectories (except the incoherent ones) approach the in-phase state. As $t \to \infty$, a δ-function appears in ρ, even when the initial density is smooth.

5.3. *Solitons*

The previous section contains no surprises; the finite-N results of Section 4 carry over to the continuum limit. Now we turn to new phenomena. We restrict attention to the averaged system with $\sin\delta = 0$, unless stated otherwise. Since this case is completely integrable, we expect to find something analogous to solitary wave solutions [37], traveling at a constant speed without changing shape. We shall see that the averaged system indeed exhibits such solutions. In addition, we study the motion of an individual oscillator when such waves occur, and show that the transformation (5.4) collapses to extremely simple form. Finally, we consider recurrence phenomena for this system.

5.3.1. *Traveling waves*

Although it is easy to obtain traveling wave solutions starting from the usual assumption $\rho(\theta,t) = \rho(\theta - Ut)$, we take a more indirect approach here to illuminate the geometrical interpretation of the traveling waves.

Recall that the phase space is partitioned into a family of three-dimensional invariant subspaces, parametrized by the incoherent density $\sigma(\psi)$. The dynamics on each of the subspaces is similar; they all have the same Lyapunov function.

Still, one of the subspaces occupies a special position geometrically. It is the subspace corresponding to the uniform distribution $\sigma(\psi)$ = constant. It corresponds to the splay state of the finite-N case, where the oscillators' phases are equally spaced. For $N = 4$, this subspace is the membrane shown in Fig. 12b.

The splay state for $N = 3$ and $N = 4$ lies at the center of the canonical invariant region, as shown in Figs. 10–13. Moreover, it is the center of the incoherent manifold itself (the dashed filament in Figs. 11–13). By analogy, we expect that the uniform distribution state for the continuum limit is located at the center of both the phase space and the incoherent manifold. The subspace parametrized by, and emanating from, this state is expected to be the most symmetric of all the subspaces. In fact, this is the *subspace of all possible traveling wave solutions*.

To see this, we derive the waves directly from the reduced equations (5.18). As noted, the special subspace is parametrized by the uniform density

$$\sigma(\psi) = \frac{1}{2\pi}. \tag{5.22}$$

The integrals in (5.18) are now easy to evaluate:

$$\oint \frac{\sin(\psi - \Psi)}{1 - \gamma\cos(\psi - \Psi)} \frac{1}{2\pi} d\psi = \frac{1}{2\pi} \oint \frac{\sin\xi}{1 - \gamma\cos\xi} d\xi = 0,$$

$$\oint \frac{\gamma - \cos(\psi - \Psi)}{1 - \gamma\cos(\psi - \Psi)} \frac{1}{2\pi} d\psi = \frac{1}{2\pi\gamma} \oint \left(1 - \frac{1 - \gamma^2}{1 - \gamma\cos\xi}\right) d\xi = \frac{1 - \sqrt{1 - \gamma^2}}{\gamma}.$$

Hence (5.18) becomes

$$\dot{\gamma} = \sin\delta \frac{(1 - \gamma^2)(1 - \sqrt{1 - \gamma^2})}{\gamma},$$

$$\gamma\dot{\boldsymbol{\Theta}} = \frac{\gamma\dot{\Psi}}{\sqrt{1 - \gamma^2}} = \cos\delta \frac{1 - \sqrt{1 - \gamma^2}}{\gamma}.$$

It is more convenient to use $\alpha = (1 - \gamma^2)^{-1/2}$. The equations then become

$$\dot{\alpha} = (\alpha - 1)\sin\delta, \quad \frac{\dot{\boldsymbol{\Theta}}}{\alpha} = \dot{\Psi} = \frac{\cos\delta}{\alpha + 1}.$$

The solution can be obtained explicitly. Assume $\boldsymbol{\Theta}(0) = \Psi(0) = 0$ for simplicity. Then the solution is

$$\alpha(t) = 1 + (\alpha_0 - 1)\,\mathrm{e}^{t\sin\delta},$$

$$\boldsymbol{\Theta}(t) = \tfrac{1}{2}\cot\delta \left[3t\sin\delta - \log\left(\frac{2 + (\alpha_0 - 1)\,\mathrm{e}^{t\sin\delta}}{\alpha_0 + 1}\right)\right],$$

$$\Psi(t) = \tfrac{1}{2}\cot\delta \left[t\sin\delta - \log\left(\frac{2 + (\alpha_0 - 1)\,\mathrm{e}^{t\sin\delta}}{\alpha_0 + 1}\right)\right].$$

In particular, when $\sin\delta = 0$ (and we let $\delta = 0$ without loss of generality), this reduces to

$$\alpha(t) = \alpha_0 \quad (\gamma(t) = \gamma_0), \quad \boldsymbol{\Theta}(t) = Ut, \quad \Psi(t) = Vt,$$

where α_0, γ_0, and

$$U = \frac{\alpha}{\alpha + 1} = \frac{1 - \sqrt{1 - \gamma^2}}{\gamma^2}, \quad V = \frac{1}{\alpha + 1} = \frac{\sqrt{1 - \gamma^2} - (1 - \gamma^2)}{\gamma^2}$$

are all constants.

From now on, focus on this integrable case $\sin\delta = 0$. Since α (or γ) is constant, the mapping used in the transformation (5.4) is stationary. Since the preimage $\sigma(\psi)$ is always stationary, the image $\rho(\theta, t)$ also looks stationary in the frame moving with $\boldsymbol{\Theta}(t)$. Moreover, the speed of the frame is the constant $\dot{\boldsymbol{\Theta}} = U$. Hence, this solution represents a traveling wave in the θ-coordinate. Fig. 14 illustrates these relations.

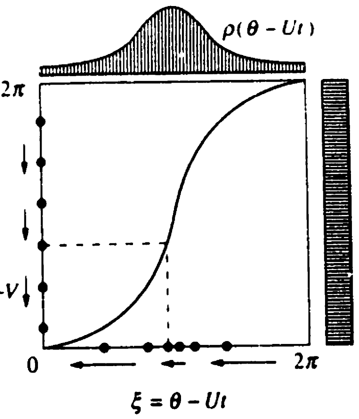

Fig. 14. Change of coordinates for the traveling wave solutions. In this simple case, the mapping curve is fixed since the distortion γ reduces to a constant. The preimage density $\sigma(\psi)$ is uniform. Individual oscillators move at uniform velocity $-V$ with respect to ψ. In the original coordinates, the oscillators move non-uniformly, hesitating near the peak of the density ρ and running rapidly in between.

The shape of the traveling wave follows from (5.16). We obtain

$$\rho(\theta, t) = \sigma\left(\frac{\partial\theta}{\partial\psi}\right)^{-1} = \frac{1}{2\pi}\frac{\sqrt{1-\gamma^2}}{1+\gamma\cos(\theta-\Theta)} = \frac{1}{2\pi}\frac{\sqrt{1-\gamma^2}}{1+\gamma\cos(\theta-Ut)}, \tag{5.23}$$

where we have written simply γ instead of γ_0. This solution is a solitary bump on the circle. It involves one parameter γ. When $\gamma = 0$, the solution reduces to the uniform distribution, i.e., the preimage $\sigma(\psi)$ itself. As γ increases, the height of the bump grows monotonically, and diverges when $\gamma \to 1$, since

$$\rho_{\max} = \max_{\xi}\frac{1}{2\pi}\frac{\sqrt{1-\gamma^2}}{1+\gamma\cos\xi} = \frac{1}{2\pi}\frac{\sqrt{1-\gamma^2}}{1-\gamma} = \frac{1}{2\pi}\sqrt{\frac{1+\gamma}{1-\gamma}}.$$

The wave speed U changes from 1/2 ($\gamma = 0$ or $\alpha = 1$) to 1 ($\gamma \to 1$ or $\alpha \to \infty$) monotonically - taller waves travel faster.

The velocity field $v(\theta, t)$ is obtained from (5.3) by substituting (5.17) and setting $\delta = 0$:

$$\begin{aligned} v(\theta, t) &= \oint \rho(\theta', t)\cos(\theta' - \theta - \delta)d\theta'\bigg|_{\delta=0} = \frac{\sqrt{1-\gamma^2}}{2\pi}\oint\frac{\cos(\theta'-\theta)d\theta'}{1+\gamma\cos(\theta'-Ut)} \\ &= -A\cos(\theta - Ut), \end{aligned}$$

$$A = \frac{1-\sqrt{1-\gamma^2}}{\gamma}.$$

Here v is the speed of individual oscillators in the *stationary* frame. In the frame of the traveling wave, the velocity of an oscillator becomes

$$v(\theta, t) - U = -[U + A\cos\xi], \quad \xi = \theta - Ut.$$

It is easy to show that $0 \le A < U < 1$ for $0 \le \gamma < 1$. Hence the oscillators always move backward relative to the density wave, and their speed is nonuniform; they hesitate near the peak of ρ

($\xi = \pm\pi$) and run rapidly through the trough ($\xi = 0$). In other words, each oscillator lingers near all the others until the time comes for it to "phase slip" abruptly.

5.3.2. Transformation

Now suppose we wish to convert the nonuniform motion of an individual oscillator into *uniform* motion by changing variables from $\xi = \theta - Ut$ (nonuniform) to, say, η (uniform). The standard technique is to use the *time of travel* as the new coordinate. The time required for an oscillator to travel from $\xi = 0$ to ξ is

$$\int_0^{\xi} \frac{d\xi}{\dot{\xi}} = \int_0^{\xi} \frac{d\xi}{-(U + A\cos\xi)} = -\frac{2}{\sqrt{U^2 - A^2}} \arctan\left(\frac{\sqrt{U^2 - A^2}}{U + A} \tan(\tfrac{1}{2}\xi)\right).$$

This must equal to the amount of time for the oscillator to travel from $\eta = 0$ to η at a constant speed W. Hence

$$\frac{\eta}{W} = -\frac{2}{\sqrt{U^2 - A^2}} \arctan\left(\frac{\sqrt{U^2 - A^2}}{U + A} \tan(\tfrac{1}{2}\xi)\right).$$

Also, we require that $\eta = \pm\pi$ when $\xi = \pm\pi$ so that the period agrees in both coordinates. Then the constant W is determined as

$$W = -\sqrt{U^2 - A^2} = -\left[\left(\frac{1}{\gamma^4} - \frac{1}{\gamma^2}\right) \cdot (1 - \sqrt{1 - \gamma^2})^2\right]^{1/2} = -\frac{\sqrt{1 - \gamma^2} - (1 - \gamma^2)}{\gamma^2} = -V.$$

Thus V denotes the converted, uniform speed of the oscillators. The transformation now becomes

$$\eta = 2\arctan\left(\frac{\sqrt{U^2 - A^2}}{U + A} \tan[\tfrac{1}{2}(\theta - Ut)]\right).$$

Next observe that the phase configuration rotates rigidly in the new coordinates, since all the oscillators have the same uniform velocity. Therefore, by going into yet another rotating frame, the oscillators can be made to appear motionless or *frozen*. This is achieved by introducing a new coordinate ψ, where

$$\eta = \psi - Vt.$$

Hence the overall transformation is

$$\tan[\tfrac{1}{2}(\theta - Ut)] = \frac{U + A}{\sqrt{U^2 - A^2}} \tan[\tfrac{1}{2}(\psi - Vt)].$$

Since

$$\frac{U + A}{\sqrt{U^2 - A^2}} = \frac{U + A}{V} = \frac{1 + \gamma}{\sqrt{1 - \gamma^2}} = \sqrt{\frac{1 + \gamma}{1 - \gamma}},$$

we have recovered the transformation (3.2) for this particular case:

$$\tan[\tfrac{1}{2}(\theta - Ut)] = \sqrt{\frac{1 + \gamma}{1 - \gamma}} \tan[\tfrac{1}{2}(\psi - Vt)]. \tag{5.24}$$

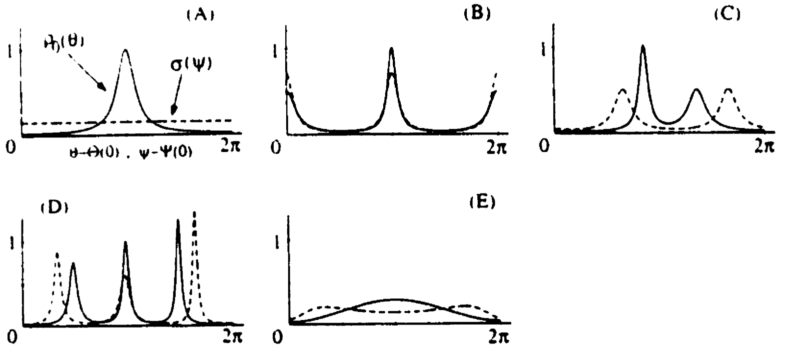

Fig. 15. Five initial densities $\rho_0(\theta)$ (solid curves) and their computed preimages $\sigma(\psi)$ (dashed curves) are shown. The preimages are incoherent, as required by the constraint (5.12). Note that ρ_0 and σ are shown translated by the amounts $\Theta(0)$ and $\Psi(0)$, respectively. Details of the cases (A)-(E) are given in Table 1. (A) 1-soliton; (B) 2-soliton, π apart; (C) 2-soliton, $\pi/2$ apart; (D) 3-soliton; (E) sinusoidal.

Thus, on this most symmetric subspace of solutions, the distortion parameter γ becomes a constant while the two characteristic phases Ψ and Θ are just linear in t.

As mentioned in Section 3.1, the transformation (3.2) between θ and ψ was inspired by these travelling waves. A slight generalization was required to extend to finite N: the three constants U, V, γ in (5.24) had to be replaced by time-dependent functions evolving according to (3.6). But the freezing of the oscillators in the ψ frame carried over perfectly to finite N: as shown earlier, all solutions of (3.1) can be written in the form (3.2), where $\{\psi_j\}$ is *constant* on trajectories.

5.4. Numerical results

We now present numerical experiments to illustrate the motion and interaction of solitons. The numerical integrations were done using the reduced system (5.9), expressed in Cartesian-type coordinates as in (3.9)-(3.11), and using (5.11) to convert the initial condition. The validity of the method was confirmed by comparing the results to those obtained from a conventional spectral method applied to the original system (5.2) and (5.3).

5.4.1. Converted densities

Fig. 15 shows five initial densities $\rho_0(\theta)$, two of which are to be used in the simulations discussed below. For each $\rho_0(\theta)$, we compute its preimage density $\sigma(\psi)$, as well as the values of (γ, Ψ, Θ), by solving (5.13)-(5.16). Table 1 summarizes the cases.

In case (A), $\rho_0(\theta)$ is the 1-soliton solution (5.23), with parameters $\gamma(0) = \gamma_1$ and $\Theta(0) = \theta_1$. The peak is at $\theta = \theta_1 \pm \pi$. For such a 1-soliton initial condition, it is easy to find the minimum of $\mathcal{U}(\Theta, \gamma)$ in (5.14). One can show that $\gamma = \gamma_1$ and $\Theta = \theta_1$ satisfies (5.13). Using these values, Ψ from (5.15) and $\sigma(\psi)$ from (5.16) can be computed. The preimage $\sigma(\psi)$ is a constant function, $\sigma(\psi) = 1/2\pi$. This was to be expected, since the 1-soliton solution $\rho_0(\theta)$ lies on the manifold parametrized by the splay state.

In cases (B) and (C), $\rho_0(\theta)$ is a superposition of two solitons with different amplitudes. (The density $\rho_0(\theta)$ must be divided by 2 to normalize it after superposition.) The phase difference between the two pulses is π for (B) and $\pi/2$ for (C). The amplitude parameters γ_1 and γ_2 for both

Table 1
Five initial densities $\rho_0(\theta)$ and the corresponding initial conditions for the reduced variables, obtained by solving (5.13)–(5.16). The resulting incoherent preimages $\sigma(\psi)$ are shown in Fig. 15. In the table, $\rho_W(\theta;\gamma_j,\theta_j) = (1/2\pi)[(1-\gamma_j^2)^{1/2}/(1+\gamma_j\cos(\theta-\theta_j))]$ denotes the traveling wave solution with an amplitude parameter γ_j and a translational offset θ_j. Angular variables are shown within $[-\pi,\pi]$.

Case	$\rho_0(\theta)$	$\gamma(0)$	$\Psi(0)/\pi$	$\Theta(0)/\pi$
(A)	$\rho_W(\theta\gamma_1,\theta_1)$	0.9505910	0	0.2500000
(B)	$\frac{1}{2}\sum_{j=1}^{2}\rho_W(\theta;\gamma_j,\theta_j)$	0.3333333	0	−0.7500000
(C)	$\frac{1}{2}\sum_{j=1}^{2}\rho_W(\theta;\gamma_j,\theta_j)$	0.7285979	−0.1040134	−0.6048600
(D)	$\frac{1}{3}\sum_{j=1}^{3}\rho_W(\theta;\gamma_j,\theta_j)$	0.4614420	−0.0826765	−0.7316964
(E)	$\frac{1}{2\pi}(1+\frac{4}{5}\sin\theta)$	0.6246950	0	−0.5000000

In this column, the parameter values are:
(A) $\gamma_1 = 0.9505910$, $\theta_1 = \pi/4$.
(B) $\gamma_1 = 0.9874146$, $\theta_1 = -3\pi/4$, $\gamma_2 = 0.9505910$, $\theta_2 = \pi/4$.
(C) $\gamma_1 = 0.9874146$, $\theta_1 = -3\pi/4$, $\gamma_2 = 0.9505910$, $\theta_2 = -\pi/4$.
(D) $\gamma_1 = 0.9900428$, $\theta_1 = 3\pi/4$, $\gamma_2 = 0.9943868$, $\theta_2 = -3\pi/4$, $\gamma_3 = 0.9964039$, $\theta_3 = -\pi/4$.

cases are chosen such that the height of the two peaks are 1 and 1/2. In both cases, the computed preimages $\sigma(\psi)$ consist of two almost symmetric bumps roughly π apart. The calculated $\sigma(\psi)$ satisfied the constraints (5.11) and (5.12) within numerical accuracy.

For these cases, the computed values of $\gamma(0)$ and $\Theta(0)$ (Table 1) are not obvious combinations of the parameters $\gamma_{1,2}$ and $\theta_{1,2}$ (although case (B) seems simple). Rather, they are obtained by minimizing $\mathcal{U}$. This potential function $\mathcal{U}$ itself *is* superposable as seen from (5.14). That is, if two densities $\rho_1(\theta)$ and $\rho_2(\theta)$ correspond to $\mathcal{U}_1$ and $\mathcal{U}_2$, respectively, then the potential corresponding to $\rho_0(\theta) = (\rho_1+\rho_2)/2$ is $\mathcal{U}(\Theta,\gamma) = (\mathcal{U}_1+\mathcal{U}_2)/2$. For the cases (B) and (C), ρ_1 and ρ_2 are two 1-soliton solutions. Then, $\min\mathcal{U}_1$ and $\min\mathcal{U}_2$ are achieved at (θ_1,γ_1) and (θ_2,γ_2), respectively. Unfortunately, (Θ,γ) is not a linear combination of these two, but is obtained in a more elaborate manner through minimization of the superposed potential functions.

The remaining two cases (D) and (E) correspond to 3-soliton or sinusoidal initial densities, respectively. The preimages are found to have somewhat irregular shapes.

5.4.2. Soliton interactions for an integrable system

For cases (B) and (C) above, we now consider the evolution of $\rho(\theta,t)$, assuming that the system is governed by the completely integrable averaged system (5.2, 5.3, 5.17) with $\delta = 0$.

Fig. 16 shows the evolution for case (B). In Fig. 16a, we plot $\gamma(t)$, $\Psi(t)$, and $\Theta(t)$ of the reduced equations, over one period of $\Psi(t)$. (The period $T \approx 16.8$.) The other phase variable $\Theta(t)$ also seems to advance by 2π during this period. The distortion parameter $\gamma(t)$ oscillates twice during one period. The periodicity is made clearer in Fig. 16b, which plots the trajectory using (γ,Ψ) as polar coordinates. As expected, the trajectory is a closed loop, corresponding to a contour of the Hamiltonian $\mathcal{H}$ in (5.19). The loop is small, indicating that the initial condition $\rho_0(\theta)$ is fairly close to an incoherent state. Since γ never assumes large values, we expect the image $\rho(\theta,t)$ to be a slight distortion of the preimage $\sigma(\psi)$ for all time.

In Fig. 16c the evolution of $\rho(\theta,t)$ is displayed directly. The spatial coordinate is co-moving with $\Theta(t)$. Therefore, only variations due to γ and Ψ should be visible in the figure, and we should see periodic motion with period T. Indeed, such recurrence is observed, the first and the

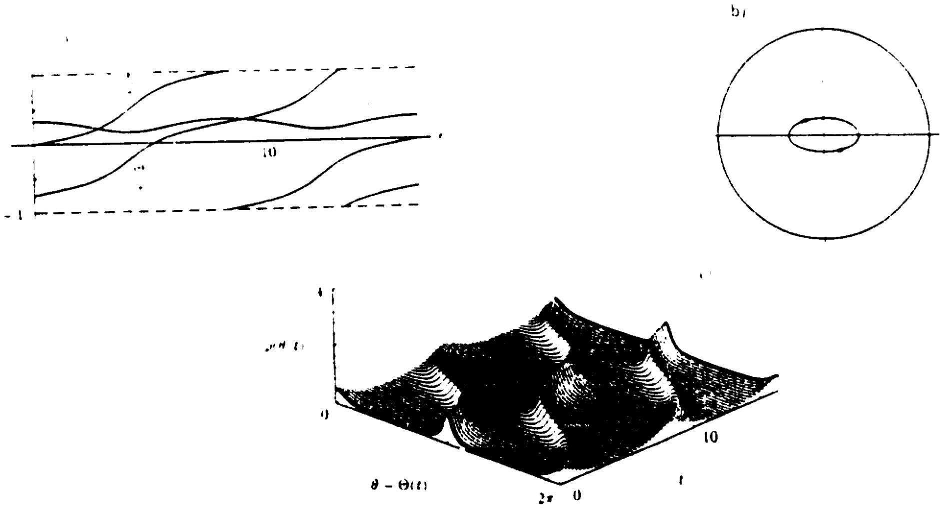

Fig. 16. Evolution of the 2-soliton case (B) for the integrable averaged system. One period of the (γ, Ψ)-dynamics ($T \approx 16.8$) is plotted here.
(a) Solution of the reduced equations. (b) In the polar diagram of γ and Ψ, the projected trajectory is a small loop. (c) The density $\rho(\theta, t)$, plotted in a frame co-moving with $\Theta(t)$. Two peaks persist for all time.

last waveforms being identical. Because of the small distortion from the preimage, the two pulses are distinguishable for all time, although an exchange of their identities can be seen.

Fig. 17 plots the evolution for case (C) in a similar manner. Again, one period in $\Psi(t)$ is computed ($T \approx 19.2$), but now $\Theta(t)$ advances more than 2π, probably because of the asymmetric shape of ρ_0 (Fig. 17a). The trajectory in Fig. 17b is still periodic, but the loop is much larger than in the previous case. Since γ becomes close to 1, we see a rather different picture of $\rho(\theta, t)$. As shown in Fig. 17c, one of the two pulses disappears and is completely absorbed by the other, then emerges from the other side.

In Figs. 16 and 17, one might be misled into thinking that the fundamental period of $\rho(\theta, t)$ is $T/2$, not T. This is because the preimage $\sigma(\psi)$ is almost symmetric, and the trajectory in (γ, Ψ) polar coordinates is almost an ellipse. The true periodicity is clearer for trajectories starting from less symmetric initial densities like (D) and (E) (results not shown).

5.4.3. *Chaotic waves for a non-averaged system*

At the end of Section 3, we pointed out that KAM-like chaos can occur in the resistively loaded array. We now present numerical results illustrating similar chaos for the continuum limit. The point is not that the chaos is particularly dramatic (it isn't), but rather that the system provides a simple, explicit example of an infinite-dimensional system whose dynamical complexity is rigorously bounded (the system's reducibility implies that the chaos is at most three-dimensional).

Consider the Josephson junction array equations (3.16) for the case of a pure resistive load. In the limit $N \to \infty$, the equations give the velocity field

$$v(\theta, t) = 1 + a \sin\theta + \varepsilon \oint \rho(\varphi, t) \sin\varphi \, d\varphi, \tag{5.25}$$

which should be used in the continuity equation (5.2). The system is reducible, since the velocity

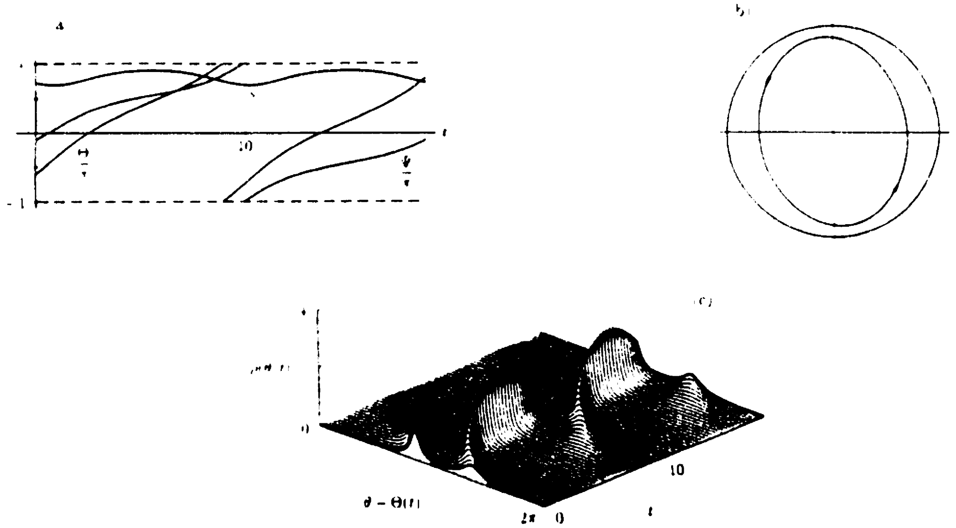

Fig. 17. Evolution of the 2-soliton case (C) for the integrable averaged system, plotted as in Fig. 16. Here $T \approx 19.2$. (a) Solution of the reduced equations. (b) In the polar diagram of γ and Ψ, the projected trajectory is a large loop. (c) The density $\rho(\theta, t)$. One pulse is absorbed by the other to form a sharp spike, but re-emerges.

takes the form (5.3) with

$$f = 1 + \varepsilon \oint \rho(\varphi, t) \sin\varphi \, d\varphi, \quad g = 0, \quad h = a. \tag{5.26}$$

We numerically integrated (5.9), for $a = 2$ and $\varepsilon = -2$. Instead of specifying the initial density $\rho_0(\theta)$, the preimage density $\sigma(\psi)$, and the initial values of (x, y, Φ) were input directly. Fig. 18 shows a chaotic case corresponding to

$$\sigma(\psi) = \frac{1}{2\pi}[1 - \tfrac{3}{4}\sin(3\psi)], \quad x(0) = 0, \quad y(0) = -0.09, \quad \Phi(0) = 0.$$

The chaos is not obvious in Fig. 18a; one would need to integrate much longer to see it, but then the graph would become cluttered with uninteresting details. It is more revealing to plot a Poincaré-section. Fig. 18b shows a section taken at $\Phi = \Phi(0) \pmod{2\pi}$. The coordinates are x and y as in Fig. 4. The section consists of 1,000 returns, computed by integration up to $t = 6283$. The trajectory seems to be part of a "chaotic sea"; it does not explore the entire region, but appears to be confined between invariant tori. Fig. 18c shows $\rho(\theta, t)$ over the same short time interval used in Fig. 18a. For clarity, the density is plotted in a frame moving with $\Theta(t)$. Small initial fluctuations grow and form two sharp spikes, then decay. Although this plot suggests that the situation is nearly recurrent, Fig. 18b strongly suggests that the dynamics is chaotic on a longer time scale.

6. Open questions

We conclude with some suggestions for future research.

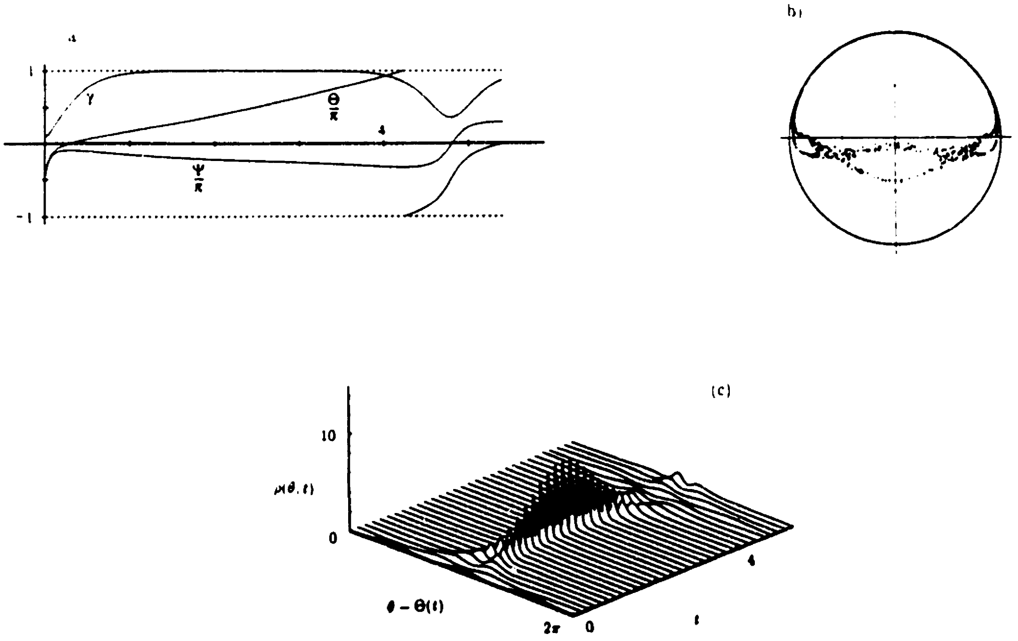

Fig. 18. Chaotic evolution of a wave in a reducible but non-integrable system (the resistively loaded Josephson array in the continuum limit). The parameters are $a = 2$ and $\varepsilon = -2$. (a) Solution of the reduced equations, for $t \leq 5.4$. (b) Chaos is visible in the Poincaré-section at $\Phi = \Phi(0)$ (mod 2π), obtained by computing up to $t = 6283$. (c) Evolution of density $\rho(\theta, t)$, for $t \leq 5.4$.

(1) Our analysis of Josephson arrays is restricted to the limit of overdamped junctions ($\beta = 0$). But there is numerical evidence [3] that even if $\beta > 0$, certain arrays still have enormously degenerate phase space structure. Does a high-dimensional manifold of incoherent states exist for these systems as well?

(2) For the overdamped systems studied here, we have shown (Section 3) that the dynamics can be reduced to a much smaller set of differential equations. Specifically, the dynamics of the N-dimensional system (3.1) is captured completely by the 3-dimensional system (3.6). Unfortunately, the reduced system appears intractable. Can one make progress on its analysis?

(3) Can one find a connection between the partially integrable systems studied here, and more familiar integrable many-body systems like the Toda lattice [37]?

(4) In any case, is there a more algebraic interpretation of the constants of motion? Goebel has recently obtained some elegant results in this direction [38].

Acknowledgments

Jim Swift provided many helpful suggestions throughout this project. Thanks to Jim Swift and Kurt Wiesenfeld for their comments on a draft of this paper. Research supported by a National Science Foundation Presidential Young Investigator award to S.H.S., and NSF Grant DMS-9111497.

Appendix A. Reduction of continuum limit systems

This appendix provides details of the reduction discussed in Section 5.1. In particular, we derive the three equations in (5.9), starting from (5.2) and (5.3).

We first express $\partial(\rho v)/\partial\theta$ in (5.2) in terms of the new coordinates. From (5.5) and (5.8),

$$\rho(\theta,t) = \sigma(\psi)\frac{\partial\psi}{\partial\theta} = \sigma(\psi)\frac{1-\gamma\cos(\psi-\Psi)}{\sqrt{1-\gamma^2}}. \tag{A.1}$$

Using (3.4), v in (5.3) can be rewritten as

$$\begin{aligned}(1-\gamma\cos(\psi-\Psi))v = {} & f(1-\gamma\cos(\psi-\Psi)) \\ & +g\left[-\gamma\cos\Theta+\cos\Theta\cos(\psi-\Psi)-\sqrt{1-\gamma^2}\sin\Theta\sin(\psi-\Psi)\right] \\ & +h\left[-\gamma\sin\Theta+\sin\Theta\cos(\psi-\Psi)+\sqrt{1-\gamma^2}\cos\Theta\sin(\psi-\Psi)\right].\end{aligned}$$

Thus,

$$\begin{aligned}\frac{\partial}{\partial\theta}(\rho v) &= \frac{\partial\psi}{\partial\theta}\frac{\partial}{\partial\psi}(\rho v) \\ &= \frac{1-\gamma\cos(\psi-\Psi)}{\sqrt{1-\gamma^2}}\frac{1}{\sqrt{1-\gamma^2}}\frac{\partial}{\partial\psi}[\sigma(\psi)(1-\gamma\cos(\psi-\Psi))v] \\ &= \frac{1-\gamma\cos(\psi-\Psi)}{1-\gamma^2}\{\sigma'(\psi)[f(1-\gamma\cos(\psi-\Psi)) \\ &\quad +g(-\gamma\cos\Theta+\cos\Theta\cos(\psi-\Psi)-\sqrt{1-\gamma^2}\sin\Theta\sin(\psi-\Psi)) \\ &\quad +h(-\gamma\sin\Theta+\sin\Theta\cos(\psi-\Psi)+\sqrt{1-\gamma^2}\cos\Theta\sin(\psi-\Psi))] \\ &\quad +\sigma(\psi)[\gamma f\sin(\psi-\Psi)+g(-\cos\Theta\sin(\psi-\Psi)-\sqrt{1-\gamma^2}\sin\Theta\cos(\psi-\Psi)) \\ &\quad +h(-\sin\Theta\sin(\psi-\Psi)+\sqrt{1-\gamma^2}\cos\Theta\cos(\psi-\Psi))]\}.\end{aligned} \tag{A.2}$$

Next, compute $\partial\rho/\partial t$ by

$$\frac{\partial\rho}{\partial t} = \frac{\partial\rho}{\partial\tau}+\frac{\partial\psi}{\partial t}\frac{\partial\rho}{\partial\psi}, \tag{A.3}$$

where τ is the "new" time coordinate and $\tau = t$. From (A.1), we find

$$\begin{aligned}\frac{\partial\rho}{\partial\tau} &= \sigma(\psi)\frac{\partial}{\partial\tau}\left(\frac{1-\gamma(\tau)\cos[\psi-\Psi(\tau)]}{\sqrt{1-\gamma(\tau)^2}}\right) \\ &= \frac{\sigma(\psi)}{(1-\gamma^2)^{3/2}}\{(1-\gamma^2)[-\dot\gamma\cos(\psi-\Psi)-\gamma\dot\Psi\sin(\psi-\Psi)]+\gamma\dot\gamma[1-\gamma\cos(\psi-\Psi)]\} \\ &= \frac{\sigma(\psi)}{(1-\gamma^2)^{3/2}}[\dot\gamma(\gamma-\cos(\psi-\Psi))-\gamma\dot\Psi(1-\gamma^2)\sin(\psi-\Psi)]\end{aligned} \tag{A.4}$$

and

$$\frac{\partial\rho}{\partial\psi} = \frac{\partial}{\partial\psi}\left(\sigma(\psi)\frac{1-\gamma(\tau)\cos(\psi-\Psi(\tau))}{\sqrt{1-\gamma(\tau)^2}}\right)$$

$$= \frac{\sigma'(\psi)}{\sqrt{1-\gamma^2}}(1-\gamma\cos(\psi-\Psi)) + \frac{\sigma(\psi)}{\sqrt{1-\gamma^2}}\gamma\sin(\psi-\Psi). \tag{A.5}$$

From this point on, only algebraic manipulations follow. For brevity, let $c = \cos(\psi - \Psi)$ and $s = \sin(\psi - \Psi)$. Substituting (5.7), (A.4), and (A.5) into (A.3), we obtain

$$\begin{aligned}(1-\gamma^2)^{3/2}\frac{\partial\rho}{\partial t} &= \sigma[\dot\gamma(\gamma - c) - \gamma\dot\Psi(1-\gamma^2)s] \\ &\quad + [\dot\Psi(1-\gamma^2) - \dot\gamma s - \dot{\boldsymbol{\theta}}\sqrt{1-\gamma^2}(1-\gamma c)][\sigma'(1-\gamma c) + \sigma\gamma s] \\ &= \sigma[\dot\gamma(\gamma - c - \gamma s^2) - \gamma s\sqrt{1-\gamma^2}(1-\gamma c)\dot{\boldsymbol{\theta}}] \\ &\quad + \sigma'(1-\gamma c)[\dot\Psi(1-\gamma^2) - \dot\gamma s - \dot{\boldsymbol{\theta}}\sqrt{1-\gamma^2}(1-\gamma c)].\end{aligned}$$

Since

$$\gamma - c - \gamma s^2 = \gamma - c - \gamma(1-c^2) = -c(1-\gamma c),$$

the final expression becomes

$$\frac{(1-\gamma^2)^{3/2}}{1-\gamma c}\frac{\partial\rho}{\partial t} = \sigma[-\dot\gamma c - \gamma s\sqrt{1-\gamma^2}\dot{\boldsymbol{\theta}}] + \sigma'[\dot\Psi(1-\gamma^2) - \dot\gamma s - \dot{\boldsymbol{\theta}}\sqrt{1-\gamma^2}(1-\gamma c)]. \tag{A.6}$$

We can now express the continuity equation (5.2) in the new coordinate system. Rewrite (A.2) as

$$\begin{aligned}\frac{(1-\gamma^2)^{3/2}}{1-\gamma c}\frac{\partial(\rho v)}{\partial\theta} &= \sigma'\sqrt{1-\gamma^2}[f(1-\gamma c) + g(-\gamma\cos\boldsymbol{\theta} + c\cos\boldsymbol{\theta} - s\sqrt{1-\gamma^2}\sin\boldsymbol{\theta}) \\ &\quad + h(-\gamma\sin\boldsymbol{\theta} + c\sin\boldsymbol{\theta} + s\sqrt{1-\gamma^2}\cos\boldsymbol{\theta})] \\ &\quad + \sigma\sqrt{1-\gamma^2}[\gamma f s + g(-s\cos\boldsymbol{\theta} - c\sqrt{1-\gamma^2}\sin\boldsymbol{\theta}) \\ &\quad + h(-s\sin\boldsymbol{\theta} + c\sqrt{1-\gamma^2}\cos\boldsymbol{\theta})].\end{aligned} \tag{A.7}$$

Substitution of (A.6) and (A.7) into (5.2) yields

$$\begin{aligned}0 &= \frac{(1-\gamma^2)^{3/2}}{1-\gamma c}\left(\frac{\partial\rho}{\partial t} + \frac{\partial}{\partial\theta}(\rho v)\right) \\ &= \sigma\{c[-\dot\gamma - g(1-\gamma^2)\sin\boldsymbol{\theta} + h(1-\gamma^2)\cos\boldsymbol{\theta}] \\ &\quad + s\sqrt{1-\gamma^2}(-\gamma\dot{\boldsymbol{\theta}} + \gamma f - g\cos\boldsymbol{\theta} - h\sin\boldsymbol{\theta})\} \\ &\quad + \sigma'\{\sqrt{1-\gamma^2}(\dot\Psi\sqrt{1-\gamma^2} - \dot{\boldsymbol{\theta}} + f - \gamma g\cos\boldsymbol{\theta} - \gamma h\sin\boldsymbol{\theta}) \\ &\quad + c\sqrt{1-\gamma^2}(\gamma\dot{\boldsymbol{\theta}} - \gamma f + g\cos\boldsymbol{\theta} + h\sin\boldsymbol{\theta}) \\ &\quad + s[-\dot\gamma - g(1-\gamma^2)\sin\boldsymbol{\theta} + h(1-\gamma^2)\cos\boldsymbol{\theta}]\}.\end{aligned}$$

This equation is satisfied for all t regardless of $\sigma(\psi)$, $c = \cos(\psi - \Psi)$, and $s = \sin(\psi - \Psi)$ if

$$\begin{aligned}&-\dot\gamma - g(1-\gamma^2)\sin\boldsymbol{\theta} + h(1-\gamma^2)\cos\boldsymbol{\theta} = 0, \\ &-\gamma\dot{\boldsymbol{\theta}} + \gamma f - g\cos\boldsymbol{\theta} - h\sin\boldsymbol{\theta} = 0, \\ &\dot\Psi\sqrt{1-\gamma^2} - \dot{\boldsymbol{\theta}} + f - \gamma g\cos\boldsymbol{\theta} - \gamma f\sin\boldsymbol{\theta} = 0.\end{aligned}$$

These are equivalent to the three equations in (5.9).

Appendix B. Symmetric constants of motion

B.1. Introduction

This appendix is concerned exclusively with the finite-N averaged system (4.1), or equivalently (4.2), with $\sin\delta = 0$. We prove that this system is completely integrable, using a more algebraic approach than in Section 4.

Recall that in the first proof, the integrability followed from the existence of $N-2$ independent constants of motion, namely $\{\psi_j\}$ (only $(N-3)$ of which are independent) and $\mathcal{H}$. The system was thus found to be reducible to a one-degree-of-freedom Hamiltonian system. This approach is similar in spirit to the inverse scattering technique [27,37] for integrable Hamiltonian systems. Our preimage $\{\psi_j\}$ is reminiscent of the time-independent eigenvalues in Lax's formalism, and the functions $(\gamma, \Psi, \boldsymbol{\Theta})$ are analogous to the time-dependent part of the scattering data. (We stress, however, that this analogy is very loose. In particular, (4.1) does *not* arise from the conservative limit of the Josephson junction equations, but rather the extremely overdamped limit. Moreover, our governing equations are not formulated explicitly in terms of a Hamiltonian.)

For the case of the Toda lattice [37], Flaschka found constants of motion of this scattering type [39]. A different set of constants, however, was found independently by Hénon [40] by direct algebraic methods. These constants have the virtue of being symmetric in their indices, but they are harder to obtain systematically. The two sets of constants of motion are equivalent to each other [37,39].

We show below that $N-2$ constants of motion of the Hénon type, i.e. symmetric ones, can be found for (4.2), and we discuss their relation to the Flaschka type constants of motion, $\{\psi_j\}$ and $\mathcal{H}$. In Section B.2, one of the constants is written down and its invaraiance is checked explicitly. Then in Section B.3 we use the permutation symmetry of the system to generate many additional constants, $N-2$ of which are proven to be functionally independent. Sections B.4 and B.5 contain several notes on the constants of motion, including their relationship to the constants from Section 4.

We would like to acknowledge the contributions of two other workers, and to thank them for generously sharing their unpublished results. Jim Swift [41] discovered the symmetric constants for the averaged system for $N = 3$ and 4, and conjectured their form for arbitrary N. Charles Goebel [38] found a way to simplify the calculations in this appendix, using Möbius transformations. He also independently realized that systems of the form (3.1) have $N-3$ constants of motion.

B.2. Invariance

For convenience, we define the following shorthand notations:

$$C_{ij} \doteq \cos[\tfrac{1}{2}(\theta_i-\theta_j)], \quad S_{ij} \doteq \sin[\tfrac{1}{2}(\theta_i-\theta_j)], \quad \mathrm{ct}_{ij} \doteq \cot[\tfrac{1}{2}(\theta_i-\theta_j)],$$

$$C_{ii|jk} \doteq \cos[\theta_i - \tfrac{1}{2}(\theta_j+\theta_k)], \quad S_{ii|jk} \doteq \sin[\theta_i - \tfrac{1}{2}(\theta_j+\theta_k)],$$

$$\boldsymbol{C}_{ij} \doteq \cos(\theta_i-\theta_j), \quad \boldsymbol{S}_{ij} \doteq \sin(\theta_i-\theta_j),$$

$$\langle p_1, p_2, p_3, \cdots, p_{N-1}, p_N\rangle \doteq S_{p_1p_2}S_{p_2p_3}\cdots S_{p_{N-1}p_N}S_{p_Np_1}.$$

We will often use trigonometric conversion formulas between sums and products, e.g.,

$$\begin{aligned} C_{31} - C_{32} &= \cos(\theta_3 - \theta_1) - \cos(\theta_3 - \theta_2) \\ &= 2\sin[\tfrac{1}{2}(\theta_1 - \theta_2)]\sin[\theta_3 - \tfrac{1}{2}(\theta_1 + \theta_2)] = 2S_{12}S_{33|12}\,. \end{aligned} \tag{B.1}$$

For the system (4.2) Swift has shown [41] several constants of motion when $N = 3$ or 4:

- for $N = 3$, $I = S_{12}S_{23}S_{31}$ is conserved, and
- for $N = 4$, $J_1 = S_{12}S_{34}$, $J_2 = S_{13}S_{24}$, $J_3 = S_{14}S_{23}$ are all conserved, hence $I = -J_1J_3 = S_{12}S_{23}S_{34}S_{41}$ is also conserved.

Motivated by these results, one expects that

$$I = \langle 1, 2, 3, \cdots, N-1, N\rangle = S_{12}S_{23}\cdots S_{N-1,N}S_{N1} \tag{B.2}$$

is a constant of motion of the system (4.2). Such a conjecture can be proved as follows. Since any θ_i is involved in exactly two of the sine terms in (B.2),

$$\begin{aligned} \frac{\partial I}{\partial \theta_i} = {} & \tfrac{1}{2}S_{12}S_{23}\cdots S_{i-2,i-1}S_{i-1,i}C_{i,i+1}S_{i+1,i+2}\cdots S_{N-1,N}S_{N1} \\ & -\tfrac{1}{2}S_{12}S_{23}\cdots S_{i-2,i-1}C_{i-1,i}S_{i,i+1}S_{i+1,i+2}\cdots S_{N-1,N}S_{N1}\,, \end{aligned}$$

where the indices are reduced modulo N. A simpler expression is obtained when this is divided by I:

$$\frac{2}{I}\frac{\partial I}{\partial \theta_i} = \mathrm{ct}_{i,i+1} - \mathrm{ct}_{i-1,i}\,. \tag{B.3}$$

Thus the change of I along a trajectory of (4.2) is

$$\frac{2}{I}\dot{I} = \sum_{i=1}^{N}\frac{2}{I}\frac{\partial I}{\partial \theta_i}\dot{\theta}_i = \sum_{i=1}^{N}(\mathrm{ct}_{i,i+1} - \mathrm{ct}_{i-1,i})\dot{\theta}_i = \sum_{i=1}^{N}\mathrm{ct}_{i,i+1}(\dot{\theta}_i - \dot{\theta}_{i+1})\,. \tag{B.4}$$

From (4.2),

$$N(\dot{\theta}_1 - \dot{\theta}_2) = (C_{11} + C_{21} + C_{31} + \cdots + C_{N1}) - (C_{12} + C_{22} + C_{32} + \cdots + C_{N2})\,.$$

C_{11} and C_{22}, C_{21} and C_{12} cancel. Then from (B.1) and analogous identities, we obtain

$$\begin{aligned} N(\dot{\theta}_1 - \dot{\theta}_2) &= (C_{31} - C_{32}) + (C_{41} - C_{42}) + \cdots + (C_{N1} - C_{N2}) \\ &= 2S_{12}S_{33|12} + 2S_{12}S_{44|12} + \cdots + 2S_{12}S_{NN|12} \\ &= 2S_{12}\left[S_{33|12} + S_{44|12} + \cdots + S_{NN|12}\right]\,. \end{aligned}$$

Hence, using a formula similar to (B.1),

$$\begin{aligned} N\,\mathrm{ct}_{12}\left(\dot{\theta}_1 - \dot{\theta}_2\right) &= 2C_{12}\left[S_{33|12} + S_{44|12} + \cdots + S_{NN|12}\right] \\ &= (S_{31} + S_{32}) + (S_{41} + S_{42}) + \cdots + (S_{N1} + S_{N2})\,. \end{aligned}$$

Each product of a cosine and a sine term was converted back to sums of sine terms.

Similar expressions are obtained for the other indices cyclically. Substitute these expressions into (B.4):

$$\begin{aligned}\frac{2N}{I} I = {} & (S_{31} + S_{32}) + (S_{41} + S_{42}) + \cdots + (S_{N-1,1} + S_{N-1,2}) + (S_{N1} + S_{N2}) \\ & + (S_{42} + S_{43}) + (S_{52} + S_{53}) + \cdots + (S_{N,2} + S_{N,3}) + (S_{12} + S_{13}) \\ & + (S_{53} + S_{54}) + (S_{63} + S_{64}) + \cdots + (S_{13} + S_{14}) + (S_{23} + S_{24}) \\ & + \cdots \\ & + (S_{2N} + S_{21}) + (S_{3N} + S_{31}) + \cdots + (S_{N-2,N} + S_{N-2,1}) + (S_{N-1,N} + S_{N-1,1}) .\end{aligned}$$

Disregarding the parentheses, we see that the first term of each row cancels with the last term of the next row. The second term of each row cancels with the second to the last term of two rows below. Similarly, all the terms cancel in pairs and disappear. As a result,

$$\dot{I} = 0 . \tag{B.5}$$

Therefore, I is a constant of motion of (4.2).

To get some intuition about what I measures, observe that I vanishes when $\theta_j = \theta_{j+1}$ for any j from 1 to N. Geometrically,this condition defines the boundary of the canonical invariant region (Section 4.4). On the other hand, I is maximized at the center of this region, corresponding to the splay state. Therefore, I is essentially a measure of the distance from the boundary of the canonical invariant region.

B.3. Independence

Since the system (4.2) is invariant with respect to exchange of two indices, $\theta_i \leftrightarrow \theta_j$, it follows that any quantity of the form

$$I = \langle p_1, p_2, \ldots, p_{N-1}, p_N \rangle = S_{p_1 p_2} S_{p_2 p_3} \cdots S_{p_{N-1} p_N} S_{p_N p_1} \tag{B.6}$$

is a constant of motion as long as $(p_1, \cdots, p_N)$ is a permutation of $(1, \cdots, N)$. By taking all possible permutations, we can generate many constants of motion. Of course, some of the constants of motion are identical (apart from sign) because of the symmetries:

$$\begin{aligned}\langle p_1, p_2, \ldots, p_{N-1}, p_N \rangle &= \langle p_2, p_3, \ldots, p_N, p_1 \rangle && \text{(rotation)} , \\ &= \pm \langle p_N, p_{N-1}, \ldots, p_2, p_1 \rangle && \text{(inversion)} .\end{aligned}$$

However, there still remain $(N-1)!/2$ constants of motion after these symmetries are considered. We show below that a sufficient number of constants of motion for integrability are included in this set.

How many independent constants of motion are required for integrability? Since (4.2) is posed in non-Hamiltonian form, $(N-1)$ constants of motion are necessary, in principle. Actually, we only need $N-2$ constants, because of the rotation invariance of the averaged system; the right hand side of (4.2) depends only on phase differences of oscillators. After a linear change of variables into the mean phase and $(N-1)$ phase differences, we see that the mean phase is decoupled, and is just driven passively by the dynamics of the phase differences. Notice that the constant of motion in (B.6) is also expressed solely in terms of phase differences. In the phase space the surface $I = \text{const.}$ is a cylinder extending in the mean phase direction.

For $N = 3$, we have $(3-1)!/2 = 1$ constants of motion, i.e.

$$I = \langle 1,2,3 \rangle = S_{12}S_{23}S_{31} \ .$$

This particular case, therefore, is already completely integrable.

For $N \geq 4$, we have more constants of motion than required. Obviously, there are relationships among them. We now provide a proof that there are $N-2$ *independent* constants of motion out of the set. (Functional relationships among the dependent constants of motion for $N = 4$ and 5 can be found explicitly, as shown in Section B.4.)

Theorem. Consider the following set of $(N-1)$ constants of motion, obtained by cyclically permuting the indices 2 to N:

$$\begin{aligned} I_1 &= \langle 1,2,3,4,\dots,N-2,N-1,N \rangle , \\ I_2 &= \langle 1,3,4,5,\dots,N-1,N,2 \rangle , \\ I_3 &= \langle 1,4,5,6,\dots,N,2,3 \rangle , \\ &\ \vdots \\ I_{N-1} &= \langle 1,N,2,3,\dots,N-3,N-2,N-1 \rangle . \end{aligned} \tag{B.7}$$

Then any $N-2$ of these constants are independent.

Proof. We construct the Jacobian matrix and then compute its rank by applying row and column operations. Our goal is to show that the matrix has an $(N-2) \times (N-2)$ minor with non-zero determinant.

Consider the $(N-1) \times (N-1)$ matrix whose (i,j) element is given by $\partial I_i / \partial \theta_j$, $1 \leq i \leq N-1$, $2 \leq j \leq N$, chosen to preserve the rotational symmetry of the indices. The elements are simplified by multiplying the ith row by a factor $2/I_i$ to produce similar expressions to (B.3). As a result of this operation, we obtain the matrix

$$\begin{pmatrix} \mathrm{ct}_{23} + \mathrm{ct}_{21} & \mathrm{ct}_{34} + \mathrm{ct}_{32} & \mathrm{ct}_{45} + \mathrm{ct}_{43} & \cdots & \mathrm{ct}_{N-1,N} + \mathrm{ct}_{N-1,N-2} & \mathrm{ct}_{N1} + \mathrm{ct}_{N,N-1} \\ \mathrm{ct}_{21} + \mathrm{ct}_{2N} & \mathrm{ct}_{34} + \mathrm{ct}_{31} & \mathrm{ct}_{45} + \mathrm{ct}_{43} & \cdots & \mathrm{ct}_{N-1,N} + \mathrm{ct}_{N-1,N-2} & \mathrm{ct}_{N2} + \mathrm{ct}_{N,N-1} \\ \mathrm{ct}_{23} + \mathrm{ct}_{2N} & \mathrm{ct}_{31} + \mathrm{ct}_{32} & \mathrm{ct}_{45} + \mathrm{ct}_{41} & \cdots & \mathrm{ct}_{N-1,N} + \mathrm{ct}_{N-1,N-2} & \mathrm{ct}_{N2} + \mathrm{ct}_{N,N-1} \\ \vdots & \vdots & \vdots & \ddots & \vdots & \vdots \\ \mathrm{ct}_{23} + \mathrm{ct}_{2N} & \mathrm{ct}_{34} + \mathrm{ct}_{32} & \mathrm{ct}_{45} + \mathrm{ct}_{43} & \cdots & \mathrm{ct}_{N-1,N} + \mathrm{ct}_{N-1,1} & \mathrm{ct}_{N2} + \mathrm{ct}_{N,N-1} \\ \mathrm{ct}_{23} + \mathrm{ct}_{2N} & \mathrm{ct}_{34} + \mathrm{ct}_{32} & \mathrm{ct}_{45} + \mathrm{ct}_{43} & \cdots & \mathrm{ct}_{N-1,1} + \mathrm{ct}_{N-1,N-2} & \mathrm{ct}_{N2} + \mathrm{ct}_{N1} \end{pmatrix} .$$

The first column, for example, only involves $\mathrm{ct}_{21}, \mathrm{ct}_{23}$ and ct_{2N} since the index 2 in (B.7) is always next to one of the indices 1, 3, or N. Only two entries in this first column involve ct_{21}. All the other entries in this column equal $\mathrm{ct}_{23} + \mathrm{ct}_{2N}$. For the other columns, a similar pattern is observed. Thus, the matrix can be reduced subtracting consecutive rows. For the rows $(N-1), \dots, 2$, subtract each row from the one above. The first row is left unchanged. Then, the matrix becomes

$$\begin{pmatrix}
\mathrm{ct}_{23}+\mathrm{ct}_{21} & \mathrm{ct}_{34}+\mathrm{ct}_{32} & \mathrm{ct}_{45}+\mathrm{ct}_{43} & \cdots & \mathrm{ct}_{N-1,N}+\mathrm{ct}_{N-1,N-2} & \mathrm{ct}_{N1}+\mathrm{ct}_{N,N-1} \\
\mathrm{ct}_{2N}-\mathrm{ct}_{23} & \mathrm{ct}_{31}-\mathrm{ct}_{32} & 0 & \cdots & 0 & \mathrm{ct}_{N2}-\mathrm{ct}_{N1} \\
\mathrm{ct}_{23}-\mathrm{ct}_{21} & \mathrm{ct}_{32}-\mathrm{ct}_{34} & \mathrm{ct}_{41}-\mathrm{ct}_{43} & \cdots & 0 & 0 \\
0 & \mathrm{ct}_{34}-\mathrm{ct}_{31} & \mathrm{ct}_{43}-\mathrm{ct}_{45} & \cdots & 0 & 0 \\
0 & 0 & \mathrm{ct}_{45}-\mathrm{ct}_{41} & \cdots & 0 & 0 \\
\vdots & \vdots & \vdots & \ddots & \vdots & \vdots \\
0 & 0 & 0 & \cdots & \mathrm{ct}_{N-1,1}-\mathrm{ct}_{N-1,N-2} & 0 \\
0 & 0 & 0 & \cdots & \mathrm{ct}_{N-1,N-2}-\mathrm{ct}_{N-1,N} & \mathrm{ct}_{N1}-\mathrm{ct}_{N,N-1}
\end{pmatrix}.$$

This matrix can be transformed into upper triangular form [42]. The result is that the diagonal elements of the matrix may be obtained recursively as:

$$\begin{aligned}
D_1 &= S_{N2}S_{22|31},\\
D_2 &= S_{N3}S_{31}S_{33|42}+S_{43}D_1,\\
D_3 &= S_{N4}S_{32}S_{41}S_{44|53}+S_{54}D_2,\\
D_4 &= S_{N5}S_{43}S_{32}S_{51}S_{55|64}+S_{65}D_3,\\
&\ \vdots\\
D_{N-4} &= S_{N,N-3}S_{N-4,N-5}\cdots S_{32}S_{N-3,1}S_{N-3,N-3|N-2,N-4}+S_{N-2,N-3}D_{N-5},\\
D_{N-3} &= S_{N,N-2}S_{N-3,N-4}\cdots S_{32}S_{N-2,1}S_{N-2,N-2|N-1,N-3}+S_{N-1,N-2}D_{N-4},\\
D_{N-2} &= S_{N,N-1}S_{N-2,N-3}\cdots S_{32}S_{N-1,1}S_{N-1,N-1|N,N-2}+S_{N,N-1}D_{N-3},\\
D_{N-1} &= 0.
\end{aligned}\tag{B.8}$$

The rank of the Jacobian matrix is given by the number of non-zero diagonal elements. If there were fewer than $N-2$ independent constants of motion in (B.7), then some of $D_1,\dots,D_{N-2}$ would have to vanish identically in some open set in the N-dimensional phase space. We show below that this cannot happen. Note that none of S_{ij} terms vanish because of the assumption that $\theta_i \neq \theta_j (i \neq j, \bmod 2\pi)$.

First, D_1 vanishes only on $\theta_2-(\theta_3+\theta_1)/2 = m\pi$, which are $(N-1)$-dimensional planes. Thus, D_1 cannot be identically zero in any open ball in the phase space.

Next, consider D_2 as a function of θ_4 by fixing the phases of the other oscillators. Then, from (B.8), D_2 becomes a linear combination of harmonics: $\sin[\frac{1}{2}\theta_4-(\theta_3-\frac{1}{2}\theta_2)]$ and $\sin(\frac{1}{2}\theta_4-\frac{1}{2}\theta_3)$. Since $\theta_2 \neq \vartheta_3+2m\pi$, it follows that $\theta_3-\frac{1}{2}\theta_2 \neq \frac{1}{2}\theta_3+m\pi$. Hence, the two harmonics are out of phase, and their superposition vanishes only at isolated values of θ_4. Therefore D_2 cannot vanish identically in any open ball, either.

Considering D_3 as a function of θ_5, a similar argument applies. We can continue this approach up to D_{N-3}.

Finally, D_{N-2} can be divided by a common factor $S_{N,N-1}$. Then, consider the result as a function of θ_{N-1}. $D_{N-2}/S_{N,N-1}$ becomes a superposition of $\sin(\frac{1}{2}\theta_{N-1}-\frac{1}{2}\theta_1)\sin[\theta_{N-1}-\frac{1}{2}(\theta_N+\theta_{N-2})]$, $\sin[\frac{1}{2}\theta_{N-1}-(\theta_{N-2}-\frac{1}{2}\theta_{N-3})]$, and $\sin(\frac{1}{2}\theta_{N-1}-\frac{1}{2}\theta_{N-2})$. The first one produces a higher harmonic term $\cos[\frac{3}{2}\theta_{N-1}-\frac{1}{2}(\theta_1+\theta_N+\theta_{N-2})]$, which cannot be eliminated by the other terms. Thus, the resultant function may vanish only at isolated θ_{N-1}, which implies D_{N-2} can vanish only on some surface in the phase space.

This concludes the proof that there are $N-2$ independent constants of motion out of (B.7). □

B.4. *Dependent constants*

This section points out some explicit relationships among dependent constants of motion. As shown above, one of the diagonal elements D_{N-1} always vanishes. Accordingly, there must be one dependence relation among $I_1, \dots, I_{N-1}$.

When $N=4$, there are $(4-1)!/2 = 3$ constants of motion, i.e. $I_1 = \langle 1,2,3,4\rangle$, $I_2 = \langle 1,3,4,2\rangle$ and $I_3 = \langle 1,4,2,3\rangle$. As Swift found, there is a simpler set of constants of motion, $J_1 = S_{12}S_{34}$, $J_2 = S_{13}S_{24}$ and $J_3 = S_{14}S_{23}$. These sets are related to each other via $J_1^2 = -I_1I_2/I_3$, $J_2^2 = -I_2I_3/I_1$ and $J_3^2 = -I_3I_1/I_2$. Such a reduction of constants of motion is possible for even N. $J_1, \dots, J_3$ are found to satisfy $J_1 + J_3 = J_2$. By eliminating $J_1, \dots, J_3$, and factoring, we obtain the relation in terms of $I_1, \dots, I_3$ as well:

$$I_1I_2 + I_2I_3 + I_3I_1 = 0 .$$

For $N > 4$, permutation of indices produces more constants of motion than the ones shown in (B.7). When $N = 5$, for instance, there are $(5-1)!/2 = 12$ constants of motion of the form (B.6), i.e. $I_1 = \langle 1,2,3,4,5\rangle$, $I_2 = \langle 1,3,4,5,2\rangle$, $I_3 = \langle 1,4,5,2,3\rangle$, $I_4 = \langle 1,5,2,3,4\rangle$, $I_5 = \langle 1,2,4,5,3\rangle$, $I_6 = \langle 1,4,5,3,2\rangle$, $I_7 = \langle 1,5,3,2,4\rangle$, $I_8 = \langle 1,3,2,4,5\rangle$, $I_9 = \langle 1,2,5,3,4\rangle$, $I_{10} = \langle 1,5,3,4,2\rangle$, $I_{11} = \langle 1,3,4,2,5\rangle$ and $I_{12} = \langle 1,4,2,5,3\rangle$. Three constants of motion out of $I_1, \dots, I_4$ are independent as proved. The "trivial" relations among $I_1, \dots, I_{12}$ are:

$$I_1I_{12} = -I_2I_7 = -I_3I_{10} = I_4I_5 = -I_6I_{11} = I_8I_9 ,$$
$$I_1I_3I_5 = -I_2I_6I_8 \quad \text{and} \quad I_1 - I_6 = -I_2 + I_5 = I_3 - I_8 .$$

These determine $I_5, \dots, I_{12}$ once $I_1, \dots, I_4$ are given. The last remaining relation is analogous to the one for $N = 4$, namely

$$I_1I_2I_3 + I_2I_3I_4 + I_3I_4I_1 + I_4I_1I_2 = 0 .$$

B.5. *Relating the two sets of constants*

Now we relate the constants $\{\psi_j\}$ and $\mathcal{H}$ found in Section 4, to the I's shown in (B.7). Consider I_1 of (B.7):

$$\begin{aligned} I_1 &= \langle 1,2,3,4,\dots,N-2,N-1,N\rangle \\ &= \sin[\tfrac{1}{2}(\theta_1-\theta_2)]\sin[\tfrac{1}{2}(\theta_2-\theta_3)]\dots\sin[\tfrac{1}{2}(\theta_N-\theta_1)] . \end{aligned}$$

The first term of the product is

$$\begin{aligned} \sin[\tfrac{1}{2}(\theta_1-\theta_2)] &= \sin[\tfrac{1}{2}(\theta_1-\Theta) - \tfrac{1}{2}(\theta_2-\Theta)] \\ &= \sin[\tfrac{1}{2}(\theta_1-\Theta)]\cos[\tfrac{1}{2}(\theta_2-\Theta)] - \cos[\tfrac{1}{2}(\theta_1-\Theta)]\sin[\tfrac{1}{2}(\theta_2-\Theta)] . \end{aligned}$$

The half-angle formula corresponding to (3.3) is

$$\sin[\tfrac{1}{2}(\theta_j-\Theta)] = \sqrt{\frac{1+\gamma}{1-\gamma\cos(\psi_j-\Psi)}}\,\sin[\tfrac{1}{2}(\psi_j-\Psi)] ,$$

$$\cos[\tfrac{1}{2}(\theta_j - \Theta)] = \sqrt{\frac{1-\gamma}{1-\gamma\cos(\psi_j - \Psi)}}\cos[\tfrac{1}{2}(\psi_j - \Psi)].$$

Thus,

$$\begin{aligned}
&\sin[\tfrac{1}{2}(\theta_1 - \theta_2)] \\
&= \frac{\sqrt{1-\gamma^2}\{\sin[\tfrac{1}{2}(\psi_1 - \Psi)]\cos[\tfrac{1}{2}(\psi_2 - \Psi)] - \cos[\tfrac{1}{2}(\psi_1 - \Psi)]\sin[\tfrac{1}{2}(\psi_2 - \Psi)]\}}{\{[1-\gamma\cos(\psi_1 - \Psi)][1-\gamma\cos(\psi_2 - \Psi)]\}^{1/2}} \\
&= \frac{\sqrt{1-\gamma^2}}{\{[1-\gamma\cos(\psi_1 - \Psi)][1-\gamma\cos(\psi_2 - \Psi)]\}^{1/2}}\sin[\tfrac{1}{2}(\psi_1 - \psi_2)].
\end{aligned}$$

Expressing the other terms similarly, we obtain

$$I_1 = \prod_{k=1}^{N} \frac{\sqrt{1-\gamma^2}}{1-\gamma\cos(\psi_k - \Psi)}\sin[\tfrac{1}{2}(\psi_k - \psi_{k+1})],$$

where indices are reduced mod N. Hence,

$$\frac{1}{N}\log I_1 = \frac{1}{N}\sum_{k=1}^{N}\log(\sin[\tfrac{1}{2}(\psi_k - \psi_{k+1})]) - \frac{1}{N}\sum_{k=1}^{N}\log\left(\frac{1-\gamma\cos(\psi_k - \Psi)}{\sqrt{1-\gamma^2}}\right).$$

From (4.5),

$$\frac{1}{N}\log I_1 = \frac{1}{N}\sum_{k=1}^{N}\log(\sin[\tfrac{1}{2}(\psi_k - \psi_{k+1})]) - \mathcal{H}.$$

This connects I_1 with $\{\psi_j\}$ and $\mathcal{H}$. For the other I's, it is clear from this derivation that only the order of summation in the first term of the right hand side is modified. In particular, if the permutation $(p_1, p_2, \cdots, p_N)$ gives a constant I, then the relation reads:

$$\frac{1}{N}\log I = \frac{1}{N}\sum_{k=1}^{N}\log(\sin[\tfrac{1}{2}(\psi_{p_k} - \psi_{p_{k+1}})]) - \mathcal{H}.$$

References

[1] E. Fermi, J. Pasta and S. Ulam, Los Alamos Rpt. LA-1940 (1955), in: Collected Papers of Enrico Fermi, vol.II (Univ. of Chicago Pr., Chicago, 1965) p. 978.
[2] K. Y. Tsang and I. B. Schwartz, Phys. Rev. Lett. 68 (1992) 2265.
[3] S. Nichols and K. Wiesenfeld, Phys. Rev. A 45 (1992) 8430.
[4] J. W. Swift, S. H. Strogatz and K. Wiesenfeld, Physica D 55 (1992) 239.
[5] D. Golomb, D. Hansel, B. Shraiman and H. Somopolinsky, Phys. Rev. A 45 (1992) 3516.
[6] S. H. Strogatz and R. E. Mirollo, Phys. Rev. E 47 (1993) 220.
[7] K.Y. Tsang, R.E. Mirollo, S.H. Strogatz and K. Wiesenfeld, Physica D 48 (1991) 102.
[8] S. Watanabe and S. H. Strogatz, Phys. Rev. Lett. 70 (1993) 2391.
[9] T. van Duzer and C.W. Turner, Principles of Superconductive Devices and Circuits (Elsevier, New York, 1981).
[10] T.P. Orlando and K.A. Delin, Foundations of Applied Superconductivity (Addison-Wesley, Reading, 1991).
[11] K.K. Likharev, Dynamics of Josephson Junctions and Circuits (Gordon and Breach, New York, 1986).
[12] W.C. Stewart, Appl. Phys. Lett. 12 (1968) 277.
[13] D.E. McCumber, J. Appl. Phys. 39 (1968) 3113.

[14] D.G. Aronson, M. Golubitsky and J. Mallet-Paret, Nonlinearity 4 (1991) 903.
[15] A.K. Jain, K.K. Likharev, J.E. Lukens and J.E. Sauvageau, Phys. Rep. 109 (1984) 310.
[16] J. Bindslev Hansen and P.E. Lindelof, Rev. Mod. Phys. 56 (1984) 431.
[17] R. Kleiner, F. Steinmeyer, G. Kunkel and P. Muller, Phys. Rev. Lett. 68 (1992) 2394; C. Pegrum, Nature 358 (1992) 193.
[18] P. Hadley and M.R. Beasley, Appl. Phys. Lett. 50 (1987) 621.
[19] P. Hadley, M.R. Beasley and K. Wiesenfeld, Phys. Rev. B 38 (1988) 8712.
[20] S.P. Benz and C.J. Burroughs, Supercond. Sci. Tech. 4 (1991) 561; Appl. Phys. Lett. 58 (1991) 2162.
[21] P. Ashwin, J.W. Swift, J. Nonlin. Sci. 2 (1992) 69.
[22] R.E. Mirollo, SIAM J. Math. Anal., in press.
[23] K. Otsuka, Phys. Rev. Lett. 67 (1991) 1090.
[24] J.W. Swift, unpublished.
[25] See e.g. L.G. Taff, Celestial Mechanics (Wiley, New York, 1985).
[26] D. Golomb, personal communication.
[27] M. Tabor, Chaos and Integrability in Nonlinear Dynamics (Wiley, New York, 1989).
[28] A.J. Lichtenberg and M.A. Lieberman, Regular and Stochastic Motion (Springer, New York, 1983).
[29] V.I. Arnold, ed., Dynamical Systems III, Encyclopedia of Mathematical Sciences, vol. 3 (Springer, Berlin, 1988).
[30] M. Hénon and C. Heiles, Astron. J. 69 (1964) 73.
[31] M.B. Sevryuk, Chaos 1 (1991) 160; 3 (1993) 211.
[32] J.W. Swift, to be published.
[33] Y. Yamaguchi, K. Kometani and H. Shimizu, J. Stat. Phys. 26 (1981) 719.
[34] N. Nakagawa and Y. Kuramoto, Prog. Theor. Phys. 89 (1993) 313.
[35] D.W. Jordan and P. Smith, Nonlinear Ordinary Differential Equations (Oxford Univ. Press, New York, 1977).
[36] P. Ashwin, G.P. King and J.W. Swift, Nonlinearity 3 (1990) 585.
[37] M. Toda, Theory of Nonlinear Lattices, 2nd Ed. (Springer, Berlin, 1988); Nonlinear Waves and Solitons (Kluwer, Dordrecht, 1989).
[38] C.J. Goebel, to be published.
[39] H. Flaschka, Phys. Rev. B 9 (1974) 1924.
[40] M. Hénon, Phys. Rev. B 9 (1974) 1921.
[41] J.W. Swift, unpublished.
[42] S. Watanabe, unpublished.

Chapter 2

Stability of periodic solutions in series arrays of Josephson junctions with internal capacitance

Shinya Watanabe and James W. Swift

Stability of periodic solutions in series arrays of Josephson junctions with internal capacitance

Shinya Watanabe
Department of Mathematics,
Massachusetts Institute of Technology
Cambridge, MA 02139
shinya@math.mit.edu

James W. Swift
Department of Mathematics,
Northern Arizona University
Flagstaff, AZ 86011-5717
James.Swift@nau.edu

May 5, 1995

Abstract

A long standing mystery surrounds the stability properties of the splay-phase periodic solutions to a series array of N Josephson junction oscillators. Contrary to what one would expect from dynamical systems theory, the splay state *appears* to be neutrally stable for a wide range of system parameters. It has recently been explained why the splay state is neutrally stable when the Stewart-McCumber parameter β (a measure of the junction internal capacitance) is zero. In this paper we complete the explanation of the mystery. We show that the splay state is indeed hyperbolic — either asymptotically stable or unstable — provided $\beta > 0$. We conclude that there is only a single unit Floquet multiplier, based on accurate and systematic computations of the Floquet multipliers for β ranging from 0 to 10. The apparent neutral stability of the splay state is a result of $N-2$ Floquet multipliers being extremely close to 1 for β larger than about 1. In addition, two more Floquet multipliers approach 1 as β gets large. We then do asymptotic analysis in the large β limit to clarify the situation. In the asymptotic approximation, $N-2$ multiplers are identically equal to 1, and two of the multipliers approach 1 in excellent agreement with the numerical results.

Abbreviated Title: Stability of periodic solutions in Josephson arrays.

1 Introduction

Arrays of Josephson junctions have been studied intensely by mathematicians because of their interesting properties as dynamical systems. A single Josephson junction oscillator is analogous to the familiar physical pendulum, and the coupling of an arbitrary number of oscillators allows us to study the connection between ordinary differential equations and partial differential equations [Pey&Kru84, Tsa&al91]. On the other hand, practical interest in Josephson junctions stems from their extremely high frequencies, but their amplitude is so small that many junctions must be coupled together in order to get a macroscopic voltage oscillation [Jai&al84, Had&al88, Ben&Bur91].

One-dimensional arrays of Josephson junctions may be classified as either series or parallel. Parallel arrays are well approximated by a nearest-neighbor diffusive coupling [Wat&al95]. This leads to discrete sine-Gordon models, which support "solitons" propagating across the junctions. In series arrays, the junctions are coupled in an all-to-all fashion. For this "global" coupling, the spatial coordinate is irrelevant, unlike in parallel arrays, and particularly good analytical progress has been made.

In this paper, we consider series arrays of N identical Josephson junctions shunted by a series LRC load (Fig. 1). After standard non-dimensionalization, the governing equations reduce to [Had&al88]:

$$\begin{cases} \beta\ddot{\phi}_j + \dot{\phi}_j + \sin\phi_j + \dot{Q} = I_b\ , \quad j = 1, \ldots, N, \\ L\ddot{Q} + R\,\dot{Q} + \dfrac{Q}{C} = \dfrac{1}{N}\displaystyle\sum_{k=1}^{N}\dot{\phi}_k. \end{cases} \tag{1}$$

Here, ϕ_j is the phase difference across the j-th junction, I_b is the DC bias current, and NL, NR, C/N are the load inductance, resistance, and capacitance, respectively. (Thus L is the inductance per junction, etc. This scaling, introduced in [Had&al88], is convenient for comparing different numbers of junctions.) As mentioned in the previous paragraph, the junctions are globally coupled even though they are arranged in series. Mathematically, the equations have permutation symmetry with respect to the indices j. The only nonlinearity is the $\sin\phi_j$

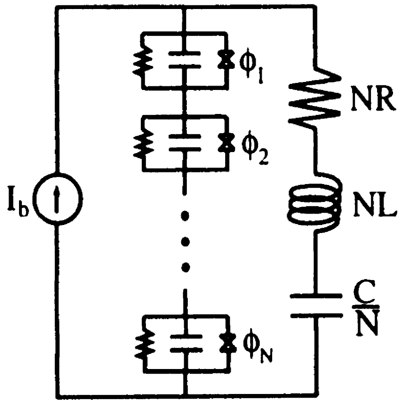

Figure 1: Circuit diagram for a series array of N identical Josephson junctions subject to a constant bias current I_b, and shunted by a series LRC load.

term. In particular, the second equation is linear. We emphasize that the bias current I_b is constant in time. The equations become much more difficult to analyse with an AC bias current. (The US voltage standard uses a series array of Josephson juctions with an AC bias current: The average voltage across the juctions is proportional to the frequency of the bias current due to the Josephson relation [Kau&al87].)

The dimensionless Stewart-McCumber parameter β is a measure of the junction internal capacitance. Junctions can be made with β ranging from 10^{-6} to 10^7 [McC88, vdZ&al94]. Much progress has been made in analysing system (1) in the limit $\beta = 0$, where the phase space of each oscillator is a circle [Jai&al84, Tsa&al91, Swi&al92, Tsa&Sch92, Str&Mir93, Wat&Str94]. In this paper we study the more difficult case when $\beta > 0$, where the shape of the oscillation in the $(\phi_j, \dot{\phi}_j)$ plane is affected by the coupling.

A mechanical analog of a *single* Josephson junction (Eq.(1) without $\dot{Q}$) is a damped pendulum of mass β, with applied torque I_b. The coupling in Eq.(1) arises in the mechanical analog if the pendula slide with friction around a common axle, and the axle is itself a torsional harmonic oscillator (Q is the angle of the axle, L is proportional to the moment of inertia, etc.).

The most important periodic solutions of system (1) are the *in-phase* and the *splay-phase* states. In this paper, "periodic" means that $\phi_j(t + T) = \phi_j(t) + 2\pi$ for all t and all j where $T > 0$ is the period. The junctions oscillate coherently in the in-phase state: $\phi_j(t) = \phi_1(t)$ for all j. The splay state is also periodic, but the individual waveforms are staggered equally in time: $\phi_j(t) = \phi_1(t + (j-1)T/N)$ for all j. (This is one splay state; the indices j can be exchanged arbitrarily due to the permutation symmetry of Eq.(1).) Technological applications of both states — the in-phase state as a high-frequency oscillator [Lik86, Had&al88] and the splay state as a voltage amplifier [Ter&Bea94] — are being sought. Since the existence of a single splay state automatically implies the existence of $(N-1)!$ splay states by the permutation symmetry, the possibility of using these states as multiple-memory device is also being studied [Ots91, Sch&Tsa94].

The linear stability of periodic solutions is quantified in terms of Floquet multipliers. A periodic solution of an ordinary differential equation (ODE) in n dimensions has n Floquet multipliers. One of these multipliers is always 1, corresponding to perturbations along the solution, and the other $n-1$ multipliers can be thought of as the eigenvalues of the fixed point of the Poincaré map. (The periodic solution of the ODE is a fixed point of the Poincaré map.) A Floquet multiplier inside the unit circle in the complex plane indicates a decaying perturbation, while those outside the unit circle are "unstable."

Previous numerical studies [Had&Bea87, Had&al88, Tsa&Sch92, Nic&Wie92] have computed Floquet multipliers for various combinations of the loads, the bias current I_b, and β. The stability properties of the two solutions appear roughly complementary (although bistable situations or chaotic attractors may arise). For example, when the in-phase state is stable, the splay state is usually unstable.

However, many numerical studies made a puzzling observation: often, the splay state is not asymptotically stable when the in-phase state is unstable; rather, it is only ***neutrally*** stable (i.e. Liapunov stable but not asymptotically stable). For an R-load with $\beta = 0$, Tsang *et al.* [Tsa&al91] found evidence that there are N Floquet multiplers on the unit circle (one complex conjugate pair and $N-2$ unit multipliers). Tsang and Schwartz found that there are $N-2$ unit multipliers for the $\beta = 0$ junctions coupled with an LC-load [Tsa&Sch92]. Nichols and Wiesenfeld [Nic&Wie92] did an excellent study of five different cases: two with $\beta = 0$ and three with $\beta > 0$. They always found, to within their numerical accuracy, $N-2$ unit multipliers when $\beta = 0$. For $\beta > 0$, they found that the splay state seems to be neutrally stable in $N-2$ directions for an LC or an LRC-load, but asymptotically stable for a C-load. This difference is surprising because the C-load is a limiting case of the LC-load. Nichols and Wiesenfeld were very careful when stating their conclusions. They warned that numerical evidence cannot *prove* neutral stability because one cannot distinguish between a unit multiplier and one that is extremely close to 1.

All previous analytical studies of this peculiar phenomenon have assumed $\beta = 0$ for simplicity. The neutral stability when $\beta = 0$ can be understood in the weak coupling limit [Swi&al92, Wie&Swi95] or in the limit $N \to \infty$ [Str&Mir93]. A rigorous explanation was obtained in [Wat&Str94], where it is shown that the phase space of the system (1) has a simple foliated structure when $\beta = 0$. This phase space structure gives rise to $N-3$ independent constants of motion, and hence causes the splay solution to have $N-2$ unit multipliers.

The present paper deals with what happens when β is positive. Since Nichols and Wiesenfeld found apparent neutral stability in two of the three cases when $\beta > 0$, an early conjecture was that the phase-space structure of the $\beta = 0$ equations might persist for $\beta > 0$, and one might hope to *prove* that the splay state is neutrally stable. But as we show numerically in Section 2, the splay solution is *not* neutrally stable when $\beta > 0$ with an LC-load. Unlike Nichols and Wiesenfeld [Nic&Wie92], we choose $L = 1$ and $C = 1/4$ since this is "close" to a C-load ($1/C$ is large compared to L). We find that either the in-phase or the splay-phase solution can be asymptotically stable, depending on β. This leads us to suspect that the neutral stability observed when $\beta > 0$ in other regions of the $L-C$ parameter space is also only approximate. Furthermore, an LRC-load is qualitatively similar to an LC-load because the resistance in the shunted load only adds to the internal resistance of the junctions.

We choose $N = 4$ for all our numerical studies, since this is the smallest N that shows the degenerate structure of the $\beta = 0$ equations. Generically there should be a single unit Floquet multiplier, but there are two unit multipliers when $\beta = 0$ and $N = 4$. (In contrast, our analysis in Section 4 will be for an arbitrary $N > 3$.)

In section 3 we present systematic computations of the Floquet multipliers as a function of β, which demonstrate that there is only a single unit multipler when $\beta > 0$. Starting with the parameters used by Nichols and Wiesenfeld [Nic&Wie92] for both the LC and C-load, we continue the branch of splay solutions between $\beta = 0$ and $\beta = 10$ using AUTO86 [Doe&Ker86]. This allows us to track the single critical real multiplier (since $N = 4$) into the regime where the splay solution is unstable. We find that this multiplier approaches 1 as $\beta \to 0$, as expected. However this multipler is also asymptotic to 1 as $\beta \to \infty$. In fact, the multiplier approaches 1 so quickly that Nichols and Wiesenfeld could not distinguish it from 1 when $\beta = 1.1$ in the LC-load case. (Our calculations are consistent with theirs.) At smaller β, where the critical multiplier is significantly smaller than 1, the splay state is unstable in a different direction and thus Nichols and Wiesenfeld did not find the state with their forward integration. On the other hand, in the C-load case it turns out that the splay state is stable for β small, and they observed an asymptotically stable splay state at $\beta = 0.1$. For both loads, we also find that N Floquet multipliers approach 1 as $\beta \to \infty$, indicating that the junctions become uncoupled in this limit.

In section 4 we carry out a perturbation analysis that takes advantage of the decoupling of the oscillators as $\beta \to \infty$. Assuming $\epsilon = 1/(I_b\sqrt{\beta}) \ll 1$, we derive the averaged equation for the phase drift of the oscillators. The averaged equation turns out to have the same form as the averaged equation when $\beta = 0$: it predicts that the splay solution has $N - 2$ unit multipliers. While for $\beta = 0$ this approximate result can be made rigorous [Wat&Str94], we view this as an "explanation" of why $N - 2$ of the multipliers are so close to unity for intermediate and large β. The averaged equations show no bistability between the splay and in-phase solution; which is stable depends on a single complex conjugate pair of multipliers. We estimate this multiplier pair from the averaged equation and find excellent agreement with our numerical results.

For any LRC-load, the averaging predicts that the in-phase state is stable for large enough $I_b\sqrt{\beta}$, while the splay-phase solution is neutrally stable for a C load in this same limit ($\epsilon \ll 1$). These conclusions are opposite of the common knowledge [Jai&al84, Had&Bea87, Wie&Swi95] which assumes $\beta = 0$. This paradox is discussed and resolved in Section 5. When I_b is large, the $\beta = 0$ limit becomes singular, and we have two competing results near $\beta = 0$.

2 Numerical integration of the equations

In this section we numerically integrate the equations (1) using a standard ODE integrator. This has the disadvantage that we cannot find unstable states. Nonetheless we will convince the reader that the degeneracy observed when $\beta = 0$ does not persist when $\beta > 0$, although the degeneracy re-appears *approximately* when β is large.

Since Nichols and Wiesenfeld observed an asymptotically stable splay state in the C-load case, we are interested primarily in the LC and LRC loads. These are not qualitatively different in the Josephson junction system because of the internal resistance of the junctions. Thus, we only consider the LC load.

We shall find that in some parameter regions of the LC-load system, there are asymptotically stable splay solutions, which persist when a small nonzero resistance is added to the load. We will also show other types of periodic solutions that can be attracting.

2.1 Time-delayed coordinates

Both the in-phase and the splay states are *phase-locked* states, and the phase relations among junctions are defined in terms of time lags rather than mere differences in angles ϕ_j at each instant t since the waveform $\phi_j(t)$ is nonuniform. A process to convert a solution $\phi_j(t)$ into the phase information is therefore necessary.

One useful algorithm [Ash&Swi93] is based on time delays between the "firings" of oscillators. We define each junction to "fire" when $\phi_j = \phi^* \pmod{2\pi}$ for some fixed ϕ^*. (We choose $\phi^* = 0$.) Let $t_j(p)$ be the time of the p-th firing of the j-th junction. We monitor firings of all the junctions, and calculate the phases every time junction N fires. Assume that p and q satisfy $t_j(q) \le t_N(p) < t_j(q+1)$.

Then we define the phase (normalized time lag) of the j-th junction to be:

$$\theta_j(p) = 2\pi\left(\frac{t_N(p) - t_j(q)}{T_j}\right) \tag{2}$$

where T_j is an approximate period of the junction. The phase $\theta_j(p)$ is approximately the angle that oscillator j covers between its most recent firing and the pth firing of oscillator N. Among the candidates for T_j, we choose $T_j = t_j(q+1) - t_j(q)$ in the following. This has an advantage that θ_j always falls in the interval $0 \leq \theta_j < 2\pi$. The "time-delayed coordinate" θ_j is an angle coordinate and we identify $\theta_j = 0$ with $\theta_j = 2\pi$.

2.2 Periodic attractors

We integrate the system (1) with $N = 4$ by an adaptive time-step Runge-Kutta integrator, and compute the time-delayed coordinates. We have tested both LC and C loads, but will focus on one representative case when $L = 1$, $R = 0$, $C = 1/4$. An array with this load exhibits a variety of periodic solutions depending on the parameters (I_b, β). The initial conditions are chosen to illustrate the transient dynamics.

Four cases are shown in Fig. 2. For each case, two graphs are shown; an upper graph shows the time-delayed coordinates θ_j. Since $\theta_N \equiv 0$ by definition, only three curves can be seen. Each lower graph shows the amplitude of the first and the second (complex) moments of θ_j's. They are R_1 and R_2 defined by

$$R_m(t)e^{i\Theta_m(t)} = \frac{1}{N}\sum_{k=1}^{N} e^{im\theta_k(t)} \ , \quad R_m \geq 0 \ . \tag{3}$$

(For general N, m ranges from 1 to floor[$N/2$].) The amplitude of the first moment R_1 was originally introduced by Kuramoto as an "order parameter" to measure the phase coherence of a population of phase oscillators [Kur84]. Indeed, $R_1 = 1$ if and only if the oscillators are in-phase. When $R_1 = 0$, we say that the oscillators are "incoherent" (this is our *definition* of an incoherent state). The splay state is characterized by $R_j = 0$ for all j. The horizontal t-axis for the figures denotes the (discrete) firing time $t_N(p)$. The first several firings are ignored since the junctions

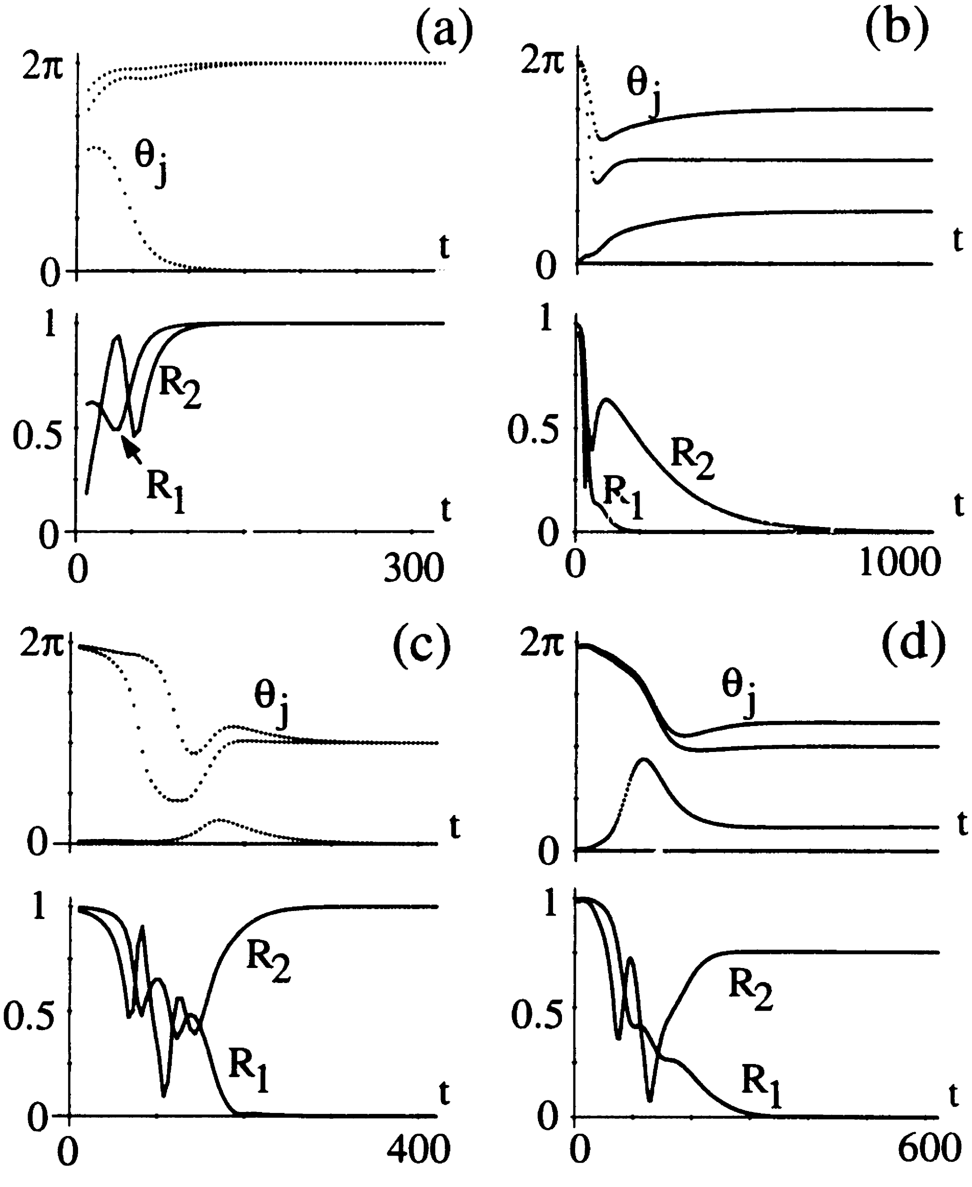

Figure 2: Time-delayed coordinates θ_j (upper graphs) and the amplitude of the first and the second Fourier coefficients R_1 and R_2 (lower graphs) as functions of t. Cases (a–c) uses $L = 1$, $R = 0$, $C = 1/4$, and $I_b = 1.5$. Only the McCumber parameter β is changed: (a) 0.7, (b) 0.15, (c) 0.3. Case (d) uses the same load but with $I_b = 2.5$ and $\beta = 1$. A trajectory converges to (a) the in-phase state, (b) the splay state, (c) the 2+2 incoherent state, and to (d) a (generic) incoherent state.

rapidly change their phases. During this transient, the time-delayed coordinates are not meaningful.

For Figs. 2(a) to (c), the bias current is fixed at $I_b = 1.5$, and only the McCumber parameter β is changed. Fig. 2(a), which shows a stable in-phase attractor, uses $\beta = 0.7$. Since $\theta_j = 0$ is identified with $\theta_j = 2\pi$, we see that four junctions have become synchronized after $t \approx 100$. This is also clear from the moments: both R_1 and R_2 converge to 1.

In Fig. 2(b), $\beta = 0.15$ is used. The phase differences converge to $2\pi/N$, thus the attractor is the splay state. The way the trajectory approaches the attractor is somewhat interesting. Note that R_1 vanishes at $t \approx 200$, after which the state is incoherent, i.e. $\sum_{k=1}^{N} \exp[i\theta_k] = 0$. If the angles θ_j are plotted on the unit circle, they are scattered so that their center of mass lies at the origin. For $N = 4$, this is possible only when the θ_j's form two "antiphase" pairs; for example $\theta_1 = \theta_3 + \pi$ and $\theta_2 = \theta_4 + \pi$. After R_1 vanishes, only the angle $\alpha = \theta_1 - \theta_2 = \theta_3 - \theta_4$ between the two pairs changes. This *slow drift* can be seen from $R_2(t)$ which also vanishes at $t \approx 1000$. The angle is then $\alpha = \pi/2$, indicating the splay-phase solution.

Fig. 2(c) uses an intermediate value $\beta = 0.3$. At $t \approx 200$, R_1 vanishes and the phases are again incoherent. Drift as in (b) occurs, but in the opposite direction. At $t \approx 300$, R_2 converges to unity, while $\alpha \to 0$ or π, depending on how one numbers the oscillators. The final state is two pairs located 180 degrees apart. We call this state the "2+2 incoherent" periodic solution.

With $I_b = 1.5$ as in Figs. 2(a–c), we did a parameter sweep of $\Delta\beta = 0.01$, and found that the splay state is stable for $\beta \leq 0.21$ and the 2+2 incoherent state is stable for $\beta \geq 0.19$. This bistability suggests that there exists an unstable generic incoherent state when $0.19 \leq \beta \leq 0.21$. By "generic," we mean that $0 < \alpha < \pi/2$.

Fig. 2(d) uses the same load, but both $I_b = 2.5$ and $\beta = 1$ are larger than the previous values. We see that R_1 vanishes at $t \approx 300$ again while R_2 stays constant for $t > 250$. The constant value is neither 0 nor 1 so that the final state appears to be a generic incoherent state with $0 < \alpha < \pi/2$. Different initial conditions converge to incoherent states with different R_2 (and thus different α.) It *appears* that there is an incoherent periodic state for each value or R_2 (or α), just as there is in the equations with $\beta = 0$. However, we believe that the states are *not* exactly periodic but are drifting very slowly towards either the splay or the "2+2 incoherent" state. In the next section we will give indirect evidence for this slow drift.

When I_b and β are larger, for example $I_b = 4$ and $\beta = 5$, there appears to be a periodic state with *any* values of the angles θ_i. During the transient dynamics the delay coordinates are not meaningful, but after this, the angles θ_j stay constant at whatever values they happened to "fall into." In other words, the oscillators are effectively decoupled, and they maintain any phase relationship. Mathematically speaking, there appears to be an attracting 4-torus with a linear flow. As with the case described in figure 2(d), however, we expect that the dynamics are actually "generic", and drift occurs on a timescale too long to observe.

2.3 Three-dimensional projection

The dynamics become more apparent by using a linear transformation of the time-delayed coordinates [Ash&Swi92, Tsa&Sch92, Wat&Str94]. Since we are only interested in the relative phase differences, we change the coordinates by, for example, $u_{0,1} = \theta_1 + \theta_2 \pm \theta_3 \pm \theta_4$ and $u_{2,3} = \pm\theta_1 \mp \theta_2 + \theta_3 - \theta_4$, then only show u_1, u_2, and u_3. Figs. 3(a–d) show the dynamics of Figs. 2(a–d), respectively, in these coordinates.

The trajectories run inside a tetrahedron in this representation. The faces of the tetrahedron correspond to when two θ_j's are identical (a "2+1+1" state). Each edge of the tetrahedron corresponds to one of two types of oscillation: "2+2" (shown as dotted lines) or "3+1" (as solid lines). Since no change in ordering of junctions occurs in Fig. 2 after a short transient, the phases maintain the relationship, say, $\theta_4 \leq \theta_3 \leq \theta_2 \leq \theta_1 \leq \theta_4 + 2\pi$. Thus, a trajectory does not escape from the tetrahedron. (Such escape, however, is not prohibited and may happen for more complicated attractors.) The four vertices correspond to the in-phase state. (There are four ways to approach this state while maintaining the ordering.) The *incoherent bar* inside the tetrahedron is the set of incoherent states for which R_1 vanishes. (The incoherent bar, indicated by a dashed line, generalizes to an

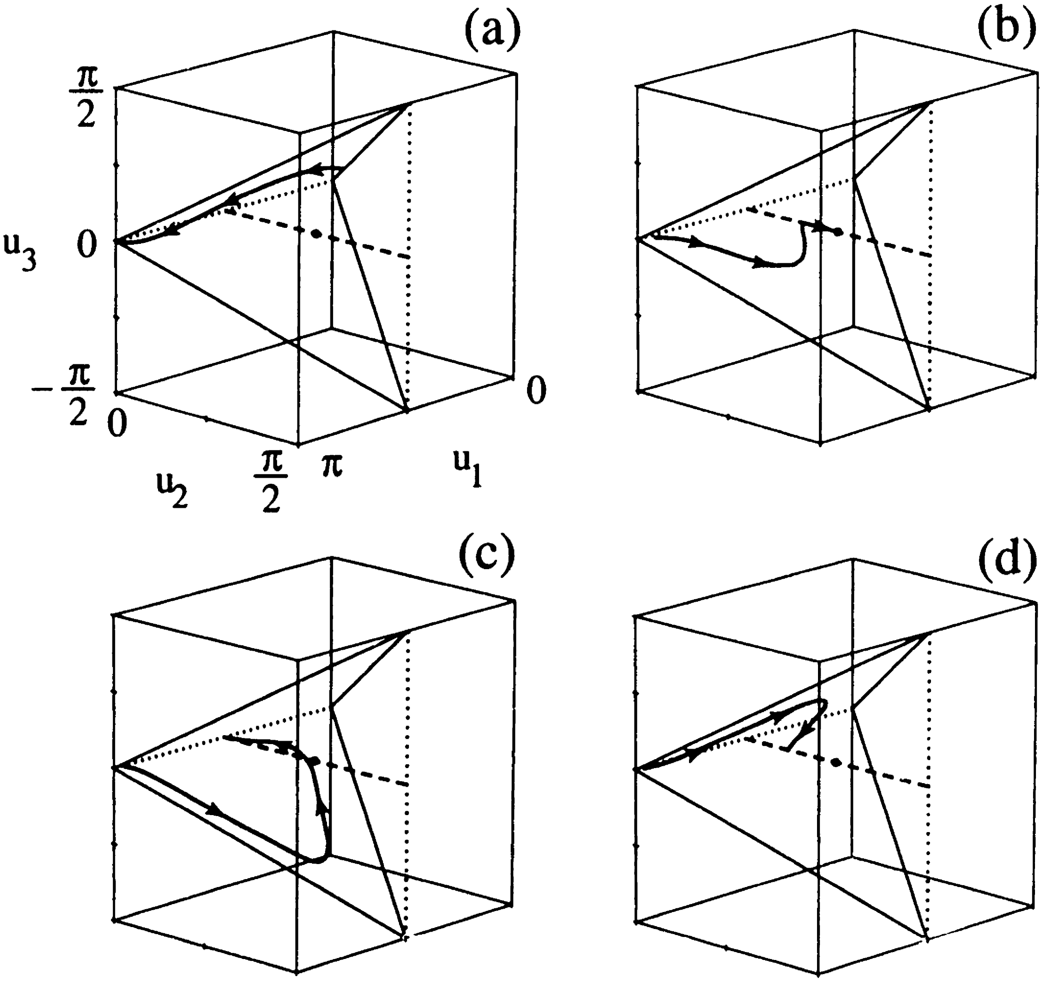

Figure 3: Projection of trajectories onto a three-dimensional space defined by a linearly transformation of the time-delay coordinates: $u_{0,1} = \theta_1 + \theta_2 \pm \theta_3 \pm \theta_4$ and $u_{2,3} = \pm\theta_1 \mp \theta_2 + \theta_3 - \theta_4$. Only the phase *differences* u_1, u_2, u_3 are shown. The cases (a–d) correspond to the cases in Fig. 2, respectively. The vertices of the tetrahedron correspond to the in-phase state while the bar inside the region is the set of incoherent states. The two endpoints of the bar are both 2+2 incoherent states, while the dot in the middle of the bar is the splay state.

$(N-3)$-dimensional incoherent manifold when there are N oscillators.) The two end points of the bar are 2+2 incoherent states, while the dot at the midpoint is the splay state. The trajectories shown are actually discrete sets of points at $\{t_N(p)\}$, but the points are connected in the figures for clarity.

In Fig. 3(a) the trajectory starts at a point inside the tetrahedron, but converges to the in-phase state at a vertex. In Fig. 3(b), on the other hand, the initial condition is near the in-phase state but the trajectory converges to the splay state. This process consists of two stages; the first fairly rapid fall onto the incoherent bar is followed by a slow drift along the bar.

In Fig. 3(c) the initial condition is also near the in-phase state, and the trajectory falls onto the incoherent bar. However, this time, it converges to the 2+2 incoherent state at the end of the bar. In Fig. 3(d) the trajectory does not appear to move along the incoherent bar once it hits the bar. The calculation is halted at $t \approx 600$. However, we expect that there is a very slow drift along the bar as described earlier.

From the above computation and visualization we obtain two new insights into the problem. First, defining phase differences of the junctions in terms of time-delays is useful not only for visualization but also as a means to *define* "incoherence." The set of all incoherent states seems to form an invariant manifold. It would be interesting to prove this starting with the original equations. However, since the definition of incoherence uses the time-delay coordinates, it is difficult to work with the ODE directly. Even for the relatively simple case with $\beta = 0$, where the splay state is known to exist for several types of the loads (which implies that an $(N-2)$-dimensional manifold of periodic solutions exists at least locally near the state [Wat&Str94]), we cannot prove that these periodic solutions are incoherent using the time-delay definition.

Second, occurrence of the drift along the incoherent bar implies that the degenerate phase space structure of the $\beta = 0$ limit is broken for $\beta > 0$. In this limit, the tetrahedron region in Fig. 3 is foliated by a family of invariant subspaces [Wat&Str94]. If such degeneracy were to persist when $\beta > 0$, then the structure would prohibit a trajectory from moving from one subspace to another, thus the drift would not occur. As a result of this drift, the splay state, the 2+2 incoherent state, or more generic incoherent states can become asymptotically stable.

2.4 Waveforms

The time-delayed coordinates θ_j are useful to investigate the dynamics, but do not show direct information on $\phi_j(t)$. Therefore, we investigate the waveforms and symmetry properties of the periodic solutions in this section.

Figures 4(a–d) show the waveforms for (a) the in-phase state, (b) the splay state, (c) the 2+2 incoherent state, and (d) the generic incoherent state, respectively. (The case (d) is close enough to being periodic.) Each upper graph displays $\sin\phi_j$ (the supercurrent through the j-th junction) as a function of t, whereas each lower graph shows the same solution in terms of the phase portrait $(\phi_j, \dot{\phi}_j)$ for all j. The dashed curve in the lower graph denotes the trajectory of an uncoupled (single) junction with the same parameters (I_b, β).

The trajectories for the in-phase state and the 2+2 incoherent state are significantly altered from the trajectory without coupling. In contrast, the trajectories for the splay state and the generic incoherent state are almost unchanged in shape. This is partly due to the parameter values; note that figures (b) and (d) have the largest β values. Furthermore, when the state is incoherent the coupling terms in equation (1), $\sum \dot{\phi}_k$, tend to cancel each other.

In all four cases, the four trajectories in the phase portraits follow the same curve. This must be the case for all but the generic incoherent state in figure (d). Let us explain: We have already given the general form of the in-phase, splay, and 2+2 incoherent solutions. Each of these states has a single waveform, with different phase shifts between the oscillators. For any incoherent state with $N = 4$, the oscillators can be numbered so that $\phi_3(t) = \phi_1(t + T/2)$, and $\phi_4(t) = \phi_2(t + T/2)$, where T is the period. In figure (d), we observe that $\phi_2(t) = \phi_1(t + c)$ for some phase shift c, but in general these two waveforms can be different. We have in fact observed two distinct waveforms for a generic incoherent state in a different parameter regime.

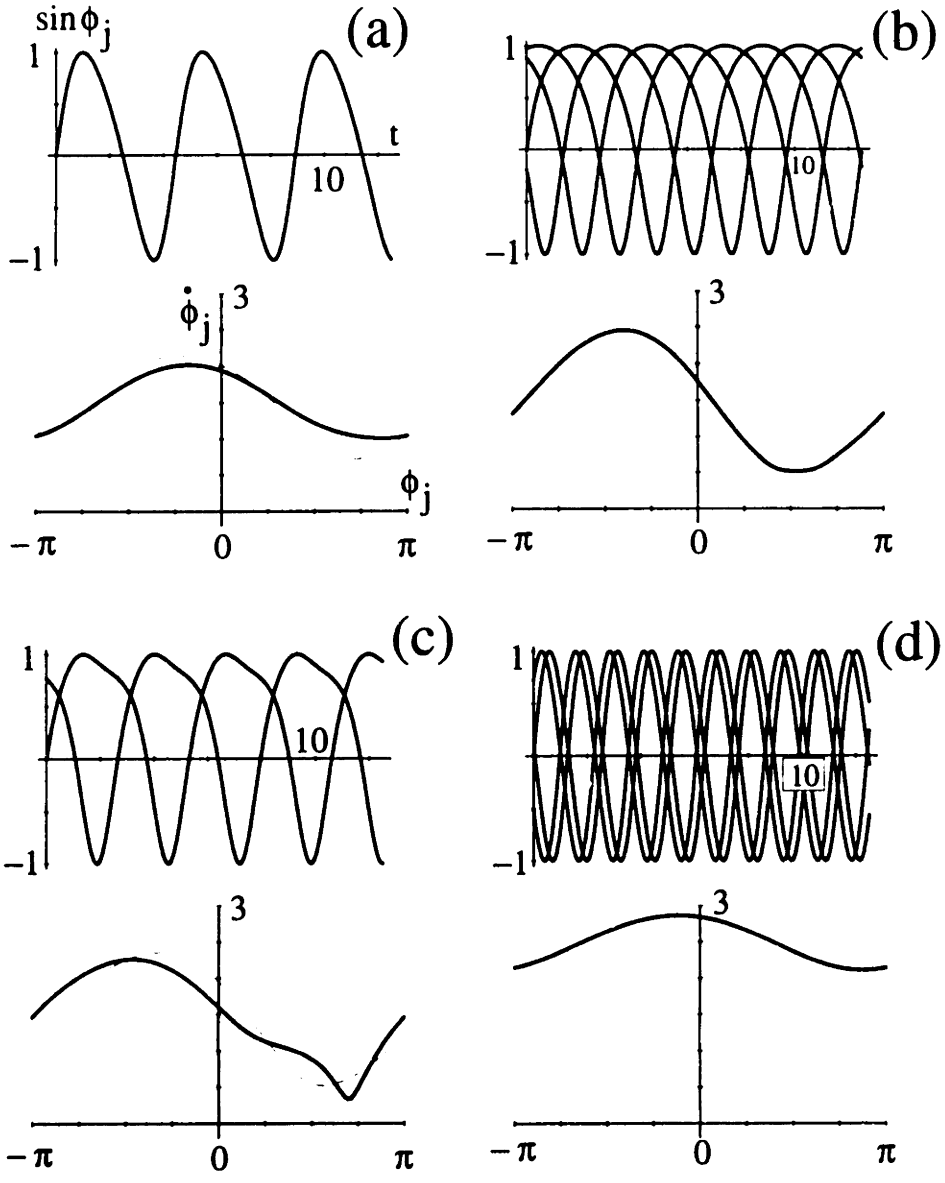

Figure 4: The supercurrent $\sin\phi_j(t)$ (upper graphs) and the phase portrait $\dot{\phi}_j$ versus ϕ_j (lower graphs) of the final state achieved in Fig. 2, respectively. The dashed curve in the phase portrait shows the trajectory of an uncoupled junction with the same I_b and β values.

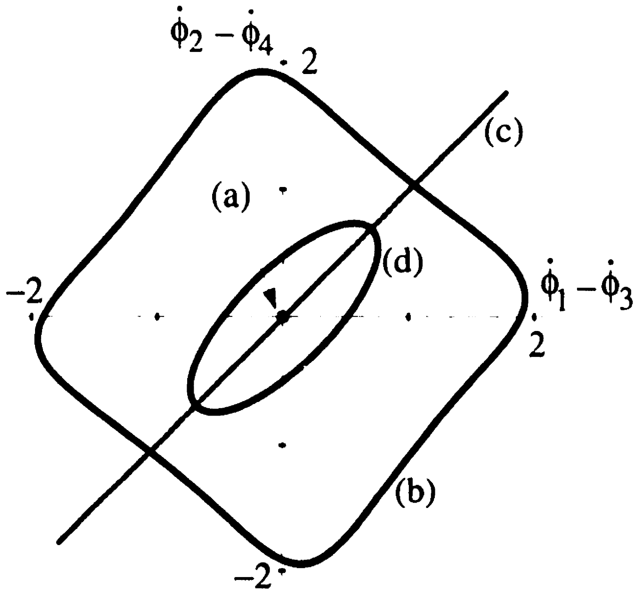

Figure 5: Lissajous figures obtained by plotting the difference of the voltages across junctions 2 and 4 versus that of junctions 1 and 3. Four figures are superimposed, corresponding to the periodic states in Fig. 2. The in-phase state (a) appears as a point at the origin.

Finally, we show a way to distinguish between the different types of oscillations which does not require the time-delay technique. In Fig. 5 we plot $\dot\phi_2 - \dot\phi_4$ vs. $\dot\phi_1 - \dot\phi_3$. Since $\dot\phi_j$ is proportional to the voltage across the Josephson junction, we call this the Lissajous figure created by the voltage signals.

All $\phi_j(t)$ are synchronized for the in-phase solution, thus the figure for case (a) appears as the point at the origin. The pattern of the other states depends on the order of the oscillators: we choose initial conditions or permute the oscillators so that $\phi_1 \le \phi_2 \le \phi_3 \le \phi_4 \le \phi_1 + 2\pi$. The splay state (b) has a 4-fold symmetry while a generic incoherent state (d) has only 2-fold rotational symmetry about the origin. The 2+2 incoherent state appears as a diagonal line with a slope +1 (The slope can also be -1, depending on initial conditions, since two different states have the correct ordering: $\phi_1 = \phi_2 = \phi_3 - \pi = \phi_4 - \pi$ or $\phi_1 = \phi_2 - \pi = \phi_3 - \pi = \phi_4 - 2\pi$ for all t.) The symmetries of the Lissajous figures are easily explained from the waveforms. For example, phase shifting the splay state by a quarter period rotates the Lissajous figure by 90 degrees.

Finally, we mention that the Lissajous figures can be extended to three dimensions using the coordinate $\dot{\phi}_1 - \dot{\phi}_2 + \dot{\phi}_3 - \dot{\phi}_4$. The resulting figures are analogous to figure 3, but they can be made without computing the time-delay coordinates.

3 Floquet multiplier computation

In this section we report on calculations of the Floquet multipliers of the splay-phase state. The Floquet multipliers provide local information which is complementary to the images of the phase space shown in the previous section. The degenerate dynamics of the equations when $\beta = 0$ is reflected by the fact that the splay state has $N - 2$ unit multipliers when $\beta = 0$. Conversely, if the dynamics is nondegenerate, then there must be exactly one unit Floquet multiplier.

We calculate the multipliers of the splay state as a function of β for two types of the shunt loads, an LC load and a purely capacitive load. We find that there is a single unit Floquet multipler when $\beta > 0$, indicating that the system is nondegenerate. However, when β is larger than about 1, there are $N-2$ multipliers *very close* to 1. This is why we observed an apparently neutrally stable incoherent state in Fig. 2(d): the Floquet multiplier which measures the speed of the drift in the incoherent manifold is extremely close to 1.

Furthermore, a complex conjugate pair of multipliers approaches 1 as $\beta \to \infty$. Thus, in the large β limit there are N unit Floquet multiplers, corresponding to the oscillators being effectively uncoupled, which we observed in the numerical integrations.

In order to calculate the Floquet multipliers, we first find a stable splay state for one set of parameters, then use a continuation method to compute the branch of periodic solutions as β is varied, holding the other parameters fixed. Solutions can be obtained regardless of stability, which clarifies the dependence of the multipliers on β.

The starting solution is found by choosing the same parameters as two of the cases studied by Nichols and Wiesenfeld [Nic&Wie92], specifically, their cases II and III:

[NWII] $N = 4$ $L = 0.75$ $R = 0$ $C = 20$ $I_b = 2.5$ $\beta = 1.1$
[NWIII] $N = 4$ $L = 0$ $R = 0$ $C = 1$ $I_b = 1.5$ $\beta = 0.1$

(We have scaled their actual parameter values to suit our definition.)

In both cases, we have chosen an initial condition close to the splay state. Since the waveform is nonuniform, $\phi_j(0) = 2\pi j/N$ is not a good starting point. Instead, we have computed the periodic solution $\phi^*(t)$ of the uncoupled equation (Eq.(4) shown later) for the given (I_b, β), then assigned the initial condition as $\phi_j(0) = \phi^*(Tj/N)$ where T is the period. The choice is especially useful for the LC-load (case II), and it enables us to obtain the splay state (or, at worst, an incoherent state extremely close to the splay state) sufficiently fast. We do not need an extrapolation technique as used in [Nic&Wie92].

Next, we sweep β up to 10 using the continuation and bifurcation package AUTO86 [Doe&Ker86]. Then, β is decreased from 10 down to almost 0. AUTO86 computes the Floquet multipliers, but not accurately enough for our purposes. To improve the accuracy, we output a point on the periodic solution at each value of β, and integrate the Jacobian matrix for one full period. The eigenvalues of the resulting matrix are the Floquet multipliers, which we compute using Mathematica. There must always be a unit multiplier corresponding to perturbation in the direction of the periodic orbit. This multiplier is computed to at least within 8 significant figures. (AUTO86, which only *estimates* Floquet multipliers for the purpose of detecting bifurcation points, has calculated the trivial multiplier within 3–7 digits.) Also, the multipliers for the starting value of β agree with those obtained in [Nic&Wie92].

Figure 6 shows the magnitude of the computed multipliers. The figures (a) and (b) correspond to [NWII] and [NWIII], respectively. The left figures show all the multipliers whereas the right ones are enlarged views of the shaded box in the left figure. To resolve the real multiplier near unity, the shaded box in the right figure is further enlarged as the inset. The number of multipliers is the same as the dimension of the system, thus there are ten multipliers in (a) and eight in (b). They are labeled as "cc" (complex conjugate pairs), "r" (real), and "u" (the unit multiplier). One sees that the unit multiplier is computed accurately, and shows no visible deviation from unity even in the inset.

Although these multipliers provide only local information around the splay state, we can roughly associate them with the global dynamics described in Section 2. For example, five multipliers in (a) and four in (b) have magnitudes well below unity, especially when β is small. They correspond to the rapid initial transient when the junctions shuffle and change firing order. After these directions are contracted, all the junctions have similar periods. The convergence speed of this initial stage is instantaneous when $\beta = 0$ and becomes slower as β becomes large. One real multiplier in (a) which always stays near 0.9 seems to correspond to a perturbation in the charge Q on the capacitor. This multiplier behaves differently from the others.

After the initial transients are over, the time-delayed coordinates described in Section 2 become meaningful, and the dynamics involves the phase differences. The three nontrivial multipliers of near-unit magnitude, shown in the blow-ups in Figs. 6(a,b), represent this dynamics. From now on, our interest is focused on these three multipliers. The incoherent manifold is the key to understanding the dynamics. Two multipliers (the c.c. pair) correspond to the dynamics transversal to this manifold. If they have magnitude greater than unity, then trajectories depart from the manifold and the in-phase state is usually stable. When their magnitude is below unity, the incoherent manifold as a whole is attracting.

The real multiplier near unity, which we call the "critical multiplier" in the following, represents the dynamics along the manifold. (We describe 4 oscillators. In general there are $N - 3$ such multipliers.) When the critical multiplier is less than 1, the splay state is attracting within the incoherent manifold. When it is larger than 1, the drift on the incoherent manifold is away from the splay state. In the $\beta = 0$ equations the critical multiplier is exactly unity, and there is no drift on the incoherent manifold.

Figure 6 shows that the magnitude of the "transverse multipliers" deviates substantially from 1 when β is small. The magnitude changes in a nontrivial fashion, switching stability at finite β in either case. Using an LC load, the

(a) LC-load

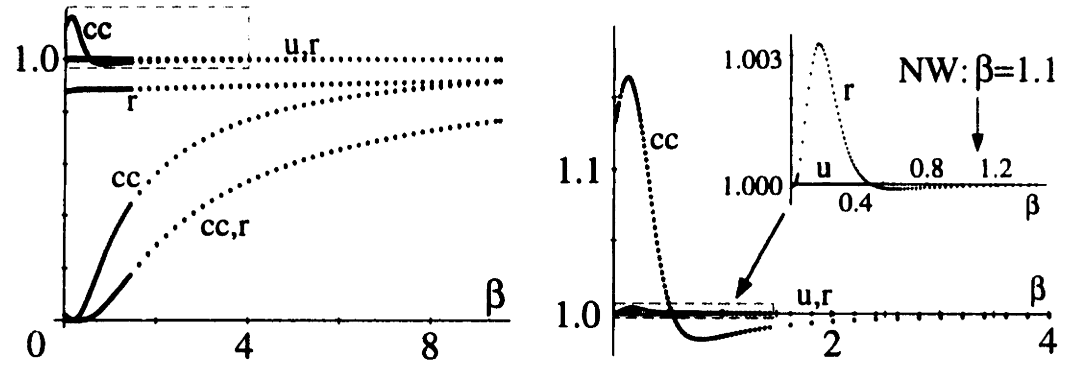

(b) C-load

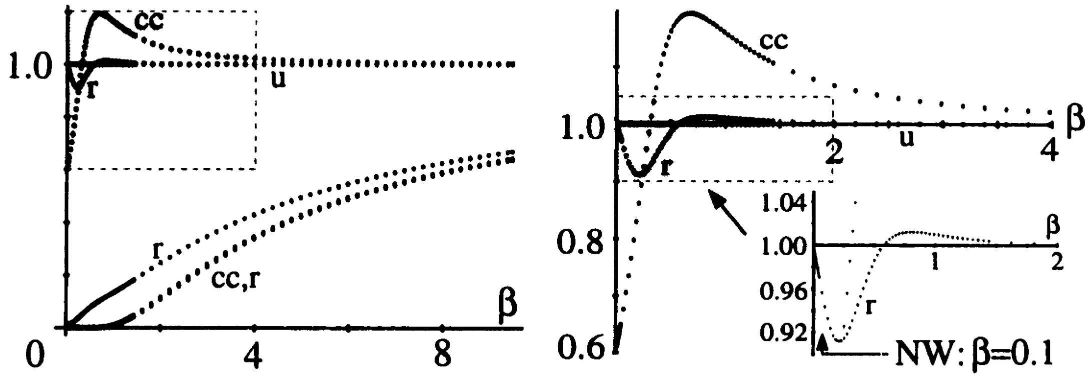

Figure 6: Dependence of the magnitude of Floquet multipliers with respect to β, for (a) an *LC* load (case [NWII]) and for (b) a *C* load (case [NWIII]). All multipliers are shown in the left figures while the shaded regions are enlarged in the right figures. In order to resolve the real multiplier near unity, another set of enlargements (of the shaded region in the right figures) are shown as insets. There are 10 multipliers for (a) and 8 for (b). The letters denote "cc" (complex conjugate pairs), "r" (real), and "u" (the unit multiplier). The arrows labeled "NW" point to the β values used in [Nic&Wie92].

incoherent manifold is repelling for small β, and attracting for larger values. For a C load, it is reversed.

The critical multiplier is extremely close to 1 at moderate β. This explains why it appeared in [Nic&Wie92] that degenerate phase space structure persists even for $\beta > 0$. However, the enlarged figures suggest that the critical multiplier is asymptotic to, but never equal to, unity. Thus, we believe that a drift occurs on the incoherent manifold for all $\beta > 0$, even though it is so slow as to be unobservable for large β. Analysis [Wat&Str94] predicts that the real multiplier must be exactly 1 at $\beta = 0$. Fig. 6 is in agreement.

4 Weak coupling limit

4.1 Small parameter

In Fig. 6 one notices that the Floquet multipliers depend on β in a simple manner when $\beta \gg 1$. In particular, it seems certain that the three multipliers with the magnitudes near unity — a complex conjugate "transverse" pair and the critical "drift" multiplier — approach exactly 1 in the $\beta \to \infty$ limit. This indicates almost complete decoupling of the four junctions. Each junction converges to a limit cycle, but the phase relations hardly change after that. In general, the coupling among junctions becomes weak regardless of the load (or of N) when β is large. The mechanism is simple; the phases ϕ_j become almost linear in t, and the charge Q in Eq.(1) becomes nearly stationary, i.e. $\dot{Q} \approx 0$. Then, since the rate of change in Q feeds back the coupling among junctions, they are only weakly coupled.

However, the effect of coupling can still accumulate over a long time scale, and eventually result in mutual phase-locking. In this section we will derive the averaged equation which describes the slow dynamics. The analysis is valid for all $N > 3$. We start by identifying a small parameter ϵ and carry out a formal perturbation expansion. The reduced averaged equation is then analyzed, which enables us to estimate the c.c. pair of Floquet multipliers near unity.

The method we use is two time-scale analysis. The fast time scale is the

Josephson frequency, and the slow scale accounts for the drift of the relative phase differences. However, let us first identify a small parameter ϵ from starting with the uncoupled equation. When β is large, the junctions are only weakly coupled so that $\dot{Q}$ in Eq.(1) is negligible at the first estimate. Then, the equation for junction j becomes the single junction equation:

$$\beta\ddot{\phi}_j + \dot{\phi}_j + \sin\phi_j = I_b. \tag{4}$$

It is more convenient to rescale time into $\tau = I_b t$. Then,

$$\frac{d^2\phi_j}{d\tau^2} + \epsilon\Gamma\frac{d\phi_j}{d\tau} + \epsilon^2\sin\phi_j = \epsilon\Gamma \tag{5}$$

where $\Gamma = 1/\sqrt{\beta}$ and $\epsilon = 1/(I_b\sqrt{\beta})$ are convenient parameters which replace I_b and β. (The reason will become evident after an approximate solution is displayed.) We hold Γ fixed at *any* value, and take $\epsilon \to 0+$. Thus, we fix β and let $I_b \to \infty$, but since the asymptotic analysis holds when $I_b\sqrt{\beta}$ is large, we can also interpret the results for fixed $I_b > 1$ and $\beta \to \infty$.

The "single pendulum" equation (4) is well studied, and possesses a unique limit cycle (of the second kind) when ϵ is sufficiently small [Lev&al78]. The solution can be approximated by posing a solution of the form

$$\begin{cases} \phi_j(\tau;\epsilon) = \sum\limits_{m=0}^{\infty} \epsilon^m y_m(T_0) \\ T_0 = \left(1 + \sum\limits_{m=1}^{\infty} \epsilon^m \omega_m\right)\tau \end{cases}$$

where the strained coordinate is used in the second equation to take account of a slight frequency change. The functions y_m must be periodic in T_0 for all $m > 0$. Since the solution is *running* periodic, y_0 grows in time. Substituting this form into Eq.(4), the unknowns y_m and ω_m can be determined order by order. The result is

$$\phi_j = (T_0 + \theta_j) + \epsilon^2\sin(T_0 + \theta_j) + \epsilon^3\Gamma\cos(T_0 + \theta_j) + \dots$$

where θ_j is an integration constant. It is a remarkable fact that when I_b *or* β is large the first correction to constant angular velocity depends only on ϵ. This is why ϵ is the "correct" small parameter. Physically, the small ϵ limit occurs when the friction is small compared to the applied torque. The period is about 2π in τ, or $2\pi/I_b$ in t. Since the period becomes small as $\epsilon \to 0$, we can think of Γ fixed, $\epsilon \to 0$ as the high-frequency limit. It can be also said that the parameter ϵ^2 measures the amplitude of the (almost harmonic) fluctuations in ϕ_j.

There are no secular terms in the lower order expansions, implying that we do not need to stretch the time coordinate at lower orders. We notice that $\omega_1 = \omega_2 = \omega_3 = 0$. At $O(\epsilon^5)$, a secular term arises for the first time, which is eliminated by choosing ω_4 appropriately: $\omega_4 = -1/2$.

4.2 Perturbation expansion for LRC load

When coupling is considered, the small parameter ϵ plays a double role; the solution ϕ_j can be approximated perturbatively, and the coupling becomes weak as $\epsilon \to 0$ since ϕ_j is almost linear in t. Because of this second role, one can still perturbatively obtain the solution of the *coupled* equations without much modification to the analysis above. The only crucial part is how to eliminate the new secular terms produced by the coupling. Some of them are j-dependent, and therefore cannot be eliminated simply by modulating the time T_0 further. We notice that it is sufficient to modulate the constant phase θ_j slowly. In this way, we obtain the slow-time equations for θ_j.

We first rescale time in Eq.(1) from t to $\tau = I_b t$ as before. The equation becomes

$$\begin{cases} \dfrac{d^2\phi_j}{d\tau^2} + \epsilon\Gamma\dfrac{d\phi_j}{d\tau} + \epsilon^2 \sin\phi_j + \epsilon\Gamma\dfrac{dQ}{d\tau} = \epsilon\Gamma\ , \quad j = 1,\dots,N, \\ L\dfrac{d^2Q}{d\tau^2} + \epsilon\dfrac{R}{\Gamma}\dfrac{dQ}{d\tau} + \epsilon^2\dfrac{Q}{C\Gamma^2} = \dfrac{\epsilon}{\Gamma N}\displaystyle\sum_{k=1}^{N}\dfrac{d\phi_k}{d\tau} \end{cases}$$

We further rescale the charge by

$$Q(\tau) = CI_b + \frac{q(\tau)}{\Gamma}\ .$$

The first term is a DC-component of Q which blows up as $\epsilon \to 0$. This happens because the DC-component of the driving term $\frac{1}{N}\sum\dot{\phi}_k$ increases without bound as $\epsilon \to 0$, and can only be balanced by the capacitive term on the left hand side.

By subtracting off this amount, the scaled remainder q behaves regularly as $\epsilon \to 0$. The equations are now

$$\begin{cases} \dfrac{d^2\phi_j}{d\tau^2} + \epsilon\Gamma\dfrac{d\phi_j}{d\tau} + \epsilon^2 \sin\phi_j + \epsilon\dfrac{dq}{d\tau} = \epsilon\Gamma \ , \quad j = 1, \ldots, N, \\ \dfrac{d^2q}{d\tau^2} + \epsilon a\dfrac{dq}{d\tau} + \epsilon^2 bq = \epsilon\dfrac{K}{N}\displaystyle\sum_{k=1}^{N}\left(\dfrac{d\phi_k}{d\tau} - 1\right) \end{cases} \tag{6}$$

where $a = R/(\Gamma L) = R\sqrt{\beta}/L$, $b = 1/(LC\Gamma^2) = \beta/(LC)$, $K = 1/L$.

A straightforward "naive" expansion breaks down, and thus we define the second slow time scale. The fast time scale T_0 is modulated at $O(\epsilon^4)$ as in the uncoupled equation, while the slow scale T_1 is found to be *much* slower than the first scale.

$$T_0 = \left(1 + \sum_{m=4}^{\infty} \epsilon^m \omega_m\right)\tau \quad , \ T_1 = \epsilon^5 T_0 \tag{7}$$

We pose the solution of the form similar to the uncoupled case.

$$\begin{cases} \phi_j(T_0, T_1; \epsilon) = \displaystyle\sum_{m=0}^{\infty} \epsilon^m y_{mj}(T_0, T_1) \ , \quad j = 1, \ldots, N, \\ q(T_0, T_1; \epsilon) = \displaystyle\sum_{m=0}^{\infty} \epsilon^m q_m(T_0, T_1) \end{cases} \tag{8}$$

We require y_{mj} and q_m to be bounded for all m and time except y_{0j}. As we go over the first few orders of expansion, we notice that $y_{1j} \equiv 0$, and $q_m \equiv 0$ for $m = 0, 1, 2$. Therefore, we start our analysis from the form:

$$\begin{cases} \phi_j(T_0, T_1; \epsilon) = y_{0j}(T_0, T_1) + \displaystyle\sum_{m=2}^{\infty} \epsilon^m y_{mj}(T_0, T_1) \ , \quad j = 1, \ldots, N, \\ q(T_0, T_1; \epsilon) = \displaystyle\sum_{m=3}^{\infty} \epsilon^m q_m(T_0, T_1) \end{cases} \tag{9}$$

The leading order term in ϕ_j is the same as in the uncoupled case except for the dependence of the phase on T_1:

$$y_{0j} = T_0 + \theta_{0j}(T_1) \quad , \ j = 1, \ldots, N. \tag{10}$$

The only nonlinear term is $\sin\phi_j$, which can be expanded in powers of ϵ after Eq.(9) is substituted:

$$\sin\phi_j = \sum_{m=0}^{\infty} \epsilon^m S_{mj} \tag{11}$$

where $S_{0j} = \sin y_{0j}$, $S_{1j} = 0$, $S_{2j} = y_{2j} \cos y_{0j}$, $S_{3j} = y_{3j} \cos y_{0j}$, $S_{4j} = y_{4j} \cos y_{0j} - (y_{2j}^2/2) \sin y_{0j}$, and so on.

Substitute these expansions into Eq.(6), and equate like powers of ϵ. At $O(1)$ and $O(\epsilon)$ the equations are trivially satisfied. At $O(\epsilon^2)$ we need to solve $\partial_0^2 y_{2j} + \sin(T_0 + \theta_{0j}) = 0$ for each j (where ∂_p is a shorthand notation for $\partial/\partial T_p$). Because y_{2j} is bounded in T_0 and T_1,

$$y_{2j} = \sin(T_0 + \theta_{0j}(T_1)) + \theta_{2j}(T_1) \ . \tag{12}$$

To the accuracy we seek the solution, modulation of θ_{2j} in T_1 is negligible, and the term can be absorbed into the initial condition of θ_{0j}. Thus, we set $\theta_{2j} = 0$.

The equation at $O(\epsilon^3)$ becomes

$$\begin{cases} \partial_0^2 y_{3j} + \Gamma \partial_0 \sin(T_0 + \theta_{0j}) = 0 \\ \partial_0^2 q_3 = \dfrac{K}{N} \displaystyle\sum_{k=1}^{N} \partial_0 \sin(T_0 + \theta_{0k}) \ . \end{cases} \tag{13}$$

Both y_{3j} and q_3 must be bounded. Thus,

$$y_{3j} = \Gamma \cos(T_0 + \theta_{0j}) + \theta_{3j} \quad , \ q_3 = c_3(T_1) - K R_1 \cos(T_0 + \Theta_1) \tag{14}$$

where $R_1(T_1)$ and $\Theta_1(T_1)$ are the amplitude and the phase of the slowly varying moment, defined in (3). We set $\theta_{3j} = 0$ for a similar reason as before, but another integration constant c_3 cannot be eliminated in such a way.

At $O(\epsilon^4)$ we obtain

$$\begin{cases} \partial_0^2 y_{4j} - \Gamma^2 \sin(T_0 + \theta_{0j}) + K R_1 \sin(T_0 + \Theta_1) + \dfrac{1}{2} \sin(2(T_0 + \theta_{0j})) = 0 \\ \partial_0^2 q_4 + a K R_1 \sin(T_0 + \Theta_1) = -\dfrac{\Gamma K}{N} \displaystyle\sum_{k=1}^{N} \sin(T_0 + \theta_{0k}) = -\Gamma K R_1 \sin(T_0 + \Theta_1) \ . \end{cases} \tag{15}$$

The solution is

$$\begin{cases} y_{4j} = -\Gamma^2 \sin(T_0 + \theta_{0j}) + \dfrac{1}{8} \sin(2(T_0 + \theta_{0j})) + K R_1 \sin(T_0 + \Theta_1) \\ q_4 = c_4(T_1) + (a + \Gamma) K R_1 \sin(T_0 + \Theta_1) \ . \end{cases} \tag{16}$$

At $O(\epsilon^5)$ we obtain

$$\begin{cases} \partial_0^2 y_{5j} - \Gamma^3 \cos(T_0 + \theta_{0j}) + K R_1 (a + 2\Gamma) \cos(T_0 + \Theta_1) \\ \qquad + \dfrac{3\Gamma}{4} \cos(2(T_0 + \theta_{0j})) + \Gamma(\omega_4 + \dfrac{1}{2}) = 0 \\ \partial_0^2 q_5 + d R_1 \cos(T_0 + \Theta_1) - \dfrac{K}{4} R_2 \cos(2(T_0 + \Theta_2)) + (b c_3 - K \omega_4) = 0 \ . \end{cases} \tag{17}$$

where $d = K\,[a(a+\Gamma) - b + \Gamma^2 - K]$. Here secular terms have appeared for the first time. We eliminate them by choosing

$$\omega_4 = -1/2 \quad , \; c_3 \equiv K\omega_4/b = -K/(2b) \ . \tag{18}$$

Then, y_{5j} and q_5 become periodic:

$$\left\{ \begin{array}{l} y_{5j} = -\Gamma^3 \cos(T_0 + \theta_{0j}) + KR_1(a + 2\Gamma)\cos(T_0 + \Theta_1) + \dfrac{3\Gamma}{16}\cos\left(2(T_0 + \theta_{0j})\right) \\ q_5 = c_5(T_1) + dR_1\cos(T_0 + \Theta_1) - \dfrac{K}{16}R_2\cos\left(2(T_0 + \Theta_2)\right) \ . \end{array} \right. \tag{19}$$

Finally, at $O(\epsilon^6)$, we obtain

$$\left\{ \begin{array}{l} \partial_0^2 y_{6j} + [\text{periodic terms in } T_0] + \dfrac{K}{2}R_1\sin(\Theta_1 - \theta_{0j}) + \Gamma(\omega_5 + \partial_1\theta_{0j}) = 0 \\ \partial_0^2 q_6 + [\text{periodic terms in } T_0] + \left[bc_4 - K\omega_5 - \dfrac{K}{N}\displaystyle\sum_{k=1}^{N}\partial_1\theta_{0k}\right] = 0 \ . \end{array} \right. \tag{20}$$

The solvability conditions are obtained by setting the non-periodic terms to zero. We may choose ω_5 arbitrarily since it can be compensated by changing θ_{0j} without affecting the solution. Thus, set $\omega_5 = 0$. Then, from the equation for y_{6j},

$$\partial_1\theta_{0j}(T_1) = -\frac{K}{2\Gamma}R_1\sin(\Theta_1 - \theta_{0j}) = -\frac{K}{2\Gamma}\cdot\frac{1}{N}\sum_{k=1}^{N}\sin(\theta_{0k} - \theta_{0j}) \tag{21}$$

for $j = 1, \ldots, N$. This is the leading order equation which governs the slow phase shift due to weak coupling of junctions. Secular terms in the equation for q_6 can be removed by

$$c_4 = \frac{K}{b}\cdot\frac{1}{N}\sum_{k=1}^{N}\partial_1\theta_{0k} = -\frac{K^2}{2\Gamma b}\cdot\frac{1}{N^2}\sum_{k=1}^{N}\sum_{\ell=1}^{N}\sin(\theta_{0\ell} - \theta_{0k}) \equiv 0 \ . \tag{22}$$

A system of equations similar to Eq.(21) has been derived in [Jai&al84] from a more informal argument, based on an assumption that current through the junctions $\dot{Q}$ is small. Compared to this approach, we have identified clearly what the small parameter is, and used systematic perturbation methods. The coefficient in the averaged system have been determined rigorously, which enables us to explain the numerical observations in Section 3, as shown below.

4.3 Floquet multipliers for LRC load

Equation (21) allows us to analytically predict a pair of Floquet multipliers around the splay state. From Eqs.(7), (10) and (21),

$$\frac{dy_{0j}}{dT_0} = 1 - \epsilon^5 \frac{K}{2\Gamma} \cdot \frac{1}{N} \sum_{k=1}^{N} \sin(\theta_{0k} - \theta_{0j}) = 1 - \epsilon^5 \frac{K}{2\Gamma} \cdot \frac{1}{N} \sum_{k=1}^{N} \sin(y_{0k} - y_{0j}) \quad . \tag{23}$$

Rewrite it as

$$\frac{dy_{0j}}{dT_0} = 1 + \frac{\kappa}{N} \sum_{k=1}^{N} \cos(y_{0k} - y_{0j} - \delta) \quad . \tag{24}$$

where

$$\kappa = \frac{\epsilon^5 K}{2\Gamma} = \frac{1}{2LI_b^5 \beta^2} \quad \text{and} \quad \delta = -\frac{\pi}{2} \quad . \tag{25}$$

Although this is a system for y_{0j}, not for ϕ_j, it is sufficient for the leading order estimate of Floquet multipliers. The splay state solution can be expressed as $\theta_{0j} = 2\pi j/N$, or $y_{0j} = T_0 + 2\pi j/N$. Equation (24) admits analytical evaluation of multipliers around the state since the Jacobian matrix is constant along the orbit [Ash&Swi92]. Thus, the Floquet exponents are simply eigenvalues of the matrix. In general, for a system of the form

$$\dot{\psi}_j = \Omega + \frac{\kappa}{N} \sum_{k=1}^{N} G(\psi_k - \psi_j) \quad , \; j = 1, \ldots, N \tag{26}$$

(where G is a 2π-periodic function), the in-phase solution has a Floquet exponent $\lambda = -\kappa G'(0)$ with multiplicity $N-1$, along with the zero exponent. The Floquet exponents around the splay state, $\psi_j = 2\pi j/N$, are

$$\lambda_p = \frac{\kappa}{N} \sum_{k=1}^{N} G'(2\pi k/N) \cdot ((e^{i2\pi/N})^{pk} - 1) \tag{27}$$

where p takes on N adjacent integer values [Ash&Swi92]. When $N = 4$ we can choose $p \in \{-1, 0, 1, 2\}$. The trivial exponent is $\lambda_0 = 1$, and the complex conjugate pair which determines stability of the splay state in directions transverse to the incoherent manifold is $\lambda_{\pm 1}$. The other $N - 3$ Floquet exponents correspond to perturbations within the incoherent manifold. (When $N = 4$, the real exponent λ_2 determines the stability of the phase within the incoherent bar.)

For Eq.(24), $G(\psi) = \cos(\psi - \delta)$, and the nontrivial Floquet exponents of the in-phase solution are $\lambda = -\kappa \sin\delta$. All the Floquet exponents of the splay-phase solution are 0 except

$$\lambda_{\pm 1} = \frac{\kappa}{2}(\sin\delta \mp i\cos\delta) \ . \tag{28}$$

Note that there is no bistability for Eq.(24): when $\kappa \sin\delta > 0$ the in-phase state is asymptotically stable and the splay state is unstable. When $\kappa \sin\delta < 0$ the in-phase state is unstable and the splay state is neutrally stable. When $\sin\delta = 0$, global analysis shows that the in-phase is unstable and the splay is neutrally stable [Wat&Str94].

For the splay state, all of the Floquet multipliers are 1, except $\mu_{\pm 1} = \exp(\lambda_{\pm 1} T)$, where $T = 2\pi/\Omega$ is the period. Substitution of Eq.(25) with $\Omega = 1$ yields

$$|\mu_{\pm 1}| = \exp\left[\pi\kappa\sin\delta\right] = \exp\left[-\frac{N\pi}{2I_b^5\beta^2 L}\right] \ . \tag{29}$$

Now, we replace y_{0j} by ϕ_j and T_0 by τ in Eq.(24). Since only (κ/Ω) — the ratio between the basic frequency and growth rate of perturbation — is important for the multipliers, the leading order estimate is unchanged. Similarly, recovering the dimensionless time t from τ does not affect Eq.(29), either. (The Floquet *exponents* are affected by scaling time, but not the Floquet *multipliers*.) Thus, two Floquet multipliers of the splay state of Eq.(1) should be well approximated by Eq.(29) as $\epsilon \to 0$.

The other Floquet multipliers of the splay solution are all 1 in the limit $\epsilon \to 0$, corresponding to neutral directions within the incoherent manifold. For $N = 4$, the single "critical" multiplier is unity in the asymptotic approximation. While the Floquet multipliers yield only local results, the global phase portrait of the averaged equation (24) has been completely analyzed [Wat&Str94]. It possesses the same degenerate structure (i.e. no drift on the incoherent manifold) as the original system Eq.(1) with $\beta = 0$. However, while the degeneracy is exact for the $\beta = 0$ case, it is only approximate for $\beta > 0$. Perhaps the slow drift on the incoherent manifold could be extracted from Eq.(1) when a higher order expansion is carried out. The drift would show up as higher harmonics in the coupling function of Eq.(24). Second moments R_2 and Θ_2 do appear in intermediate expressions;

see Eq.(19). However, we went to the next order in the expansion and found that the coupling function is still purely sinusoidal, i.e. there is no drift. It could be that there is no drift to all orders in ϵ, implying that the drift is exponentially small.

In the averaged equations (24), the degenerate phase space is foliated by invariant three-dimensional subspaces [Wat&Str94]. Each subspace is transversal to the incoherent manifold, thus is parametrized by the incoherent state it crosses. The in-phase state is connected to this incoherent state via the subspace. The flow in the subspace can be either toward the in-phase or to the incoherent state. The two nontrivial Floquet multipliers $\mu_{\pm 1}$ correspond to this dynamics (evaluated at the splay state). Therefore, they must be the complex conjugate pair in Fig. 6 whose magnitude is near unity. Fig. 7(a) shows comparison of the computed data in Fig. 6(a) with the formula (29). There is a good agreement. The error becomes less than 10^{-4} for $\beta > 2$ (or $\epsilon < 0.3$ since $I_b = 2.5$).

It is clear from Eq.(29) that , for small ϵ, the splay state is always stable in the directions transverse to the incoherent manifold. Conversely, we expect the in-phase state to become unstable as $\epsilon \to 0$. This agrees with previous computation of Floquet multipliers around the in-phase state [Had&al88].

4.4 Other loads

One notices that Eq.(29) does not involve R or C. When the shunt load involves L, it dominates the load when ϵ is sufficiently small (the high-frequency limit), and the in-phase state becomes always unstable. For RC or C loads, similar analysis to the previous sections can be carried out. We again obtain the same equation (24) as the modulation equation with the parameters:

$$\begin{array}{rlll} RC \text{ load:} & \kappa = 1/(2RI_b^3\beta^2) & \text{and} & \delta = \pi \\ C \text{ load:} & \kappa = C/[2I_b^2\beta(C+\beta)] & \text{and} & \delta = \pi/2 \end{array} . \qquad (30)$$

The in-phase state is stable (or unstable) when $\kappa \sin \delta > 0$ (or < 0, respectively). Therefore, for an RC load, the parameter values are marginal and indeterminate at this order. Complex attractors may easily arise for the original system (1).

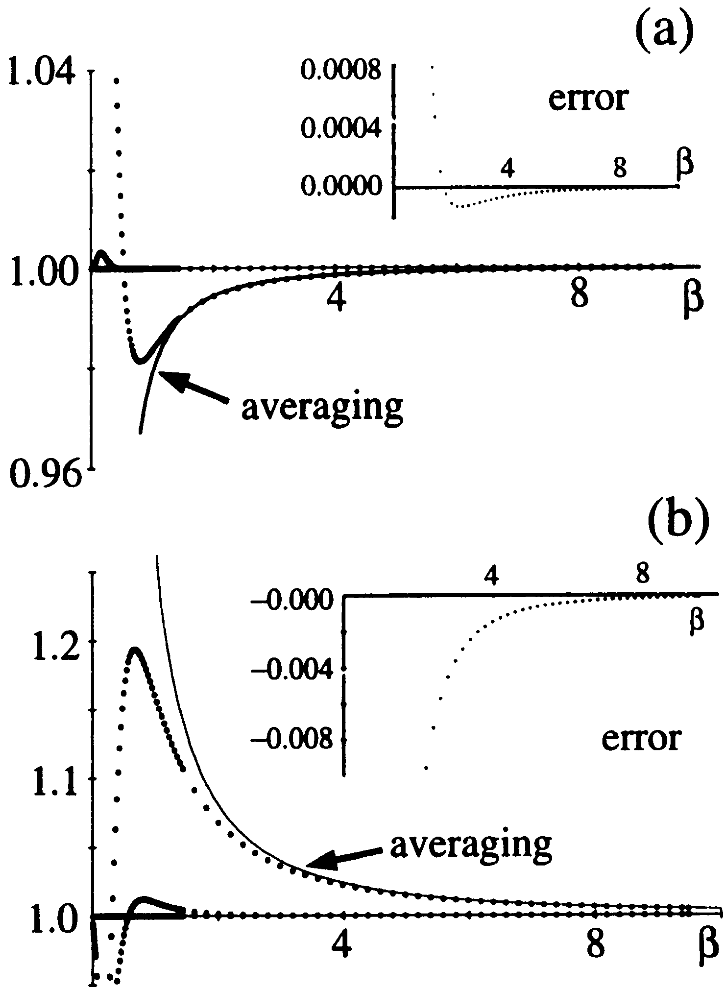

Figure 7: Magnitude of a complex conjugate pair of Floquet multipliers around the splay state as a function of β. Computation (dots; same as in Fig. 6 except scaling) and averaging theory (curve; see text) show an excellent agreement for large β. The error is shown in the insets. (a) LC load (case [NWII]), (b) C load (case [NWIII]).

On the other hand, the in-phase state is stabilized for small ϵ with a C load. The magnitude of the nontrivial Floquet multipliers around the splay state is always larger than unity:

$$|\mu_{\pm 1}| = \exp\left[+\frac{C\pi}{2I_b^2\beta(C+\beta)}\right] . \tag{31}$$

Fig. 7(b) compares this approximation with the computed complex conjugate pair near unity in Fig. 6(b). Good agreement is achieved for $\beta > 4$ ($\epsilon < 0.3$).

5 Discussion

Previous analytical studies of the stability of the in-phase and splay-phase states have assumed the overdamped limit $\beta = 0$. It is common knowledge [Jai&al84, Had&Bea87, Wie&Swi95] that the in-phase state is stable for inductive loads and unstable for capacitive loads. Our result with nonzero β is opposite: the in-phase state is unstable when L is included and stable for a purely capacitive load, provided $I_b\sqrt{\beta}$ is large enough. To resolve the paradox we did experiments with the LC-load considered in section 2, varying I_b and β. First we consider $\beta = 0$. For I_b greater than approximately 2.1, the in-phase state is stable. However, there is a bifurcation curve $\beta = f(I_b)$ which is asymptotic to $\beta = 0$ as $I_b \to \infty$. For $\beta < f(I_b)$ the in-phase state is stable, but for $\beta > f(I_b)$ the in-phase state is unstable and the splay solution is apparently neutrally stable. (There is no observed hysteresis.) For example, at $I_b = 4$, the in-phase state is stable for $0 \leq \beta < 0.25$, and the splay is neutrally stable for $\beta > 0.25$. Since $\beta = f(I_b)$ is asymptotic to $\beta = 0$ we have the two competing results: when $\beta = 0$ the in-phase is stable for I_b sufficiently large, while for $\beta > 0$ the in-phase is unstable for I_b sufficiently large! This singular behavior must be taken into account when one selects the load in applications in order to operate the series Josephson arrays in a desired state.

Singular behavior also occurs in the C-load system. Although the in-phase is unstable when $\beta = 0$, for any $\beta > 0$ the in-phase is stable for I_b sufficiently large. Bifurcation curves in the I_b–β plane which are asymptotic to $\beta = 0$ are seen in the results of numerical computation of the Floquet multipliers of the in-phase state in Fig. 2 of Hadley et al. [Had&al88].

In summary, we have shown that the apparent neutral stability of the splay-phase state over a wide range of parameters is only approximate when $\beta > 0$. When I_b and β are moderate, we can easily find asymptotically stable splay solutions for an LC or C-load. When $I_b\sqrt{\beta}$ is large, the averaged equations predict no drift on the incoherent manifold — which implies a neutrally stable splay state. This "explains" why the drift on the incoherent manifold is so slow as to be unobservable. It is understandable that previous researchers concluded that the splay solution is neutrally stable when $\beta > 0$, but this is now seen to be a red herring in "the mystery of the neutrally stable splay."

Acknowledgments

Authors thank Steve Strogatz and Kurt Wiesenfeld for helpful comments. JWS acknowledges support by an Organized Research Grant from NAU. SW is supported in part by NSF grants DMS-9057433 and DMS-9111497 through Steve Strogatz, and by the A.P. Sloan dissertation fellowship.

References

[Ash&Swi92] P. Ashwin and J.W. Swift, "The dynamics of n identical oscillators with symmetric coupling", *J. Nonlin. Sci.* **2**, 69–108 (1992).

[Ash&Swi93] P. Ashwin and J.W. Swift, "Unfolding the Torus: Oscillator Geometry from Time Delays", *J. Nonlin. Sci.* **3**, 459–475 (1993).

[Ben&Bur91] S.P. Benz and C.J. Burroughs, "Two-dimensional arrays of Josephson junctions as voltage-tunable oscillators", *Supercond. Sci. Tech.* **4**, 561–567 (1991).

[Doe&Ker86] E.J. Doedel and J.P. Kernévez, "Auto: Software for continuation and bifurcation problems in ordinary differential equations", Appl.Math.Rep., California Institute of Technology, (1986).

[Had&Bea87] P. Hadley and M.R. Beasley, "Dynamical states and stability of linear arrays of Josephson junctions", *J. Appl. Phys.* **50**, no.10, 621–623 (1987).

[Had&al88] P. Hadley, M.R. Beasley, and K. Wiesenfeld, "Phase locking of Josephson-junction series arrays", *Phys. Rev. B* **38**, no.13, 8712–8719 (1988).

[Jai&al84] A.K. Jain, K.K. Likharev, J.E. Lukens and J.E. Sauvageau, "Mutual Phase-Locking in Josephson Junction Arrays", Phys. Rep. **109**, 310–426 (1984).

[Kau&al87] R.L. Kautz, C. A. Hamilton, and F. L. Lloyd, "Series-array Josephson voltage standards", IEEE Transactions on Magnetics, **23**, 883–890 (1987).

[Kur84] Y. Kuramoto, *Chemical oscillations, waves, and turbulence*, Springer-Verlag, Berlin (1984).

[McC88] Technical review of Josephson junctions and arrays can be found in *Physica* **B 152**, 1–302 (1988).

[Lev&al78] M. Levi, F.C. Hoppensteadt, and W.L. Miranker, "Dynamics of the Josephson junction", *Quart. Appl. Math.*, July, 167–198 (1978).

[Lik86] K. K. Likharev, *Dynamics of Josephson junctions and circuits*, Gordon and Breach, New York (1986).

[Nic&Wie92] S. Nichols and K. Wiesenfeld, "Ubiquitous neutral stability of splay-phase states", *Phys. Rev. A* **45**, no. 12, 8430–8435 (1992).

[Pey&Kru84] M. Peyrard and M.D. Kruskal, "Kink dynamics in the highly discrete sine-Gordon system", *Physica* **14D**, 88–102 (1984).

[Ots91] K. Otsuka, "Winner-takes-all dynamics and antiphase states in modulated multimode lasers", *Phys. Rev. Lett.* **67**, no. 9, 1090–1093 (1991).

[Sch&Tsa94] I.B. Schwartz and K.Y. Tsang, "Antiphase switching in Josephson junction arrays", *Phys. Rev. Lett.* **73**, no.21, 2797–2800 (1994).

[Str&Mir92] S.H. Strogatz and R.E. Mirollo, "Stability of incoherence in a population of coupled oscillators", *J. Stat. Phys.* **63**, no. 3/4, 613-635, 1991.

[Str&Mir93] S.H. Strogatz and R.E. Mirollo, "Splay states in globally coupled Josephson arrays: Analytical prediction of Floquet multipliers", *Phys. Rev. E* **47**, no. 1, 220-227, 1993.

[Swi&al92] J.W. Swift, S.H. Strogatz, and K. Wiesenfeld, "Averaging of globally coupled oscillators", *Physica* **D 55**, 239-250 (1992).

[Ter&Bea94] E. Terzioglu and M.R. Beasley, "Series Josephson junction arrays as a high output voltage amplifiers", submitted to *Proc. Appl. Supercond. Conf.*, (1994).

[Tsa&al91] K.Y. Tsang, R.E. Mirollo, S.H.Strogatz, and K. Wiesenfeld, "Dynamics of a globally coupled oscillator array", *Physica* **D 48**, 102-112 (1991).

[Tsa&Sch92] K.Y. Tsang and I.B. Schwartz, "Interhyperhedral diffusion in Josephson-junction arrays", *Phys. Rev. Lett.* **68**, no.15, 2265-2268 (1992).

[vdZ&al94] H.S.J. van der Zant, T.P. Orlando, S. Watanabe, and S.H. Strogatz, "Vortices trapped in discrete Josephson rings", *Physica* **B 203**, 490-496 (1994).

[Wat&Str94] S. Watanabe and S.H. Strogatz, "Constants of motion for superconducting Josephson arrays", *Physica* **D 74**, 197-253 (1994).

[Wat&al95] S. Watanabe, S.H. Strogatz, H.S.J. van der Zant, T.P. Orlando, "Whirling modes and parametric instabilities in the discrete sine-Gordon equation: experimental tests in Josephson rings", *Phys. Rev. Lett.* **74**, no.3, 379-382 (1995).

[Wie&Swi95] K. Wiesenfeld and J.W. Swift, "Averaged equations for Josephson junction series arrays", to appear in *Phys. Rev. E*, (1995).

Chapter 3

Dynamics of circular Josephson junction arrays and the discrete sine-Gordon equation

Shinya Watanabe, Steven H. Strogatz,
Herre S.J. van der Zant, and Terry P. Orlando

Dynamics of circular Josephson junction arrays and the discrete sine-Gordon equation

Shinya Watanabe and Steven H. Strogatz*
Department of Mathematics,
Massachusetts Institute of Technology,
Cambridge, Massachusetts 02139

Herre S. J. van der Zant† and Terry P. Orlando
Department of Electrical Engineering and Computer Science,
Massachusetts Institute of Technology,
Cambridge, Massachusetts 02139

May 9, 1995

Abstract

We study the damped driven discrete sine-Gordon equation with a periodic boundary condition as a model of a circular array of N Josephson junctions connected in parallel. The system traps an integer number of kinks, and supports two branches of traveling wave solutions, distinguished by the frequencies.

In the low-frequency region, a propagating kink induces radiation that phase-locks to the kink. The kink, then, tends to propagate at a set of certain velocities corresponding to the wave number of radiation. Unexpectedly, the wave numbers outside the first Brillouin zone are physically relevant, due to the nonlinearity of the system.

In the high-frequency region, the traveling wave solutions are spatially and temporally uniform. We show that these "whirling periodic solutions" undergo parametric instabilities at certain drive strength. We analyze the onset of the instabilities, then numerically study the secondary bifurcations and complex spatiotemporal behaviors that occur past the onset.

The dynamics of the phase-locking and the parametric instabilities in the two regions is reflected as "resonant steps" in the current-voltage characteristics of the Josephson ring. We measure a ring of $N = 8$ underdamped junctions; the observed voltage locations of these steps are in good agreement with the predictions.

1 Introduction

For decades, the dynamics of one-dimensional (1D) long continuous Josephson junctions have been studied [Lik86] because of their possible applications in superconducting electronics. For example, Josephson flux-flow oscillators operate in the millimeter and sub-millimeter wave range (order of a terahertz) and, when operated under resonant conditions, they can achieve very narrow linewidths [Ust&al91]. The long continuous junctions are well modelled by the perturbed sine-Gordon equation. Therefore, interest in the junctions has been fueled also by the mathematical aspect [McL&Sco78, Kiv&Mal89]. From their point of view, the junctions are an ideally controlled laboratory to test the theory of nonlinear dynamics and wave propagation, for example, interactions of sine-Gordon kinks and antikinks.

One-dimensional parallel arrays consisting of small-area Josephson junctions can be viewed as discrete versions of long continuous junction. Technologically, the discrete arrays have advantages over continuous junctions in that the output impedance and frequencies can be higher [Ust&al95]. Mathematically, they provide a framework to study the relation between discrete and continuous systems. A single junction is a phase oscillator analogous to a mechanical pendulum. Parallel arrays of N junctions are equivalent to systems of N pendula coupled to their neighbors by diffusive interactions [Sco69, Nak&al74, Cir&al81].

The dynamics of such 1D discrete arrays has not been investigated in detail. Compared to the integrable conservative sine-Gordon equation, the effects of discreteness and damping destroy the integrability, and the phase space becomes highly complex. Currently, there is a growing interest in such non-integrable lattices obtained from completely integrable partial differential equations [Dun&al83]. Although exact solutions are almost never expected in these "perturbed" problems, solitons may still survive.

Regardless of whether the governing equations are perturbed or not, boundary conditions are important in the sine-Gordon systems. An infinite domain is mathematically simple, but has less connections to applications. For finite continuous Josephson junctions, both open-ended [Cos&al78, Pac&al81] and annular [Dav&al83, Ust&al92] geometries have been studied. The annular junctions lead to periodic boundary conditions, which avoid complications caused by the reflection of kinks at the boundaries. Moreover, the circular geometry "traps" an integer number of kinks in a ring, which makes it possible to study the dynamics of a single isolated kink.

In this paper, we present a systematic study of a 1D discrete array of N underdamped Josephson junctions in a circular geometry. As a discrete counterpart of the annular long junctions, such an array still traps an integer number of kinks. However, the kinks are affected by the lattice structure, and the geometry is extremely useful to isolate the discreteness effects from the boundary effects. We study the dynamics of the array by analytical, experimental, and numerical methods. The theoretical results are interpreted in terms of the current-voltage (I-V) characteristics, and tested against experimental measurements on arrays of $N = 8$ Josephson junctions.

The paper is organized as follows. In Section 2, we first derive the discrete damped driven sine-Gordon equation as the model equation of the circuit, then review the properties expected of the I–V curve if the system were approximated by the continuous dissipative sine-Gordon equation. The I–V curve depends on the number M of trapped kinks, and for $M = 1$, the system supports a traveling wave in the form of a single kink. The traveling wave solutions trace out two distinct branches on the I–V characteristic, and the waveforms on these branches are quite different. This distinction between the two branches will be a key to the analysis in the later sections.

In Section 3, we explain our experiments, including a description of how to vary parameters in the system. We also show a typical I–V for different M values, and use that result to determine the last free parameter in the system.

Our junctions become highly underdamped and discrete as the temperature is decreased. Then, novel structures show up in the experimental I–V characteristic. These structures are many "steps," almost vertical segments in the I–V where V is nearly constant over a range of I. In Section 4, we classify these steps into two types. We show numerical evidence that, even in a discrete ring, soliton solutions of the continuous equations still survive as traveling waves. However, the waveforms as well as the I–V characteristics can be significantly altered. In Sec.4.2 we will see the effect of discreteness in the waveform. In Sec.4.3 branches of traveling waves for the discrete system are found by numerical continuation methods on the I–V characteristics. These sections reveal that there are two types of mechanisms that generate the steps.

The first type of step, in the low-voltage region, is explained in Section 5. Because of the discrete lattice structure, a small amplitude wave is radiated in the wake of a moving kink, and the wave and the kink phase-lock to form a traveling wave. A formula obtained from the phase-locking condition is tested experimentally, and shows good agreement with the data. The formula predicts that it is possible to distinguish the lattice eigenmode m from $m+N$ in a discrete array of N oscillators. We will explain the origin of this non-intuitive observation in Sec.5.3.

The second type of step, in the high-voltage region, is analyzed in Section 6. We linearize the nonlinear system around a simple basic state, and perform a linear stability analysis. In sections 6.1–6.3, we derive the voltage locations of the steps in this region, and test the predictions against experiments. The analysis is extended to arrays with free boundaries in Sec.6.4–6.5.

The analysis in Section 6 is restricted to the neighborhood of the first bifurcation from the assumed basic state. The dynamics becomes highly nonlinear along a step further away from the branching points. We investigate this nonlinear dynamics by numerical methods in Section 7. Various secondary bifurcations occur as we move up the step, leading to increasingly complex spatiotemporal dynamics, although it appears that the dynamics becomes restabilized once the amplitude of oscillation becomes large enough.

Finally, Section 8 is a summary, and also states several future directions.

2 Model of Josephson rings

Figure 2.1(a) shows a schematic drawing of our discrete Josephson ring with $N = 8$ junctions. The experimental apparatus consists of an outer ring and an inner island, both of which are made of niobium, a superconducting material. The two rings do not touch each other except at eight places of area 2 μm^2 where the two superconducting layers are separated by a thin ($\sim$ 10 Å) Al_2O_x oxide barrier. At these eight places tunnel Josephson junctions are formed, and they are denoted by their standard circuit symbol, crosses. The same amount of bias current is injected from 8 probes. They distribute within the rim, go through one of the junctions, and are then extracted from the probe attached to the inner island. The voltage is measured between the two superconductors at $V+$ and $V-$.

This section is a preliminary study of the Josephson ring. We first derive the model equations for the array in Sec. 2.1. In Sec. 2.2 we approximate the model by the continuum limit and find traveling wave solutions. This simple study reveals two distinct branches of periodic solutions, and serves as a good starting point to approach more difficult discrete equations.

2.1 Model equations

In Fig. 2.1(b), the cells $j-1$ through $j+1$ are shown schematically. The two horizontal lines represent the outer and inner superconductors. Superconducting wires can be viewed as inductors, and support dynamic voltage drops; the horizontal currents through these inductors are denoted as I_j^{top} (upper) and I_j^{bot} (lower). The bias current I_j^{in} is injected from the top of the junction j, and I_j^{out} is extracted from below.

The state of a junction j is described by its phase difference $\phi_j(t)$. The voltage drop across the junction is then given by the Josephson voltage-phase relation:

$$V_j = \frac{\Phi_0}{2\pi}\dot{\phi}_j \tag{2.1}$$

where $\Phi_0 = h/(2e)$ is the flux quantum, h is the Planck's constant, and e is the charge of an electron.

A single junction is well described by the RCSJ (resistively and capacitively shunted junction) model [Orl&Del91]. In this model the junction consists of a capacitive, a resistive, and a superconducting branch, all connected in parallel. For this model, Kirchhoff's current law at the top and the bottom nodes of the

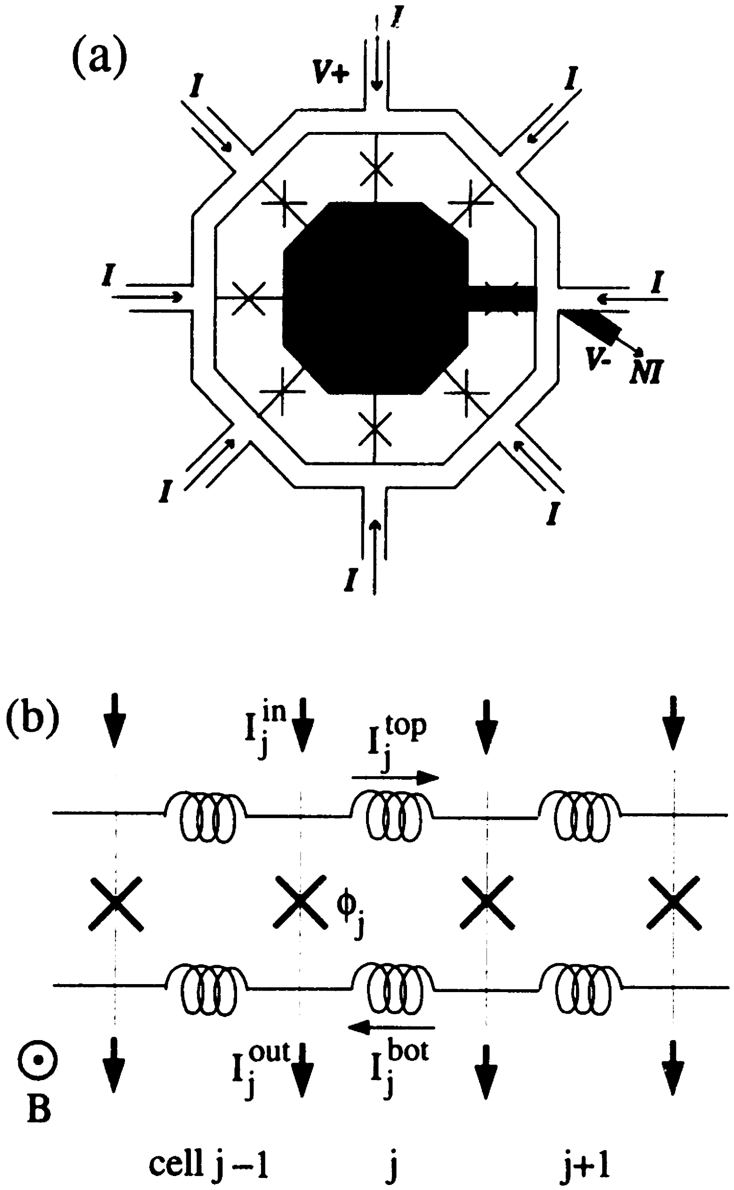

Fig. 2.1 (a) Schematic drawing of a discrete ring of $N = 8$ Josephson junctions. (b) Three cells in the array.

junction j reads:

$$C\dot{V}_j + V_j/R + I_c \sin\phi_j = I_j^{\rm in} - I_j^{\rm top} + I_{j-1}^{\rm top} = I_j^{\rm out} - I_j^{\rm bot} + I_{j-1}^{\rm bot} \qquad (2.2)$$

where C and R are the internal capacitance and resistance of a junction, respectively, and I_c is the critical current. We have assumed that the junctions are fabricated to be uniform in all their properties.

A third equation comes from the nature of *phases* in the superconducting state; a line integral of the phase differences around a closed loop on a superconductor must equal the magnetic flux enclosed by the loop [Orl&Del91]. For a loop around cell j, this requires

$$\phi_{j+1} - \phi_j = 2\pi\Phi_j/\Phi_0 \qquad (2.3)$$

where Φ_j is the total flux penetrating the cell. (The dependence on the magnetic field comes from requiring the ϕ's to be gauge-invariant [Orl&Del91].) In our experiment, we impose a uniform external field $\Phi^{\rm ext}$ perpendicular to the array. There is also a contribution of an induced field. We only take into account of the contribution of the horizontal currents into the adjacent cell. The effect of longer range inductances has been studied and found to be negligible. (See Sec.2.3.) Then,

$$\Phi_j = \Phi^{\rm ext} - (L_1 I_j^{\rm top} + L_2 I_j^{\rm bot}) \qquad (2.4)$$

where L_1, L_2 are the top and bottom inductances, respectively.

Eliminate V_j, $I_j^{\rm top}$, and $I_j^{\rm bot}$ from Eqs.(2.1–2.4) to obtain

$$\frac{1}{\omega_p^2}\ddot{\phi}_j + \frac{\Gamma}{\omega_p}\dot{\phi}_j + \sin\phi_j = \frac{I_j}{I_c} + \Lambda^2(\phi_{j+1} - 2\phi_j + \phi_{j-1}) \quad , \; j = 1, \ldots, N \qquad (2.5)$$

where

$$\omega_p^2 = 2\pi I_c/(\Phi_0 C) \quad , \quad \Gamma/\omega_p = \Phi_0/(2\pi I_c R) \quad , \quad \Lambda^2 = \Phi_0/(2\pi I_c L) \; , \qquad (2.6)$$

and

$$I_j = (L_1 I_j^{\rm in} + L_2 I_j^{\rm out})/L \quad , \qquad (2.7)$$

where $L = L_1 + L_2$. It is more customary to write these equations in terms of the following parameters:

$$L_J = \Phi_0/(2\pi I_c) \qquad \text{(the Josephson inductance)} \qquad (2.8)$$

and

$$\beta = 2\pi I_c C R^2/\Phi_0 \qquad \text{(the dimensionless Stewart-McCumber parameter)} \; . \qquad (2.9)$$

Then,

$$\omega_p = 1/\sqrt{L_J C} \quad , \quad \Lambda^2 = L_J/L \quad , \quad \Gamma = 1/\sqrt{\beta} \, . \tag{2.10}$$

Here ω_p is called the "plasma frequency" of a Josephson junction, and is the resonance frequency of the internal capacitance and the Josephson inductance of a junction.

By assumption, we inject and extract dc currents uniformly, so I_j is independent of j. After rescaling time by $1/\omega_p$, the governing equations become:

$$\ddot{\phi}_j + \Gamma\dot{\phi}_j + \sin\phi_j = I/I_c + \Lambda^2\nabla^2\phi_j \quad , \quad j = 1, \ldots, N \tag{2.11}$$

where $\nabla^2\phi_j = (\phi_{j+1} - 2\phi_j + \phi_{j-1})$ is the nearest neighbor diffusive coupling term. These equations can be viewed as a discretized version of the damped driven sine-Gordon equation.

A useful *mechanical analog* is a chain of N pendula ($\ddot{\phi}_j + \sin\phi_j$), each of which is viscously damped ($\Gamma\dot{\phi}_j$), driven by a constant torque (I/I_c), and coupled to its nearest neighbors by torsional springs ($\Lambda^2\nabla^2\phi_j$). The parameter Γ is the damping factor while Λ^2 measures the spring constant. It is also a measure of discreteness; when $\Lambda^2 \gg 1$, the solutions are expected to be approximated well by the continuum approximation, but as Λ^2 becomes small, the discrete nature of the equations show up. (See Sections 3 and 4.)

We now consider the boundary conditions for our ring. The circular geometry imposes a periodic boundary condition, but there is an arbitrariness by an integer multiple of 2π since ϕ_j are angle variables:

$$\phi_{j+N}(t) = \phi_j(t) + 2\pi M \qquad \text{for all } j \text{ and } t \tag{2.12}$$

where the winding number M is an integer. Each 2π twist in the phase can be regarded as one kink, thus M denotes the total number of kinks in the ring. The number M is given as a parameter, and is held *fixed* for all t. That is, M kinks are "trapped" in the ring, and the number stays invariant under the dynamics.

A kink is also called a vortex, a topological charge, or a fluxon. The last name comes from the relation between the phase and the magnetic flux. From Eq.(2.3,2.12), we obtain

$$M = (\phi_{N+1} - \phi_1)/(2\pi) = \left(\sum_{j=1}^{N} \Phi_j\right) / \Phi_0 \, , \tag{2.13}$$

meaning that the total flux through the array must be quantized in the unit of the flux quantum, and M denotes the ratio.

Equations (2.11,2.12) constitute our *model system.* There are symmetries in the system which can be seen by defining another set of angles

$$\psi_j = \phi_j + 2\pi Mj/N \tag{2.14}$$

which eliminates the M-dependence of the boundary condition. The governing equations Eq.(2.11) remain unchanged except the sinusoidal nonlinearity term, $\sin\phi_j = \sin(\psi_j - 2\pi Mj/N)$. Clearly, the system remains invariant under the change of the parameter $M \to M + N$ since this term is kept the same. Moreover, it can also be shown that, if there is a solution $\{\psi_j(t)\}$ for the system with $M = M_0$, then there is a corresponding solution $\{\psi_{N-j}(t)\}$ for the system with $M = -M_0$. Spatial structure of these solutions are just mirror images, and especially when we look at the spatially averaged quantities, these two solutions are indistinguishable. Due to these symmetries, the number of kinks can be restricted to $M = 0, \ldots, \text{floor}[N/2]$ without loss of generality.

Although we will mainly deal with the circular arrays in this paper, we extend our analysis in Section 6 to an array with open ends. In this case, the governing equations Eq.(2.11) remain the same for $j = 2, \ldots, N-1$. To keep the form of the equations identical at the endpoints $j = 1$ and N, we define artificial phases ϕ_0 and ϕ_{N+1} and the boundary conditions:

$$\phi_0(t) = \phi_1(t) - 2\pi f \quad , \quad \phi_{N+1}(t) = \phi_N(t) + 2\pi f \ . \tag{2.15}$$

The parameter $f = \Phi^{\text{ext}}/\Phi_0$ (called "frustration") is in a sense analogous to M/N for the ring, but can take all real values. From symmetry, it can be restricted to $0 \le f \le 1/2$.

We close this section by introducing a characteristic voltage. Under the above non-dimensionalization and scaling of time, the voltage-phase relation Eq.(2.1) becomes:

$$V_j = \frac{\Phi_0\omega_p}{2\pi}\dot{\phi}_j = V_0\dot{\phi}_j/\Lambda \tag{2.16}$$

where $V_0 = \Phi_0\omega_0/(2\pi)$ and $\omega_0 = 1/\sqrt{LC}$. This frequency ω_0 is the frequency of an electromagnetic wave propagating in the array when it is approximated as an LC-transmission line. When the system converges to a periodic attractor of frequency ω, for example, then

$$V = V_0\omega/\Lambda \tag{2.17}$$

is the measurable voltage, averaged in space and time.

2.2 Continuum approximation

Continuous sine-Gordon equations are better studied than the discrete counterpart, even when damped and driven [McL&Sco78, Mar&Imr80, Mag80, Bur&Lif83, Mag83]. It is natural to study the discrete problem by perturbing off of the continuous approximation. Although the I-V characteristic derived from this approximation is significantly altered in the discrete system (as we will discuss in later sections), it is still useful to review this case before we discuss the discrete model. In particular, this simple analysis reveals two distinct branches in the I-V characteristics, and solutions in the two branches are qualitatively different. We emphasize this difference because it will become a crucial point for our studies of the discrete arrays.

An obvious way to take a continuum limit is to change the spatial coordinate j to a continuous variable $x = j/N$, and to approximate the coupling term of Eq.(2.11) by the spatial derivatives:

$$\nabla^2\phi_j(t) \to \phi(x+1/N,t) - 2\phi(x,t) + \phi(x-1/N,t) = \frac{1}{N^2}\phi_{xx}(x,t) + \dots \quad (2.18)$$

If we retain only the second derivative, then the discrete equations Eq.(2.11) are approximated by the continuous damped driven sine-Gordon equation:

$$\phi_{tt} + \Gamma\phi_t + \sin\phi = I/I_c + \lambda^2\phi_{xx} \quad , \quad x \in [0,1] \quad (2.19)$$

where $\lambda = \Lambda/N$, with boundary conditions

$$\phi(x+1,t) = \phi(x,t) + 2\pi M \quad , \quad \phi_x(x+1,t) = \phi_x(x,t) \qquad \text{for all } x,\, t. \quad (2.20)$$

Such a system also arises as the model equations for an annular long (continuous) Josephson junction when the surface damping (the term proportional to ϕ_{xxt}) is negligible.

Conservative sine-Gordon equations (i.e., with $\Gamma = I = 0$) in a periodic domain support kink (soliton) solutions. Even in the presence of the damping and the drive, similar traveling waveforms can exist [Mag80, Bur&Lif83] and, in this case, can become an attractor. To see the existence, let us seek traveling wave solutions for the system (2.19,2.20) of the form

$$\phi(x,t) = h(\xi) \quad , \quad \xi = x + ut \quad (2.21)$$

for a constant u, where u is to be determined as part of the solution. This reduces to finding a solution of an ordinary differential equation

$$(u^2 - \lambda^2)h''(\xi) + u\Gamma h'(\xi) + \sin h(\xi) = I/I_c \quad (2.22)$$

with the boundary condition

$$h(\xi+1) = h(\xi) + 2\pi M \qquad \text{for all } \xi. \tag{2.23}$$

Equation (2.22) is the equation for a *single* driven damped pendulum, with an effective mass $(u^2 - \lambda^2)$ and a damping factor $u\Gamma$.

Consider first when $u > \lambda$. By scaling the independent variable as $\xi = \sqrt{u^2-\lambda^2}\eta$, Eq.(2.22) takes the "standard form" for the single pendulum equation:

$$\frac{d^2h}{d\eta^2} + \alpha\frac{dh}{d\eta} + \sin h = I/I_c \tag{2.24}$$

with

$$\alpha = \Gamma/\sqrt{1-(\lambda/u)^2}\ . \tag{2.25}$$

This system has been well documented, e.g. in [Bur&Lif83, Str94], and we quickly review results necessary for our purpose. It is an autonomous second order system, and its phase space is a cylinder: $h \in [0, 2\pi]$ and $dh/d\eta \in (-\infty, \infty)$. (We identify $h = 0$ with $h = 2\pi$.) For a given α, a unique (running) periodic attractor exists for sufficiently large I. As I is decreased, the attractor disappears either by a homoclinic (when $0 < \alpha < \alpha^*$) or by a saddle-node infinite-period ($\alpha > \alpha^*$) bifurcation, where $\alpha^* \approx 1.2$ is a constant. We denote this critical current value by $I = I^*(\alpha)$. It is known that $I^* \to 0$ ($I^*/\alpha I_c \to 4/\pi$) as $\alpha \to 0$, $I^* \to 1$ as $\alpha \to \alpha^*$ from below, and $I^* = 1$ for $\alpha \geq \alpha^*$. For the parameter region $\alpha < \alpha^*$ and $I^* < I < 1$, the periodic attractor coexists with two fixed points, one attracting and another being a saddle point.

The periodic attractor satisfies

$$h(\eta + T_{\mathrm{SP}}) = h(\eta) + 2\pi \qquad \text{for all } \eta, \tag{2.26}$$

where $T_{\mathrm{SP}}(\alpha, I)$ is the period of the "single pendulum" periodic solution. The boundary condition Eq.(2.23) can be satisfied only on this attractor. Then, the fundamental period of Eq.(2.23) must be $1/M$. The period is related to T_{SP} by the scaling:

$$1/M = \sqrt{u^2-\lambda^2}\,T_{\mathrm{SP}}(\alpha, I)\ . \tag{2.27}$$

From Eqs.(2.25,2.27), we obtain

$$\begin{aligned} u &= \lambda\left[1-(\Gamma/\alpha)^2\right]^{-1/2}, & (2.28)\\ T_{\mathrm{SP}}(\alpha, I) &= \sqrt{\alpha^2-\Gamma^2}/(M\Gamma\lambda)\ . & (2.29) \end{aligned}$$

Now treat α as a free parameter. Then, Eq.(2.29) implicitly determines $I(\alpha)$. Since the phase ϕ (or h) changes by $2\pi M$ over the period 1 in ξ, or $1/u$ in t, the average frequency is

$$\omega = 2\pi M/(1/u) = 2\pi Mu \ , \tag{2.30}$$

which can be converted to the averaged voltage by Eq.(2.17) to approximate the voltage for the discrete system. In this way, the I–V curve is traced out as α is varied.

The valid range of α is (Γ, ∞). As $\alpha \to \infty$, the other variables tend to the limits $u \to \lambda$, $T_{\mathrm{SP}} \to \infty$, $\omega \to 2\pi M\lambda \equiv \omega_\ell$, $V \to 2\pi MV_0/N \equiv V_\ell$, and $I \to [I + (\Gamma\omega_\ell)^2]^{1/2} \equiv I_\ell$. In the opposite limit of $\alpha \to \Gamma$, they tend to the limits $u \to \infty$, $T_{\mathrm{SP}} \to 0$, $\omega \to \infty$, $V \to \infty$, and $I \to \Gamma\omega$. This latter limit is simply the Ohmic line where voltage is proportional to current.

When $u < \lambda$, there is another branch of traveling wave solutions. We convert the variables in Eq.(2.22) by

$$\xi = -\sqrt{\lambda^2 - u^2}\eta \ , \quad h = \pi - g \ . \tag{2.31}$$

Then, the equation becomes the standard form again:

$$\frac{d^2g}{d\eta^2} + \alpha\frac{dg}{d\eta} + \sin g = I/I_c \tag{2.32}$$

with

$$\alpha = \Gamma/\sqrt{(\lambda/u)^2 - 1} \ , \quad \text{or} \quad , \quad u = \lambda\left[1 + (\Gamma/\alpha)^2\right]^{-1/2} \ . \tag{2.33}$$

Equation (2.30) is now changed to

$$T_{\mathrm{SP}}(\alpha, I) = \sqrt{\alpha^2 + \Gamma^2}/(M\Gamma\lambda) \ . \tag{2.34}$$

The parameter α now runs from 0 to ∞, and Eqs.(2.33,2.34) draws another branch of the I–V curve.

As $\alpha \to \infty$, we find $u \to \lambda$, $T_{\mathrm{SP}} \to \infty$, $\omega \to \omega_\ell$, $V \to V_\ell$ (from below), and $I \to I_\ell$. Thus, the two branches coincide at $(I, V) = (I_\ell, V_\ell)$. As $\alpha \to 0$, we obtain $u \to 0$, $T_{\mathrm{SP}} \to \infty$, $\omega \to 0$, $V \to 0$, and $I \to 0$.

Equations (2.28,2.29,2.33,2.34) are numerically solved by a squeezing algorithm. The two branches of the resulting I–V characteristic are shown in Fig. 2.2. The parameters $M = 1$, $N = 4$, $\Lambda = 1$ (thus, $\lambda = 0.25$), and $\Gamma = 0.1$ are used (in order to make a comparison with a direct integration of the discrete system in Sec. 4.2 which uses these values). The first branch (corresponding to $u > \lambda$)

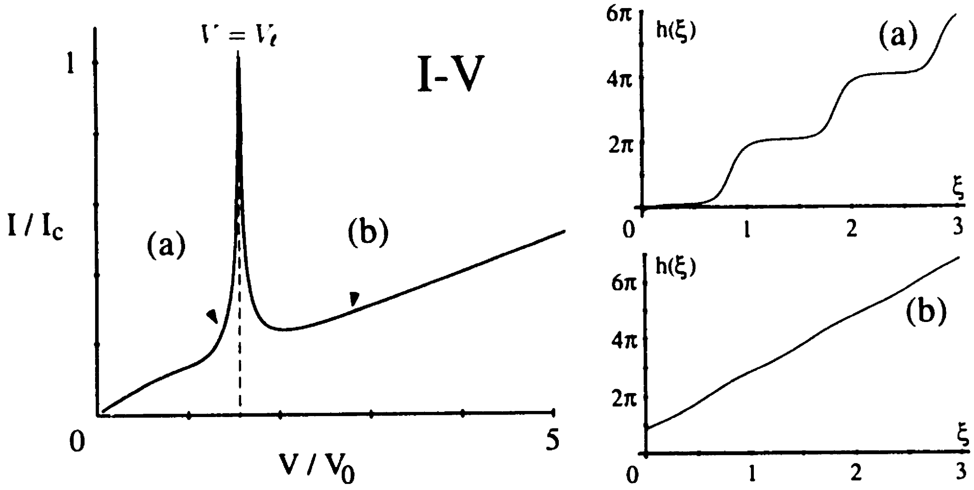

Fig. 2.2 A branch of traveling wave solutions for the continuous system (2.19,2.20), shown in terms of an I–V characteristic. One kink ($M = 1$) is trapped in a ring, with the parameters $\Gamma = 0.1$, $N = 4$, $\Lambda = 1$, thus $\lambda = \Lambda/N = 0.25$. (The parameters are the same as those to be used in Fig. 4.2 later.) A sharp peak at $V = V_\ell$ separates the low- and the high-voltage regions. One waveform is shown from each region. (a) the low-voltage region in which a kink maintains its characteristic shape, (b) the high-voltage region in which it is "stretched" over the ring.

appears in the region $V > V_\ell$ while the second one ($u < \lambda$) in $0 < V < V_\ell$. We call these two regions the ***high-voltage*** and the ***low-voltage*** regions from now on. For $M = 0$, the critical voltage $V_\ell = 0$, thus there is no low-voltage region exists but only the high-voltage one does.

The calculation does not determine the stability of the solutions. It has been shown that the low-V region is entirely stable and that the negative resistance (slope) part of the high-V region is unstable [Mag80, Bur&Lif83]. The stability of the positive resistance part in the high-V region, which one might expect to be stable, is subtle. Detailed analysis [Mag80, Bur&Lif83, Mag83] has been made only for the case $M = 0$. Burkov and Lifsic showed [Bur&Lif83] that the part of the I–V curve is unstable for all $I < I_c$. However, the analysis assumes an infinite domain, so does [Mag80]. In the periodic domain Maginu [Mag83] showed that the branch is mostly stable, including when $I < I_c$, but can be occasionally destabilized. We will come back to this point in Section 6.

In Fig. 2.2 we also show computed traveling waveforms $h(\xi)$ at two points marked (a) and (b) in the I–V curve with a positive slope. Three periods $\xi \in [0, 3]$

are shown. The waveform at (a) (the low-V region) exhibits a sharp kink in each period; the phase h stays almost constant except at certain ξ's when it changes rapidly by 2π. The width of the kink (called the penetration depth) shrinks to 0 as $u \to \lambda$. The critical velocity is often called the "speed of light" of a kink since this shrinkage mechanism is analogous to Lorentz contraction. The value V_ℓ is the voltage corresponding to this velocity.

The waveform in the high-V region contracts in the same way as $u \to \lambda$ from above. However, the solution corresponding to the negative slope part is unstable, and is therefore not observed in this current-biased system. Thus, the stable waveform in (b) appears qualitatively different from that in (a). Now, the phase h changes almost linearly in ξ, and there is no particular location that could be called a kink in a usual sense. Since a full 2π-twist of phase is still trapped in each period, we regard this state of the kink as being "stretched". As V increases, the modulation in the waveform decreases.

Finally, when $M > 1$, we note that the traveling waveforms will appear identical to those for $M = 1$ except the ξ coordinate is scaled by $1/M$. For example, for $M = 3$, the waveforms corresponding to (a,b) remain unchanged, but ξ changes from 0 to 1 while the phase h still changes from 0 to 6π. (In the I-V curve, the voltage axis is also scaled by M since the phases now change by $2M\pi$ during each circulation period of a given kink.) The kinks repel one another and distribute themselves evenly around the ring. This is the only possible configuration consistent with a traveling wave.

3 Experiments on Josephson rings

In this section we discuss our experiments in detail. In Sec. 3.1 we describe the experimental setup, including how to control parameters and how to measure the *I*-*V* characteristics. In Sec. 3.2 we present several experimentally measured *I*-*V* characteristics when the coupling parameter Λ is large. The *I*-*V* depends on the number of trapped kinks M. From this dependence we can extract the value of a remaining unknown parameter L.

3.1 Experimental setup

We have measured more than 10 different Josephson rings with different junction parameters, geometries and fabricated with different technologies. All junctions are made of niobium with aluminum tunnel barriers and show nearly ideal junction behavior indicating the high quality of the junctions. The junctions are generally made as a commercial process and, as a consequence, junction parameters are well controlled and highly uniform. Variations in junction parameters are expected to be less than 5-10 %.

In this paper, we discuss the results of one ring in detail. Its results are representative for the other rings. The ring is fabricated with a four mask selective-niobium-anodization process at AT&T Bell laboratories and MIT Lincoln Laboratory. The outer ring diameter is 48 μm and the Josephson junctions have areas of 2 μm^2. The junction capacitance is determined from circuit diagnostics yielding $C = 95$ fF [vdZ&al94-1]. The junction resistance is assumed to be $R = NR_{\text{array}}$ where R_{array} is the measured array resistance.

The damping and coupling parameters Γ and Λ^2 are determined mainly by the junction material and electronic properties but can also be controlled, to a certain extent, by changing the temperature T, because a lower T increases the critical current $I_c(T)$ of a junction. The parameter Γ is proportional to $I_c(T)^{-1/2}$ whereas Λ^2 is proportional to $I_c(T)^{-1}$. The temperature dependence of $I_c(T)$ is well described by the Ambegaokar-Baratoff dependence [Duz&Tur81] with $I_c(0)R_{\text{n}} = 1.9$ mV where $R_{\text{n}} = NR_{\text{array,n}}$ is the normal state resistance of a junction. In practice, one can decrease I_c in an accurate way by one order of magnitude below its zero temperature value. Close to the critical temperature $T_c = 9.2$ K of niobium, $I_c(T)$ changes too rapidly with T to stabilize the temperature accurately.

Since our junctions are high quality tunnel junctions, the *I*-*V* characteristic

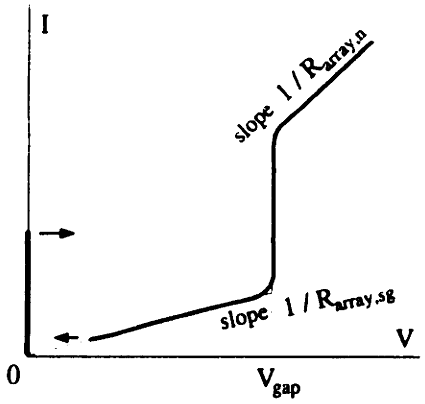

Fig. 3.1 Schematic I-V characteristic of a ring ($M = 0$), showing the voltage-dependent conductance. The branch at $V = 0$ is the superconducting state, and the branch at $V > 0$ is the finite voltage state. There is hysteresis between the two branches. Our experiments are carried out below V_{gap}, thus the subgap resistance $R_{\mathrm{array,sg}}$ determines the damping factor Γ rather than the normal state resistance $R_{\mathrm{array,n}}$.

for the array is highly nonlinear, as shown in Fig. 3.1 [Lik86, Orl&Del91]. For high voltage, the I-V is linear with a slope equal to $1/R_{\mathrm{array,n}}$, but there is a steep decrease of the current at the "gap" voltage $V = V_{\mathrm{gap}}$. Below the gap, the "subgap" resistance $R_{\mathrm{array,sg}}$ is determined by the number of quasiparticles (paired electrons) and hence is temperature dependent. In the present paper we work only within the gap region where the instantaneous voltages across junctions are smaller than the gap voltage. Hence, we use $R_{\mathrm{array,sg}}$ to determine the damping coefficient Γ. Just below T_c the parameters are $\Gamma \approx 0.3$ and $\Lambda^2 \approx 10$. As we lower the temperature down to about $T = 4.2$ K, both parameters are decreased to $\Gamma \approx 0.03$ and $\Lambda^2 \approx 2.2$. Thus, our junctions are *underdamped*, and (moderately to highly) *discrete.*

In our ring with $\Lambda^2 > 1$, the current is actually injected at one node, instead of at all nodes as assumed in the derivation of the model equation (2.11). Uniform current injection requires a more complicated fabrication technology, as additional pieces of metal (to be used as normal resistors) are needed to connect the nodes with the superconducting current leads. The parameter Λ^2 not only measures discreteness but also the typical length scale over which currents are spread out. Thus, for arrays with $\Lambda^2 < 1$, the normal metal resistors are essential; we have obtained good agreement between, for instance, the expected depinning current in highly discrete arrays and data taken on linear arrays built this way [vdZ&al94-2]. However, for larger Λ^2, we believe that the need for normal metal resistors is not as strong and our results in fact confirm this. Comparison with numerical simulations on arrays with uniform current injection are in good quantitative agreement with our data on rings with one-node injection, as will be shown in this paper.

3.2 I–V characteristics

Arrays are measured in a He-4 probe with standard equipment. At room temperature the leads are filtered with radio-frequency-interference filters with a cut-off frequency of 10 kHz. Inside the vacuum can, a small magnet produces a magnetic field Φ^{ext} perpendicular to the array. Figure 3.2 plots typical I-V curves for rings cooled down in different applied magnetic fields. The bias current is swept up and down at an *extremely slow* rate of about 0.001 Hz. A typical frequency of oscillation of the junctions (Josephson frequency) is on the order of 100 GHz; thus we virtually observe no transient at all, and the measured voltages reflect an average over trillions of cycles. Each point on the I–V curve corresponds to an attractor of the system. The measured voltage corresponds to the average frequency on an attractor because of the relation Eq.(2.17).

The number of vortices M is controllable: cooling the system down in a magnetic field of *about* M flux quanta Φ_o corresponds to trapping *exactly* M kinks in the ring. As shown in Fig. 3.2, when the ring is cooled through T_c in zero field ($M = 0$), the I-V curve follows the superconducting states (the $V = 0$ axis) up to a "depinning current" and jumps to a finite voltage at $I = 0.84 I_c$. (The schematic Fig. 3.1 corresponds to this case.) With $M = 1$ applied to the ring, the depinning current nearly vanishes and the voltage starts to increase as soon as current is injected. This part of the I–V curve is qualitatively similar to the low-voltage region in Fig. 2.2. Near $V = 0.2\,\mathrm{mV}$, the average voltage saturates. The saturation voltage is the analog of V_ℓ in Fig. 2.2. In general, when the I–V curve becomes almost vertical, we call the vertical part of the curve a *step*. At the top of the step, around $I_{max} = 0.55 I_c$, a sudden jump to the high-voltage region occurs.

For $M = 2, 3$, and 4, we also see steps, but at different saturation voltages, about 0.35, 0.43, and 0.48 mV, respectively. On the other hand, we have observed that the I-V curve for $5\Phi_o$ ($= (N/2 + 1)\Phi_o$) is identical to the one when cooling down with $3\Phi_o$ ($= (N/2 - 1)\Phi_o$). This is consistent with the symmetry of the

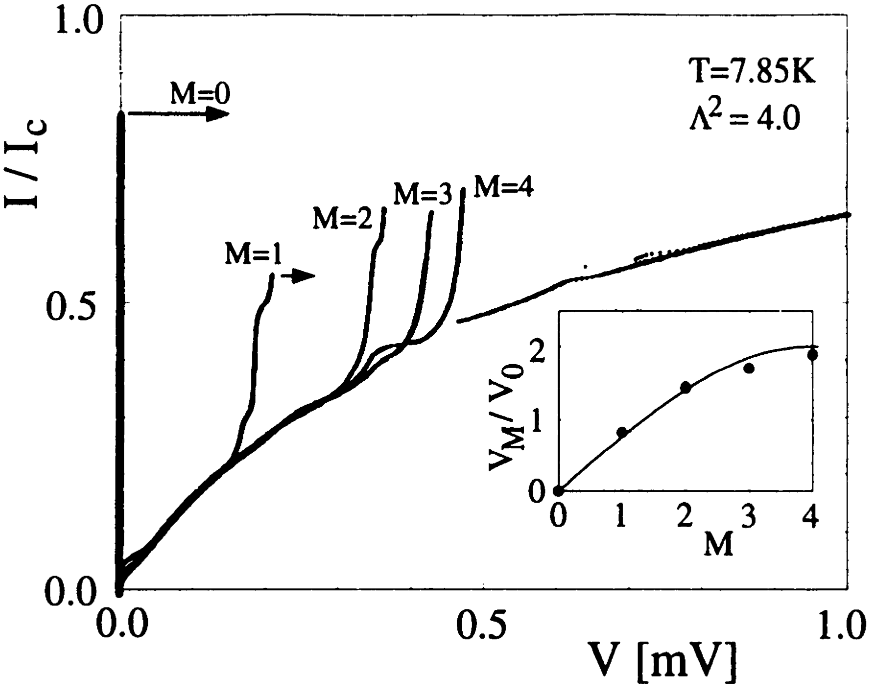

Fig. 3.2 Experimental I-V curves corresponding to the five possible situations with M kinks trapped in a $N = 8$ ring. Measured parameters: $\Lambda^2 = 4.0$, $\Gamma = 0.17$ Inset: voltage position of the steps vs. M. Curve is Eq.(3.1) with a fitting value $V_0 = 0.25$ mV.

model system discussed in Sec. 2.1. Specifically, the I-V curve is invariant under $M \to N - M$ for $M = 0, 1, \ldots, \text{floor}[N/2]$. Thus, a total of 4 different steps can be observed in our ring of 8 junctions.

Figure 3.2 shows that the voltage locations of the steps are not proportional to M. In contrast, in the continuous approximation, the critical voltage $V_\ell(M) = 2\pi M V_0/N \equiv V_M$ is proportional to M [Dav&al83, Ust&al92]. Therefore, this nonlinear dependence on M is a signature of discreteness [Ust&al95]. van der Zant *et al.* have performed [vdZ&al94-1] a linear analysis of one-dimensional (1D) parallel arrays with open ends for $\Lambda^2 \gg 1$. In such a system, resonances occur at voltages determined by the dispersion relation of a 1D discrete, linear transmission line of inductances L and junction capacitances C. A similar analysis for a ring geometry yields that the resonant voltage peaks are given by

$$V_M/V_0 = 2\,|\sin(M\pi/N)|\ . \tag{3.1}$$

(We denote the saturation voltages for the discrete rings by the same notation

V_M, or more formally $V_\ell(M)$, as in the continuous rings.) In the inset of Fig. 3.2, we plot the voltage position of the resonant steps as a function of M. The solid curve is Eq.(3.1) with a fitting parameter $V_0 = 0.25\,\mathrm{mV}$. (This indicates that $L = 18.5$ pH, a reasonable value for our geometry.)

The two data points near the Brillouin zone edge ($M = N/2$) are somewhat lower than predicted by Eq.(3.1). Including mutual-inductance interactions between cells in the ring explains this effect quantitatively[vdZ&al94-1]. However, since the deviation is fairly small, we conclude that considering only the self-inductance L in our model system is a good approximation, thus justifying our assumption in Eq.(2.4).

Now that the last unknown parameter L has been determined by this analysis, there will be no adjustable parameters in the rest of this paper.

4 Steps in the I–V characteristics

Our experiments indicate that for sufficiently large Λ^2, say $\Lambda^2 > 10$, the I–V curves are smooth. These curves exhibit only one step around V_M which is an analog of the critical voltage V_ℓ of the continuum approximation of Sec.2.2. However, when Λ^2 is decreased by lowering the temperature, novel structures appear which significantly alter the I–V curve of the continuous approximation.

These structures are described in Sec. 4.1. The dynamics is then simulated in Sec. 4.2. We observe that the motion of each phase $\phi_j(t)$ is the same, up to time lags. This indicates that *traveling waves* still exist even though the ring is now discrete. The corresponding branches of periodic solutions are numerically followed in Sec. 4.3. There are two distinct regions as in the continuum approximation. Novel steps appear in both regions of the I–V, but we obtain a strong evidence that these steps are created by separate mechanisms.

4.1 Novel features of I–V characteristics

As temperature is decreased, the array becomes underdamped and discrete. This is a parameter regime that has not been much studied before. In the particular sample we discuss, both parameters can be decreased as low as $\Lambda^2 = 2.2$ and $\Gamma = 0.03$. One experimental I-V curve for $T = 7.0$ K, trapping one kink $M = 1$, is shown in Fig. 4.1(a). The overall structures are similar to before; for low voltages, a large resonant step occurs at $V = 0.75V_0$. At $I = 0.35I_c$, a jump to the high-voltage region occurs. When the current is decreased, the system follows a "return path" in the high-voltage region, and when I becomes as small as $0.25I_c$, the system jumps back to the low-voltage region.

However, there are also new structures that were not present for higher T. The steps in the high-voltage region are very clear. The return path is a smooth curve only down to $V = 4.2V_0$, and shows three "glitches" at $V = 3.8V_0$, $3.1V_0$, and $2.2V_0$. As shown in Fig. 4.1(a), there is even hysteresis when biasing on the glitch at $V = 2.2V_0$.

There are also new structures in the low-voltage part, shown enlarged in the right figure of Fig. 4.1(a). In the first upgoing part of the I–V curve we observe these fine structures. Beside the largest step near $V = 0.78V_0$, which probably corresponds to the critical voltage $V_\ell(M)$, there is also an almost vertical part at $V = 0.64V_0$. Although subtle, there is also a smaller fluctuation at $V = 0.45V_0$, which starts to become more pronounced when T is further decreased.

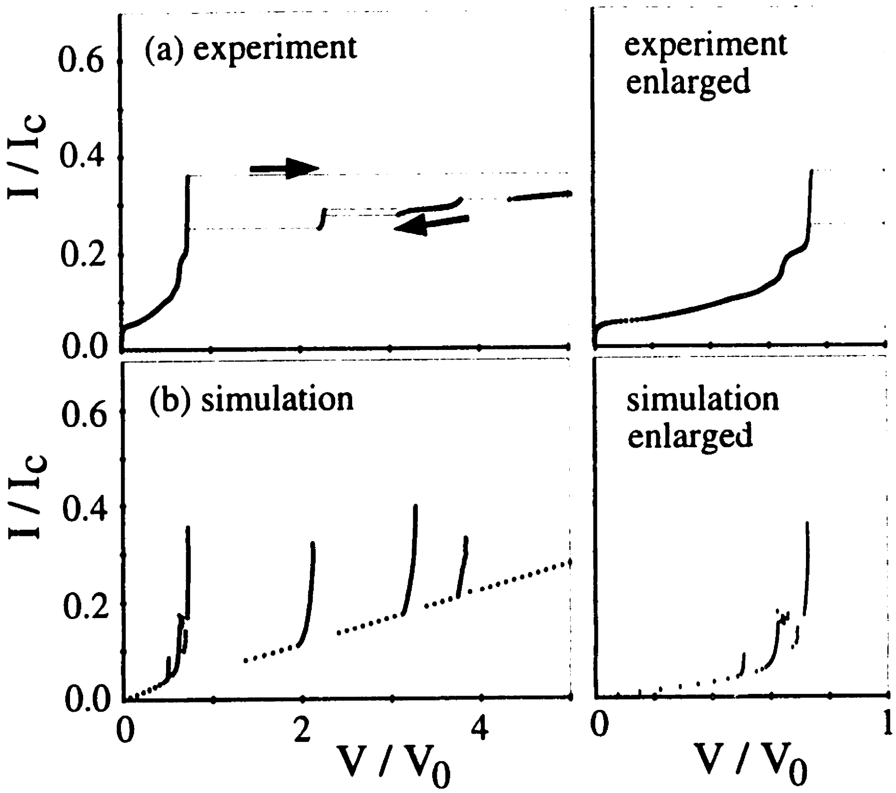

Fig. 4.1 (a) Experimental I-V curve for $N = 8$, $M = 1$, $\Lambda^2 = 2.6$, and $\Gamma = 0.035$ showing structures both in the low- and the high-voltage regions. (b) I-V curve generated by a direct integration of the model system using the same parameter values. The two figures on the right of (a,b) are enlarged views of structures in the low-V region.

To gain insight into the origin of these new structures, we have integrated Eqs.(2.11,2.12), and drawn an I-V characteristic in Fig. 4.1(b) using the parameters from the experiments in (a). As in the experiment, I is slowly swept up and down several times, and for each I, the system is given sufficient time to converge to an attractor. After the convergence, we measure an average frequency, then convert it into the average voltage according to Eq.(2.17).

In Fig. 4.1(b) we observe similar structures to those found in the experiments. In the high-voltage region, there are three steps which occur at similar voltage positions as in the experiments. There are also three clear steps in the low-voltage region at similar voltage locations to those in (a). For a fixed I (e.g. $0.25I_c$), multiple attractors can coexist, resulting in the hysteresis loops.

The height of the steps, however, are considerably larger in the simulations than in the experiment. Since the height depends on the size of basins of attraction, it is possible that thermal noise plays an important role. Also, since the return path is considerably higher in the experiment, we perhaps need to include the effect of the realistic voltage-dependent conductance in the RCSJ model. Nonetheless, our study in the present paper mainly focuses on understanding the mechanisms for the structures and predicting their voltage (i.e. horizontal) locations. For this purpose, the model system provides an adequate approximation.

4.2 Waveforms

Our numerical studies indicate that many data points on the I–V curve correspond to *periodic* solutions. These periodic solutions are the discrete analog of the traveling waves found in the continuum approximation in Sec. 2.2.

Figure 4.2 is an I–V curve, obtained by the simulation of an $N = 4$ ring with $M = 1$ kink. (We chose a smaller N to reduce the size of computation discussed in Sec. 4.3.) Dots represent the computed data while the solid curve is the continuum approximation with the same parameter values. (In fact, the curve is just reproduced from the I–V curve in Fig. 2.2 since we have used these parameter values for the figure.) The computed data points are clearly separated into the low- and the high-voltage regions. Two steps are visible in the low-V side while there is only one step in the high-V side. Therefore, even for this small ring, qualitative features of the I–V curve are similar to Fig. 4.1.

Two points marked as (a) (in the low-V region) and (b) (high-V) are chosen from the data, just as we did in the continuum approximation, and the solutions are studied more carefully To numerical accuracy, solutions at both points are found to be strictly periodic (running) solutions of the form:

$$\phi_j(t) = \phi_j(t+T) + 2\pi \qquad \text{for all } j,\ t \tag{4.1}$$

where T is the period. The point (a), whose voltage is lower than (b), has a longer period since

$$V/V_0 = \omega/\Lambda = 2\pi/(T\Lambda)\ . \tag{4.2}$$

All four phases $\phi_j(t), j = 1, \ldots, 4$, for both (a) and (b) are shown in Fig. 4.3 for three periods. (The horizontal axis is time, scaled by the period.) The waveform for the junction $j = 1$ is shown thicker than the others for clarity. Clearly, the four waveforms are identical but only shifted in time by $T/4$ from j to $j+1$. Thus,

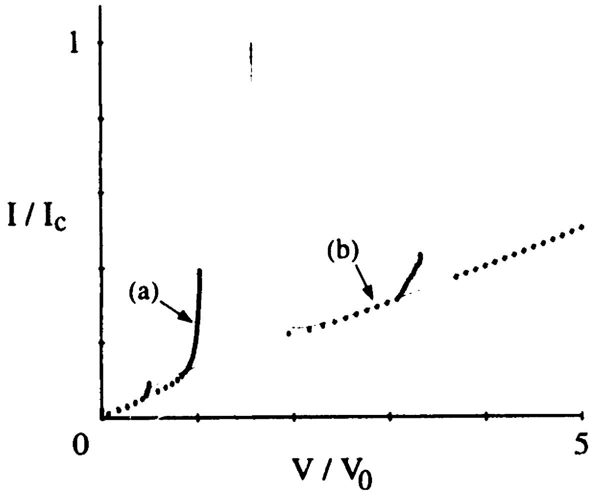

Fig. 4.2 I-V curve for a $N = 4$ ring with $M = 1$, $\Lambda^2 = 1$, $\Gamma = 0.1$. Dots represent data points from direct integration of the model while the curve is the branch of traveling waves in a continuous approximation (reproduced from the I-V in Fig. 2.2) using the corresponding parameter $\lambda = 0.25$.

the solutions are not only periodic, but traveling waves of the form:

$$\phi_j(t) = f(t + Tj/N) \tag{4.3}$$

where f is the waveform.

Note that the array is *discrete* in space, and we only see a set of four phases at any given time. Nonetheless, there is apparently a *continuous* waveform propagating through the array, which can be visualized in the (ϕ, t)-plane as in Fig. 4.3. In contrast to the continuum system, we are not able to observe the waveforms by taking instantaneous spatial snapshots. In other words, space and time are *not* treated on equal footing for a traveling wave in a discrete system. This leads to a non-intuitive consequence described in Sec. 5.3.

The waveforms for the two cases (Figs. 4.3(a,b)) are quite different. In the low-V region (a), the waveform is wiggly, and the phases change nonuniformly in time. The "wiggle" consists of a sharp change in ϕ by almost 2π (a kink), with a small oscillation of two crests per period superimposed on it. This can be intuitively understood from the mechanical analog: pendula driven by a relatively small torque have just enough energy to overturn. For most of their cycle, they are hanging near the bottom ($\phi \approx 0 \bmod 2\pi$). At $t \approx 0, T, 2T, \ldots$, the pendulum ϕ_1, for example, flips by 2π. Then, since the pendulum is underdamped, the flip is

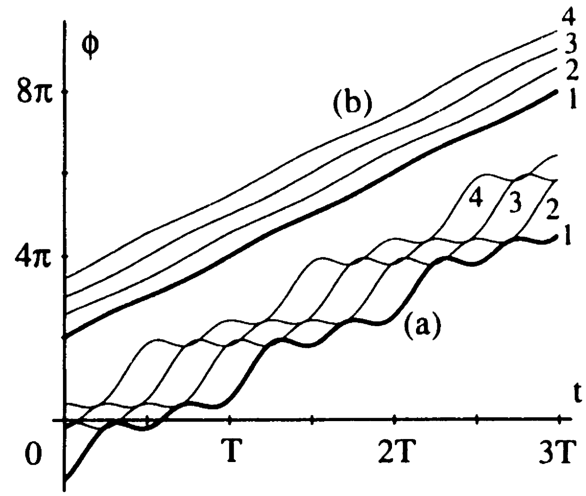

Fig. 4.3 Solutions at points marked as "a" ($I = 0.25I_c$, $V = 0.997V_0$) and "b" ($I = 0.292I_c$, $V = 2.90V_0$) in Fig. 4.2. All $\phi_j(t)$, $j = 1, \ldots, 4$ are shown for three periods. [The period is $T = 6.30$ for (a) and 2.17 for (b).] The solutions are traveling waves propagating in a discrete ring.

followed by an overshoot, which appear as the "ringing" oscillation in Fig. 4.3(a).

It is difficult to give mathematically rigorous existence proofs of traveling waves in discrete media. Levi [Lev88] has proved existence for the limiting case when the width of a kink is "thin" (only one junction overturning at a time). The solution (a) in the figure is indeed a computed example of Levi's solution. (For $N = 2$ it reduces to a "caterpillar" solution [Lev90].) However, for larger Λ values, the thickness increases and several pendula may overturn at the same time (especially for larger N). Numerically, the traveling waves still seem to persist, though it is an open problem to establish this mathematically.

In contrast to the wiggly waveform of (a), the waveform in the high-V region Fig. 4.3(b) can be well approximated by a straight line. Though the winding number is still M, there is no rapid change in phases as in (a). It is as if M kinks were "stretched" uniformly across the ring in the high-V region. In the language of the mechanical analog, all the pendula are rotating almost rigidly. This happens when the applied torque I is large, but the damping factor Γ is also important. Notice that (as shown in Fig. 4.2) similar bias current values are used for (a) and (b). But since Γ is small, the pendula have relatively large inertia, and are hard to stop once they start rotating. This is the high-V branch, and for the same value of I, the two branches can coexist.

4.3 Continuation of periodic solutions

In Fig. 4.2 the low-V region is not approximated well by the continuum limit, but still the solutions seem to be traveling waves. Thus, we wonder how much of the numerical simulation can be explained in terms of traveling wave solutions of the discrete equations. In this section, we study the original model system using a bifurcation and continuation package AUTO86 [Doe&Ker86] that can "continue" a one-parameter family of periodic solutions as the parameter is varied continuously.

Specifically, we start from a "known" periodic solution $\phi_j(t+T) = \phi_j(t) + 2\pi$ provided for one set of parameters. Then AUTO86 continues a branch of periodic solutions as a parameter (the bias current I in this case) is varied. It is harder to find a branch of *traveling waves* as it leads to a system of delay-differential equations. We content ourselves with continuing general periodic solutions, then later check that they are indeed traveling waves, by outputting the computed waveforms. AUTO86 rephrases the computation of periodic solutions as a boundary value problem with an additional integral condition (to remove arbitrariness of time translation). The problem is discretized by a collocation method, and Newton's method obtains a solution [Doe&Ker86].

We have used the same parameters as before, i.e. $N = 4$, $M = 1$, $\Lambda^2 = 1$, and $\Gamma = 0.1$. The initial solution is found by a direct integration of the model system (2.11,2.12) at a large I (e.g., $0.8I_c$) where the system is attracted to the high-voltage part of the I–V quickly. The waveform of the solution is almost straight, like in Fig. 4.3(b). The continuation algorithm does not depend on stability of the solutions; the whole branch is then resolved, including the unstable part. Also, AUTO86 uses pseudo-arclength parametrization [Doe&Ker86] which makes it possible to continue beyond the turning points of the parameter I.

The result is shown as a curve (partly solid, partly dotted) in Fig. 4.4. (In the inset of the figure, the curve is shown together with the data points from numerical simulations used in Fig. 4.2). Somewhat surprisingly, the apparently disjoint branches in the low- and high-V regions are successfully connected. The almost uniform waveform in the high-V region is continuously deformed to the wiggly solution of the low-V region. The sharp peak present in the continuous sine-Gordon equation at $V = V_\ell$ is now rounded and much lower. Predicting the voltage location and the height of the transition peak between the two regions is important, but we do not know how to describe this curious loop.

The solid part of the continued curve is stable whereas the unstable portion

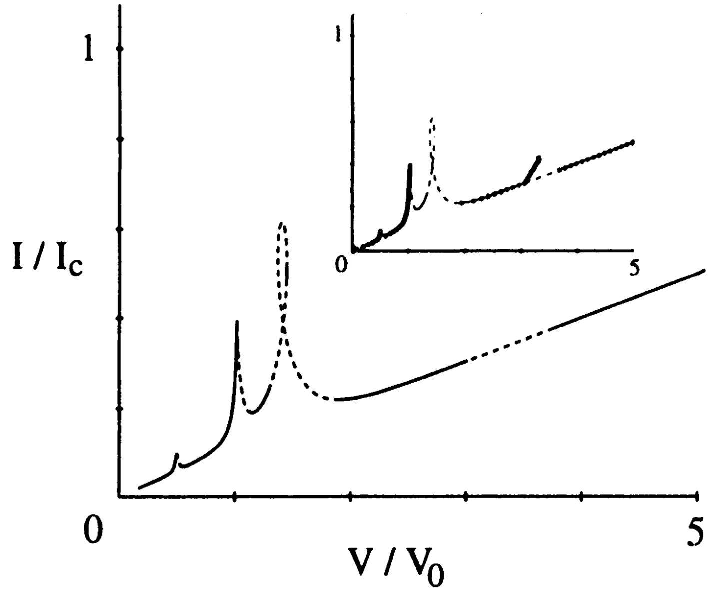

Fig. 4.4 I–V curve for the same set of parameters as in Fig. 4.2. The curve denotes a branch of periodic solutions continued by AUTO86. Solid (dashed) part of the curve corresponds to stable (unstable) solutions, respectively. Inset: the same curve is shown with data points from simulation, as in Fig. 4.2.

is shown dotted. (Stability is determined by monitoring Floquet multipliers in AUTO86, and also checked by our program which integrates the Jacobian flow.) In the inset, we find no data points from the direct simulation in the unstable part. They lie on the stable part of the curve. There are two stabilized segments on or near the "loop", where we do not see any data points. We think there are indeed attractors located at these segments, but are not accessible in the phase space by our procedure of ramping I up and back down. We would need a more elaborate preparation of the initial condition and the bias current I to see these stable states.

In Fig. 4.4 we confirm that *all* the data points in the low-voltage region correspond to simple traveling wave solutions. In contrast, points on the step in the high-voltage region are off from the branch of periodic solutions. Moreover, they seem to *emanate* from the branch at a point where the stability of the periodic solution switches. Therefore, the steps in the two regions are created by different mechanisms.

In Sections 5 and 6, we examine the low- and the high-voltage regions, respectively. For the low-V part, we will look for a condition for which kinks and small oscillations form wiggly traveling waves together. For the high-V part, we expect that the steps are created by an instability of a simple traveling wave solution, and more complicated attractors emerge from the onset.

5 Low-voltage region

In Section 4 we observed that the low-voltage part of the I–V curve is substantially different in the discrete arrays from its continuous analog. The curve can exhibit substructures and peaks, and the waveform of the solutions in this region are wiggly, as in Fig. 4.3(a). The waveform consists of a kink and a superimposed small amplitude wave. The kink might be described by the continuous sine-Gordon approximation, but there is no analog for the superimposed wave. The generation of this "radiation" by a moving kink is an essential feature introduced by discreteness.

The mechanism for generating these small-amplitude waves has been studied since early simulations of Currie *et al.* [Cur&al77] in which small amplitude waves were generated in the wake of a kink in a highly discrete one-dimensional sine-Gordon system in an infinite domain. Part of the kinetic energy of the kink is taken away by the emitted waves, causing it to slow down. This decay process was carefully studied by Peyrard and Kruskal [Pey&Kru84]. They showed that a moving kink appears as a time-dependent forcing term in the equations of motion for the radiated waves, and certain linear modes are excited when their natural frequencies resonate with the forcing frequency. They also found that the precise shape of the kink was relatively insignificant in determining the resonant frequencies; those are determined by the eigenfrequencies of the lattice itself. Boesh *et al.* [Boe&al89] made a more formal study of this phenomenon in terms of phonon bands. They also made a change of variables to a collective coordinate in order to explicitly separate the kink from the radiation. This approach was especially successful in determining the Peierls-Nabarro frequency of a kink trapped in a potential well [Boe&Wil89].

Although a Josephson junction has loss mechanism while oscillators in these studies are conservative, excitation of certain modes still occurs in the Josephson ring and is sustained when underdamped. Recently, Ustinov *et al.* [Ust&al93] applied Peyrard and Kruskal's method to a highly dicrete Josephson ring, and showed that resonances occur between the moving kinks and the generated wave. This enabled them to predict a set of voltages for steps in the low-voltage region of the I–V curve when $M = 1$. The results were in good agreement with their simulations. In Sec.5.1–5.2 we follow this argument while clarifying their reasoning of the dispersion relation. In Sec.5.2 the formula is tested experimentally, and we generalize it to when there are multiple kinks in a ring. The formula is not periodic in the mode number of the radiation, which results in a non-intuitive consequence that one can distinguish mode m from $m + N$. Sec.5.3 discusses this peculiar effect.

5.1 Phase-locking of kink and radiation

The dispersion relation of the linear modes plays an important role in coupling of kink and the modes. It was derived in [Ust&al93] by plugging into the sine-Gordon equation Eq.(2.11) the exponential form $\phi_j(t) = \phi_0 \exp i(\omega_r t + kpj)$ where ω_r is the frequency of the radiation, k is the wave number, and p is the lattice spacing. Then, the equation was linearized by replacing $\sin\phi_j$ by ϕ_j. However, the phases are not librating at small angles, and this linearization is not consistent.

What we need is an approximate form of a large amplitude kink, and the dispersion relation of linear waves *around the kink.* The kink can be approximated crudely by a step function

$$\phi_j^*(t) = \begin{cases} 0 \ , & j < vt \\ 2\pi \ , & j > vt \end{cases} \tag{5.1}$$

where v is the velocity of the kink. (Peyrard and Kruskal approximated the kink a little more precisely, but the resonance condition is unaltered.) Then, we derive equations for the deviation $u_j(t) = \phi_j(t) - \phi_j^*(t)$, which is assumed to be small enough that terms of $O(u^2)$ are negligible. The linearized system is

$$\ddot{u}_j + \Gamma \dot{u}_j + u_j = \Lambda^2 \nabla^2 u_j \tag{5.2}$$

For an underdamped chain, the dispersion relation for the mode $u_j = \exp i(\omega_r t + kpj)$ is

$$\omega_r^2(k) = 1 + 4\Lambda^2 \sin^2(kp/2) \ . \tag{5.3}$$

The formula for resonances obtained in [Pey&Kru84, Boe&al89] requires that the linear mode moves with the kink:

$$v = \frac{\omega_r}{k} = \text{phase velocity} \ . \tag{5.4}$$

Given the kink velocity v, this determines the wave number that can *phase lock* with the motion of the kink.

When the condition Eq.(5.4) is met and the kink and the particular linear mode couple, the whole structure forms a traveling wave. The phases ϕ at lattice points then undergo identical motion with a time lag. This is what we observed in Sec.4.2 for the Josephson rings.

5.2 Preferred velocities

The system studied by Peyrard and Kruskal [Pey&Kru84] is a conservative system (no damping $\Gamma = 0$, no drive $I = 0$) in an infinite domain. (However, for simulations, they used an absorbing boundary condition to avoid reflections.) A moving kink radiates linear waves, and gradually slows down by losing its energy. A surprising phenomenon they discovered was that the decay of the kink speed was highly nonuniform: there was a discrete set of velocities at which the decay rate abruptly became small. The kink cruised at these velocities in a quasi-stationary fashion.

Moreover, by adding a small external drive ($I/I_c < 10^{-3}$) at each site j to compensate the small energy loss, the kink propagation at these velocities was made truly steady. The existence of such "preferred" velocities implies from Eq.(5.4) that the system prefers certain wave numbers for the small-amplitude radiated waves. There is a *selection criterion* for the wavenumbers.

The proposed criterion for their system is based on their numerical observations. The roots k for Eq.(5.4) can be obtained as intersections of two graphs, $1 + 4\Lambda^2 \sin^2(kp/2)$ and $(vk)^2$. For a given v, there can be multiple roots. As v is varied, a pair of roots coalesce and disappear, and these v's are observed to agree with the preferred velocities remarkably well. The quasi-stationary propagation of kinks implies that little energy is taken away from the kink by the radiation in the moving frame of the kink. Their criterion explains a sudden change in the decay rate, but it still remains mysterious why it can also explain that the rate becomes nearly zero.

In the Josephson ring, we also observe similar "preferred" velocities of the kink. Actually, these could be better described as "allowed" velocities. For a ring, there is a different selection criterion from that of Peyrard and Kruskal, which comes from a purely geometric constraint: the wave number has to conform with the imposed periodic geometry. For one kink ($M = 1$), the wave number has to satisfy [Ust&al93]

$$k = 2\pi m/(Np) \tag{5.5}$$

where $m = 1, 2, \ldots$ is the mode number of the linear wave.

Substituting this into Eqs.(5.3,5.4) reduces to

$$v = \frac{Np}{2\pi m}\left[1 + 4\Lambda^2 \sin^2(m\pi/N)\right]^{1/2} . \tag{5.6}$$

At these velocities, the excited mode m is phase-locked to the kink, and together they form a wiggly traveling wave.

The kink speed is related to the average rotation frequency of a junction ω by $\omega = 2\pi/T = 2\pi v/(Np)$ which is converted to the average dc-voltage

$$\frac{V}{V_0} = \frac{\omega}{\Lambda} = \frac{1}{m}\left[\frac{1}{\Lambda^2} + 4\sin^2(m\pi/N)\right]^{1/2} , \tag{5.7}$$

This is the formula derived by Ustinov *et al.* [Ust&al93] which explain their numerical observations of the steps in the low-voltage region well.

To clarify the physical origin of the resonance condition Eq.(5.6), it is helpful to recall a mechanical analog of the system. We imagine a ring of N pendula, each coupled to its nearest neighbors, whose phases ϕ_j are measured from the downward vertical. In the low-voltage region, as described in Sec.4.2, a given pendulum hangs almost straight down for much of the time, but overturns rapidly when the kink passes by. Then, because the pendulum is underdamped, its overshooting causes it to "ring" for several oscillations. This ringing is the essence of the radiation excited by the kink. A resonance occurs if the pendulum rings precisely an integer number of times between successive passages of the kink. The ringing frequencies are the lattice eigenfrequencies of small oscillations about the kink, and the circulation frequency of the kink is $\omega = 2\pi v/(Np)$. Eq.(5.6) is a matching condition ($\omega_r = m\omega$) of these frequencies.

The formula has been tested against experimental data in Fig. 5.1, which shows the substructures in the low-voltage region of the I–V characteristic. A single kink ($M = 1$) is trapped in the ring. It uses an even smaller value $\Lambda^2 = 2.2$ (more discrete) than in Fig. 4.1(a), making the structures clearer. In total, six resonant steps are present, corresponding to local minima in the differential resistance dV/dI. In the inset of the figure, Eq.(5.7) is drawn as a solid curve. A good agreement between the model and the experiment is obtained without any free parameters.

When there is more than one kink ($M > 1$), the resonance formula can be generalized by assuming that the kinks evenly distribute themselves around the ring, as occurs for the continuous system (Sec.2.2). Then, for a junction to ring an integer number of times between consecutive passage of kinks, the wavenumber should be restricted to $k = 2\pi mM/(Np)$. The frequency of a junction now becomes $\omega = 2\pi Mv/(Np)$. Thus, the generalized formula of Eq.(5.7) is

$$\frac{V}{V_0} = \frac{\omega}{\Lambda} = \frac{1}{m}\left[\frac{1}{\Lambda^2} + 4\sin^2(mM\pi/N)\right]^{1/2} . \tag{5.8}$$

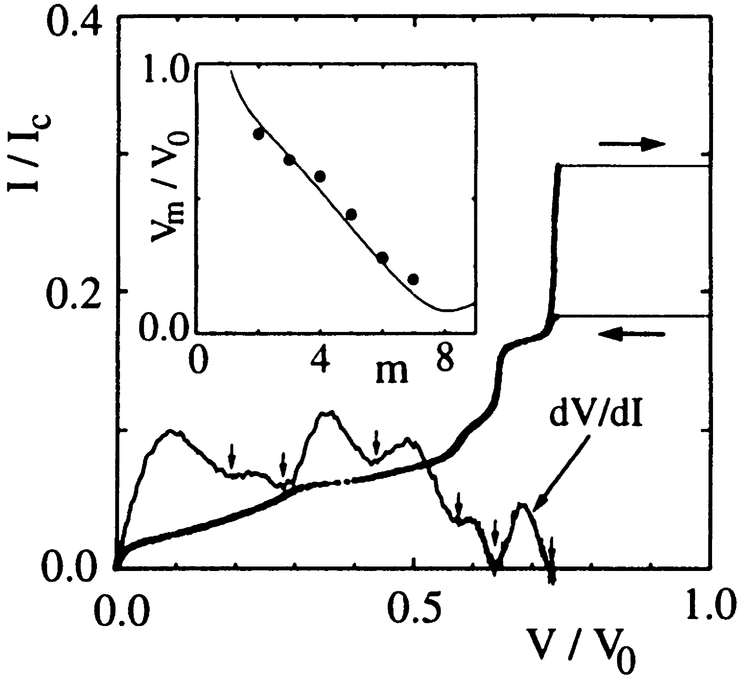

Fig. 5.1 Experimental I-V curve for $N = 8$, $M = 1$, $\Lambda^2 = 2.2$, and $\Gamma = 0.13$. The solid curve shows dV/dI; note six dips corresponding to six resonant steps in the I-V curve. Inset: voltage position of these six steps vs mode number m. Curve is the formula Eq.(5.7) without a free parameter.

We have not tested this formula against the experimental data. However, when tested against simulations of an $N = 8$ junction array with parameters $\Lambda^2 = 2.2$ and $\Gamma = 0.13$, the formula predicts the step locations reasonably well. For example, when there are $M = 3$ kinks, we observe steps at $V/V_0 = 0.68$ and 1.8; they are close to the values predicted by the above formula: $V/V_0 = 0.78$ ($m = 2$) and 2.0 ($m = 1$). For $M = 4$, we observe only one major step at $V/V_0 = 2.0$, again close to the formula with $m = 1$: $V/V_0 = 2.1$. We observe several extra steps that we cannot explain, but the mechanism and the formula seems to be valid for $M > 1$.

When $\Lambda^2 \gg 1$ and $m = 1$, the formula (5.8) reduces to Eq.(3.1), which predicts the location V_M of the tallest step in the low-voltage region. However, the derivation of Eq.(3.1) uses [vdZ&al94-1] a linear analysis of one-dimensional discrete transmission line rather than the phase-locking mechanism described here. It is not clear whether the two different physical pictures of dynamics coincide on this particular step.

5.3 High wave number resonances

The formula Eq.(5.7,5.8) has peculiar consequences. Ordinarily, one expects that in a discrete ring of N junctions, only $N/2$ steps are distinct, or perhaps N at most, as assumed in [Ust&al93]. But because the formula is not periodic in the mode number m, the voltages V_m and V_{m+N} are predicted to be different for all m. This paradox can be resolved by either finding a reason to restrict the wave numbers m from 0 to $N-1$ (or maybe $-N/2+1$ to $N/2$) or by showing that these high wave number steps can actually be observed. We could not find any reason for restricting the wave numbers, thus it seems that m can indeed take values outside the first Brillouin zone, up to $m = \infty$, at least in principle. This may be non-intuitive since the deviation $u_j(t)$ can be expanded as a discrete Fourier series for all t. But to test the idea, we return to the numerical study of the I-V curves.

The existence of steps with $m > N$ is clearly indicated by the I-V curve shown in Fig. 5.2, using a small (but realizable) damping $\Gamma = 0.02$. (Simulations indicate that the steps corresponding to high wave numbers can be observed in a parameter region given approximately by $\Lambda \leq 1$ and $\Gamma \leq 0.05$. A larger damping washes out these resonances.) One kink $M = 1$ is trapped. The mode numbers m, given at the base of the steps, were determined by carefully examining the traveling waveforms $\phi_j(t) = f(\xi)$, where $\xi = t + Tj/N$. (Recall that there exists such a continuous waveform, even in the discrete lattice, as discussed in Sec.3.2.)

As shown in the inset of Fig. 5.2, a waveform with $m = 9$ small oscillations can occur in a ring of $N = 8$ junctions. The corresponding step lies between the $m = 7$ and $m = 8$ steps; this is expected from Eq.(5.7), which predicts that V_m is non-monotonic in m, and specifically that V_9 lies between V_7 and V_8. The non-monotonicity also explains why the steps for $m = 10, \ldots, 14$ are not visible in Fig. 5.2; they are hidden under the stronger resonances for $m = 7, \ldots, 9$, which occur at approximately the same positions. The location of the next detectable step, corresponding to $m = 15$, is well predicted by Eq. (5.7).

The physical relevance of mode numbers outside the first Brillouin zone is readily understood in terms of the pendulum analog. The integer m is the number of times each pendulum oscillates between consecutive sweeps of the circulating kink. This number can be arbitrarily large, if the kink is moving sufficiently slowly (as it will be, near the bottom of the I-V curve). Of course, in a *linear* discrete system, one cannot distinguish between mode m and $m+N$; the difference is that

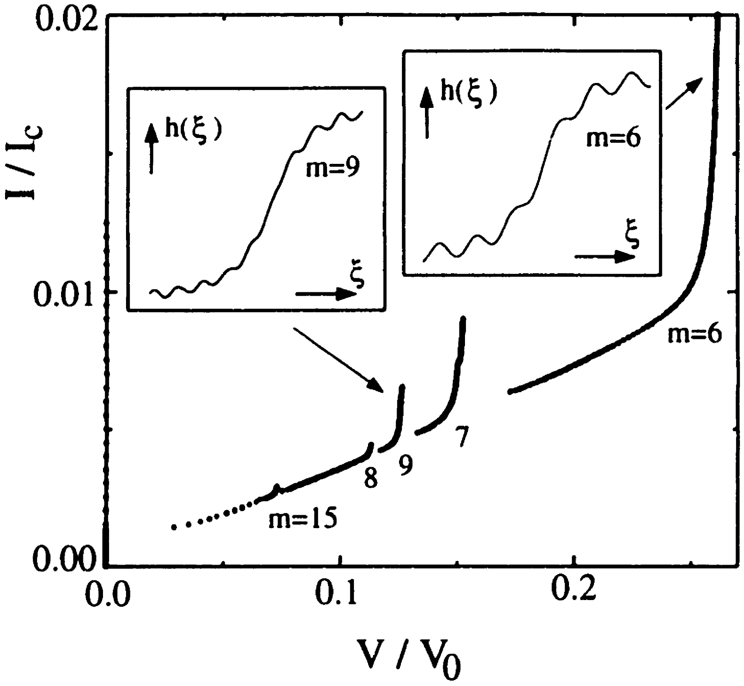

Fig. 5.2 Numerical I-V curve of the model system with $N = 8$, $M = 1$, $\Lambda^2 = 1.0$, and $\Gamma = 0.02$ showing high wave number resonances. The mode number m of linear waves is indicated below each step. Inset: traveling waveforms on the $m = 6$ and $m = 9$ steps.

there is nothing analogous to a circulating kink in a linear system. The rotation of the kink—an inherently *nonlinear* phenomenon—provides the crucial reference that allows one to discriminate mode m from $m + N$.

6 High-voltage region

In this section we discuss the resonant steps in the high-voltage region of the I-V characteristics. Unlike the low-voltage steps, these steps do not arise from a phase-locking mechanism; instead, they emanate from bifurcation points where a simple periodic solution becomes unstable.

Our analysis is motivated by Maginu [Mag83] who studied the stability of the "spatially homogeneous periodic solutions" in a continuous Josephson junction equation with a periodic boundary condition. These solutions are the traveling wave solutions in the high-voltage region where kinks are stretched. His analysis for $M = 0$ proves that such solutions can become destabilized by a parametric instability mechanism, and spatially inhomogeneous solutions emerge. He briefly mentions that, for $M > 0$, the homogeneous solutions can again be destabilized.

Our aim in this section is to analyze such parametric instabilities for a general finite $N > 2$, both with no external magnetic field ($M = 0$) and with a magnetic field ($M = 0, 1, \ldots$). Also, we are more interested in estimating the voltage locations for these instabilities rather than proving that they do occur. In Sec. 6.1 we start from a general framework for the stability analysis of periodic solutions. In Sec. 6.2, the Josephson ring with no trapped kinks ($M = 0$) is analyzed. A small perturbation around the basic in-phase state is decomposed into modes, each of which obeys a Hill's equation. In the regime of interest, Hill's equation may be approximated by a Mathieu equation. We also estimate the frequency/voltage zones in which the basic solution is destabilized. In Sec. 6.3, the analysis is extended to the case $M > 0$. The modes are now coupled, but due to the whirling form of the basic state, the mode m is only coupled to $m \pm M$. Because of this simplicity, it is straightforward to predict the resonant frequencies.

This instability analysis can be extended to different boundary conditions and to continuous systems. We extend our analysis to discrete arrays with open ends in Sec. 6.4. This approach explains the so-called zero-field steps when $f = 0$, and predicts novel steps (generalization of the zero-field steps) at various combination frequencies when $f > 0$. Our analysis is similar to what has been used for predicting locations of so-called Fiske steps in a continuous Josephson junction with a large Λ^2. Sec. 6.5 is a discussion of this curious "coincidence", and shows that both the Fiske and the zero-field steps may be understood within a uniform framework in the discrete arrays regardless of the boundary conditions.

6.1 Stability analysis

We first review a general stability property of periodic solutions in the model system. We denote the basic periodic solution by $\phi_j^*(t)$ where $\phi_j^*(t+T) = \phi_j^*(t)+2\pi$ and T is the minimum period. We study the linear stability of this solution by linearizing around the basic state:

$$\phi_j(t) = \phi_j^*(t) + u_j(t) \tag{6.1}$$

where u_j is the perturbation. By substituting Eq.(6.1) into Eq.(2.11) and retaining only the first order in u, we obtain

$$\ddot{u}_j + \Gamma \dot{u}_j + \left[\cos \phi_j^*(t)\right] u_j = \Lambda^2 \nabla^2 u_j \quad , \; j = 1, \ldots, N \; . \tag{6.2}$$

The boundary conditions for a ring array become

$$u_{j+N}(t) \equiv u_j(t) \qquad \text{for all } t \text{ and } j \tag{6.3}$$

while, for a linear array,

$$u_0(t) \equiv u_1(t) \quad , \; u_{N+1}(t) \equiv u_N(t) \qquad \text{for all } t. \tag{6.4}$$

This is a linear system of $2N$ first-order ordinary differential equations with time-periodic coefficients.

The local stability of the trivial solution $u_j \equiv 0$ is determined by the Floquet multipliers [Nay&Moo79, Jor&Smi87]. There are $2N$ independent functions, each of which satisfies

$$u_j(t+T) = \mu u_j(t) \quad , \text{ for all } t \text{ and } j \tag{6.5}$$

for some (possibly complex) number μ. Such a μ is a Floquet multiplier. If all $2N$ multipliers satisfy $|\mu| < 1$, then the trivial solution is stable. If some μ satisfies $|\mu|$¿1, it is unstable.

One of the multipliers can be easily found. It corresponds to the eigenmode

$$u_j(t) = \dot{\phi}_j^*(t) \tag{6.6}$$

It can be easily seen that this satisfies the governing equation Eq.(6.2) and the boundary condition Eq.(6.3) or (6.4) as well as the condition Eq.(6.5). The corresponding multiplier is $\mu = 1$. In the original system Eq.(2.11), this is a perturbation along the periodic orbit ϕ_j^*.

Another general property of the multipliers can be seen when we transform the variables according to

$$u_j(t) = e^{-\Gamma t/2} v_j(t) \tag{6.7}$$

which converts Eq.(6.2) into

$$\ddot{v}_j - p_j(t) v_j = \Lambda^2 \nabla^2 v_j \quad , \; j = 1, \ldots, N \tag{6.8}$$

where $p_j(t) = \Gamma^2/4 - \cos\phi_j^*(t)$. This set of equations can be cast into a time-dependent Hamiltonian system, which implies[Gel&Lid58] that all the multipliers for Eq.(6.8) must lie on the unit circle or, otherwise, the multipliers must come in pairs such that their products are unity. Since the transformation Eq.(6.7) scales the multipliers by a factor of $\exp(-\Gamma T/2)$, this symmetry requires the μ's to lie on the circle of

$$\text{radius} = e^{-\Gamma T/2} \tag{6.9}$$

(which we shall denote as C) or, otherwise, they come in pairs μ_1 and μ_2 such that

$$\mu_1 \mu_2 = e^{-\Gamma T} \; . \tag{6.10}$$

In addition, since all the u_j are real, the multipliers must be real or, otherwise, must come in complex conjugate pairs.

6.2 Ring, $M = 0$

6.2.1 Approximation of stability boundaries

The simplest case is a ring array of Josephson junctions with $M = 0$ (no kink trapped). In this case, the basic solution is the in-phase solution

$$\phi_j^*(t) = \phi^*(t) \tag{6.11}$$

Expand u_j into the discrete Fourier series

$$u_j(t) = \sum_{m=0}^{N-1} A_m(t) e^{2\pi i m j/N} \; . \tag{6.12}$$

Then, Eq.(6.2) becomes

$$\ddot{A}_m + \Gamma \dot{A}_m + \left[\omega_m^2 + \cos\phi^*(t)\right] A_m = 0 \quad , \; m = -\frac{N}{2} + 1, \ldots, \frac{N}{2} \tag{6.13}$$

where

$$\omega_m = 2\Lambda \left|\sin(m\pi/N)\right| \tag{6.14}$$

is the lattice eigenfrequency of the m-th Fourier mode. The modes are decoupled, and each obeys a Hill's equation Eq.(6.13). Each equation gives two Floquet multipliers which must satisfy the symmetry constraint Eq.(6.10). Thus there are only two possibilities: (1) μ_1 and μ_2 are a complex conjugate pair lying on the circle C', (2) they are real with the product relation Eq.(6.10).

The mode $m = 0$ can be analyzed easily. The modal equation is

$$\ddot{A}_0 + \Gamma \dot{A}_0 + [\cos \phi^*(t)]\, A_0 = 0 \ . \tag{6.15}$$

One "eigenfunction" which satisfies Eq.(6.5 is the trivial solution:

$$A_0(t) = \dot{\phi}^*(t) \ , \tag{6.16}$$

accounting for the unit multiplier $\mu_1 = 1$. This eigenfunction is always (neutrally) stable. Because of the relation Eq.(6.10), there must be a second eigenfunction corresponding to a multiplier $\mu_2 = \exp(-\Gamma T)$. Perturbations in this direction always decay.

For the other Fourier modes we expect generic behavior, i.e. change of stability as parameters are varied. To estimate when the stability switches, we approximate the whirling solution $\phi^*(t)$. For the in-phase solution, the coupling term $\nabla^2 \phi_j$ in Eq.(2.11) vanishes. Thus, the equation reduces to the single junction equation:

$$\ddot{\phi} + \Gamma \dot{\phi} + \sin \phi = I / I_c \ . \tag{6.17}$$

It is more convenient to scale time by $\tau = \omega t$ where $\omega = I/(\Gamma I_c)$. Then,

$$\frac{d^2\phi}{d\tau^2} + \Gamma \omega^{-1} \frac{d\phi}{d\tau} + \omega^{-2} \sin \phi = \Gamma \omega^{-1} \ . \tag{6.18}$$

For any fixed $\Gamma > 0$, the whirling periodic solution can be obtained perturbatively as $\omega \to \infty$. There is no need to modulate the time coordinate for several lower order expansions, and we obtain [Wat&Swi95]:

$$\phi(\tau) = \tau + \frac{1}{\omega^2} \sin(\tau) + \frac{1}{\omega^3} \Gamma \cos(\tau) + O(\omega^{-4}) \ . \tag{6.19}$$

Since the correction term quickly becomes small, taking only the first term $\phi^*(t) \approx \omega t$ would be sufficient to estimate the multipliers. Under this assumption, and after rescaling time as above, Eq.(6.13) becomes the damped Mathieu equation in the standard form

$$A_m''(\tau) + \gamma A_m'(\tau) + (\delta + \epsilon \cos \tau) A_m(\tau) = 0 \tag{6.20}$$

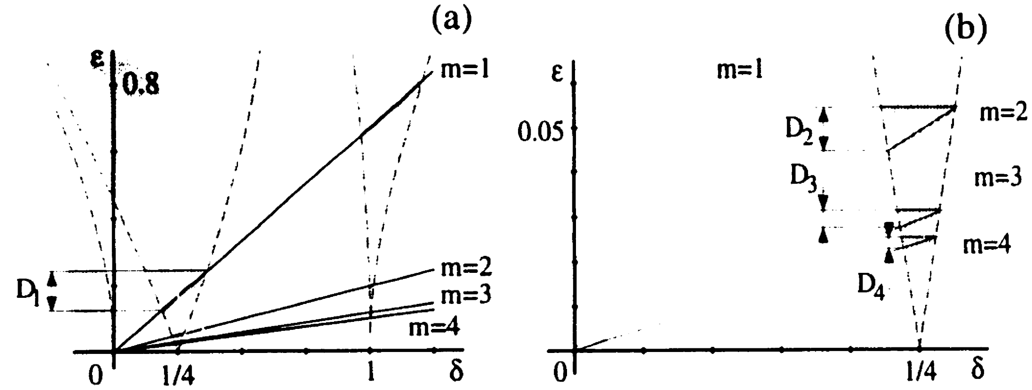

Fig. 6.1 Intervals D_m where the m-th mode grows due to parametric excitation. (See texts.) The parameter $\epsilon = 1/\omega^2$ essentially denotes the forcing frequency. Shaded regions are Mathieu tongues. (b) is an enlarged view of (a).

where $\gamma = \Gamma/\omega$, $\delta = \omega_m^2/\omega^2$, and $\epsilon = 1/\omega^2$.

Depending on (δ, ϵ), the stability of the solution $A_m \equiv 0$ can be determined graphically as in Fig. 6.1 for $N = 8$, $\Lambda = 1.6$. The shaded regions are Mathieu tongues in which perturbations grow exponentially. Since the parameters are related by

$$\delta = \omega_m^2 \epsilon \ , \tag{6.21}$$

the allowed parameters are confined to an operating line through the origin as ω is varied. The slope of the line depends on the mode number m. Since $\omega_{N-m} = \omega_m$, there are only $N/2 = 4$ lines shown in the figure. Sufficiently large ω corresponds to a point near the origin, thus all modes are stable (in the sense that $A_m(\tau) \to 0$ as $\tau \to \infty$). As ω is decreased, the operating point along each line crosses the tongues. Then, the modes become unstable for some interval of ω, and are later restabilized when the point exits the tongue. In the experiment and numerical simulations, we only see instabilities corresponding to the first tongue, emanating from $(\delta, \epsilon) = (1/4, 0)$. Thus, we focus our attention on this tongue alone.

The ϵ axis is inversely proportional to ω^2. Therefore, we are able to interpret an instability interval (D_1 in Fig. 6.1(a), for example) as the frequency range where the mode is unstable. In Fig. 6.1(b), such intervals for modes $m = 2$ to 4 are shown. The upper (lower) boundary of D_m is the lowest (highest) frequency of the interval, which we call $\omega = \Omega_m^-$ (Ω_m^+, respectively). We estimate $\Omega_m^\pm$ by approximating the boundary of the tongue. (See Jordan and Smith [Jor&Smi87] for an illustration of the required perturbative calculation.) Including the effect of damping, the boundary is [Jor&Smi87]

$$\delta = \frac{1}{4} \mp \frac{\epsilon}{2}\sqrt{1 - \left(\frac{\gamma}{\epsilon}\right)^2} + O(\epsilon^2) \tag{6.22}$$

for $0 < \epsilon \ll 1$, i.e. $\omega \gg 1$. When $\gamma > \epsilon$ (or $\omega > 1/\Gamma$), the tongue disappears for small ϵ, and the mode A_m is always stable. Otherwise, Eq.(6.22) gives us the estimate. For example, when we further assume $\Gamma\omega \ll 1$, then Eq.(6.22) becomes

$$4\omega_m^2 = \omega^2 \mp 2\sqrt{1 - (\Gamma\omega)^2} = (1 \pm \Gamma^2)\omega^2 \mp 2 + O(\Gamma^4\omega^4) \ .$$

Thus,

$$\Omega_m^{\pm} \approx \left[\frac{4\omega_m^2 \pm 2}{1 \pm \Gamma^2}\right]^{1/2} \approx \frac{2\omega_m}{1 \pm \Gamma^2}\left(1 \pm \frac{1}{4\omega_m^2}\right) \ . \tag{6.23}$$

Hence, the m-th resonant frequency is $\omega \approx 2\omega_m$ with a small correction, as expected from the theory of Mathieu equations.

6.2.2 Comparison with numerics and experiments

This approximation Eq.(6.23) for the m-th resonant frequency explains the numerical I-V curve very well. In Fig. 6.2(a) we show such an I-V together with the predicted instability intervals D_m for $N = 8$, $\Lambda = 1.6$, and $\Gamma = 0.035$. Frequencies ω in the formula Eq.(6.23) are converted to voltages according to the relation $V/V_0 = \omega/\Lambda$. The instability intervals D_1 through D_4 agree well with the intervals where the return path is disrupted. We expect that bifurcations occur at both ends of each D_m. As is well-known for the first Mathieu tongue, they are both "subharmonic" or "period-doubling" bifurcations. Clearly from Fig. 6.2(a), $\omega = \Omega_m^-$ is a supercritical bifurcation; a stable branch of solutions emanates at that point from the in-phase solution branch. On the other hand, $\omega = \Omega_m^+$ is subcritical; a sudden jump occurs, and carries the system to a distant attractor in the phase space.

Comparison with an experiment is shown in Fig. 6.3. There are resonant steps which are associated with instability intervals of the whirling mode branch. The voltage positions of the steps are in good agreement with the leading order estimate of the formula Eq.(6.23) $\omega = 2\omega_m$ (curve in the inset). No fitting parameter is used. The predicted instability intervals D_m contain the observed steps, however, they are smaller than the observed intervals. We have not studied the reasons for this premature jump; one reason might be that, near the stability boundaries, thermal noise kicks the system out of the in-phase state. Also, we notice that

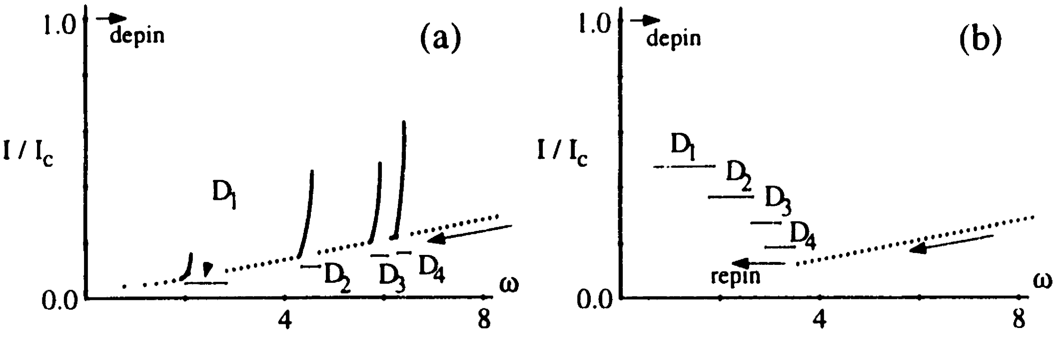

Fig. 6.2 Numerical I–V characteristics. (Frequency ω is used for the horizontal coordinate instead of voltage.) The interval D_m corresponds to the formula Eq.(6.23). Parameters: $N = 8$, $M = 0$, $\Gamma = 0.035$, and (a) $\Lambda = 1.6$, (b) $\Lambda = 0.8$.

the $m = 4$ step is missing in the experiment. This can be understood from the numerics in Fig. 6.2(a). The gap between intervals D_3 and D_4 is so small that there is little support for the $m = 4$ step. When the bias current in the numerics is swept a little faster, we observe that a trajectory does not stop at the $m = 4$ step, either, but makes a jump to the $m = 3$ step immediately.

Therefore, one sees that observation of the steps is closely related to the instability intervals D_m. It is necessary to study the locations and *widths* of D_m more carefully. Recall that a step seems to emanate from the lower-frequency end of each D_m. Thus, to have the m-th step, it is necessary that the whirling mode not only become unstable, but it must also *regain stability* at lower frequencies.

To illustrate this point more clearly, we show another numerical I–V curve in Fig. 6.2(b), using the same parameters as in (a) except that Λ is now reduced by half to 0.8. Now, we do not see a step at all, but the system jumps back to the superconducting state ($V = 0$) once the return branch becomes unstable. This is because all D_m overlap for this parameter set, and there is no point on the whirling branch for a step to bifurcate from. In the figure D_2 through D_4 are estimated by the formula Eq.(6.23). Ω_1^- is not shown since the estimate becomes clearly irrelevant due to the curvature of the tongue.

Occasionally, we observe "remnants" of steps in which the top part of a step still appears on the I–V, but the bottom part does not reach the whirling branch and is missing. This happens when the overlapping of the intervals D_m is relatively small, and a trajectory "fortunately" jumps into the domain of attraction of an attractor with a highly nonlinear motion. We are unable to analyze these more

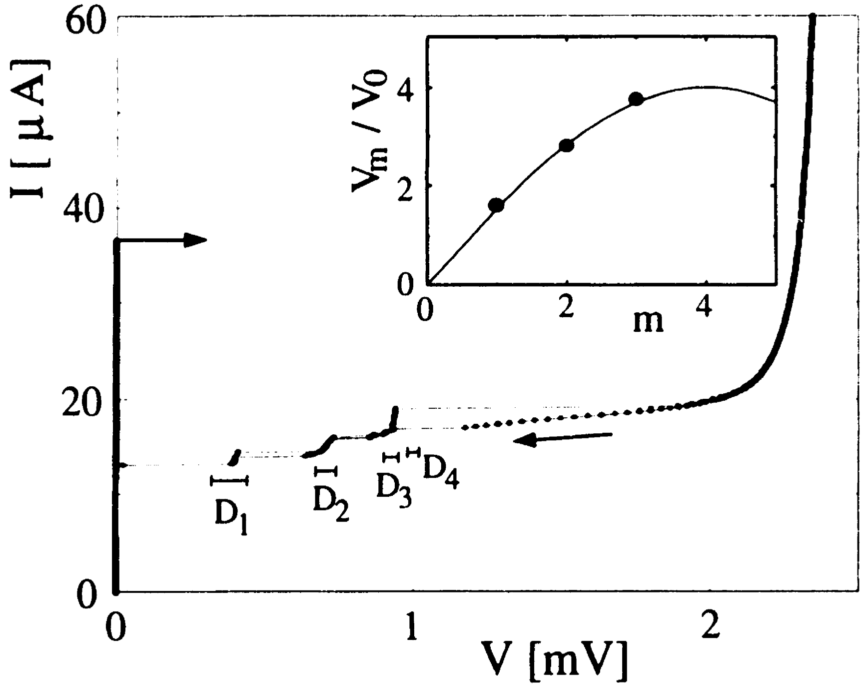

Fig. 6.3 Experimental I-V characteristic with $N = 8$, $M = 0$, $\Lambda^2 = 2.6$, and $\Gamma = 0.035$, which shows three resonant steps in the high-voltage region. The interval D_m corresponds to the formula Eq.(6.23). Inset: dots are measured voltage positions of the steps vs mode number m; curve is the leading order estimate $\omega = 2\omega_m$.

complicated attractors; but see Section 7 for numerical studies of the dynamics in this nonlinear regime.

6.2.3 Parameter regime for steps

In our experiments, these steps are observed only when the temperature is low, and when the system is underdamped and discrete. We make a rough estimate of the parameter regime when we expect to see the m-th step. The conditions are already described above; to summarize them, firstly, the instability interval D_m must exist. Damping causes the Mathieu tongue to shrink, and thus can kill the instability of higher wave numbers. (For the discrete ring, wavenumbers near $m = N/2$ are the first to be killed.) This occurs if Eq.(6.22) does not have a root, i.e. $\gamma > \epsilon$. Since $\omega \approx 2\omega_m$, this relation translates into

$$\omega_m < 1/(2\Gamma) \ . \tag{6.24}$$

Secondly, the intervals must have a space in between so that the whirling mode regains stability. For this to happen, it is necessary to have

$$\Omega^{+}_{m-1} < \Omega^{-}_{m} \tag{6.25}$$

for $m > 1$.

Thirdly, the basic solution $\phi^{*}(t)$ must exist. (Otherwise, the whole analysis is meaningless.) For the single junction equation Eq.(6.17), the periodic solution $\phi = \phi^{*}$ exists if and only if $I > I^{*}$ where $I^{*}(\Gamma)$ is the bifurcation current defined and discussed in Sec. 2.2 below Eqs.(2.24,2.25)). (At $I = I^{*}$ either a homoclinic or an infinite-period saddle-node bifurcation occurs.) Near $I \approx I^{*}(\Gamma)$, the branch of the in-phase solution on the I–V curve must be bent, and the motion deviates substantially from the whirling solution. As I is decreased below $I^{*}(\Gamma)$, the system is back in the superconducting state. Thus, there is a frequency ω_{min} below which the whirling in-phase oscillation cannot be sustained. Hence, any frequencies ω which appear in the analysis must at least satisfy:

$$\omega > \omega_{\text{min}} = I^{*}(\Gamma)/(\Gamma I_c) \tag{6.26}$$

to guarantee existence of ϕ^{*}.

After substituting the dispersion relation Eq.(6.14) into the three conditions, we obtain

$$\frac{[2 + I^{*}(\Gamma)/(\Gamma I_c)]^{1/2}}{4N\sin(m\pi/N)} < \frac{\Lambda}{N} < \frac{1/\Gamma}{4N\sin(m\pi/N)} \tag{6.27}$$

and

$$\frac{\Lambda}{N} > \frac{1}{2N\left[\sin((2m-1)\pi/N)\sin(\pi/N)\right]^{1/2}} \,. \tag{6.28}$$

(Scaling of Λ by N seems natural as will be seen below.) For the onset of the $m = 1$ step to exist, only the first relation is necessary. For the onsets of the $m > 1$ steps, both relations (6.27,6.28) must hold.

In Fig. 6.4(a) the shaded area is the parameter region in the $(\Lambda/N, \Gamma)$-plane where the onset of the m-th step can be observed for $N = 8$ rings. As shown, Γ has to be sufficiently small, or the onset will not be possible. For a fixed Γ, only an interval of Λ/N allows the onset.

For small Γ, $I^{*}(\Gamma)$ is almost linear, thus the left hand side of Eq.(6.27) does not depend strongly on Γ. Together with Eq.(6.28), this implies that the lower boundary of Λ/N is almost vertical. This estimate is affected by the curvature of the Mathieu tongue when N is large and m is small. On the other hand,

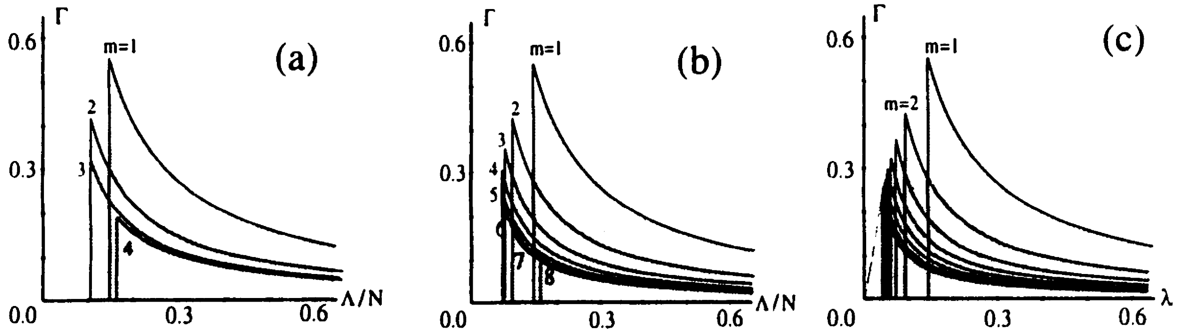

Fig. 6.4 Estimated regions in the parameter plane where an onset of the m-th step is expected to occur. For (a) $N = 8$ and (b) $N = 16$, the regions are given by Eqs.(6.27,6.28)) while, for (c) the continuum limit, Eqs.(6.31,6.32) are used. Small Γ and an intermediate Λ is necessary to expect the onsets.

the hyperbola in Fig. 6.4(a), given by the right hand side of Eq.(6.27), remains accurate for any N as long as Γ is small.

In Fig. 6.4(b) we show the region for $N = 16$. Now, there can be $N/2 = 8$ intervals at most so that $m = 1$ to 8 are shown. Qualitatively, the picture is unchanged.

The analysis and estimate can be extended to a continuous Josephson ring, whose governing equation is given by Eq.(2.19) and boundary condition in Eq.(2.20) with $M = 0$. We linearize the system around the in-phase whirling solution $\phi(x,t) = \phi^*(t) \approx \omega t$, then use Fourier series to decompose the perturbation into modes:

$$\phi(x,t) = \phi^*(t) + \sum_{m=-\infty}^{\infty} A_m(t) e^{2\pi i m x} \tag{6.29}$$

Then, $A_m(t)$ obeys the same equation Eq.(6.13) except m now ranges from $-\infty$ to ∞. The dispersion relation is also modified to

$$\omega_m = 2\pi\lambda m \; . \tag{6.30}$$

The conditions Eqs.(6.24–6.26) are unchanged. Thus, the onset of the m-th instability is expected to occur in the parameter region

$$\frac{[2 + I^*(\Gamma)/(\Gamma I_c)]^{1/2}}{4\pi m} < \lambda < \frac{1/\Gamma}{4\pi m} \tag{6.31}$$

and

$$\lambda > \frac{1}{2\pi[m^2 - (m-1)^2]^{1/2}} = \frac{1}{2\pi\sqrt{2m-1}} \tag{6.32}$$

The inequalities are, of course, the limit of Eqs.(6.27,6.28) as $N \to \infty$ while m is fixed, and where λ is identified with Λ/N.

The region is shown in Fig. 6.4(c). Again, we obtain a qualitatively similar picture. The only difference is that the tip of the shaded region approaches the origin as $m \to \infty$. Maginu [Mag83] has shown a numerical example of the period doubled solution in the continuous system, using a parameter set which translates into our expressions as $\Gamma = 0.15$, $I = 0.25$, and $\lambda \leq 0.17$. This is indeed within the shaded region in Fig. 6.4(c).

Finally, we note that Doedel *et al.* [Doe&al88] have obtained such a parameter region of instability for $N = 2$ junctions. They impose a constraint $I = (5/3)\epsilon$ and considers when $\epsilon \to 0$ (the conservative limit), thus comparison of our result with theirs is difficult. However, they find a similar tendency that damping must be small and the coupling be intermediate to see the period-doubling bifurcation from the in-phase solution.

6.3 Ring, $M > 0$

We turn to the case when there are M kinks trapped in a ring. For the high frequency region these kinks are "stretched," and the periodic solution is the whirling (but not in-phase) state:

$$\phi_j^*(t) \approx \omega t + \frac{2\pi M j}{N} \ . \tag{6.33}$$

(This is again the leading order term of a formal perturbation expansion. The next term is $O(\omega^{-2})$.) The perturbation is stil expanded in the discrete Fourier series Eq.(6.12). The modes are, however, now coupled The coupling can be of a long range, but under the approximation Eq.(6.33), the m-th mode is only coupled to the $(m \pm M)$-th modes:

$$\ddot{A}_m + \Gamma \dot{A}_m + \omega_m^2 A_m + \frac{1}{2}\left(e^{i\omega t} A_{m-M} + e^{-i\omega t} A_{m+M}\right) = 0 \ . \tag{6.34}$$

The trivial perturbation is still

$$u_j = \dot{\phi}_j^* \tag{6.35}$$

which corresponds to the $m = 0$ mode when we use the approximation Eq.(6.33) since $\dot{\phi}_j^* \approx \omega$ for all j.

In the previous section it was sufficient to approximate the instability boundaries only up to $O(\epsilon)$, where ϵ is the magnitude of the parametric forcing. Our analysis is the same here, by formally introducing ϵ in Eq.(6.34). Also, we neglect the effect of Γ for simplicity since the small damping was not important for the earlier estimates when $M = 0$. Then,

$$\ddot{A}_m + \omega_m^2 A_m + \epsilon \left(e^{i\omega t} A_{m-M} + e^{-i\omega t} A_{m+M} \right) = 0 \tag{6.36}$$

where $\epsilon = 1/2$. (We do not rescale time as we did in the previous section; it was more intuitive to use the picture of the Mathieu tongues for $M = 0$, but it is no longer useful for $M > 0$.) The lattice eigenfrequency ω_m is the same as in Eq.(6.14).

For $\epsilon = 0$, Eq.(6.36) is a set of harmonic oscillators with frequencies ω_m. Since the m-th oscillator is coupled only to the $(m \pm M)$-th ones, resonances occur in the $O(\epsilon)$ expansion at frequencies

$$\omega \approx \omega_\ell \pm \omega_{\ell+M} \tag{6.37}$$

for each integer ℓ. (We use m as a running index while ℓ is fixed.)

We analyze solutions near these frequencies [Nay&Moo79]. First, choose the positive sign. Let

$$\omega = \omega_\ell + \omega_{\ell+M} + \epsilon\sigma \tag{6.38}$$

where σ is a detuning parameter. We use the two time-scale method. Expand $A_m(t)$ in powers of ϵ.

$$A_m(t;\epsilon) = \sum_{p=0}^{\infty} \epsilon^p A_{mp}(T_0, T_1) \tag{6.39}$$

where $T_0 = t$ and $T_1 = \epsilon T_0$ are the fast and the slow time scales, respectively. We treat T_0 and T_1 as independent variables. Thus,

$$\frac{d}{dt} = \partial_0 + \epsilon \partial_1 \quad , \quad \frac{d^2}{dt^2} = \partial_0^2 + 2\epsilon \partial_0 \partial_1 + \epsilon^2 \partial_1^2 \tag{6.40}$$

where $\partial_p^s = \partial^s / \partial T_p^s$. We require A_{mp} to be bounded in T_0 for all m and all $p \geq 1$.

Substitute Eqs.(6.39,6.40) into Eq.(6.36), and equate like powers of ϵ. At $O(1)$, we obtain

$$\partial_0^2 A_{m0} + \omega_m^2 A_{m0} = 0 \quad . \tag{6.41}$$

The solution is

$$A_{m0}(T_0, T_1) = B_m(T_1) e^{i\omega_m T_0} + C_m(T_1) e^{-i\omega_m T_0} \tag{6.42}$$

for $m \neq 0$. Since $A_m = A^*_{-m}$ is necessary for the u_j's to be real, $A_{mp} = A^*_{-mp}$, too. Using $\omega_{-m} = \omega_m$,

$$B_m = C^*_{-m} \quad , \quad C_m = B^*_{-m} \quad . \tag{6.43}$$

Also, all indices are N-periodic.

At $O(\epsilon)$, we obtain

$$\partial_0^2 A_{m1} + \omega_m^2 A_{m1} = -2\partial_0\partial_1 A_{m0} - \left(e^{i\omega T_0} A_{m-M,0} + e^{-i\omega T_0} A_{m+M,0}\right) \tag{6.44}$$

which become, upon substitution of Eq.(6.42),

$$\begin{aligned}-(\partial_0^2 A_{m1} + \omega_m^2 A_{m1}) = 2i\omega_m \left(B'_m e^{i\omega_m T_0} - C'_m e^{-i\omega_m T_0}\right) \\ +B_{m-M} e^{i(\omega+\omega_{m-M})T_0} + C_{m-M} e^{i(\omega-\omega_{m-M})T_0} \\ + B_{m+M} e^{-i(\omega-\omega_{m+M})T_0} + C_{m+M} e^{-i(\omega+\omega_{m+M})T_0}\end{aligned} \tag{6.45}$$

where prime denotes differentiation with respect to the slow time T_1. Substitute Eq.(6.38). Then,

$$\begin{aligned}-(\partial_0^2 A_{m1} + \omega_m^2 A_{m1}) = 2i\omega_m \left(B'_m e^{i\omega_m T_0} - C'_m e^{-i\omega_m T_0}\right) \\ +B_{m-M} e^{i\sigma T_1} e^{i(\omega_\ell+\omega_{\ell+M}+\omega_{m-M})T_0} + C_{m-M} e^{i\sigma T_1} e^{i(\omega_\ell+\omega_{\ell+M}-\omega_{m-M})T_0} \\ + B_{m+M} e^{-i\sigma T_1} e^{-i(\omega_\ell+\omega_{\ell+M}-\omega_{m+M})T_0} + C_{m+M} e^{-i\sigma T_1} e^{-i(\omega_\ell+\omega_{\ell+M}+\omega_{m+M})T_0}\end{aligned} \tag{6.46}$$

The natural frequency on the left hand side is $\pm\omega_m$, and when the forcing terms on the right hand side have this frequency, then resonance occurs and the expansion Eq.(6.39) ceases to be uniformly valid. We will eliminate these secular terms in order to find the stability boundary of the whirling state.

On the right hand side, the first and the second terms are secular, and they can be eliminated by setting B_m = const. and C_m = const., if there are no other secular terms. This is the case for most m's except when $m = \pm\ell$ and $\pm(\ell + M)$. For $m = \ell$, the fifth term is

$$B_{\ell+M} e^{-i\sigma T_1} e^{-i\omega_\ell T_0} \quad ,$$

which is secular to the natural frequency of the left hand side $\omega = \omega_\ell$. This can be canceled out by the second term by imposing

$$-2i\omega_\ell C'_\ell + B_{\ell+M} e^{-i\sigma T_1} = 0 \quad . \tag{6.47}$$

For $m = \ell + M$, the fourth term,

$$C_\ell e^{i\sigma T_1} e^{i\omega_{\ell+M} T_0} \quad ,$$

now resonates with the natural frequency $\omega = \omega_{\ell+M}$. So, we impose

$$2i\omega_{\ell+M} B'_{\ell+M} + C_\ell e^{i\sigma T_1} = 0 \quad . \tag{6.48}$$

Now, solve Eqs.(6.47,6.48) to obtain

$$B_{\ell+M}(T_1) = -2\lambda\omega_\ell e^{i(\lambda+\sigma)T_1} \quad , \quad C_\ell(T_1) = e^{i\lambda T_1} \tag{6.49}$$

where

$$4\omega_\ell\omega_{\ell+M}\lambda^2 + 4\sigma\omega_\ell\omega_{\ell+M}\lambda + 1 = 0 \quad ,$$

or,

$$\lambda = -\frac{\sigma}{2} \pm \frac{1}{2}\sqrt{\sigma^2 - \frac{1}{\omega_\ell\omega_{\ell+M}}} \quad . \tag{6.50}$$

C_ℓ will have an exponentially growing component in T_1 if the argument of square root is negative. Otherwise, the solution is purely oscillatory and stable. The transition to the instability occurs at

$$\sigma = \pm(\omega_\ell\omega_{\ell+M})^{-1/2} \quad , \quad \lambda = -\sigma/2 \quad . \tag{6.51}$$

From Eq.(6.49), $B_{\ell+M}$ and C_ℓ oscillate at frequencies $(\lambda + \sigma) = +\sigma/2$ and $\lambda = -\sigma/2$, respectively, in the T_1 scale. Eqs.(6.46) for $m = -\ell$ and $-(\ell + M)$ are merely conjugates of $m = \ell$ and $\ell + M$, respectively, so that we obtain the same conclusion. Substituting Eq.(6.51) into Eq.(6.38), the estimate of the tongue of instability emanating from $\omega_\ell + \omega_{\ell+M}$ at $\epsilon = 0$ is

$$\omega = \omega_\ell + \omega_{\ell+M} \pm \frac{\epsilon}{\sqrt{\omega_\ell\omega_{\ell+M}}} = \Omega_\ell^\pm \quad , \quad \epsilon = 1/2 \quad . \tag{6.52}$$

The whirling solution is unstable within $\omega \in D_\ell$ where $D_\ell = (\Omega_\ell^-, \Omega_\ell^+)$ as we defined before for the case $M = 0$. Indeed, the interval given in Eq.(6.52) reduces to Eq.(6.23) for $M = 0$ with $\Gamma = 0$.

However, the type of bifurcation at the onset of instability is different when $M \neq 0$. From Eqs.(6.42,6.49,6.51), nontrivial modes at the onset take the form:

$$\begin{cases} A_{\ell 0} = \exp(-i\sigma T_1/2)\exp(-i\omega_\ell T_0) = \exp[-i(\omega_\ell + \epsilon\sigma/2)T_0] \\ A_{\ell+M,0} = \sigma\omega_\ell \exp(i\sigma T_1/2)\exp(-i\omega_{\ell+M} T_0) = \sigma\omega_\ell \exp[i(\omega_{\ell+M} + \epsilon\sigma/2)T_0] \ . \end{cases} \tag{6.53}$$

We choose the independent frequencies to be

$$\omega = \omega_\ell + \omega_{\ell+M} + \epsilon\sigma \quad , \quad \Delta\omega = \omega_{\ell+M} - \omega_\ell \ . \tag{6.54}$$

Then,

$$\begin{cases} A_{\ell 0} = \exp(-i\omega T_0/2)\exp(i\Delta\omega T_0/2) \\ A_{\ell+M,0} = \sigma\omega_\ell \exp(i\omega T_0/2)\exp(i\Delta\omega T_0/2) \ . \end{cases} \tag{6.55}$$

Thus, if we strobe the system at discrete times $T_0 = 2\pi k/\omega$, k = integer, to construct a Poincaré section, we would observe these amplitude variables oscillating at:

$$\text{the slow frequency} = \Delta\omega/2 \ . \tag{6.56}$$

The instability, therefore, generically leads to a Hopf bifurcation.

Analysis near $\omega = \omega_\ell - \omega_{\ell+M}$ can be carried out in a similar way. We find Eq.(6.50) arises as the stability criterion again (with a real λ corresponding to the stable situation), but the argument of the square root is now changed to $\sigma^2 + 1/(\omega_\ell\omega_{\ell+M})$. Thus, it is always positive, and the trivial solution is stable. There are no instabilities near these frequencies. When $\ell = 0$ or $\ell + M = 0$, Eq.(6.42) must be replaced. We do not pursue this exceptional case.

Fig. 6.5 compares the formula Eq.(6.52) with (a) experiment and (b) numerical simulation. (The I-V curves are the same as Fig. 3.1(a,b), respectively.) In the inset of Fig. 6.5(a), only the leading order estimate $\omega \approx \omega_m + \omega_{m+M}$ is compared to the observed voltage positions of the three resonant steps corresponding to $m = 1, 2, 3$. (Now, m is used to label the instability intervals.) The inset shows that the agreement is again very well without any fitting parameter.

The validity of the correction term in Eq.(6.52) can be checked by Fig. 6.5(b) which shows the Ohmic branch disrupted at each instability interval D_m. At $\omega = \Omega_m^+$ the bifurcation is subcritical while at $\omega = \Omega_m^-$ it is supercritical. In Section 7 we will look at dynamics along a step.

6.4 Arrays with open ends

For parallel arrays with open ends, the boundary condition Eq.(2.12) is replaced by Eq.(2.15). The strength of the external field is measured by the frustration f, which can assume any real value unlike M. The notion of the parametric instability holds in this case, too. The results are, however, more complicated. The parameter f can be restricted to $0 \le f \le 1/2$ as described in Section 2. Arrays with no frustration $f = 0$ are simple to analyze, as the modes decouple again,

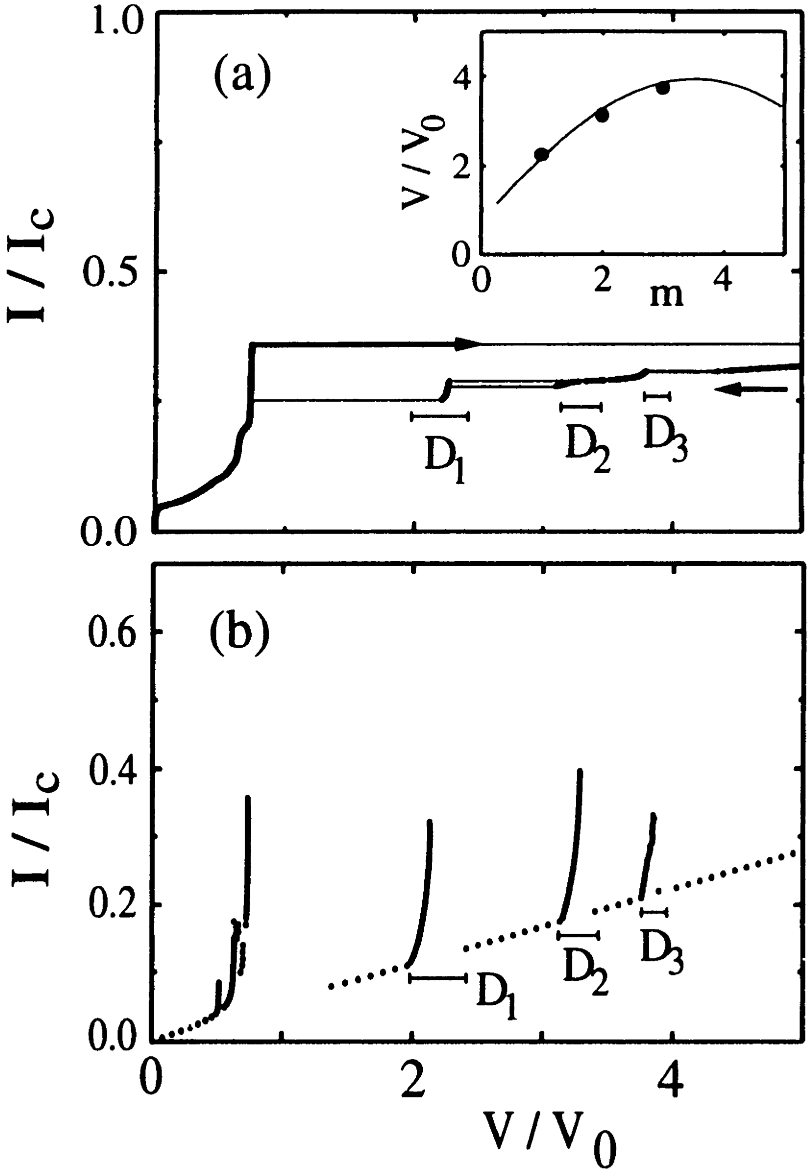

Fig. 6.5 (a) Experimental I-V characteristic with $N = 8$, $M = 1$, $\Lambda^2 = 2.6$, and $\Gamma = 0.035$ (same as Fig. 4.1(a)). The interval D_m corresponds to the formula Eq.(6.52). Inset: dots are measured voltage positions of the steps versus mode number m; curve is the leading order estimate $\omega = \omega_m + \omega_{m+M}$. (b) Numerical I-V curve (same as Fig. 4.1(b)). Voltage intervals D_1 to D_3 agree well with the intervals where the whirling solution becomes unstable.

so we treat this case separately. Frustrated arrays ($f > 0$) are not completely analyzed yet, and we will supplement analysis with numerical methods.

The first step for our analysis is to find the basic state for the ohmic branch of the I-V characteristics. In analogy to the ring, a linear function of the form

$$\phi_j(t) = \phi_j^*(t) \approx \omega t + 2\pi f j \tag{6.57}$$

is a good approximation. This solution undergoes parametric instabilities, and resonant steps also arise in the I-V curve for these arrays. To estimate the voltage locations, we linearize around the solution ϕ^*, then get the same system Eq.(6.2) with the boundary condition Eq.(6.4).

6.4.1 Zero field

When $f = 0$, the whirling solution Eq.(6.57) is j-independent and in-phase. The lattice eigenmodes are easily found. Expand u_j into the discrete Fourier cosine series [Pre&al92]

$$u_j(t) = \sum_{m=0}^{N-1}{}' \, A_m(t) \cos\left(m\pi(j - 1/2)/N\right) \quad , \quad j = 1, \ldots, N \tag{6.58}$$

which satisfy the open end boundary conditions Eqs.(6.4), instead of Eq.(6.12) for the ring. (Here, the prime for summation denotes a factor of 1/2 only in front of the $m = 0$ term.) Its inverse is

$$A_m(t) = \frac{2}{N} \sum_{j=1}^{N} u_j(t) \cos\left(m\pi(j - 1/2)/N\right) \quad , \quad m = 0, \ldots, N - 1 \; . \tag{6.59}$$

After substitution of (6.58) into the linearized system Eq.(6.2), we find that each mode is decoupled again so that we obtain the same equations Eq.(6.13) with the resonance condition $\omega \approx 2\omega_m$. Only the dispersion relation is different:

$$\omega_m = 2\Lambda \left|\sin(m\pi/2N)\right| \; . \tag{6.60}$$

Therefore, $N - 1$ instead of floor$[N/2]$ different resonant steps are observable.

Figure 6.6 shows the measured voltage steps versus mode number for an open-ended array with $N = 9$ junctions. As expected, $N - 1 = 8$ steps are present. The solid curve is the resonance condition $\omega = 2\omega_m$. As in the case of rings, no fitting parameters enter the analysis and good agreement exists between the data and theory.

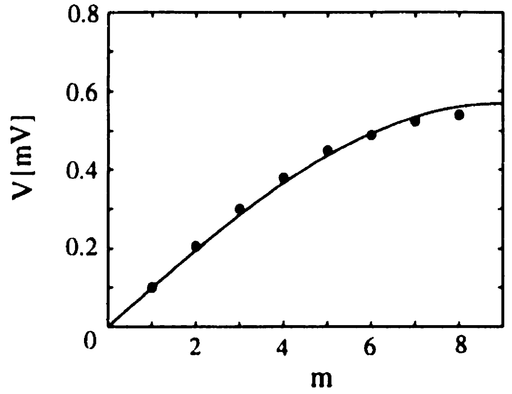

Fig. 6.6 Voltage locations of the zero-field steps in an open-ended array with $N = 9$ junctions. Parameters are $\Lambda^2 = 4.0$, $\Gamma = 0.063$, $f = 0$. dots: measured voltage positions of the steps versus mode number m; solid curve: theoretical estimate $\omega = 2\omega_m$ converted to voltages.

6.4.2 Frustrated arrays

Next, we turn to the more interesting case $f > 0$. Now the modes are coupled because of the j-dependence of the basic solution ϕ_j^* in Eq.(6.2). The coupling is also more complicated than in a ring with an integer $M > 0$.

Substituting the expansion Eq.(6.58) into Eq.(6.2) and using orthogonality, we obtain the modal equations:

$$\ddot{A}_m + \Gamma \dot{A}_m + \omega_m^2 A_m + \sum_{n=0}^{N-1}{}' \, c_{mn}(t) A_n = 0 \tag{6.61}$$

where the coupling coefficients are

$$c_{mn}(t) = c_{nm}(t) = \sum_{j=1}^{N} \cos\left(m\pi(j-1/2)/N\right) \cos\left(n\pi(j-1/2)/N\right) \cos\left(\phi_j^*(t)\right) . \tag{6.62}$$

Using the approximation Eq.(6.57), this can be written as

$$c_{mn}(t) = a_{mn}\cos(\omega t) - b_{mn}\sin(\omega t) \tag{6.63}$$

where

$$\begin{bmatrix} a_{mn} \\ b_{mn} \end{bmatrix} = \begin{bmatrix} \cos(\pi f) & -\sin(\pi f) \\ \sin(\pi f) & \cos(\pi f) \end{bmatrix} \begin{bmatrix} \alpha_{mn} \\ \beta_{mn} \end{bmatrix} \tag{6.64}$$

and

$$\alpha_{mn} + i\beta_{mn} = \sum_{j=1}^{N} \cos\left(m\pi(j-1/2)/N\right)\cos\left(n\pi(j-1/2)/N\right)\exp\left[2\pi i f(j-1/2)\right] \ . \tag{6.65}$$

When $2fN \neq$integer, this sum reduces to

$$\alpha_{mn} + i\beta_{mn} = (1/8)\sum_{s=1}^{4} i\left[1 - \exp(iq_s\pi)\right] / \sin(q_s\pi/2N) \tag{6.66}$$

where $q_{1,2} = 2fN \pm (m+n)$ and $q_{3,4} = 2fN \pm (m-n)$. Given (m, n, f), the last form allows easy evaluation of the coefficients, but the general trends of coupling strengths among modes are not so transparent. When $2fN$ =integer ("commensurate" frustrations), arguments of the summation become simplified, but bookkeeping of all combinations of (m, n) is still tedious. Since one of the denominators becomes small when $q_s \approx 0$ (mod $2N$) for some s, the modes m and n are most strongly coupled, roughly speaking, near such frustrations as $2fN = m - n$. However, even at these frustration values, the other terms do not necessarily vanish, and the situation is not as clean as in the ring geometry with $M > 0$.

We have not yet analyzed the above system. Instead, we determine the instability intervals numerically to see the general pattern. For a fixed ω, we integrate the system Eq.(6.2) for one period $T = 2\pi/\omega$, and compute $2N$ Floquet multipliers μ_j. The whirling mode is destabilized for the frequency ω in the intervals $|\mu_j| > 1$ for some j. For the basic state $\phi_j^*(t)$, we use the whirling mode approximation Eq.(6.57) rather than the exact periodic solution of the governing equation Eq.(2.11). This cuts down the numerical effort extensively not only because the system size is halved, but also we do not need to find the periodic solution and its period. They are trivially "known". More importantly, finding the periodic solution in the unstable case requires continuation, which is not an easy task. As we have obtained a very good agreement in the previous sections for the case of the ring by using the whirling mode approximation, we expect this approach to be meaningful and effective here as well.

Figure 6.7 is an example of a computation for an $N = 8$ array frustrated by $f = 0.07$ at the open ends. For this small frustration, we do not observe the low-voltage region. The high-voltage region in the I-V characteristic is shown in Fig. 6.7(a). Magnitudes of the Floquet multipliers $|\mu_j|$ estimated by the above method are shown in Fig. 6.7(b). In both figures the horizontal axis is the frequency ω, converted to the normalized voltage V/V_0.

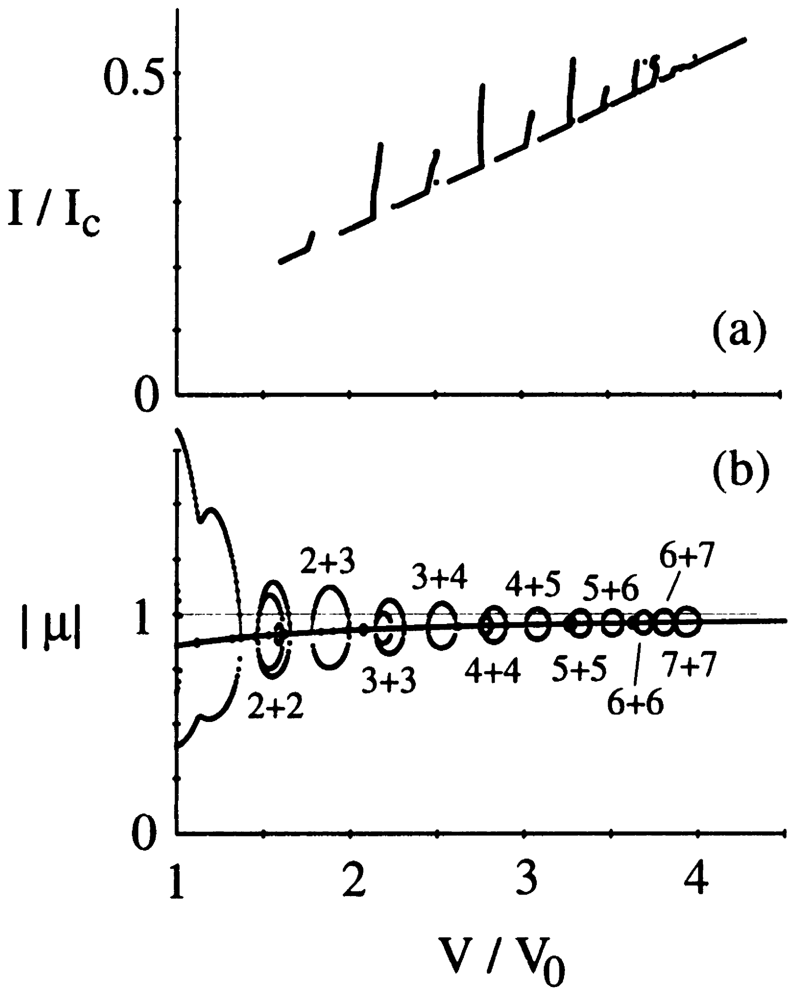

Fig. 6.7 (a) A partial view of a numerical I–V characteristic for the $N = 8$ ring, with $\Lambda^2 = 2.6$, $\Gamma = 0.08$, and $f = 0.07$, showing more than $N - 1$ steps. (b) Magnitude of Floquet multipliers for the same parameters. (The basic solution is approximated by the whirling solution.) The whirling solution branch becomes unstable when magnitude of the largest multiplier exceeds unity. Such voltage ranges agree with the intervals in (a) where the return path is disrupted. The instabilities occur due to resonances at combination frequencies: such combinations are numbered. For example, "3+4" in (b) denotes the resonance near $\omega = \omega_3 + \omega_4$.

In Fig. 6.7(a) the ohmic branch is disrupted at about ten intervals; the voltage positions of the intervals agree with the regions in Fig. 6.7(b) in which at least one $|\mu|$ exceeds unity. This confirms the validity of the whirling approximation.

In Fig. 6.7(b) the magnitudes of the multipliers seem to be "symmetric" with respect to a certain curve; this is due to the symmetry of Eq.(6.10). The curve is the radius of the circle C, given by

$$\exp(-\Gamma T/2) = \exp(-\Gamma\pi/\omega) = \exp\left[-\Gamma\pi(V/V_0)^{-1}/\Lambda\right] \ . \qquad (6.67)$$

In Fig. 6.7(b), we do not see the trivial multiplier of unit magnitude (nor its symmetric counterpart with magnitude $\exp(-\Gamma T)$). This is the only significant error introduced by the whirling approximation. The two multipliers are now approximated as a complex conjugate pair on the circle C, and have radius Eq.(6.67). Fortunately, these multipliers are not related to predicting the instability intervals, as shown in Fig. 6.7(b); thus this effect is not important in our study.

A more substantial effect in Fig. 6.7 is due to the non-zero f. There are instability intervals corresponding to $\omega \approx 2\omega_m$, $m = 2, \ldots, 7$ as marked in Fig. 6.7(b). Interestingly, we also see that combination frequencies corresponding to $\omega = \omega_m + \omega_{m+1}$, $m = 1, \ldots, 6$ are excited. This coexistence of various combination frequencies is an effect not seen in the ring, and because of this, it is possible to have more than $N - 1$ resonant steps from N junctions.

Moreover, as f increases, other combination frequencies, such as $\omega_m + \omega_{m+2}$, are excited. This pattern is seen in Fig. 6.8 which shows the (approximated) instability zones as a function of both ω (converted to voltages V/V_0) and f. The frustration f is varied from 0 to 0.6, thus the figure is symmetric with respect to the horizontal $f = 0.5$ line. The shaded areas represent parameter sets for unstable whirling solutions. Fig. 6.7(b) is calculated along the $f = 0.07$ line (indicated by a dashed line in Fig. 6.8). Some combination resonances are numbered. For example, "3+5" in the figure means the resonance $\omega \approx \omega_3 + \omega_5$.

The stability calculation assumes that ϕ^* exists and can be approximated well by the whirling solution. Since substituting the assumed form Eq.(6.57) into the governing equation reduces to the single junction equation Eq.(6.17), the frequency still needs to satisfy Eq.(6.26). Since $I^*(\Gamma)/(\Gamma I_c) \approx 4/\pi$ [Guc&Hol83] for $\Gamma = 0.08 \ll 1$, this minimum voltage for $\Lambda = 1.6$ is about $V/V_0 \approx (4/\pi)/1.6 \approx 0.8$. Thus, all voltages shown in Fig. 6.8 satisfy this condition. In addition, there is a critical voltage similar to $V_\ell(M)$ which separates the low- and the high-V regions in a ring. Since these steps branch off from the return path (high-V), the

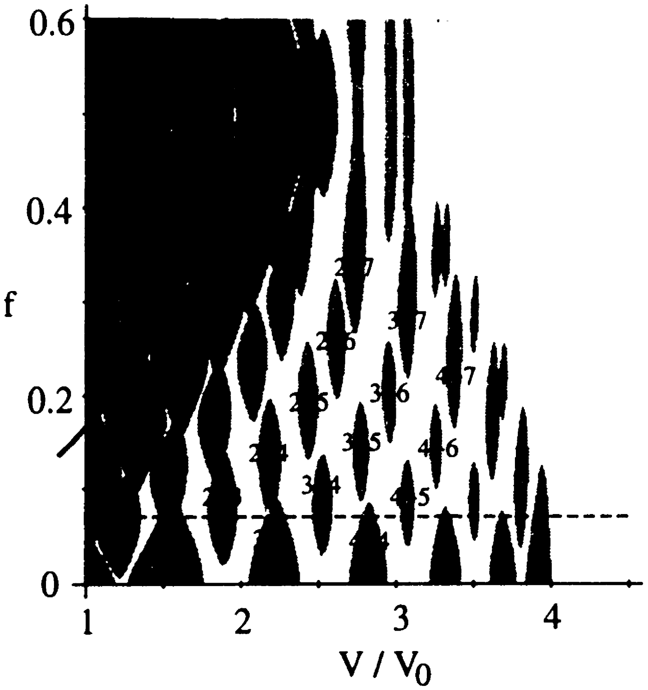

Fig. 6.8 Stability estimate of the whirling solutions with respect to the whirling frequency ω (converted into voltages V/V_0) and frustration f. The other parameters are fixed: $N = 8$, $\Lambda^2 = 2.6$, and $\Gamma = 0.08$. White areas correspond to stable whirling solutions while shaded ones correspond to unstable solutions. Fig. 6.7(b) is taken along the horizontal line $f = 0.07$. Some combination resonances are marked; for example, "2+3" indicates the resonance at $\omega \approx \omega_2 + \omega_3$. The solid curve is the critical voltage $V_\ell(f)$ corresponding to the "speed of light" in the system.

region below this critical voltage is meaningless. The critical voltage is given by

$$V_\ell(f)/V_0 = 2\sin(f\pi) \quad , \tag{6.68}$$

and M in the formula Eq.(3.1) for a ring is replaced by fN. This curve is shown in Fig. 6.8 as a solid curve.

The pattern of the combination resonances is fairly clear for the chosen parameter set, and (in principle) may be analytically explained by considering the coupling coefficients of the modal equations. Qualitatively, as f is increased, the m-th Fourier mode becomes coupled to further and further modes $m + 1$, $m + 2$, and so on. Roughly, we see mode m coupled to $m + 2fN$ when f is small. For example, the resonances 2+4, 3+5 and 4+6 all occur near the line $f = 2/(2N) = 0.125$. However, this rule is not strict as we observe resonances

2+6 and 4+7, for instance, for $f = 0.25$. Thus, the situation is more complicated than in a ring.

Each instability zone corresponds to a resonant step as we observed in Fig. 6.7. We always fix f, thus we cross these zones horizontally. The bifurcation on the left side of the zone is supercritical while it is subcritical on the right side. When two zones overlap, we do not see onsets of two steps but only one. Thus, the width of the zones is important.

The width depends mainly on Λ. If we recall our analysis in a ring with $M = 0$, then the width is, from Eq.(6.23), about $2\omega_m \times 2/(4\omega_m^2) = 1/\omega_m$ which is proportional to $1/\Lambda$. The separation between two resonant frequencies is proportional to Λ so that the relative size of the instability interval would change like $1/\Lambda^2$ as Λ is changed. From Eq.(6.52), we obtain the same dependence on Λ for the ring with $M \neq 0$. Although we do not have an analogous explicit expression for the frustrated open-ended arrays, we have observed a similar trend in our computations. As Λ is decreased from the value of Fig. 6.8, the instability zones grow and overlap, and would eventually kill the resonant steps by eliminating the stable regions.

The effect of damping Γ is primarily expressed through the curve Eq.(6.67). It controls the radius of the circle C, and thereby governs the overall stability. For small Γ, the circle is near the unit circle, and the largest Floquet multipliers easily cross over to the unstable region. As Γ becomes large, this crossover becomes more difficult, and some instability intervals are killed, in which case most of the shaded zones in Fig. 6.8 would be eliminated. Therefore, we conclude that the resonant steps can be observed only in an intermediate regime of the parameters. In particular, we expect the dependence on Λ and Γ to be qualitatively similar to Fig. 6.4.

6.5 Discussion: comparison to Fiske and zero-field steps

In this section we continue our discussion of arrays with *open ends*, and relate our study to previous analyses developed for a continuous Josephson junction.

In the last section, a testable prediction is obtained that it is possible to observe more than $N-1$ steps in a discrete array of N junctions with open ends. In preliminary experiments we have observed 14 steps in an $N = 9$ junction linear array. Although we have not yet made this into a quantitative comparison, the prediction appears to be correct.

These steps are generalizations of the so-called *zero-field steps* (ZFS) which have been intensively studied in a continuous Josephson junction [Soe&al84, For&al90] (and, only recently, in a discrete array [Ust&al95]) with open ends when no external magnetic field is applied. In the continuous system the dispersion relation is given by Eq.(6.30) and is linear in the mode number m. Since the period-doubling bifurcation triggers the instability at zero field [Tak82, Cha&Che80], the steps are seen at $\omega \approx 2\omega_m = 2m\omega_1$, i.e. at even multiples of the first eigenfrequency ω_1.

There are also additional steps called the *Fiske steps* (FS) that appear only when an external magnetic field is applied. These steps occur in an upgoing part of the I-V, i.e. in the low-voltage region $V < V_t(f)$. Their locations are observed to be at $\omega \approx m\omega_1$ where m is an integer. Thus, the first zero field step (ZFS1) is observed at the same voltage position as the second Fiske step (FS2), but ZFS1 occurs at $f = 0$ while FS2 occurs at higher f when $V_t(f)$ exceeds the voltage corresponding to $2\omega_1$.

In the literature, there are several explanations of the m-th Fiske step. Some authors [Due&al81, Ern&al83, Soe&al83] describe that, on the FS1, a moving kink travels down the array, and upon its exit, a breather or a localized plasma wave reflects at the boundary. When the reflected wave returns to the other side, the next kink enters. On the FS2, a kink and a reflected wave travel in the opposite directions. This so-called "fluxon picture" is only qualitative, and it is not clear why a breather or a plasma wave (which should be a standing wave by definition) should run back from one boundary to another and is reflected as the next kink. These authors are more interested in the application of the junctions to flux-flow oscillators, thus are urged to explain the dynamics in a very long junction (compared to the penetration depth) near the top of a step. In this regime, the motion is highly nonlinear and little analysis has been made, hence even a qualitative description may be useful. Our approach, however, is to first analyze the bottom part of a step clearly, then gradually follow the step toward the top. From this point of view, the qualitative reasoning does not explain the *origin* of the steps.

Other authors [Lik86, Sol72] take a more quantitative approach to explain the Fiske steps in terms of excitation of the m-th cavity mode (linear standing wave) by a moving train of kinks. They write the sine-Gordon equation Eq.(2.19) and assume a basic state

$$\phi^*(x,t) = \omega t + fx \tag{6.69}$$

(the boundary conditions being $\phi_x(0,t) = \phi_x(1,t) = f$). However, instead of linearizing around this state, they write an incorrect perturbation equation

$$u_{tt} + \Gamma u_t - \lambda^2 u_{xx} = \sin \phi^* - I/I_c \tag{6.70}$$

for the perturbation u. The right hand side is thought as a periodic forcing term, and resonance occurs when $\omega = m\omega_1$. Although this "derives" the right set of frequencies, the analysis is inconsistent since Eq.(6.70) now has an $O(1)$ quantity on the right hand side while the left hand side is $O(u) \ll O(1)$.

An improved explanation follows Kulik [Kul67] who correctly linearized the equation and employed Floquet theory. This method has been applied both to the zero-field steps [Tak82, Cha&Che80] and to the Fiske steps [Enp&al81, Cha&al82] in relatively short continuous junctions. Kulik assumed a single-mode excitation, but Enpuku *et al.* [Enp&al81] showed that multi-mode oscillations (combination resonances) are necessary to explain the experimental data. The analysis of [Enp&al81] is similar to the continuous version of our analysis in Sec.6.4. They assume the basic state to be the whirling solution Eq.(6.69), and derive modal equations that are the continuous analog of our Eq.(6.61). Then, they estimate the solutions of the equations by the method of harmonic balance while we study the system perturbatively by introducing ϵ. Their agreement between predictions and experiments is very good.

This coincidence of their analysis and ours is not obvious — indeed, it is puzzling since Fiske steps occur in the *low*-voltage region while our assumption of the whirling solution is valid only in the *high*-voltage region. In our underdamped discrete arrays, the basic state in the low-voltage region is far from linear in j, and an assumption like Eq.(6.69) is not accurate. Fortunately, everything becomes consistent when one notices the parameter values used. The assumption Eq.(6.69) is also valid when the penetration depth (width of the kink) is much larger than the length of the continuous junction, i.e. $\lambda^2 \gg 1$. (This is indeed the regime where the Fiske steps are observed.) Then, the kink will appear still "stretched" over the whole array.

This analogy suggests that our analysis in Sec.6.4 is perhaps also applicable to predicting Fiske steps in discrete Josephson arrays with open ends when $\Lambda^2 \gg 1$. In the continuous system, one encounters a difficulty in predicting the Fiske steps due to linearity of the dispersion relation Eq.(6.30); one forcing frequency ω can correspond to multiple combinations of modes. However, in the discrete arrays, identifying the combination for a particular step is perhaps easier since, e.g., $\omega_1 + \omega_2 \neq \omega_0 + \omega_3$ etc.

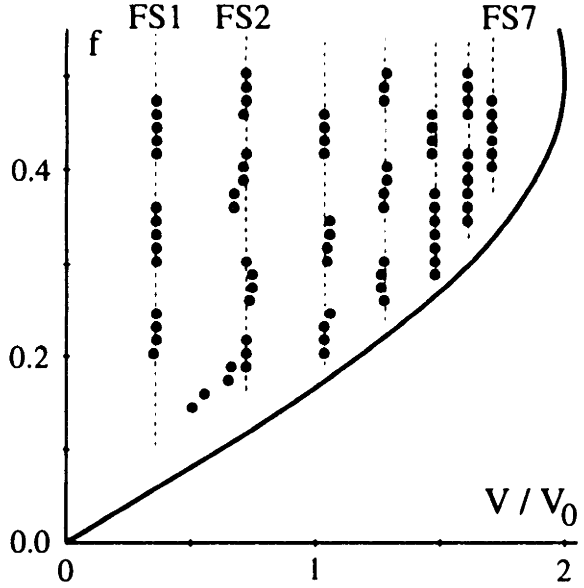

Fig. 6.9 Dots represent the voltage locations of Fiske steps observed experimentally in an open-ended array of $N = 9$ junctions with $\Lambda^2 = 4.1$ and $\Gamma = 0.12$ at $T = 7.3$ K [vdZ&al94-1] varying frustration f. The steps are located along the dashed lines of constant voltages, FS1 (the first Fiske step) through FS7 (the seventh). There is a zone structure similar to Fig. 6.8. The solid curve is the critical voltage $V_\ell(f)$.

Recently, measurements have been made on Fiske steps in open-ended arrays of $N = 9$ to 20 junctions [vdZ&al94-1, Ust&al92]. In Fig. 6.9, a measurement using $N = 9$ and $\Lambda^2 = 4.1$ is shown. The locations of the steps (in terms of V/V_0) are mapped out as a function of f. We see zones (clusters of data points) similar to those in Fig. 6.8, but they are located in the low-voltage side of the critical voltage $V_\ell(f)/V_0 = 2\sin(\pi f)$ (shown as a solid curve).

The data points appear to lie on a set of vertical lines, corresponding to a set of f-independent voltages. In terms of frequencies, these selected voltages agree reasonably well with the lattice eigenfrequencies ω_m, given by Eq.(6.60). As described as above, this is why the m-th Fiske step is thought to be originated from excitation of the m-th cavity mode. But these locations may be also explained in terms of combination resonances between mode 0 (translation) and m whose summed frequencies still equal ω_m. This should then be derived from the modal equations Eq.(6.61).

We hope to investigate this point in the future. However, even at this stage,

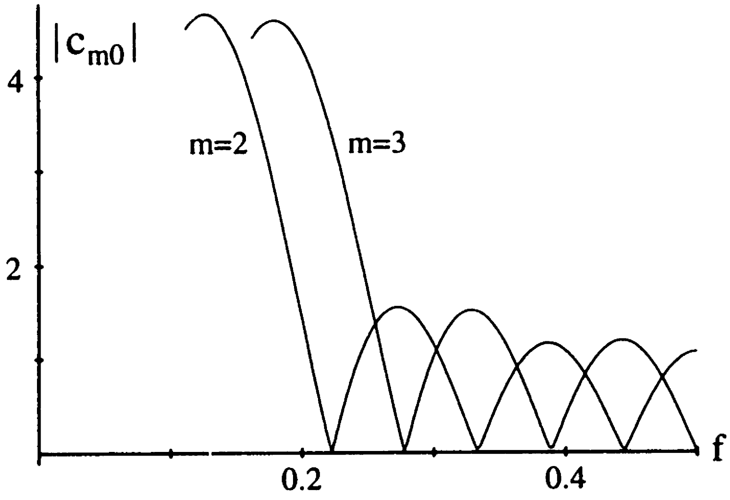

Fig. 6.10 Magnitudes of the coupling coefficients between the mode 0 and $m = 2$ or 3. The magnitudes appear to be large at the frustrations where Fiske steps are observed in Fig. 6.9.

we may ask how strong the couplings between these modes are, by numerically evaluating the magnitude of the coupling coefficient c_{0m} in Eq.(6.63). If it is large, then it is likely to survive in the presence of damping and to cause instability of the basic solution. (The magnitude corresponds to ϵ used in the analysis of a ring with $M > 0$. See Eq.(6.36).)

Fig. 6.10 shows the magnitude $|c_{0m}|$ for $N = 9$ as a function of f. Only $m = 2$ and 3 are shown for brevity. Since Fiske steps occur only when the resonance frequency is in the low-voltage region, we only consider the range

$$V(\text{step}) < V_\ell(f) \; . \qquad (6.71)$$

Since $V(\text{step})/V_0 = \omega_m/\Lambda$, this condition simplifies (for $0 < f < 1/2$) to

$$f > m/(2N) \; . \qquad (6.72)$$

For both $m = 2$ and 3, only this frustration range is shown.

Now we compare the numerical predictions with the experimental data. In Fig. 6.10, we see peaks in $|c_{20}|$ at $f = 0.28$, 0.38, and 0.5. In Fig. 6.9, FS2 are observed in the neighborhood of these frustrations. FS2 appears at $f < 0.22$ in the experiment, too, which corresponds to the rapid rise of $|c_{20}|$ in Fig. 6.10. For FS3, we find peaks in Fig. 6.10 at $f = 0.33$ and 0.44. Again, steps are observed at these frustration values in the experiment.

Therefore, this very preliminary observation suggests that analysis of the coupled modal equations Eq.(6.61) leads to estimates of the Fiske step locations. If this conjecture indeed works out, then we may understand both the Fiske and the zero-field(-type) steps in a continuous or a discrete medium in a simple unified manner. Moreover, calculating up to the leading order corrections, we may be able to estimate the voltage intervals and parameter regions where we see such structures, in a similar manner to our analysis in a ring.

7 Dynamics along a step

In this section, we numerically study the dynamics along a step in the high-voltage region after the whirling solution becomes unstable. Our analysis in the previous section provides much information at the onset of instability, which we will test against simulations in this section. The dynamics far from the onset is hard to analyze; we follow the bifurcation sequence of attractors numerically, and visualize the dynamics using, e.g., Poincaré sections. Although this study is only qualitative and preliminary, a generic feature of the dynamics along a step is found; namely, the dynamics is simple both at the bottom and at the top of a step while it can become quite complicated in the middle. At the top of a step, large amplitude oscillations appear to be sustained "naturally." We focus our attention on the Josephson rings to avoid further complications due to reflections from open boundaries. We discuss the dynamics when there is no trapped kink ($M = 0$) in Sec.7.1, and when there is a kink ($M = 1$) in Sec.7.2.

7.1 $M = 0$

We have simulated rings with both $N = 8$ and $N = 10$ Josephson junctions. There seems to be a relation between the size of the ring and the complexity of the dynamics. The rings with $N = 10$ junctions are more interesting in the sense that we observe bifurcation sequences. For $N = 8$ with $M = 0$, on the other hand, we did not observe bifurcations after the initial period-doubling bifurcation. In this section, we report observations on the $N = 10$ ring.

Parameter values $\Lambda^2 = 1$ and $\Gamma = 0.1$ are used, and the numerical I–V curve is shown in Fig. 7.1. Four steps are seen. Since $M = 0$, there is no low-voltage region in this case. The superconducting ($V = 0$) state goes up all the way to $I = I_c$. A jump to the right occurs at the critical current, and the system is then on the ohmic line where the attractor is the in-phase whirling solution. As I is decreased, the I–V follows its return path. The in-phase state is stable down to $V/V_0 = 4.2$, but it becomes unstable for almost all the lower voltages.

The intervals of instability D_1 through D_5 are estimated as in Section 5, and shown in Fig. 7.1 as horizontal bars. There are small gaps between neighboring intervals, where the whirling solution recovers stability. Thus, there are onsets of instability occuring along the ohmic line. The only exception is the onset of the mode $m = 5$. Since D_4 and D_5 overlap, there is no onset for the perturbation of this mode. Indeed, we do not observe the fifth step in the simulation. The first

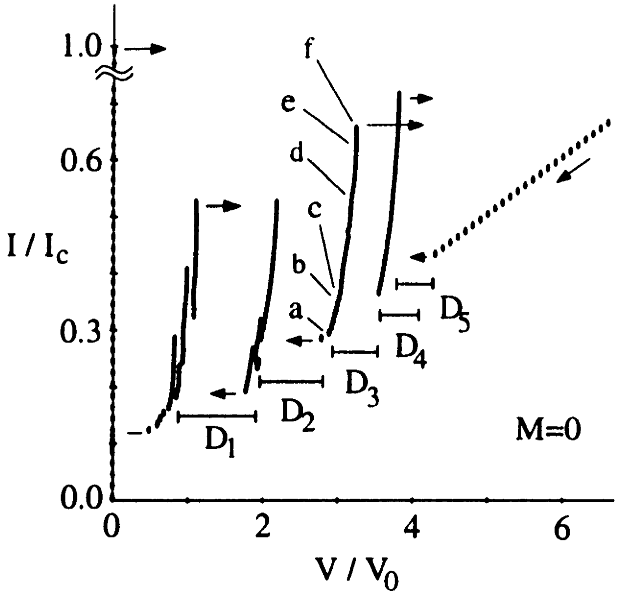

Fig. 7.1 Numerical I-V for $N = 10$, $M = 0$, $\Lambda^2 = 1.0$, and $\Gamma = 0.1$. There is no low-voltage region, and four stpes are observed in the high-voltage region. The whirling in-phase solution becomes unstable in the intervals D_1 through D_5. The third step, which emanates from an edge of D_3, is studied in detail at points marked from "a" to "f".

and second steps (at the left of D_1 and D_2) appear to have substructures.

The dynamics along the $m = 3$ step, which emanates from the left edge of D_3, is now carefully studied. Attractors at the six points marked from "a" through "f" on Fig. 7.1 are visualized in the following. The first set of graphs is Fig. 7.2, in which $\sin\phi_2$ is plotted against $\sin\phi_1$. This is a Lissajous figure made of supercurrents through the two junctions. Fig. 7.2(a) to (f) correspond to the points "a" to "f" on Fig. 7.1, respectively.

Figure 7.2(a) shows the stable in-phase solution before instability sets in. As I is increased, the solution period-doubles (Fig. 7.2(b)), as expected from our analysis in the previous section. The attractor is now a double loop, and becomes more complicated as I is increased. However, this process is *not* the start of a period-doubling cascade to chaos. Instead, the next bifurcation is a secondary supercritical Hopf bifurcation to a 2-torus (Fig. 7.2(c)). When the torus breaks, an apparently irregular motion emerges (Fig. 7.2(d)). This attractor appears chaotic, but our preliminary computation of the largest Lyapunov exponent for (d) is zero, thus it is likely to be a quasi-periodic attractor with more than two frequencies.

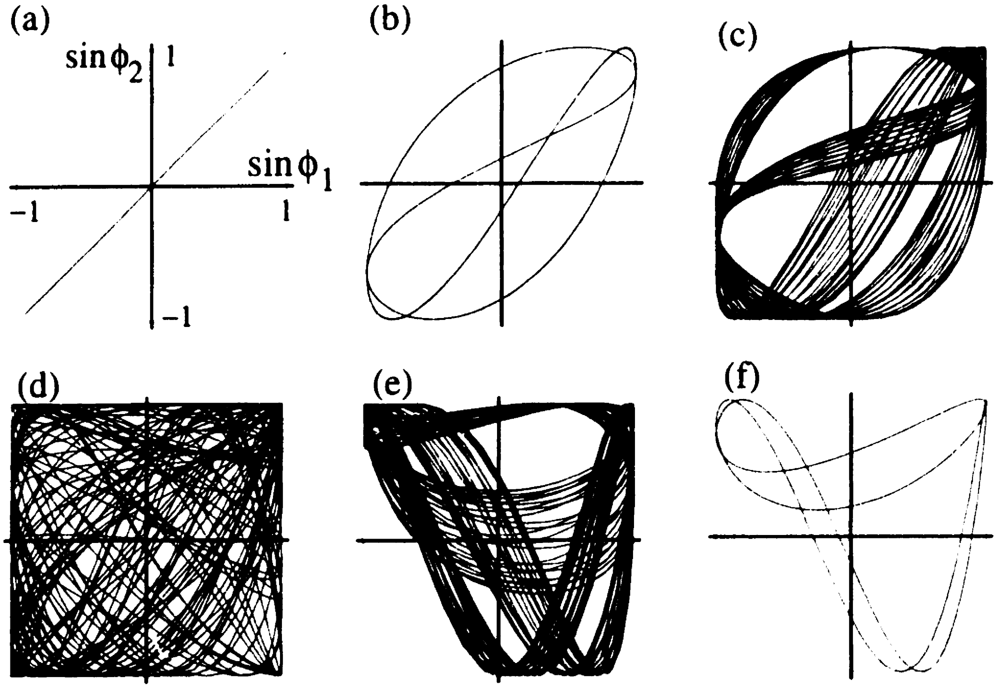

Fig. 7.2 Lissajous figures made of two supercurrents $\sin\phi_1$ and $\sin\phi_2$, showing temporal dynamics of the system. (a) in-phase, (b) period-doubled, (c) 2-torus, (d) irregular, (e) reversion to 2-torus, and (f) period-doubled. The labels (a-f) denote positions on a step in Fig 7.1.

Somewhat unexpectedly, the dynamics does *not* become more complicated as the bias current is increased further. In fact, reversion to a 2-torus attractor occurs as in Fig. 7.2(e), then the torus shrinks back to a period-doubled limit cycle in Fig. 7.2(f), which then disappears as I is increased slightly more. This causes a jump from the step to the whirling branch as shown in the I–V curve in Fig. 7.1.

To eliminate one frequency from these diagrams, Poincaré sections are calculated by strobing the phases at each time the mean phase $N^{-1}\sum_{k=1}^{N}\phi_k$ becomes 0 (mod 2π). Then, these sections are projected onto a plane as shown in Fig. 7.3. The axes of the projected plane are still $\sin\phi_2$ versus $\sin\phi_1$. Only three cases (c–e) are shown since the periodic attractors in (a,b,f) would, of course, appear as just one or two dots in the section. In Fig. 7.3(c), we see two "lines"; these are actually two closed loops, but projected in an unfortunate direction. It confirms that the attractor is quasi-periodic with two frequencies. Fig. 7.3(d) still appears irregular despite the removal of one frequency. Reversion to a 2-torus is clearly seen from the two closed loops in Fig. 7.3(e).

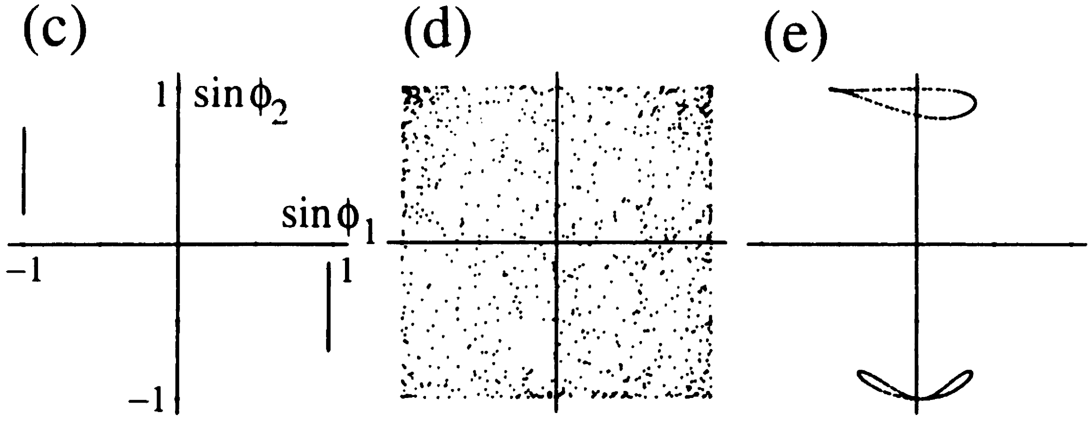

Fig. 7.3 Projections of Poincaré sections at test points (c–e). (c) two closed loops appearing as if two lines, (d) apparently irregular, (e) two closed loops.

Figures 7.2 and 7.3 only show temporal dynamics. To visualize the corresponding spatial structures, we first show instantaneous waveforms (snapshots) in Fig. 7.4. (Here, a waveform means a graph of $\phi_j(t)$ versus j, for fixed t.) For all the cases, five snapshots of the waveforms, when the mean phase $\bar{\phi}$ becomes 0, π, 2π, 3π, and 4π, are shown.

Instead of the in-phase solution for (a), which would show five straight lines, we show the case (a'). This case uses a slightly larger I than (a), and occurs immediately after the period doubling. The waveforms in (a') are still almost straight, but with a slight modulation, as expected. The phases between the second snapshot ($\bar{\phi} = \pi$) and the fourth (3π) are opposite. Thus, the solution requires a 4π increase in $\bar{\phi}$ to complete its period, as expected for period-doubling. We observe three crests and troughs in the waveforms, consistent with the step number $m = 3$ and the parametric excitation of spatial Fourier mode $m = 3$.

Fig. 7.4(b) is still a period-doubled limit cycle, but its spatial amplitude is larger as it is far from the onset. The junctions seem to have separated into four "clusters". Junctions 2 and 3 as well as 7 and 8 are pairs almost in phase, while junctions 4-5-6 and 9-10-1 are triplets, oscillating in a zig-zag fashion. In Fig. 7.4(c), a quasi-periodic solution, we observe that asymmetry is generated. The clustering is not as rigid as in (b); it appears in the figure as a pair 2-3 sitting next to another pair 4-5. Unlike in (b), there is a movement in the j-direction, and the pairs and triplets change members on a longer time scale. This shift seems to explain the second frequency. In Fig. 7.4(d), the amplitude is further increased,

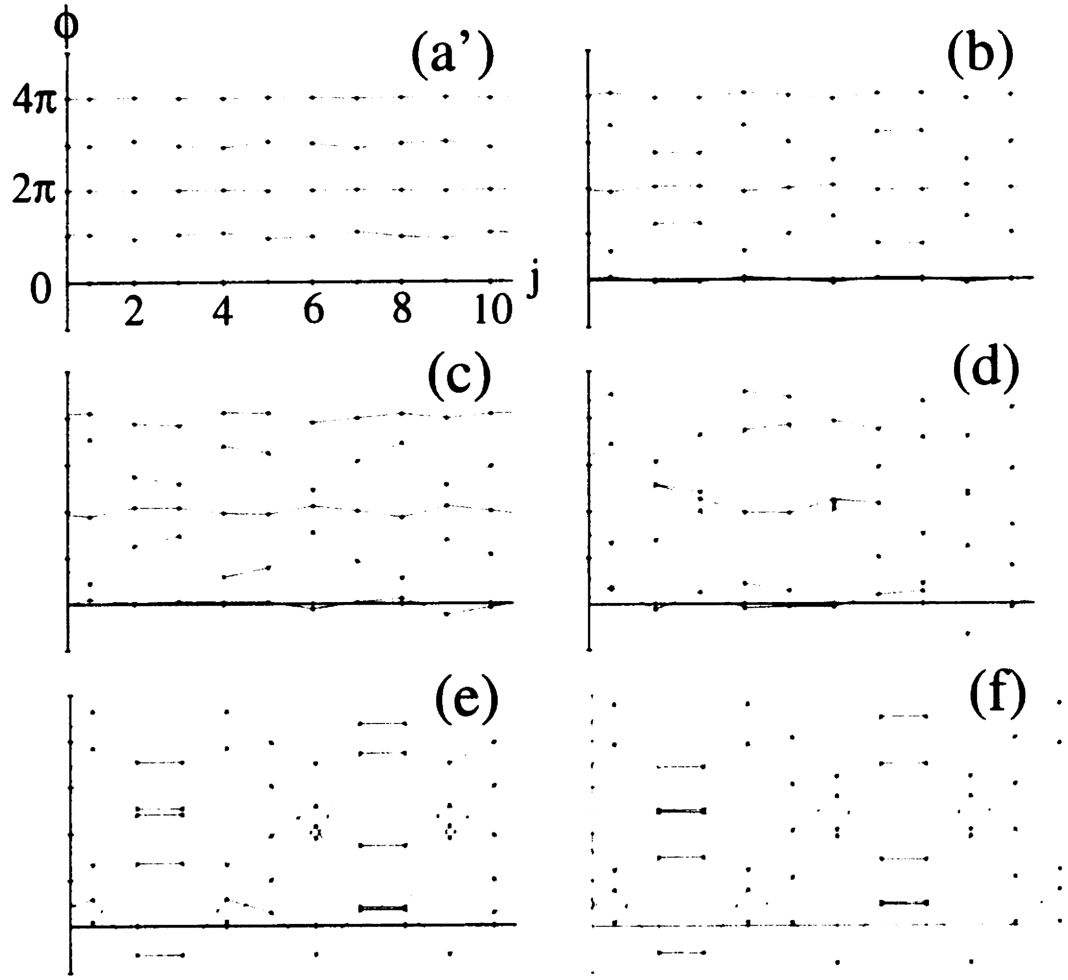

Fig. 7.4 Snapshots of ϕ_j at five instances of time when the average phase equals to 0, π, 2π, 3π, and 4π. (a') immediately after period-doubling, (b) still period-doubled, (c) asymmetric appearance when quasi-periodic, (d) irregular, (e) regeneration of pairs and triplets, (f) periodic (period-doubled) motion.

and we start to observe "kinks and antikinks" where ϕ changes from one junction to the next rapidly (more than π). We do not see a stationary pattern, and the dynamics is complicated.

From this point, the pattern becomes simpler which seems to be related to regeneration of the clusters. In Fig. 7.4(e), two pairs and two triplets are formed again, and are fairly rigid. However, there is still a horizontal motion. In Fig. 7.4(f), the clusters are now fixed. The pattern repeats itself in a periodic way, and a large amplitude standing wave (breather) is formed.

Such changes in the spatio-temporal dynamics may be more quantitatively seen in terms of the discrete Fourier modes $A_m(t)$ (defined in Eq.(6.12)). In Fig. 7.5 time-series of the magnitudes $|A_m(t)|$ are shown. In Fig. 7.5(a,b), only A_3 is excited, with (b) showing a larger magnitude. Let us check the oscillation frequency. As we see about 46 crests in (a,b) from $t = 0$ to 100, the period is $T = 2 \times 100/46$. (Two crests in the magnitude corresponds to one full cycle in A_3.) Thus, the frequency of the $m = 3$ mode is $2\pi/T \approx 1.45$. This is close to the natural frequency $\omega_3 = 1.61$, computed from Eq.(6.14) for $\Lambda = 1$, $m = 3$ and $N = 10$. If we include the correction term, then ω equals Ω_3^- rather than $2\omega_3$, and A_3 should oscillate at $\Omega_3^-/2$. From Eq.(6.23), this gives about 1.45 which is in agreement with the observed frequency in Fig. 7.5(a,b).

In Fig. 7.5(c) we observe the modes 1,2, and 4 are slightly excited. The mode $m = 2$ appears to have an incommensurate frequency from A_3. All modes are excited in Fig. 6.5(d) although the $m = 3$ mode is still the most active one. The mode $m = 1$ apparently fluctuates aperiodically. As the standing wave structure starts to be formed, we observe decay of the modes $m \neq 3$ in Figs. 7.5(e,f). In (f), virtually only A_3 is active, with a much larger amplitude than in (b).

7.2 $M = 1$

We now consider similar numerical experiments for the case when one kink ($M = 1$) is trapped in a ring. Figure 7.6 shows the I-V characteristic for $M = 1$, but otherwise with the same parameter values as in Fig. 7.1. There are now four intervals of instability, denoted by D_1 to D_4, corresponding to the resonance frequencies $\omega \approx \omega_m + \omega_{m+M}$. The intervals D_3 and D_4 overlap, and we do not see the $m = 4$ step. The other intervals are separated by gaps, though tiny, from which three steps emanate. For this case, the low-voltage region can also be seen in the I-V.

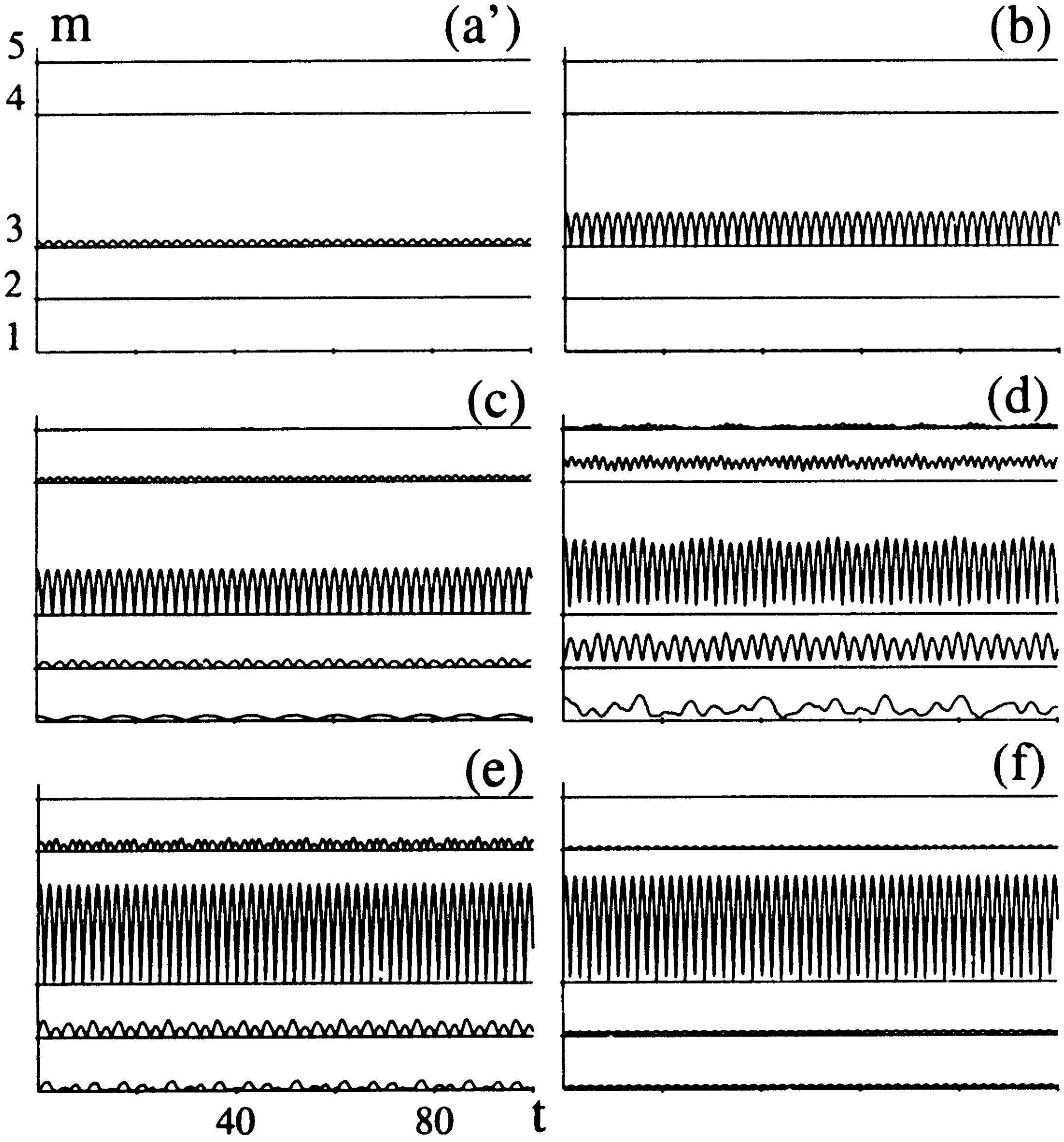

Fig. 7.5 Magnitudes of discrete Fourier modes $|A_m(t)|$ as a function of t. Only the $m = 3$ mode is excited in (a') and (b). The other modes are activated from (c) to (e), but are suppressed again in (f).

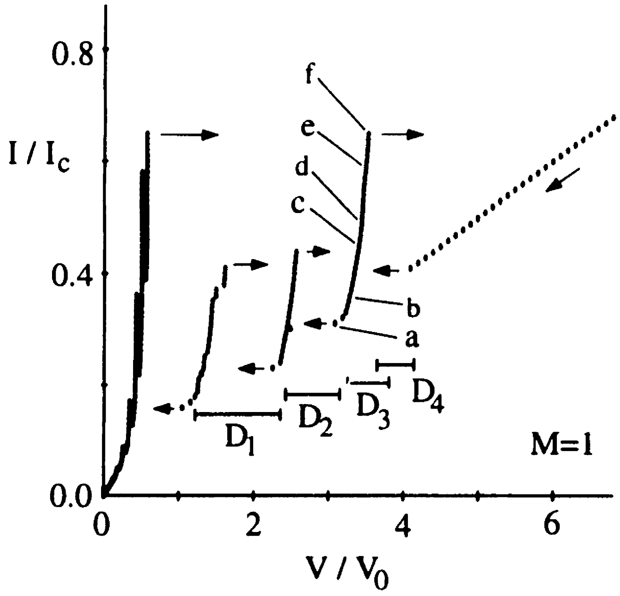

Fig. 7.6 Numerical I-V for $N = 10$, $M = 1$, $\Lambda^2 = 1.0$, and $\Gamma = 0.1$. Three steps in the high-voltage region are clear. The whirling solution becomes unstable in the intervals D_1 through D_4. The third step, which emanates from an edge of D_3, is studied in detail at points marked from "a" to "f".

Again, the $m = 3$ step is studied in detail, at the points marked "a" through "f". We first study the temporal dynamics by (projections of) Poincaré sections. The definition of the section as well as the coordinates are the same as before. Fig. 7.7 shows the sections for (a–f). In (a) we see only one point near (0.4,0.9), corresponding to the periodic whirling solution before instability. As I is increased slightly from this value, a Hopf bifurcation takes place, as expected from Eq.(6.56). The resulting 2-torus appears in the section as a closed loop. As I is increased further, the loop becomes larger. In (b) it appears as a figure "8" due to the projection.

Further bifurcations occur as I becomes larger, and the section at (c) appears complicated. However, this may be again just a quasi-periodic solution with a complex shape or more than two frequencies. We have not measured the Lyapunov exponents. In this region we observe another section as in (d), which may form a very complex but single loop. These rather complicated attractors exist till higher current values, for example, at (e). But at the top of the step, we observe again a closed loop. This shows that the attractor at (f) is only a quasi-periodic solution with two frequencies. Somehow, in a manner that is not yet clear, this solution

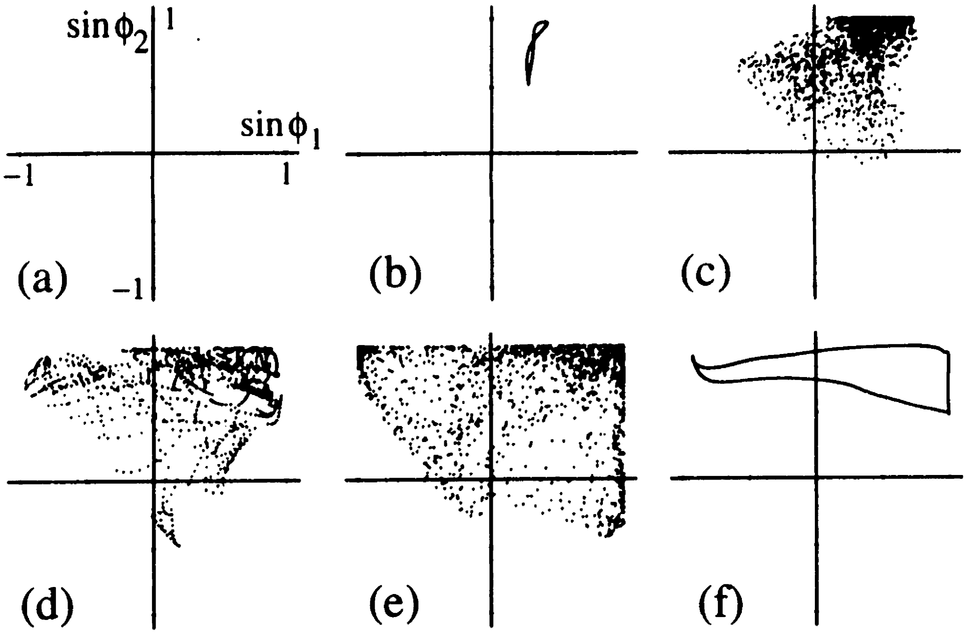

Fig. 7.7 Projections of Poincaré sections at test points (a–f). (a) one dot near (0.4,0.9) indicating a periodic attractor, (b) a closed loop after Hopf bifurcation corresponding to quasi-periodicity with two frequencies, (c–e) complex attractors in the middle of a step, (f) a quasi-periodic attractor.

disappears or loses stability at (f), causing a jump to the ohmic branch.

Fig. 7.8 shows magnitudes of the discrete Fourier modes in order to study spatio-temporal structures. To compute the "modes" we have subtracted from the phases ϕ_j the whirling solution component $2\pi j/N$. Then, the resulting part is processed by the discrete Fourier transform. The case (a') again uses a slightly larger I than (a) in order to show the dynamics immediately after instability sets in.

In both (a,b), two wavenumbers $m = 3$ and $m = 4$ are excited in agreement with the combination resonance described in Sec.6.3; the $m = 3$ step is created by instability of the whirling solution with respect to both modes $m = 3$ and $m + M = 3 + 1 = 4$. The magnitudes of these modes are almost stationary. We have examined the real parts of A_3 and A_4 at (b), and observed that they oscillate at frequencies (2π/period) 1.50 and 1.79, respectively. The values are close to the natural frequencies of the modes $\omega_3 = 1.62$ and $\omega_4 = 1.90$. When the correction term $(-\epsilon\sigma/2) = -1/(4\sqrt{\omega_3\omega_4})$ is subtracted, the values become 1.48 and 1.76, respectively. The mode $m = 1$ is also seen to have a small magnitude. We think

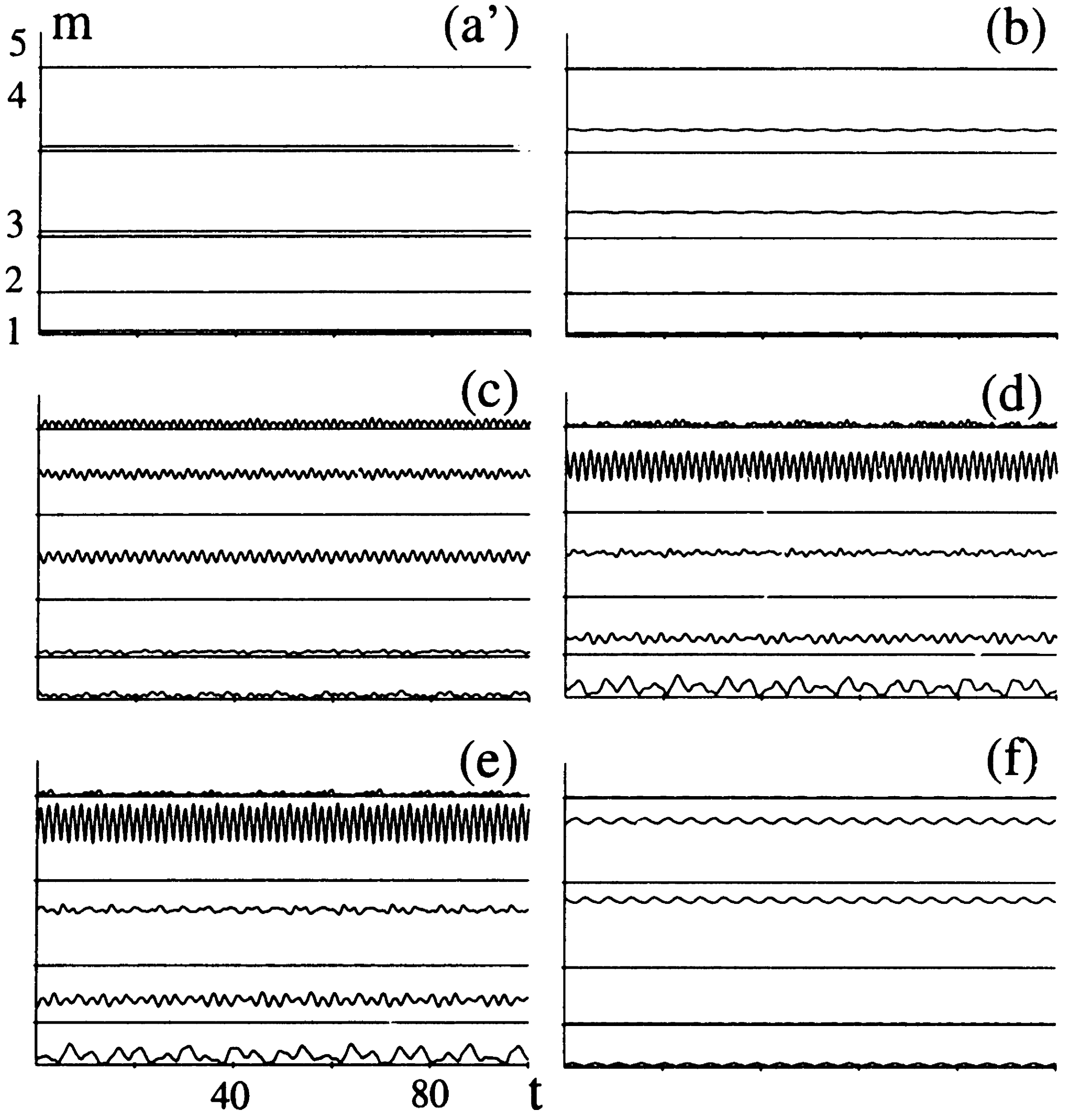

Fig. 7.8 Magnitudes of discrete Fourier modes $|A_m(t)|$ (after subtracting the whirling mode profile $2\pi j/N$ from phases ϕ_j) as a function of t. After onset of instability, the modes $m = 3$ and $m = 4$ are excited in (a') and (b). The other modes are active in (c–e) which is suppressed again in (f).

this originates from the discrepancy between the true waveform of the whirling solution and the assumed fit $2\pi j/N$. In fact, the real part of A_1 in (b) (not shown in the figure) oscillates at a frequency 3.30, a sum of two frequencies of A_3 and A_4. Thus, this is the "forcing frequency" for the linear modes $\Omega_3^- = \omega_3 + \omega_4 - \epsilon\sigma$ of Eq.(6.52).

In (c) through (e) the other modes are excited and appear aperiodic, but these modes are suppressed at the top of the step, (f). There, only the modes $m = 3$ and 4 contribute again, with much larger amplitudes than in (b).

7.3 Discussion

For both $M = 0$ and 1, we have studied the dynamics on the steps other than $m = 3$ in a similar manner. We have found both generic and step-dependent features.

Generically, the dynamics become simple (either periodic or quasiperiodic with two frequencies) near the onset *and* near the top of the steps. Near the onset, the solution is approximated well by the whirling solution with a small-amplitude excitation of one (for $M = 0$) or two (for $M = 1$) lattice eigenmodes superimposed. Near the top of a step, the fluctuation amplitude becomes large. The dynamics here can be described by interacting kinks and antikinks.

In the middle of a step, the behavior is step dependent. The solutions can become complicated as described above, or just quasiperiodic with two frequencies, as on the $m = 4$ step for $M = 0$. They can even remain periodic as observed in our simulation of $N = 8$ junctions. Steps with small m, e.g. the steps $m = 1$ and 2 in Fig. 7.1 or the step $m = 1$ in Fig. 7.6, contain substructures. We speculate that these finer steps come from combination of two mechanisms we discussed in this paper. When the number of kinks and antikinks are small compared to the junction number N, they have enough room to move back and forth in the j-direction. This causes excitation of small amplitude waves around the kinks, and they may phase-lock with the kink as we described in Section 5. However, since kinks and antikinks collide, annihilate, or reflect, it is not clear how this phase-locking can be achieved in order to predict the location of substructures quantitatively.

8 Conclusion and future directions

In the present paper we have studied underdamped discrete Josephson rings by analytical and numerical methods, using experiments as check points. Experimental I-V curves with $N = 8$ junctions show novel features, i.e. *steps* both in the low- and the high-voltage regions. The mechanisms which cause the steps are different in the two regions: phase-locking of a kink and a linear wave, forming a traveling wave, in the low-V region; versus parametric instabilities in the high-V region. We have also extended the analysis of parametric instabilities to discrete arrays with open ends, and compared this approach to previous analyses of Fiske steps in a continuous Josephson junction. We have studied the primary bifurcations in detail, and followed further secondary bifurcations by simulation. The dynamics at the top of a step seems to become simple, but with a large amplitude.

We list possible future directions and open problems.

[1] For a continuous ring, there is a clear cut voltage $V_t(M)$ (e.g. in Fig. 2.2) that separates the two regions. What happens near this voltage is fairly well understood. How should one think of this voltage, then, in the discrete case? In Fig. 4.4, we have shown evidence that this voltage smears out. This question is related to the existence of traveling wave solutions, and how the branches of such solutions would appear in the I-V characteristics.

[2] Can the prediction of the high wave number resonances (Sec.5.3) be experimentally observed? We have emphasized that this is an inherently nonlinear phenomenon. Are there any other systems where wavenumbers outside the first Brillouin zone become relevant?

[3] The calculation of parametric instabilities in a frustrated linear array (Sec.6.4.2) appears tractable. Does the same analysis also predict the locations of Fiske steps as combinations of mode 0 and m (Sec.6.5)?

[4] The dynamics along a step (Sec.7) is strongly nonlinear. Unfortunatelly, we lack powerful tools to analyze this fully nonlinear regime. One important question (both theoretically and technologically) is how the height of a step is determined. The $m = 3$ step in Fig. 7.1 ($M = 0$) appears to terminate in a saddle-node bifurcation of periodic solutions. The $m = 3$ step in Fig. 7.6 ($M = 1$) seems to never come back to a periodic state but to end as a quasi-periodic state. In either case, the attractors seem to disappear when the steps are terminated. This coincides with a conclusion by Forest *et al.* [For&al90], obtained for a continuous ring with one trapped kink $M = 1$; they showed numerical evidence that the jump

at the top of a step is a nonexistence phenomenon, as opposed to an instability mechanism. They assumed the length of the ring is infinite so that the problem can be mapped out on a geometrical picture involving global connection of fixed points. Can a similar approach be useful for our discrete, finite length rings?

[5] Yet another question on the dynamics along a step is how complicated it can be at the middle of the step. Maginu [Mag83], in his study of a continuous ring as well as an $N = 2$ array, has used Λ as a bifurcation parameter rather than I. He showed that, for both cases with no trapped kink $M = 0$, a period-doubling cascade to chaos can occur as Λ changes. Although this is not the natural parameter to vary in Josephson experiments, this may be a theoretically convenient bifurcation parameter to choose, even for study of the dynamics with general N and M.

Acknowledgments

The authors thank Mauricio Barahona, Amy Duwel, and Enrique Trias for helpful discussions, and acknowledge the support of AT&T, IBM, and MIT Lincoln Laboratory in the fabrication of the samples. Research supported in part by NSF Grants DMR-9402020 (to TPO), DMS-9057433 and DMS-9111497 (to SHS and SW). HSJvdZ acknowledges the support from Dutch Foundation for Fundamental Research on Matter (FOM), as does SW for A.P. Sloan dissertation fellowship.

References

[*] present address: Department of Theoretical and Applied Mechanics, Cornell University, Ithaca, NY 14853.

[†] present address: Department of Applied Physics, Delft University of Technology, P.O. Box 5046, 2628 CJ Delft, The Netherlands.

[Lik86] K.K. Likharev, *Dynamics of Josephson junctions and Circuits*, Gordon and Breach, New York (1986).

[Ust&al91] A.V. Ustinov, T. Doderer, R.P. Huebener, J. Mygind, V.A. Oboznov, and N.F. Pedersen, *IEEE Trans. Appl. Supercond.*, **3**, 2287 (1991).

[McL&Sco78] D. McLaughlin and A.C. Scott, in *Solitons in Action*, (eds. K. Longren and A.C. Scott, Academic Pr., New York, 1978).

[Kiv&Mal89] Y.S. Kivshar and B.A. Malomed, *Rev. Mod. Phys.*, **61**, 763 (1989).

[Ust&al95] A.V. Ustinov, M. Cirillo, B.H. Larsen, V.A. Oboznov, P. Carelli, and G. Rotoli, *Phys. Rev. B*, **51**, 3081 (1995).

[Sco69] A.C. Scott, *Am. J. Phys.*, **37**, 52 (1969).

[Nak&al74] K. Nakajima, T. Yamashita, and Y. Onodera, *J. Appl. Phys.*, **45**, 3141 (1974).

[Cir&al81] M. Cirillo, R.D. Parmentier, and B. Savo, *Physica*, **3D**, 565 (1981).

[Dun&al83] D.B. Duncan, J.C. Eilbeck, H. Feddersen, and J.A.D. Wattice, *Physica*, 68D, 1 (1983).

[Cos&al78] G. Costabile, R.D. Parmentier, B. Savo, D.W. McLaughlin, and A.C. Scott, *Appl. Phys. Lett.*, **32**, 587 (1978).

[Pac&al81] S. Pace, B. Savo, and R. Vaglio, *Phys. Lett.*, **82A**, 362 (1981).

[Dav&al83] A. Davidson and N.F. Pedersen, *Appl. Phys. Lett.*, **44**, 465 (1984); A. Davidson, B. Dueholm, B. Kryger, and N.F. Pedersen, *Phys. Rev. Lett.*, **55**, 2059 (1985).

[Ust&al92] A.V. Ustinov, T. Doderer, R.P. Huebener, N.F. Pedersen, B. Mayer, and V.A. Oboznov, Phys. Rev. Lett. **69**, 1815 (1992).

Heat Transfer in an Enclosed Rod Array

by

Randall D. Manteufel

Submitted to the Department of Mechanical Engineering
on May 22, 1991 in partial fulfillment of the
requirements for the degree of
Doctor of Philosophy

Abstract

An effective thermal conductivity (k_{eff}) and edge conductance model (h_{edge}) are developed theoretically for an enclosed rod array. The k_{eff} model is applicable in the interior of the rod array, and the h_{edge} model is applicable from the array edge to the enclosing wall. The k_{rad} model is derived theoretically, considering 1D heat transfer in either a square (SQ) or equilateral-triangular (EQ) array. A Monte Carlo and matrix-inversion technique are used to calculate the radiative transfer coefficients for both SQ and EQ arrays and are compared with Hill & Wilhelm's layer-transmittance model and Zehner's parallel-plate model. The radiative portion of the k_{eff}/h_{edge} model is validated analytically for the problem of 1D radiative transfer in a semi-infinite square array. A working hypothesis for the $k_{conv/cond}$ model is based on experimental studies in the literature and consists of a stagnant gas array conduction factor, F_{cond}, and a critical Rayleigh number, Ra_{crit}. Numerical calculations are reported for F_{cond} and compared with the analytical work of Rayleigh and others. A 2D, lumped k_{eff}/h_{edge} model is derived analytically using the Kirchoff transformation for either square, hexagonal or circular cross-sectional geometries. The lumped k_{eff}/h_{edge} model is applied to the problem of heat-generating nuclear spent fuel assembly, and is validated using experimental data from a series of real PWR tests (E-MAD), simulated PWR tests (SAHTT), consolidated BWR tests (REA), simulated 217-rod LMFBR tests (SNL), and 8x8 tests.

Thesis Supervisor: Neil E. Todreas
Title: Professor of Nuclear Engineering

[Boe&Wil89] R. Boesch and C.R. Willis, Phys. Rev. B **39**, 361 (1989).

[Ust&al93] A.V. Ustinov, M. Cirillo, and B.A. Malomed, Phys. Rev. B **47**, 8357 (1993).

[Nay&Moo79] A. H. Nayfeh and D. T. Mook, *Nonlinear Oscillations* (John Wiley & Sons, New York, 1979).

[Jor&Smi87] D. W. Jordan and P. Smith, *Nonlinear Ordinary Differential Equations*, 2nd ed. (Oxford Univ. Pr., Oxford, 1987).

[Gel&Lid58] I.M. Gel'fand and V.B. Lidskii, Amer. Math. Soc. Transl. **8**(2), 143 (1958).

[Wat&Swi95] S. Watanabe and J.W. Swift, preprint.

[Doe&al88] E.J. Doedel, D.G. Aronson, and H.G. Othmer, *IEEE Trans. Circ. Sys.*, **35**, no.7, 810 (1988).

[Pre&al92] W.H. Press, S.A. Teukolsky, W.T. Vetterling, and B.P. Flannery, *Numerical Recipes in Fortran* (2nd ed., Cambridge Univ. Pr., Cambridge, 1992).

[Guc&Hol83] J. Guckenheimer and P. Holmes, *Nonlinar oscillations, dynamical systems, and birfurcations of vector fields*, (Springer-Verlag, New York, 1983).

[Soe&al84] M.P. Soerensen, R.D. Parmentier, P.L. Christiansen, O. Skovgaard, B. Dueholm, E. Joergensen, V.P. Koshelets, O.A. Levring, R. Monaco, J. Mygind, N.F. Pedersen, and M.R. Samuelsen, *Phys. Rev. B*, **30**, 2640 (1984).

[For&al90] M.G. Forest, S. Pagano, R.D. Parmentier, P.L. Christiansen, M.P. Soerensen, and S.-P. Sheu, *Wave Motion*, **12**, 213 (1990).

[Tak82] K. Takanaka, *J. Phys. Soc. Jpn.*, **51**, 1089 (1982); K. Takanaka and T. Nagashima, *Sol. State Comm.*, bf 48, 839 (1983).

[Cha&Che80] J.-J. Chang and J.T. Chen, *Phys. Rev. B*, **22**, 2392 (1980).

[Due&al81] B. Dueholm, E. Joergensen, O.A. Levring, J. Mygind, N.F. Pedersen, M.R. Samuelsen, O.H. Olsen, and M. Cirillo, *Physica*, **108B**, 1303 (1931).

[Ern&al83] S.N. Erné, A. Ferrigno, and R.D. Parmentier, *Phys. Rev. B*, **27**, 5440 (1983).

[Soe&al83] M.P. Soerensen, N. Arley, P.L. Christiansen, R.D. Parmentier, and O. Skovgarard, *Phys. Rev. Lett.*, **51**, 1919 (1983).

[Sol72] L. Solymar, *Superconductive Tunnelling and Applications*, John Wiley and Sons, New York (1972).

[Kul67] I.O. Kulik, *Sov. Phys. JETP*, **24**, 1307 (1967).

[Enp&al81] K. Enpuku, K. Yoshida, and F. Irie, *J. Appl. Phys.*, **52**, 344 (1981).

[Cha&al82] J.-J. Chang, J.T. Chen, and M.R. Scheuermann, *Phys. Rev. B*, **25**, 151 (1982).

Acknowledgments

I am very much thankful for the support I have received during my memorable and enjoyable years at MIT. Although the period of my stay is felt to be so brief in retrospect, I still find too many names to acknowledge even using this narrow `\baselineskip`. Therefore, I would like to name only ———

Prof. Steve Strogatz not only introduced me to an interesting topic to work on and guided me throughout the course of this thesis, but also provided me with mental, financial, and linguistic support. In addition, I had opportunities to meet many researchers through him, which gave me a flavor of "the research community." I consider myself fortunate to have worked with the bright, considerate, and pleasant advisor as his first student.

Prof. Rubén Rosales accepted to be in my thesis committee in his sabbatical year, in addition to grading my homeworks and exams in three of his previous courses. I had been also constantly helped by the supporting stuff in the Mathematics department, especially Ms. Phyllis Ruby and Maureen Lynch.

Profs. Jim Swift, Kurt Wiesenfeld, and Mary Silber gave me valuable comments and suggestions on my first problem (Chapter 1) which was crucial to "kick off" my graduate research. It was also a very interesting (and weird) experience to work with Jim on my second project (Chapter 2) without meeting him in person. (We are *net surfers.*)

Prof. Terry Orlando, my thesis co-advisor, and Dr. Herre van der Zant responded to Steve's letter the next day, and thus weekly meetings started. Connection of my research to "real" experiments enhanced this thesis (Chapter 3), and moreover, this collaboration was pleasant. I thank them for not using many jargons to explain the problem to me.

Prof. Yoshiki Kuramoto and organizers of the summer workshop "Complex Systems II" (1993) helped my stimulating stay in Kyoto. Dept. of Theoretical & Applied Mechanics and Center for Applied Mathematics at Cornell Univeristy kindly provided my office spaces during the 1994/95 winter. It was inspiring for me, in particular, to come to know the views of Profs. Richard Rand and John Guckenheimer on coupled oscillators.

Fellow graduate students provided me with opportunities for my physical, spiritual, and spirituous recoveries, as well as with kind answers to my occasional dumb questions. Among them, I am most indebted to Peter Schmid, Carlos Celentano, Rodney Worthing, Dan Mahoney, and Jianke Yang. My office mate from the first day of arrival, Dmitry Vaynblat, has been an *extraordinarily* smart person, but fortunately with moderate athletic skills which made my ideal companion in swimming, tennis, soccer, water polo, and ping-pong. I thank the lab-mates, Mauricio Barahona, Amy Duwel, and Enrique Trías, in my second home at MIT for useful discussions and extra ice creams.

Carlos Mendizabal with his daughter Vanezza, as well as Martha, Cecilia, Erika Aviles and Douglas Spencer provided Latino musics, Cacho, Singani, and homey atmosphere, and made my first two years comfortable and relaxed.

I am also grateful for people who helped me to have this opportunity to come to MIT. Especially, I thank Profs. Paul K. Newton and Masahiro Shoji for their encouragement to pursue further graduate study, Judy & Joel Scallen for hosting my first year in the U.S., and Reiko & Masahiko Arita for many packages and goods to survive Boston winters.

Finally, I would like to thank Mieko & Yoshio Watanabe for their understanding and dedication.

——— Research funded in part by NSF grants DMS-9057433 and DMS-9111497 through Steve Strogatz, and the Alfred P. Sloan Foundation doctoral dissertation fellowship. A part of computation was carried out on a Connection Machine 5, supported in part by Project SCOUT: ARPA Contract# MDA972-92-J-1032.

end of thesis (200 pages)